University of South-Eastern Norway

www.usn.no

FMH606 Master's Thesis 2021

<Energy and Environmental Technology>

Design of an Industrial Chlorination Reactor using CPFD Simulations

Zahir Barahmand

Faculty of Technology, Natural sciences and Maritime Sciences

Campus Porsgrunn

University of South-Eastern Norway

www.usn.no

Course: FMH606 Master's Thesis, 2021

Title: Design of an Industrial Chlorination Reactor using CPFD Simulations

Number of pages: 160

Keywords: fluidized bed, reactor design, Computational Fluid Dynamics for particles, CPFD, reactor optimization, cyclone, circulating fluidized bed, Aluminum production, chlorination reactor, Alcoa process, reactor optimization

Student:	Zahir Barahmand
Supervisor:	Chandana Ratnayake
External partner:	Chameera Jayarathna, SINTEF Tel-Tek

University of South-Eastern Norway

www.usn.no

Summary:

Aluminum is now the world's second most used metal. Since aluminum has a unique combination of appealing properties and functionalities, it allows for significant energy savings in many applications, such as vehicles and buildings. Although this energy-saving leads to lower CO_2 emissions, the production process of aluminum still dramatically impacts the environment.

The process used almost exclusively in the aluminum industry is the Hall-Héroult process with a considerable amount of carbon footprint with high energy consumption. As the best alternative, Alcoa's process (which is not industrialized yet) is based on the chlorination of processed aluminum oxide, reducing the traditional method's negative impacts.

In continuation of Alcoa's effort, the present study aims to investigate the possibility of a new sustainable and low-carbon aluminum production process by designing an industrial fluidized bed reactor equipped with an external (due to high corrosion inside the reactor) gas-solid separation unit to handle a total of 0.6 kg/s of solid reactants and produce aluminum chloride as the main product. The research focuses on determining the best bed height based on the available reaction rates, determining the best reactor dimension to reduce particle outflow under isothermal conditions (700°C), and optimization the reactor to achieve minimum channeling in the bed, enhancing the hydrodynamics through Computational Particle Fluid Dynamic (CPFD) simulations using commercial software; Barracuda®. The optimization stage includes changes in the reactor geometry, fluid inflow pattern, and distribution system.

On the other hand, The relevant process is an exothermic reaction in a fluidized bed reactor, where solid alumina reacts with chlorine and carbon monoxide and produces aluminum chloride as the main product of the process, besides carbon dioxide can be separated. The previous studies have assumed an isothermal condition at 700℃, which is the optimum temperature for this reaction. The reactor's temperature has been kept in the range of 650-850℃ (most preferably 700℃) because below that temperature range, the reaction rate drops and above that range, the alumina (which usually is γ-alumina) will be transferred to θ-alumina and α-alumina phases which is not desirable for the purpose.

Based on previous simulation studies (isothermal), the CPFD method has been utilized to thermal study and simulate the overall heat transfer of the system, including convective fluid to the wall, fluid to particle, and radiation heat transfer. By comparing the thermal results from Barracuda®, it is found that the needed total heat duty transferred to the environment agrees well with the Gibbs reactor simulation in Aspen Plus® (~ 1.62 MW). Radial and axial heat transfer coefficient profiles at different levels show that almost all the heat has been transferred in the lower half of the reactor, making the design more challenging. At the steady-state, the range for the fluid temperature inside the reactor has been recorded 700-780℃.

In the present study, Autodesk Inventor®, Barracuda®, and Aspen Plus® are used for 3D modeling of the reactor, CPFD simulation for multiphase (solid-gas) reaction, and process simulation for validating the CPFD results, respectively.

Preface

The report has been written as a part of the subject FMH606 master thesis at the University of South-Eastern Norway, spring semester 2021.

I would like to express my sincerest gratitude to my supervisors Prof. Chandana Ratnayake from USN/SINTEF and Dr. Chameera Jayarathna from SINTEF Tel-Tek, for their guidance, recommendations, and unwavering support. They have been incredibly supportive of my ideas and the work I have had about this research project. They have been very patient and kind with my questioner nature, and whenever I have needed help, they were available. I am ecstatic to be working under their supervision and feeling highly fortunate.

I would thank Sam and Rosemary Clark from CPFD Software for all Barracuda® virtual reactor training and their unbelievable technical support and assistance. They gave invaluable support to make this model more realistic based on available information.

I extend my deepest thanks to Espen Tjønneland Wefring and Bjørnar Gjesdal for their kind support and advice during the project to brighten some unclear points about the reaction.

I value supports and guidance that the department of process and environmental engineering's members, especially Prof. Lars A. Tokheim have provided.

Finally, I would also like to appreciate my friend's kind effort during various stages of my thesis preparation.

Porsgrunn, 19.05.2021

Zahir Barahmand

Contents

Nomenclature

Symbol	Description	Units
A	Discrete particle acceleration	[m/s^2]
a	The absorption coefficient of the fluid mixture	[1/m]
a_f	The absorption coefficient of fluid	[1/m]
A_p	The particle's surface area	[m^2]
a_p	The equivalent particle absorption coefficient	[1/m]
A_{pr}	The projected area of particle	[m^2]
A_{po}	The overall surface area of that particle	[m^2]
A_s	Equivalent volume average area density	[m^2]
A_w	The area of the thermal wall	[m^2]
C	Concentration	[mole/m^3]
$\hat{C}$	The average concentration in the control volume	[mole/m^3]
C_d	Drag coefficient	[-]
C_{in}	The concentration of substances that enters the control volume	[mole/m^3]
C_{out}	The concentration of substances that leaves the control volume	[mole/m^3]
C_p	The average specific heat capacity for the entire reactant mixture	[j/K]
$c_{p,f}$	Fluid heat capacity	[j/K]
D	Cyclone diameter	[m]
$\acute{D}$	Drag function	[N]
D_d	Diameter of the cyclone's dust outlet	[m]
D_e	Diameter of the cyclone gas exit	[m]
D_{FBR}	Fluidized bed reactor diameter	[m]
$D_{m,s}$	The non-reacting material diffusion coefficient	[m^2/s]
D_p	Particle drag function	[N]
d_p	Particle diameter	[m]
d_{50}	Cut-point or separation size when the efficiency of a cyclone is 50%.	[m]
E	Activation temperature	[K]
E_a	Activation energy	[kj/mole]

E_p	Equivalent emission of the particles	[J/s]
F	Rate of momentum exchange per volume between the fluid and particle phases	[N/m^{3}s]
f_d	Fraction of contact time by the dense particle phase	[-]
F_{wp}	A calculated view factor	[-]
G	Incident radiation to be solved	[j/m^{2}s]
g	Gravity acceleration	[m/s^2]
H	Enthalpy of the control volume	[j]
H	Height of the cyclone inlet	[m]
$\widehat{H}$	Specific enthalpy	[j/kg]
h_d	Dense particle phase's heat transfer coefficient	[W/m^{2}K]
h_{fw}	The local fluid-wall heat transfer coefficient	[W/m^{2}K]
h_l	Lean particle phase's heat transfer coefficient	[W/m^{2}K]
H_r	The heat-generation expression refers to the net effect of all reactions where there are several reactions	[j]
$\dot{H}_i$	Convective enthalpy of input streams to the control volume	[j]
$\dot{H}_e$	Convective enthalpy of output streams to the control volume	[j]
k	Reaction rate	[mole/m^{3}s]
k_0	Arrhenius pre-exponential factor	[1/s]
k_B	The boundary layer mass transfer rate	[m/s]
k_D	The diffusion rate through the non-reacting material	[1/s]
k_f	Thermal conductivity of the fluid	[W/mK]
k_R	The first-order reaction rate	[mole/m^{3}s]
L	Cell length	[m]
L_b	Length of the cyclone body	[m]
L_c	Length of the cyclone cone	[m]
m	Mass	[kg]
m_p	Particle mass	[kg]
m_s	The mass of solid material in the reacting solid core	[kg]
$\dot{m}_{acc}$	The rate at which mass accumulates within the control volume	[kg/s]
$\dot{m}_{in}$	The rate at which mass enters the control volume	[kg/s]
$\dot{m}_{out}$	The rate at which mass leaves the control volume	[kg/s]

n	The refractive index of the fluid mixture	[-]
n_f	The refractive index of the fluid	[-]
N_p	Number of particles	[-]
Nu_p	The particle Nusselt number	[-]
P	Pressure	[pa]
ΔP	Pressure drop in cyclone	[pa]
Pr	Prandtl number	[-]
$P_{45\mu m}$	The weight fraction of particles smaller than 45μm	[-]
q_r	Radiation energy	[j]
q_{wp}	Radiation between a thermal wall cell and nearby particles	[j]
$\dot{Q}_r$	The heat generated by the reaction	[j]
$\dot{Q}_T$	The heat transferred to the environment	[j]
r	Reaction rate	[mole/m^{3}s]
$\hat{r}_A$	The net rate of formation of the substance	[mole/m^{3}s]
r_c	The radius of the reacting solid core	[m]
r_d	Discrete reaction rate	[mole/s]
Re_L	Reynolds number	[-]
R_g	Gas constant	[j/moleK]
r_p	Particle radios	[m]
r_{va}	Volume-average reaction rate	[mole/m^{3}s]
S	Length of the vortex finder	[m]
T	Temperature	[K]
T_{act}	Activation temperature	[K]
T_p	Particle temperature	[K]
$\bar{T}_p$	the Temperature-weighted average of particles in a cell	[K]
T_{ref}	Reference temperature	[K]
T_w	The temperature of the wall	[K]
U	The energy of the control volume	[j]
u_f	Fluid velocity	[m/s]
u_{mb}	Minimum bubbling velocity	[m/s]
u_{mf}	Minimum fluidization velocity	[m/s]

u_p	Particle velocity	[m/s]
u_{sf}	Fluid superficial velocity in the reactor	[m/s]
V	Volume	[m^3]
$\dot{V}$	Volumetric flow rate	[m^3/s]
V_{cell}	Cell volume	[m^3]
v_{cp}	Control volume for each particle	[m^3]
$\dot{V}_{in}$	Volumetric flow rate which enters the control volume	[m^3/s]
$\dot{V}_{out}$	Volumetric flow rate which leaves the control volume	[m^3/s]
V_p	Particle volume	[m^3]
W	Width of the cyclone inlet	[m]
w	Subscript for thermal wall	[-]
$\dot{W}_f$	Friction work in the control volume	[j]
$\dot{W}_V$	Added work associated with the volume change	[j]
X	Particle position	[m]
x_f	Mass fraction of fluid	[-]
y_f	Mole fraction of fluid	[-]

Greeks

Γ	Radiation diffuse coefficient	[mm]
ε_p	Particle emissivity	[-]
$\bar{\varepsilon}_p$	Volume-weighted average of particle emissivity	[-]
ε_w	The emissivity of the thermal wall	[-]
ε_{wp}	The effective emissivity between the wall and the particles in a cell	[-]
η	Cyclone efficiency	[-]
θ_{cp}	Close-pack volume fraction	[-]
θ_f	Fluid Volume fraction (voidage)	[-]
θ_p	Particle volume fraction	[-]
μ_f	Fluid dynamic viscosity	[kg/ms]
$\vartheta_{f.in}$	Fluid superficial velocity at the cyclone's inlet	[m/s]
ρ	Mass density	[kg/m^3]

$\hat{\rho}$	Specific mass density	[1/m^3]
ρ_b	Bulk density	[kg/m^3]
ρ_c	The gas mass concentration at the reacting solid core	[kg/m^3]
ρ_{in}	The mass density of substances that enters the control volume	[kg/m^3]
ρ_f	Fluid density	[kg/m^3]
ρ_{Ps}	The gas mass concentration at the particle surface	[kg/m^3]
ρ_p	Particle density	[kg/m^3]
ρ_s	The density of solid material in the reacting solid core	[kg/m^3]
ρ_∞	The gas mass concentration in the bulk gas	[kg/m^3]
σ	The Stefan-Boltzmann constant	[W/m^{2}K^4]
σ_f	The equivalent fluid scattering coefficient	[1/m]
σ_p	Equivalent particle scattering factor	[1/m]
τ	Inter particle stress	[N/m^2]
$\emptyset$	The particle probability distribution function	[-]
φ	Particle sphericity	[-]
$\emptyset_s$	Particle sphericity	[-]
ψ	Sphericity	[-]
Ω_p	Particle volume	[m^3]

1 Introduction

Aluminum is now the second most used metal globally [1]. This is due to the fact that aluminum has a unique combination of appealing properties and functionalities allowance for significant energy savings in many applications, for example, in vehicles and buildings. Besides, recycled aluminum is highly energy-efficient, using only 5% of primary production energy [2]. Although this energy-saving leads to lower CO_2 emission, the production process of aluminum still has a massive impact on the environment [3]. One of the aluminum industry's key targets (such as many other industries) has remained the manufacturing of aluminum with the lowest carbon footprint possible, thanks to growing concern about global climate change [4]. The industrial sector contributes approximately 21% of global greenhouse gas (GHG) emissions, with aluminum industries accounting for 1.0 percent (11.5 tons of CO2 per ton of aluminum) [5], and many key players in the global aluminum sector have taken the lead and made progress in reducing CO_2 emissions in their smelting operations. This becomes more important when the significant increase in the global aluminum market size from around 150 billion dollars in 2019 to 250 billion by 2027 with a compound annual growth rate of 5.7% during the period (Figure 1.1) is reported [6].

Figure 1.1: Global aluminum market forecast [7]

The process which is used almost exclusively in the aluminum industry is the Hall-Héroult process. This process has turned aluminum metal into a commodity product since its invention in 1886 [8]. Alumina is dissolved in a cryolite bath in this continuous process, and aluminum is produced by electrolysis. In this cryolite-alumina melt electrolysis, aluminum oxide is dissolved in molten cryolite (Na_3AlF_6) and afterward electrolytically reduced to aluminum at almost 960°C. Carbon anodes are used in the process, which is consumed during electrolysis, resulting in the formation of CO_2. This process suffers from relatively high heat loss from the electrolytic cells and increased CO_2 emissions from the anodes, even though manufacturers have gradually improved their production processes. Besides, the Hall-Héroult process is moving down to its potentially lowest energy consumption and CO_2 emissions during decades. [9]

In 2001, Jomar Thonstad, professor of Electrochemistry at the Norwegian University of Science and Technology, and his colleagues in their book [10] have been mentioned that "the Hall-Héroult process remains the only modern method of producing aluminum today, having withstood many attempts to replace it. No other mechanism seems to be threatening it for the next twenty years or so". Well, it has been 20 years now.

Alternative aluminum processing strategies have been under intense investigation due to the comparatively high energy usage and carbon footprint associated with anode consumption [10]. In continuation of this, in 1973, an innovative process was introduced by Alcoa Corporation, and it had several advantages compared to the commonly used method (Hall-Héroult) at that time [11]. Alcoa's process is based on the chlorination of processed aluminum oxide. The chlorination process has the advantages of being more compact and operating at a lower temperature than the Hall-Héroult process, normally 700°C. The chemical carbon footprint of the two processes, however, is similar since aluminum chloride is created by carbochlorination of aluminum oxide, which includes aluminum oxide reacting with carbon (C) and chlorine gas (Cl_2) to form aluminum chloride ($AlCl_3$) and CO_2. As a result, the same amount of CO_2 is extracted per kilogram of aluminum in classical electrolysis [12]. There are some significant differences, although, that make this process interesting:

- This process does not necessitate the use of pure aluminum oxide as a raw material exclusively. Consequently, the Bayer process could be skipped, eliminating the issue of disposing of vast amounts of red sludge [12].

- Carbochlorination can result in relatively high CO_2 concentrations in the process gas, making CO_2 capture and storage easier to implement [13].
- The mechanical properties of carbon, which is merely a chemical reactant in aluminum chloride production by chlorination, are not needed. As a result, biocarbon can be used instead of coke from petroleum refineries, required by the Hall-Héroult process, which requires anodes with high mechanical strength and density [12, 13].

Around the time of the Alcoa process's implementation, a great deal of work was conducted on both the process and the chlorination of raw materials. Later, interest waned, but it has recently reappeared. Theoretically, many minerals containing sufficient amounts of aluminum can be directly chlorinated. Naturally, minerals with such a weak thermodynamic bond to aluminum, such as clay minerals bauxite and kaolinite, as well as hydrated aluminum sulfates, are preferred [14]. However, promising experiments using leucite-type minerals have been recorded. This is important in Norway's sense because these minerals are linked to anorthosite [15], a member of the plagioclase feldspar sequence found in abundant deposits in the region.

In continuation of Alcoa's effort and based on the alumina chlorination process, the present study is part of a massive project that studies the possibility and feasibility of a new low carbon aluminum production process. This process (in this report called the New Sustainable Aluminum Production (NSAP) process) includes several stages, and the present study focuses on alumina chlorination as the heart of the system, which occurs in a fluidized bed reactor.

1.1 Objectives

Until now, fluidized bed technology has been studied in a wide range of applications. Even though it is a well-known technology, designing such a reactor with ideal and realistic operating conditions continues to be a challenge. Not only the complex hydrodynamics and uncertain nature of the particle's behavior in the fluidized bed reactor make the engineering complex, but also the highly corrosive environment inside the reactor makes the design very challenging. In order to accomplish this feat, the following objectives have been completed:

1- Study and conduct a background study on aluminum production processes and advantages of chlorination fluidized bed.
2- Conduct a comprehensive literature review on fluidization to demonstrate the fundamental design parameters, their different correlations.
3- Study a full review of alumina chlorination reaction and the kinetics.
4- Reviewing design criteria and considerations.
5- Design and optimization of a single reactor.
6- Design and simulation of the gas-solid separation unit (cyclone).
7- Thermal study of the reactor.

1.2 Scope and Methodology

The project's scope is to design an industrial fluidized bed reactor equipped with a gas-solid separation unit (cyclone) to handle a total of 0.6 kg/s of solid reactants and produce aluminum chloride as the main product. This research focuses on determining the best bed height based on the available reaction rates, determining the best reactor dimension to reduce particle outflow under isothermal conditions (700°C). When it comes to reaction, pure γ-alumina is considered as the solid reactant. Although this means there are no other side reactions, in section 3.5, some possible side reactions are studied based on the given alumina composition.

In continuation of the "M.S. Student Project- MP-23-20, USN" [16], this project starts with finding an acceptable range for superficial velocity after selecting the best regime in the fluidized bed reactor. The initial reactor dimensions can be calculated based on this information. Then, it comes to one of the most important steps, which is model development. In this stage, the best boundary conditions, such as pressure and model parameters such as particle sphericity and void fraction, and most importantly, reaction rates, have been modified to reach the best model. When all the parameters and simulation settings are acceptable, the reactor can be modified to reach the best hydrodynamics, maximum reaction efficiency, and minimum particle outflow. Autodesk Inventor® and Barracuda® Virtual Reactor (version 20.1) are used for 3D modeling of the reactor and CFD simulation for multiphase (solid-gas) reaction, respectively.

1.3 Report Structure

The achievement of these objectives is described in the following chapters.

Chapter 2 gives general background information about the current aluminum production method and its possible alternatives, and in the end, the best alternative (chlorination process) will be studied in more detail. In continuation, some background about hydrodynamics in a fluidized bed will be reviewed because this topic has a crucial role in the present study.

Chapter 3 because of the importance of chemistry in the present study, after a brief introduction about the necessary background, the alumina chlorination process will be studied in detail. In the end, some possible side reactions will be studied.

Chapter 4 gives a deep insight into CPFD simulations and Barracuda Virtual Reactor®. The drag models, chemistry, and heat transfer in Barracuda will be reviewed in this chapter

Chapter 5 covers design considerations and essential factors in the design because many factors have been taken into account to have a reasonable and realistic model.

Chapter 6 gives a step-by-step view of the design procedure and shows how the last generation of the reactor has been achieved. All the results and discussions will be covered here.

Chapter 7 covers the conclusion and suggestions for future works.

2 Literature review

2.1 Aluminum Production Processes

2.1.1 Hall-Héroult Process (As the Dominant Process)

The Hall-Héroult (H-H) process is used in alumina reduction cells to manufacture primary aluminum, after two young men, oceans apart, independently developed and patented a new manufacturing aluminum method around 140 years ago. This discovery in 1886 by Charles M. Hall in the United States and Paul T. Héroult in France provided the world with the gleaming light metal at reasonable prices. In this method, solid alumina (Al_2O_3) is dissolved in an electrolyte predominantly composed of liquid cryolite (Na_3AlFe_6). The electrolyte is altered with calcium fluoride, aluminum fluoride, and/or other additives. [14]

In a typical alumina reduction cell, multiple prebaked carbon anodes are immersed in the electrolyte, and as an intermediate product, oxide ions from alumina dissolution are discharged electrolytically onto the anodes. On the other hand, the oxide intermediate reacts further with the carbon anodes, eventually consuming them by producing gaseous carbon dioxide (CO2). Inside the electrolyte is a molten aluminum reservoir enclosed in a preformed composite lining and thermally sealed by refractory and insulation components inside a steel shield. Hence, aluminum is molded by reducing aluminum-containing anions at the electrolyte-metal interface. Although the term cathode is often used to refer to the whole tank of liquid metal and electrolyte, the actual acting cathode is the metal pad or aluminum pool's top surface. The following reaction (2.1) can be the overall reaction of dissolved alumina with carbon to form the products. [10]

$$½\ Al_2O_3\ (dissolved) + ¾\ C\ (s) \rightarrow Al\ (l) + ¾\ CO_2\ (g) \qquad (2.1)$$

As detailed in section 2.1.2, this process's total energy consumption is approximately 150–190 (106 BTU/ton). Using titanium diboride cathodes will also substantially reduce energy consumption (up to 20%). The manufacturing of a permanent anode is a more challenging task, and while large-scale experiments are in progress in Japan, Europe, and the United States, no success has been reported. More immediately, sophisticated controls can increase H-H cell efficiency by up to 5%. To anticipate anode effects and to optimize its positioning, the pattern of individual cell voltage variations can be monitored and analyzed. Higher energy costs also induce cells to run at lower current densities, resulting in higher efficiency.[12]

In Figure 2.1, the main parts of an industrial Hall-Héroult cell are presented [9]. In the following, some of the main components and the functionalities will be discussed.

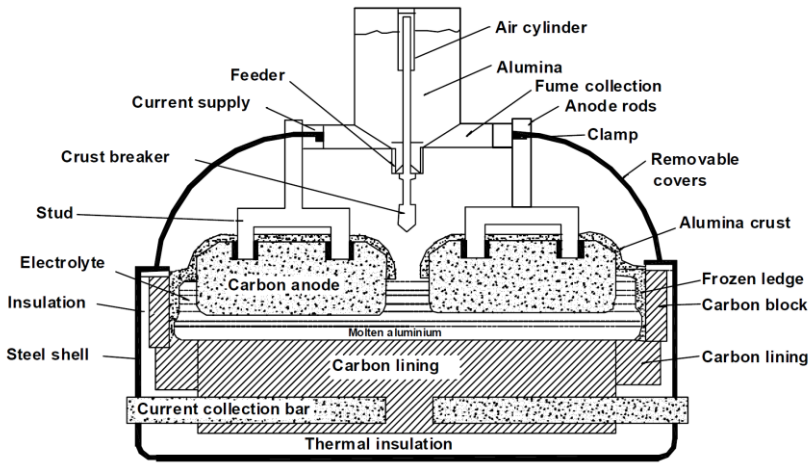

Figure 2.1: Cross-sectional scheme of an industrial Hall-Héroult cell with prebaked anodes [9]

2.1.2 Other Possible Alternatives

The search for feasible alternative processes for aluminum production has been accelerated by rising prices and a lack of large blocks of electrical energy. For instance, the electrolysis of aluminum chloride, sulfide, nitride; carbothermic reduction of ore or alumina; and disproportioning reactions of aluminum sulfide or the mono-chloride route can be considered as possible alternatives. The aluminum industry is undergoing significant changes. It can no longer be selective when it comes to developing sites based on the cost of electricity. Due to the limited electricity available for expansion, the next generation of aluminum smelters must now optimize their energy efficiency. This shift has also had an impact on the importance given to alternative process technology. [17]

Primary aluminum production, which uses only the Hall-Héroult process, accounts for nearly 5% of all electricity produced in the United States [12]. This part covers some practical possibilities to minimize electrical energy consumption and areas where R&Ds are required to put these opportunities into practice. Some alternative processes are as below:

- Fourteen techniques for converting alumina to metal by direct carbothermic reduction;
- Direct reduction of bauxite to an aluminum-silicon alloy;
- The Sub-chloride process;
- Sulfide disproportionation process;
- The Nitride process;
- Chloride electrolysis ;
- Sulfide electrolysis;
- Nitride electrolysis;
- Non-aqueous electrolysis;
- Miscellaneous processes.

In terms of electrical energy consumption and total energy requirements, these processes were compared to existing Hall-Héroult technology. In the following, a description of some of these processes can be found [12].

1. **Hall-Héroult Process:** Electrolysis of Al_2O_3 in Na_3AlF_6 melt at 960°C in 50-200 KA cells with the consumable carbon anode, aluminum pool cathode.
2. **Alcoa Smelting Process (ASP):** Electrolysis of AlCl3 in LiCl-NaCl melt at 700°C with a multi-cell bipolar stack of graphite electrodes where anodes are not consumed.
3. **Direct Carbo-Thermic Reduction to Aluminum:** Electric arc furnace (EAF) reduction of alumina with petroleum coke
4. **Direct Carbo-Thermic Reduction to Al-Si Alloy:** Oxygen blown blast furnace type operation reducing bauxite with petroleum coke
5. **Sub-chloride or Gross Process:** Pre-reduction of bauxite in electric furnace followed by exposure to $AlCl_3$ vapor. Which selectively removes aluminum metal as AlCl. Subsequent cooling produces aluminum according to $AlCl \rightarrow 2Al+AlCl_3$.
6. **Disproportion action of Aluminum Sulfide (Al_2S):** Reaction of Al_2O_3 with recycled Al_2S_3 in the presence of C gives Al_2S. Subsequent cooling produces Al according to $3Al_2S \rightarrow Al_2S_3+4Al$.
7. **Nitride Intermediate:** Formation of the nitride according to $Al_2O_3+3C+N_2 \rightarrow AlN+3CO$ in an induction furnace, nitride decomposes under vacuum to give aluminum.
8. **Sulfide Electrolysis:** Formation of Al_2S_3 followed by electrolysis in fluoride or chloride fused salt bath to give aluminum and sulfur.
9. **Nitride Electrolysis:** Electrolysis of dissolved AlN in cryolite at 727°C.
10. **Mono-Chloride Process:** Aluminum is extracted from bauxite with aluminum chloride at 1800°C.
11. **Toth Process:** Reduction of aluminum chloride with manganese metal. Manganese chloride is converted to oxide then reduced to metal in a blast furnace.

Table 2.1 gives comparative data about the energy consumption of these methods. All of the non-electrolysis processes necessitate extremely high temperatures that can only be reached in an electric furnace, and in each case, electrical energy consumption (8-10 kWh/lb) is estimated to be higher than that of a Hall-Héroult cell (6-8 kWh/lb). [12]

In a blast furnace, however, direct reduction of bauxite to an aluminum-silicon alloy is possible. To achieve higher temperatures, oxygen rather than air must be used, but the overall thermal energy requirements are about one-

third of those of the Hall-Héroult process. Aluminum produced by aluminum chloride electrolysis in a fused chloride melt is a proven method (ASP). The electrolytic step uses 4.5 kWhr/lb of aluminum at Alcoa's 15,000 ton/yr plant, but the extra steps compared to the H-H process require more thermal energy than the formation of prebaked anodes for the H-H cell. As a result, the ASP's total energy consumption is only slightly better than H-H's.

Table 2.1: Energy consumption of some aluminum production processes

Process No.	Electrical Energy Consumed (kWh/lb)	Thermal Energy Equivalent (10^6 BTU/ton)	Other Thermal Energy Consumption (10^6 BTU/ton)	Total Energy (10^6 BTU/ton)
1	6.0 - 8.0	125 - 165	25 [1]	150 - 190
2	4.5	95	35	130
3	8.0 - 14.0	165 - 290	-	165 - 290
4	-	-	70	70
5	8.6 (2.8)[2]	180 (60)	- (60)	180 (120)
6	10	210	-	210
7	NA	-	-	NA
8	5.0 – 6.0	100 - 125	-	100 - 125
9	3.6	75	60	135
10	6.5	135	-	135
11	10 - 12	210 - 250	80	290 - 330

The conclusion is that, except for chloride electrolysis (Alcoa Smelting Process), there is no technology for producing aluminum metal that can compete with the Hall-Héroult process in electrical energy consumption [12]. In the future, sulfide or perhaps nitride electrolysis replaces the pre-reduction step with natural aluminum chloride treatment of the ore, maybe the viable options. Before a promise can be identified, each of these ideas requires extensive study.

2.1.3 Chlorination Process (As the Best Alternative)

The electrolytic decomposition of aluminum chloride in a fused chloride melt will yield aluminum. Alcoa has developed this process (ASP) to the point where a demonstration plant with a capacity of 15,000 tons/year has been built. The process involves chlorinating Bayer aluminum to produce aluminum chloride, which is then decomposed in a bipolar multi-electrode cell with a novel [18] design (Figure 2.2) to produce aluminum and chlorine. At a temperature of 730°C, the electrolyte is approximately equimolar sodium and lithium chlorides with about 5-mole percent aluminum chloride. The process has a low specific electrical energy consumption of 4.5 kWhr/lb, which is one of its main advantages. The non-consumable, bipolar electrodes are spaced very closely (0.25"), which accounts for this low energy. The anode-cathode distance in the Hall-Héroult cell is between 1.0 and 2.0", with a voltage loss of 2.0V. The electrolyte's ohmic losses in the ASP correspond to less than 0.5V of the cell's operating voltage. [12]

[1] As fuel and consumable materials in anode fabrication.

[2] The number in the parentheses shows that value for pre-reduction in blast furnace.

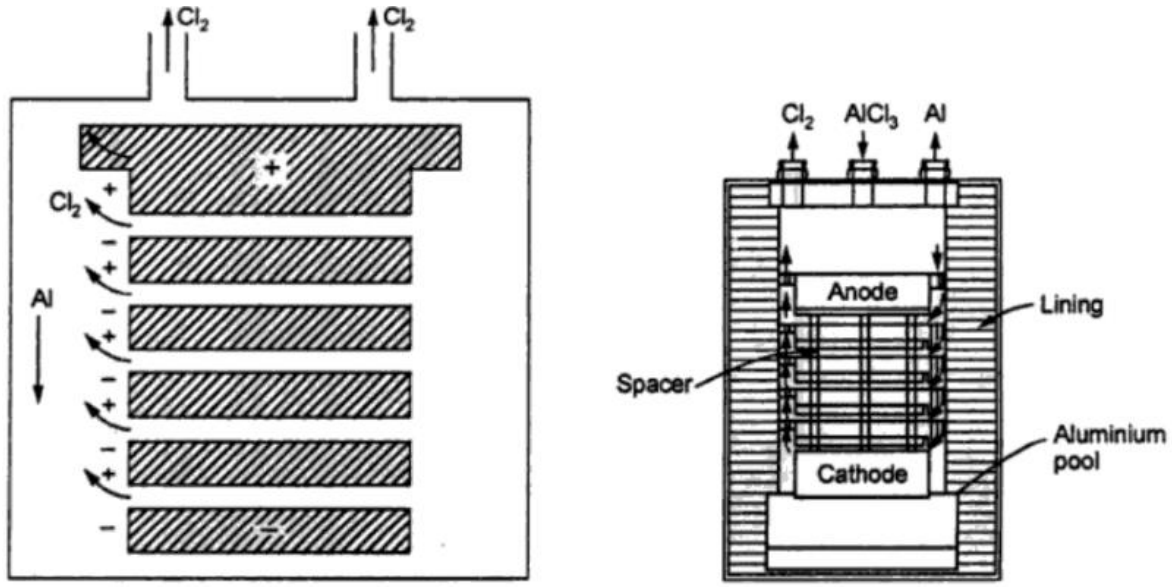

Figure 2.2: Schematic Alcoa bipolar cell (left) and some details of the bipolar cell (right) [12]

2.1.3.1 Process Engineering

The flow diagram in Figure 2.3 shows the various stages of the ASP. The patent literature contains more information on this topic. As shown in Table 2.2, Bayer alumina with impurities is used as the ASP's raw material. In practice, the alumina is impregnated with carbon in a two-stage fluidized bed system fired with fuel oil during the chlorination step. The top stage operates at a low temperature, allowing unburned fuel oil to condense on the alumina feed to the lower stage, which operates at 900°C. The fuel oil is crushed and coked at the lower stage. The feed rate is adjusted so that the amount of carbon deposited exceeds the stoichiometric requirement for converting the oxide to carbon dioxide. [12]

The industry has turned its attention to the two-step process of converting alumina to aluminum chloride and then further reducing the aluminum chloride to aluminum metal after failing to find a cost-effective procedure for direct carbothermic reduction of alumina. In the patent literature, two chlorination processes are mentioned. The first is a fluidized bed that converts aluminum to aluminum chloride ($AlCl_3$) at a temperature of 590°C. Hydrogen chloride, aluminum hydroxy chloride, aluminum oxychloride, and sodium chloride are also delivered in minor but significant amounts. The sodium comes from the alumina, which contains sodium as an impurity from the Bayer process. [19]

The following simplified general reaction can be used to reflect carbothermic chlorination of alumina [19]:

$$Al_2O_3 + (n)C + 3Cl_2 \rightarrow 2AlCl3 + (2n\text{-}3)CO + (3\text{-}n)CO_2 \ , \ where\ 1.5 \leq n \leq 3 \qquad (2.2)$$

The following sequential reactions can explain the carbothermic chlorination of alumina as the reaction progresses with the production of carbon dioxide and carbon monoxide:

$$\begin{gathered} Al_2O_3 + 3CO + 3Cl_2 \rightarrow 2AlCl3 + 3CO2 \\ C + CO2 \rightarrow 2CO \ , \ bounded\ reaction \end{gathered} \qquad (2.3)$$

Unreacted alumina and carbon, as well as oxychlorides and sodium chloride, are removed in a two-stage condensation process. The sodium chloride is washed out, and the alumina is recycled to the first stage of the process after the condensate is oxidized to regenerate chlorine. The aluminum chloride is then condensed at 65°C in a fluid bed. The uncondensed hydrochloric acid is removed in an absorption column, providing a useful byproduct.

Table 2.2: Specification for the Alumina feed for the Alcoa Smelting Process [12]

Component	**%**	**Component**	**%**
Al2O3	99.426 % min	NaO2	0.4 max
SiO2	0.025 % max	TiO2	0.005 max
Fe2O3	0.03 max	ZnO	0.02 max
CaO	0.06 max	V2O5	0.002 max
MgO	0.002 max	Cr2O3	0.002 max
NiO	0.005 max	K2O	0.005 max
MnO2	0.002 max	Li2O	0.001 max
P2O5	0.005 max	CaO2	0.1 max

The chlorination in the second process is done in a molten salt bath with 70 percent aluminum chloride and 30 percent sodium chloride at temperatures ranging from 780 to 815°C. As a catalyst, cuprous or cupric chloride is added to the bath. The bath is fed with Bayer alumina and brushed coke, and chlorine bubbles up from the bottom. Carbon monoxide is promoted as a viable alternative reductant. As in the previous method, the oxychlorides and sodium chloroaluminate are condensed from the aluminum chloride vapor.

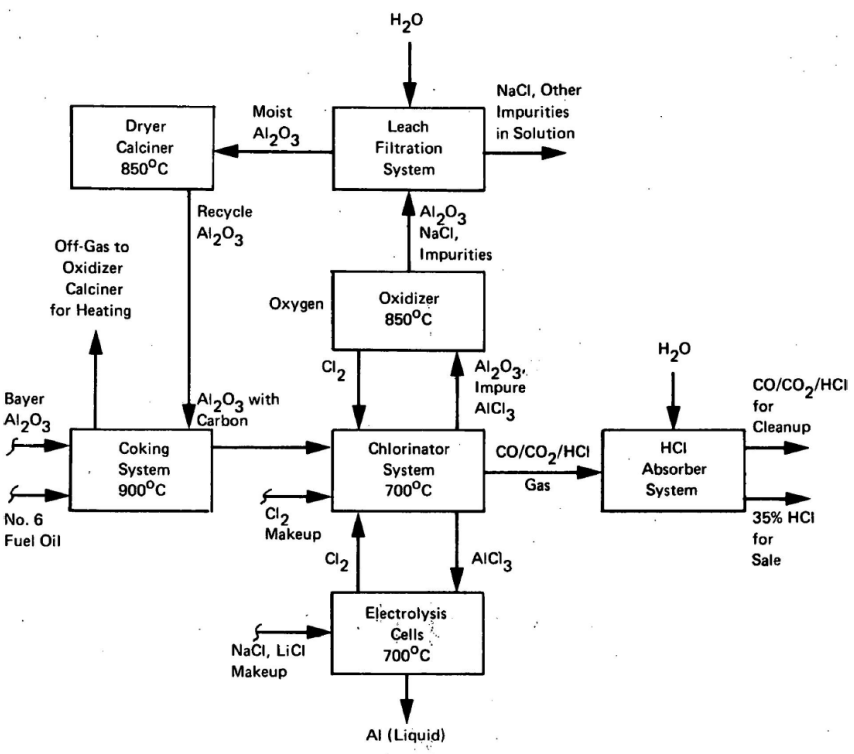

Figure 2.3: Flow diagram for Alcoa Smelting Process [12]

The aluminum chloride is fed into the electrolytic cell, where it dissolves quickly in the electrolyte of lithium-sodium chloride. The cell is depicted in section in Figure 2.4, and the patent [20] literature includes a detailed description of the components. Each cell is made up of 20 to 30 bipolar carbon electrodes that are stacked horizontally. Each electrode's upper surface is a cathode, which produces aluminum. The chlorine produced on the lower surface travels through channels to a central space by a gas lift action, where it circulates electrolytes. The aluminum is swept off the cathode by the electrolyte circulation, and it falls to the sump rather than collecting

on the surface. This enables the use of a small inter-electrode spacing. High current efficiency is dependent on cell construction and electrolyte flow patterns. Electrolyte circulation also ensures that there is enough aluminum chloride in the cell. This is important because a local lack of aluminum chloride leads to an alkali metal deposition, which can degrade the graphite surface by forming an intercalation compound. This is especially true of potassium, so every effort is made to keep the bath's potassium level as low as possible. Even though aluminum chloride is highly soluble in the melt, the concentration is usually maintained below 10 percent, ideally closer to 6.5 percent. Lower conductivity, greater viscosity, more recycling, and potential assault on the cell's refractory lining are all disadvantages of higher concentration. The complete exclusion of moisture and oxide species from the cell is critical for cell operation (hence the aluminum chloride's diligent purification). The presence of oxides causes two issues: sludge formation and consumption of the graphite electrodes' anode face. [12]

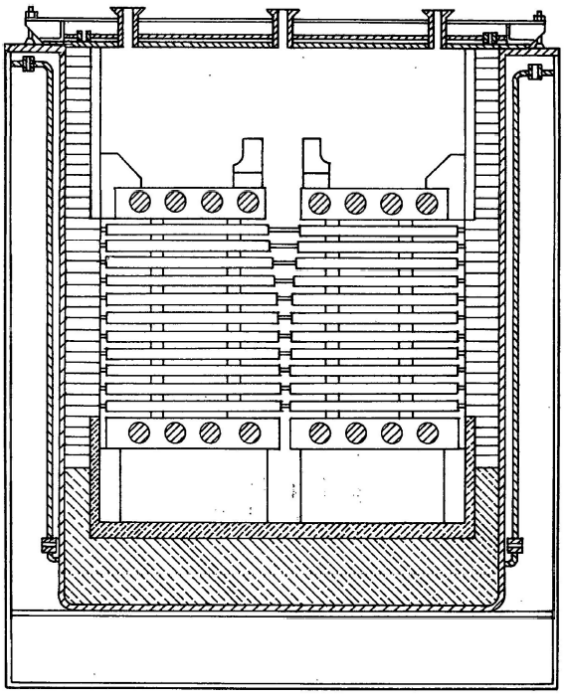

Figure 2.4: Alcoa Smelting process bipolar Cell [12]

2.1.3.2 Comments on the Alcoa Smelting Process

As previously stated in section 2.1.3.1, the ASP has a lower electrical energy requirement (4.5 kWhr/lb) than the Hall-Héroult process (6-8 kWhr/lb); this is one of the main advantages of the process. Table 2.3 [12] shows the differences between the two processes. The smaller anode-cathode separation of the ASP outweighs the chloride's higher reversible decomposition voltage and slightly lower chloride melt conductivity. The thermal energy required for chlorination is marginally higher than that required for the production of prebake anodes. The ASP is considered a technically feasible alternative to the Hall-Héroult procedure. Because ASP technology is more advanced than Hall-Héroult, there is a potential for downtime or periods of low current efficiency. The current efficiency is heavily dependent on the cell's ability to maintain optimal hydrodynamic flow. Alcoa has done much research on this and can achieve high efficiency on a routine basis. Thermal management and condensation of the electrolyte's volatile components have also been extensively studied [19] and do not currently represent any operational issues. The purity of the aluminum chloride feed appears to be the key to trouble-free operation; oxides cause sludge formation, and sodium chloride carry-over slowly alters the bath's composition. Many techniques and devices for ensuring aluminum chloride purity of 99.9% are described in the patent literature. The ability of the ASP to withstand power failure is another significant operational advantage over the Hall-Héroult procedure [19].

Table 2.3: Comparison of ASP and H-H cells

	ASP	H-H
Current Density (A/in^2)	5 - 15	5 – 7 at the anode 2 – 4 at the cathode
Anode Cathode Distance in	0.25	1.5 – 2.0
Reversible Decomposition Voltage (V)	1.8	1.2[3]
Anode polarization (V)	0.4	0.5
iR losses in electrolyte (V)	0.5	2.0
Voltage per cell (V)[4]	2.7	3.7

2.2 Hydrodynamics

Because of interactions between the gas and solid phases, fluidized beds have highly complex hydrodynamics. The movements of gases and solids are complex to define and explain. Hydrodynamics in a fluidized bed reactor deals with the mechanics of gas-solid suspensions and the hydrodynamic properties of gas-solid contacts. The dilute suspension's clustering nature, which was first observed from the relatively high gas-solid slip velocity, has been the most significant point of concern from a theoretical perspective. On the other hand, the impact of structural factors such as column diameter, wall shape, gas distributor design, exit configuration, solid separation and recycling equipment, as well as operating conditions, on the performance of circulation systems are the main hydrodynamic concerns from an engineering standpoint which is relatively interrelated with scientific aspects. [21]

Any of the mechanical interactions in the model must be considered in a mathematical model in order to correctly simulate all of the flow processes associated with gas-solid flows. These interactions, which are dependent on the mean and fluctuating components of the gas and solid velocity fields, are described by [22] as follows:

1. The interaction between average gas and solid velocity results in the drag force between the two phases.
2. The gas-phase Reynolds stresses are created by the interaction of average and fluctuating gas velocities.
3. The interaction between average and fluctuating solid velocities in the solid assembly that causes stresses.
4. The interaction of particles with a fluctuating gas velocity, resulting in an interfacial flux of kinetic energy correlated with arbitrary motion.

2.2.1 Particle motion and solids mixing mechanisms

Studying fluidized bed hydrodynamics ([23], [24]) has indicated that the solids volume concentrations in the fluidized bed reactor can be classified into mainly four regions (Figure 2.5). Cross-sectional average solids volume concentrations of usually 0.1 to 0.2 characterize the bottom region, where solid particle acceleration occurs. A dilute region follows the transition zone, occupying most of the riser height and marked by low solids volume concentrations (> 1%). The fluid dynamics throughout the exit zone are governed by the exit geometry at the reactor's top (see section 5.1) [21].

[3] Includes depolarizing action of carbon anode

[4] Because of the ASP multi-cell bipolar stack setup, practical cell voltages cannot be compared, and figures do not directly correspond with the kWhr/lb cited for the two processes' current efficiencies.

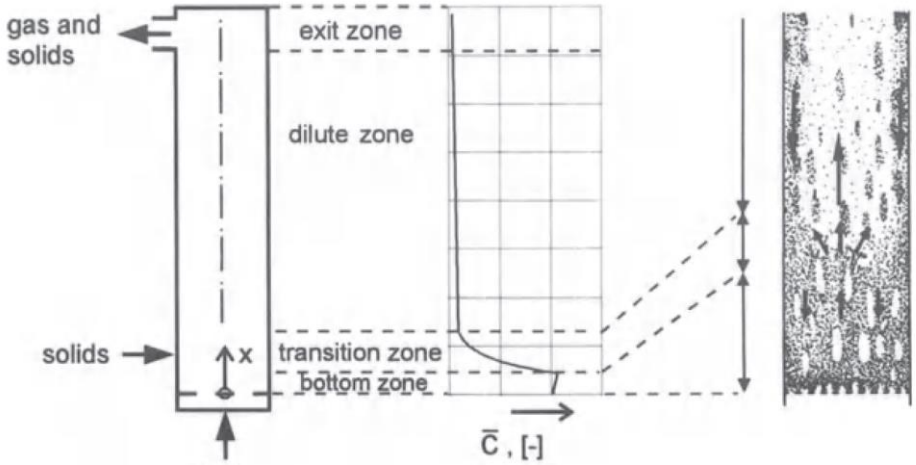

Figure 2.5: Solids motion and of different solids volume fractions zones[5] [21].

2.2.1.1 Particle motion in the bottom zone

Svensson et al. [25] reported that the dense bottom zone of a fluidized bed experiences hydrodynamic activity similar to bubbling or turbulent fluidized beds, with fluidization gas flowing through the reactor's bottom typically in the form of voids, based on pressure variations at the bottom. These voids break and push solids into the transfer zone as they hit the bottom zone's surface. Since there have not been enough local experiments on solids mixing in the bottom zone of a fluidized bed, it is safe to conclude that the mixing processes are identical to those in bubbling fluidized beds. According to [26], "the transport in the wakes of rising voids is the essential mixing mechanism."

2.2.1.2 Particle motion in the dilute zone

The presence of two phases (lean and dense phase) can be used to describe the dilute region. According to studies in local hydrodynamics [23], the lean phase comprises an upward-moving dilute suspension, while the dense phase is made up of downward traveling particle clusters. The dense phase is made near the riser wall for the most part and has solids concentrations that are at least marginally greater than the lean phase. For the sake of convenience, the dense phase is often believed to be constrained to a layer near the wall. Figure 2.6 demonstrates radial profiles of local solids mass fluxes collected by a suction probe as an example of solids motion in the dilute zone [27]. Reduced solids fluxes[6] are plotted against r / R to demonstrate the results. The upward solids mass fluxes are highest at the reactor's core and decline as they approach the sidewall, while the downward mass fluxes are the opposite. Under these operating conditions, comparatively high downward-moving mass fluxes have been observed at the wall.

The presence of a radial profile of local average solids velocities is another feature of the dilute region. It is reported that the reactor's core has the highest solids velocities (Figure 2.7), with mean solids velocities of 1.5 to 2 times the superficial gas velocity [28]. Showing a dominant downward movement of solid particles near the sidewall, negative values are registered. In 1992 [29], a high-speed video camera to perform a more thorough analysis of the acceleration of downward flowing solids in regions near the wall has been used. At velocities ranging from -0.3 to -O.4 m/s, high-density particle swarms were observed descending in contact with the wall. Falling solids were observed to drop with a velocity of -1 m/s as strands a few millimeters from the wall.

[5] The arrows on the right-hand side of the sketch show the major solids flow paths.

[6] Averaging the local disparity between upward and downward mass fluxes across the cross-sectional area yielded $G_{s,local}/G_{s,int}$..

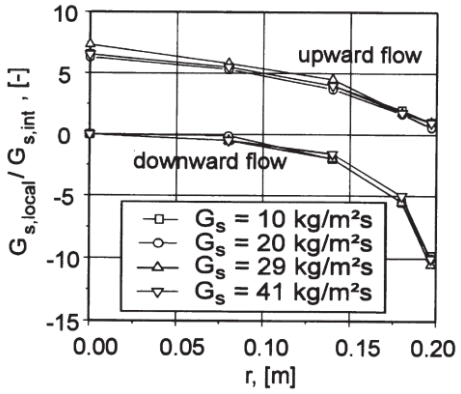

Figure 2.6: Radial profiles of solids mass fluxes (H = 15.6m, D = 0.4m, U = 5m/s, x = 10.8m) [21]

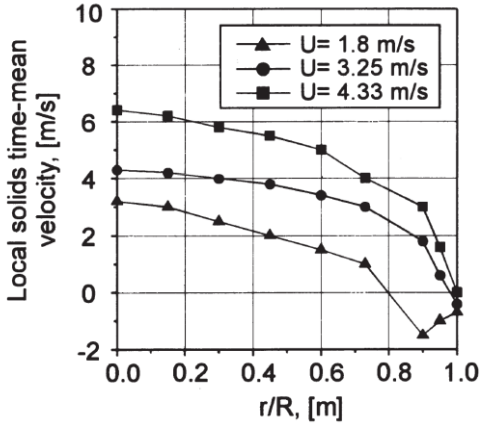

Figure 2.7: Radial profiles of solids velocities (H = 11 m, D = 0.14m, G_s = 24.5 kg/m^{2}s, x = 3.3 m) [21]

2.2.1.3 Particle motion in the transition zone

A transition from the dense bottom zone to the dilute zone happens in this zone, with low solids volume concentrations of solid and the gas phase [30]. Significant volumes of solids are released from the bottom zone into the transition zone through bursting voids. Solids from the dilute zone are carried back into the zone by dropping clusters. As a consequence, this is a high-intensity mixing region. Solid particles are mixing in the transfer region; on the other hand, the phenomenon has not yet been studied separately [21].

2.2.1.4 Particle motion in the exit zone

In the literature, two primary forms of exit geometries have been identified as smooth and abrupt exits. The first is a smooth bent pipe from the top of the fluidized bed reactor to the gas separation unit (cyclone) entry, with no impact on the reactor's flow regime, and the second geometry includes a sharp 90° take-off just below the reactor's end cap. Experiments using an abrupt exit [31] have revealed increasing solids concentrations at the top of the riser, as seen in Figure 2.8. This effect is caused by solids colliding with the reactor's end cap. Heavier particles, which cannot follow the gas flow through the outlet, are mirrored at the riser's top, allowing solids to accumulate in this region.

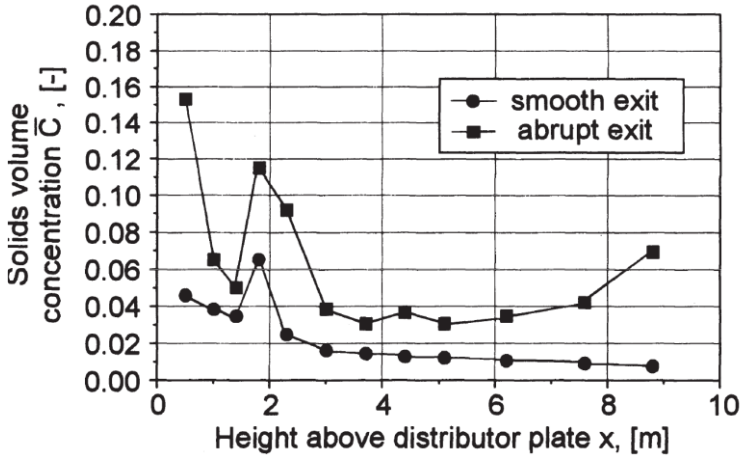

Figure 2.8: Effect of exit geometry on solids volume fraction [21]
(H = 9.3m, D = 0.15m, U = 7.1 m/s, G_s = 73 kg/m^{2}s)

2.2.2 Dissimilar particles Fluidization

Solid segregation happens when different solids with varying sizes and/or densities are fluidized, closely related to solids mixing. Solids segregation in bubbling fluidized beds has gained much interest recently [32]. The consequences of segregation are commonly unfavorable. However, big coal feed pellets stay in the lower part of the riser in CFB, resulting in high combustion efficiencies. On the other hand, coarse particles should still stay in the riser's lower height and should not be elutriated in Multi-Solid Fluidized Beds (MSFB) [33].

3 Alumina Chlorination

3.1 Reaction Basics

Chemical engineering is based on material and energy balances. They are the heart of chemical reaction engineering when combined with chemical kinetics. By adding transport phenomena, there is the intellectual framework for developing chemical reactors. The study of chemical reactor design starts in this chapter, which blends material balances with kinetic expressions for elementary chemical reactions. The equations are based on the project's primary reaction, which is γ–alumina chlorination to produce aluminum chloride and carbon dioxide as a part of the new sustainable aluminum production (NSAP) process.

3.1.1 Material Balance

Consider any area of space with a finite volume and well-defined boundaries that distinguish it from the rest of the system. Mass and energy laws can be extended to such an area, known as a control volume. Mass and energy have their own set of conservation rules. For mass,

$$\dot{m}_{in}(t) = \dot{m}_{out}(t) + \dot{m}_{acc}(t) \tag{3.1}$$

Where, $\dot{m}_{in}(t)$ is the rate at which mass enters the control volume, $\dot{m}_{out}(t)$ is the rate at which mass leaves the control volume, and $\dot{m}_{acc}(t)$ (or $\frac{d}{dt}m(t)$) is the rate at which mass accumulates within the control volume. The words "entering" and "leaving" refers to the flow of substance through the control volume boundaries. It is possible to rewrite the equation (3.1) in terms of volumetric flow rate and density. [34]

$$\dot{V}_{in}(t)\rho_{in} = \dot{V}_{out}(t)\rho_{out} + \frac{d}{dt}(\hat{\rho}V) \tag{3.2}$$

where $\dot{V}$ is volumetric flow rate, ρ is the mass density and $\hat{\rho}$ is the average mass density in the control volume when $\hat{\rho}V = m$ and V is the volume.

Different ways of representing the total mass balance for a flow system with accumulation can be found in equations (3.1) to (3.2). The derivatives disappear in steady-state flow, the system's total mass remains stable, and the final mass equilibrium clearly states that everything that comes in is equal to everything that goes out.

In the area of fluidized bed reactor design, chemical reactions that turn one kind of mass into another are the primary concern. For each substance, a material balance can be given; but, since chemical reactions are inevitable, the formation rate of the component within the control volume must now be taken into account. For any substance A, a brief component balance is,

$$\text{Input} + \text{Formation} = \text{Output} + \text{Accumulation} \tag{3.3}$$

or mathematical expression for this is,

$$\dot{V}_{in}(t)C_{in} + \hat{r}_A V = \dot{V}_{out}(t)C_{out} + \frac{d}{dt}\hat{C}V(t) \tag{3.4}$$

Where, C is the concentration of substance A in moles per volume, $\hat{r}_A$ is the net rate of formation of substance A in moles per volume per time, and $\hat{C}$ is the average concentration of substance A in the control volume. Several chemical reactions may be taking place simultaneously, with some producing A and others consuming it. $\hat{r}$ is the net rate, which is positive if component A is produced and negative if it is consumed. Concentrations and reaction rates will differ from point to point within the control volume unless the system is well mixed. $\hat{C}$ and $\hat{r}_A$ denote spatial averages, and the component balance refers to the entire control volume. [34]

3.1.2 Energy Balance

A flow reactor's thermal energy balance can be written in a reasonably general way as below,

$$\frac{dU}{dt} = \dot{H}_i - \dot{H}_e + \dot{W}_f + \dot{W}_V + \dot{Q}_r + \dot{Q}_T \tag{3.5}$$

where, $\frac{dU}{dt}$ is the accumulation of energy, $\dot{H}_i$ and $\dot{H}_e$ are convective enthalpy of input and output streams respectively, $\dot{Q}_r$ is the heat generated by the reaction, $\dot{Q}_T$ is the heat transferred to the environment[7] (radiation, convection, and conduction), $\dot{W}_V$ is added work associated with the volume change, and $\dot{W}_f \geq 0$ is the friction work.

By neglecting volume and friction work, equation (3.5) can be simplified as,

$$\frac{dU}{dt} = \dot{H}_i - \dot{H}_e - \dot{Q}_r - \dot{Q}_T \tag{3.6}$$

In thermodynamics, one of several energy expressions is *enthalpy H*, which simply is defined as [35],

$$H \triangleq U + PV \tag{3.7}$$

Working on the left-hand side of equation (3.6) results,

$$U = H - PV \Rightarrow \frac{dU}{dt} = \frac{d(H - PV)}{dt} = \frac{dH}{dt} - P\frac{dV}{dt} - V\frac{dP}{dt} = \frac{dH}{dt}$$

$$H = m\widehat{H} \Rightarrow \frac{dH}{dt} = \frac{d\left(m\widehat{H}\right)}{dt} = m\frac{d\widehat{H}}{dt} + \widehat{H}\frac{dm}{dt} = m\frac{d\widehat{H}}{dt}$$

$$\frac{dU}{dt} = \frac{d}{dt}(\hat{\rho}V) \tag{3.8}$$

In the same manner, by simplification of the right-hand side, the thermal energy balance is turned to,

$$\frac{d}{dt}\left(\hat{\rho}V\widehat{H}\right) = \dot{V}_{in}\rho_{in}\widehat{H}_{in} - \dot{V}_{out}\rho_{out}\widehat{H}_{out} + \hat{r}_A V\Delta\widehat{H}_r + \dot{Q}_r - \dot{Q}_T \tag{3.9}$$

This is an integral balance that can be applied to the whole system. The enthalpies are defined relative to a reference temperature (T_{ref}). The temperature would commonly be used to replace the enthalpy expressions.

$$H = \int_{T_{ref}}^{T} C_p \tag{3.10}$$

Where, C_p is the average specific heat capacity for the entire reactant mixture. Taking the thermodynamics convenient into account, for exothermic reactions $\Delta H_r < 0$. The heat-generation expression refers to the net effect of all reactions where there are several reactions. As a consequence, the $\Delta H_r r$ expression is an implicit summation of all m potential reactions [34]:

$$\Delta H_r r = \sum_{Reactions} (\Delta H_r)_i (r)_i = \sum_{i=1}^{m} (\Delta H_r)_i (r)_i \tag{3.11}$$

[7] Is positive when the heat leaves the control volume and includes all heat transport mechanisms

3.1.3 Reaction Rate and Temperature Dependency

Temperature influences most reaction rates and most laboratory experiments consider temperature to be a significant factor in improving reaction yield or selectivity. Sometimes this effect has been ignored, and the reactors were designed to be isothermal, with the operating temperature determined by the rate constant. Even for isothermal reactors, temperature effects have been considered in a real-life application since the operating temperature must be defined in the specification. The temperature dependency enters the design equations explicitly for non-isothermal reactors, where the temperature changes from point to point inside the reactor.

For elementary reactions, the rate constant is quite often expressed as,

$$k = k_0 T^n \exp\left(\frac{-E_a}{R_g T}\right) = k_0 T^a \exp\left(\frac{-T_{act}}{T}\right) \tag{3.12}$$

where, k_0 is the pre-exponential factor, a constant for each chemical reaction n is equal to 0, 0.5 or 1 depending on the used specific theoretical model, E_a is the activation energy in joule per mole, R_g is the gas constant equal to 8.3145 joules per mole per kelvin, T is the temperature in kelvin, T_{act} which has the unit of kelvin called activation temperature. The activation temperature is not the same as the actual temperature. It is just a way of describing the compound quantity E_a/T in a more convenient way. Classical Arrhenius theory is represented by $n = 0$; "collision theory of bimolecular gas-phase reactions" is represented by $n = 0.5$, and transition state theory is represented by $n = 1$. The exponential dependency $\exp(-T_{act}/T)$ overwhelms the reasonably slight difference in rate constant due to the pre-exponential temperature dependence T^n. A plot of $ln(k)$ versus T^{-1} would be roughly linear for most of the reactions, and the slope of this line will be used to measure E_a. Plots of $ln(k/T^m)$ versus T^{-1} for the same reactions would also be roughly linear, showing that evaluating m using this strategy is pointless. [34]

In general, the reaction rate for a chemical reaction of two species ($A + B \rightarrow C$) can be calculated as below,

$$r = k[A]^n[B]^m \tag{3.13}$$

where, r is the reaction rate in mole per time, $[X]$ is the concentration of specie X in mole per volume, and the $n + m$ gives the reaction's order.

3.2 Alumina Chlorination

In section 2.1.3.1, by equations (2.2) and (2.3), the Alcoa process's overall chlorination reaction has been introduced, where solid-phase alumina (Al_2O_3) reacts with the gaseous chlorine and carbon monoxide at 700 ℃. It is vital to know that there are many types of alumina with different purities and size distribution, which affects the reaction rate.

The Romans called materials with a styptic or astringent flavor "alumen." Impure forms of aluminum sulfate and alum, both of which occur naturally in volcanic areas, could have been among them. Our term alumina appears to be derived from the mineral alumen [36].

Thermodynamically, the production of aluminum chloride ($AlCl_3$) from non-bauxitic domestic resources is a feasible method [37]. To determine the feasibility of this method, reaction rate considerations are required. Furthermore, Thermodynamic results on gaseous metal chlorides, on the other hand, were inadequate to determine chlorination chemical purification [38].

The stoichiometry of chlorination of gaseous reactants is as follows,

$$\gamma\text{-}Al_2O_3\,(s) + 3Cl_2\,(g) + 3CO\,(g) \rightarrow 2AlCl_3\,(g) + 3CO_2\,(g) \tag{3.14}$$

Al2O3: In nature and different thermal conditions, alumina is found in different phases (specifically, this project deals with γ-Alumina). These phases can be transformed into each other. Figure 3.1, as an example, shows the transformation sequence of different alumina sources in different temperatures [39].

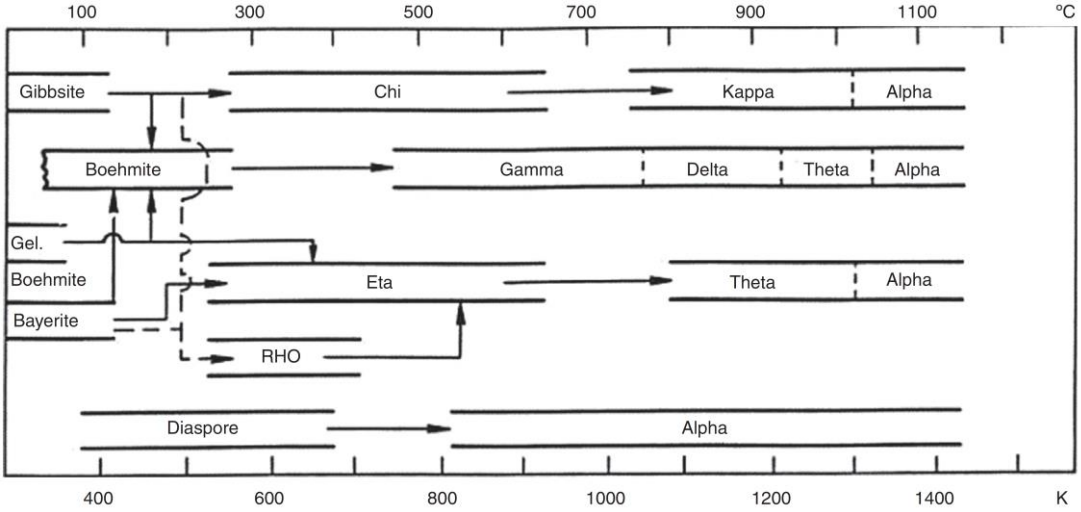

Figure 3.1: Phase transformation of alumina

$AlCl_3$: because of low vapor pressure (1 atm) at 169.7℃, the gas phase is almost in the form of gaseous. However, during chlorination at high temperatures, both gaseous $AlCl_3$ and Al_2Cl_6 are present in the process. It has a shallow melting point of about 192℃.

$$2AlCl_3 \rightleftarrows Al_2Cl_6 \tag{3.15}$$

$AlCl_3$ in the gaseous phase is in equilibrium with Al_2Cl_6. Table 3.1 shows their volume percentage at different temperatures [40].

Table 3.1: Volume percentage of $AlCl_3$ and Al_2Cl_6 in equilibrium

Temperature (K)	**600**	**800**	**1000**	**1200**
$AlCl_3$ (%)	2.1	35.5	88.4	98.7
Al_2Cl_6 (%)	97.9	64.5	11.6	1.3

CO and Cl_2: At the 1 atm pressure, CO and Cl_2 are in equilibrium with phosgene ($COCl_2$). The volume percentage of each in a mixture with different temperatures is given in Table 3.2 [40].

Table 3.2: Volume percentage of CO + Cl_2 and $COCl_2$ in equilibrium

Temperature (K)	**800**	**1000**
CO (%)	30.8	48.16
$COCl_2$ (%)	30.8	48.16
Cl_2 (%)	38.4	3.68

An equimolar mixture of CO and Cl_2 can contain small amounts of COCl2 in the normal temperature range of chlorination. However, This is not an issue because the reaction of alumina with phosgene is faster than an equimolar mixture of CO and Cl_2 [41].

$$Cl_2 + CO \rightleftarrows COCl_2 \tag{3.16}$$

3.3 Related Experiments and Results

The experimental techniques for obtaining gas-solid contact and extracting gaseous materials containing $AlCl_3$ and impurity elements are crucial in deciding the rate of chlorination. It is apparent that in a vertical reaction chamber in which solid particles collapse against rapidly rising gases, a flawless gas-solid interaction is nearly achieved, and the product's diffusion of reaction products from the pores to the gas stream controls the reaction rate predominantly. The gas-solid interaction is not intimate in a crucible within a vertical tubular furnace, and the gas-phase diffusion barrier controls the rate of reaction significantly. It must also be highlighted that the chlorination rate determined in the laboratory can only be used with extreme caution in a pilot plant or industrial plant.

Experiments of different CO/Cl_2 molar ratios revealed that $CO/Cl_2 = 1$ has the highest chlorination rate, and this is clear from overall reactions (3.14), which involve equimolar concentrations of CO and Cl_2 [40].

It is investigated [42] in an experiment with a fluidized bed reactor (0.075m diameter) and 66 mm of bed height, with 0.25 kg of Al_2O_3 particles with the size 0.06-mm and approximately 3.9 moles per second of an equimolar CO and Cl_2 mixture flow. The results showed that,

1. Unlike the experiments in a thermo-gravimetric balance, dehydration at 873 K and subsequent chlorination at that temperature followed a linear behavior when the weight percent of chlorinated alumina was plotted against time.
2. At 973 K, the findings were almost similar to those at 873 K.
3. For chlorination at 873 K, CO consumption was nearly constant and approximately equivalent to 83 percent.
4. The related findings for a sample dehydrated at 873 K and chlorinated at 673 K indicated a significantly slower chlorination rate, with CO consumption falling from 80% at 20 minutes to 60% at 180 minutes.
5. At 873 K, changing the Al_2O_3 height in the fluidized bed from 66 to 132 mm improved CO consumption from 83 to 87 percent.

As heated above 1,050°C, alumina transforms into the alpha phase (α-alumina). This results in a material that is denser, less porous, and less reactive. It is reported [43] that under the same laboratory conditions, the same temperature range (700-900°C), and the same time span (8 hours) for chlorination of 0.2 kg of charge in a vertical furnace, just half as much $AlCl_3$ was collected from α-alumina as from γ-alumina.

The optimal temperature for chlorinating aluminous resources with $CO + Cl_2$ is between 600° and 900°C, with 650 to 750°C being the most expected range. According to [42], 600°C could be a reasonable operating temperature for an alumina chlorination fluidized bed. In an industrial chlorination reactor, reactor's lining erosion and chlorination are significantly reduced at lower chlorination temperatures; hence, chlorination at as low a temperature as practicable tends to be desirable for designers.

Commercial chlorination reactor's construction materials must be kept cold enough to prevent being chlorinated. As a result, it seems that externally heated chambers are not feasible. An appropriate series of reactions must be chosen to produce enough heat to keep the internal reactor temperature up while retaining a temperature gradient that allows for a relatively cold and nearly non-reacting wall [40].

3.4 γ-Alumina Chlorination Kinetics

In 1981, Toth et al. [44] had studied the temperature and partial pressure dependency and the influence of photo-irradiation of the reactive gases to find reaction rate for γ-alumina chlorination with carbon monoxide and chlorine in different temperatures. The alumina sample in the experiment has the following characteristics (Table 3.3),

Table 3.3: Alumina specification in the experiment

Sample:	γ-alumina

Type:	CK-300
Produced by:	Ketjen, Netherland
Shape:	Cylindrical
Size:	1.6 mm diameter, 5-7 mm length, 10-15 mg width
Impurity:	100 ppm Fe_2O_3, 90 ppm SiO_2, 10 ppm Na_2O
Surface area:	Large (160 m^2g^{-1} by N_2 adsorption)

To do this experiment, isothermal TG measurements were taken at temperatures ranging from 327 to 850°C. Figure 3.2 and Figure 3.3 show some of the conversion curves as well as the temperature dependency of the specific initial reaction rate (R_0). The reaction rates for phosgene are higher than the mixture of CO and Cl_2 up to around 920 K, as observed, while the data obtained with both are almost the same [41]. Unlike [45], solid samples have been preheated before chlorination, and as a result, they have been gotten rid of the uncontrolled behavior of the change in the sample's reactivity taking place due to structural changes.

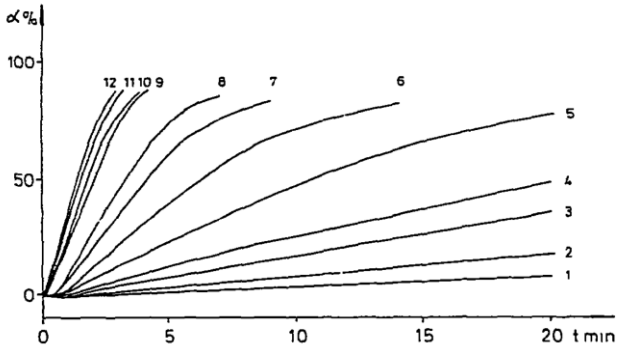

Figure 3.2: Reaction conversion vs. time graphs
(1) 649 K (2) 674 K (3) 698 K (4) 723 K (5) 775 K (6) 830 K (7) 878 K (8) 922 K (9) 973 K (10) 1023 K (11) 1064 K (12) 1123 K

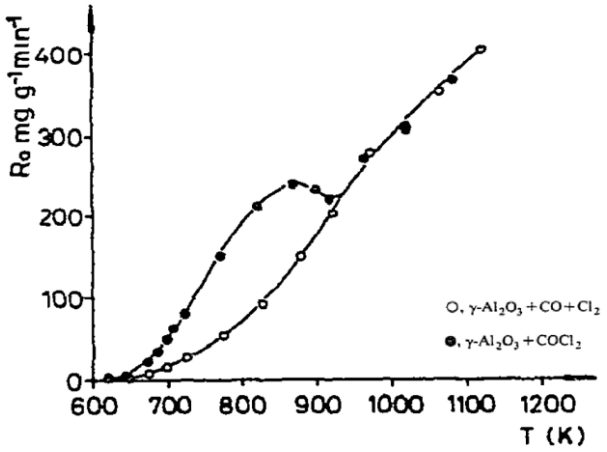

Figure 3.3: Specific initial reaction rate (R_0) vs. temperature (T)

The Arrhenius style of specific reaction rate (R_0) is illustrated in Figure 3.4. These types of graphs are thought to be typical of porous solids gasification processes [46]. The activation energies (E_1) computed by the rate constant of the first-order kinetic equation and initial reaction rate are 106 and 118 kJ/mole. Between temperatures 775-878 K, E_2 is almost half [8] of the E_1 and equal to 56 kJ/mole, and for the range between 920-1123 K, E_3 is the

[8] This is typical of the area that is influenced by both chemical reactions and pore diffusion.

lowest and equal to 23 kJ/mole, indicating that the process at these temperatures is effectively regulated by external mass transfer.

In conclusion, comparing this experiment with a fluidized bed reactor to chlorinate very fine alumina particles shows that the fluidized bed's reaction rate will be much quicker than the experiment. Figure 3.5 verifies this phenomenon. This results from an experiment [45] that has studied chlorination of two different sizes (7.9 mm and 0.125 mm) of γ-alumina with an equimolar mixture of CO and Cl_2.

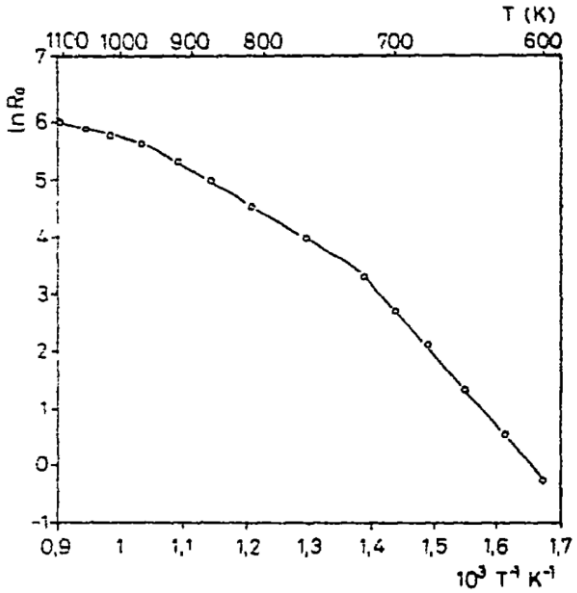

Figure 3.4: Arrhenius plot of the reaction

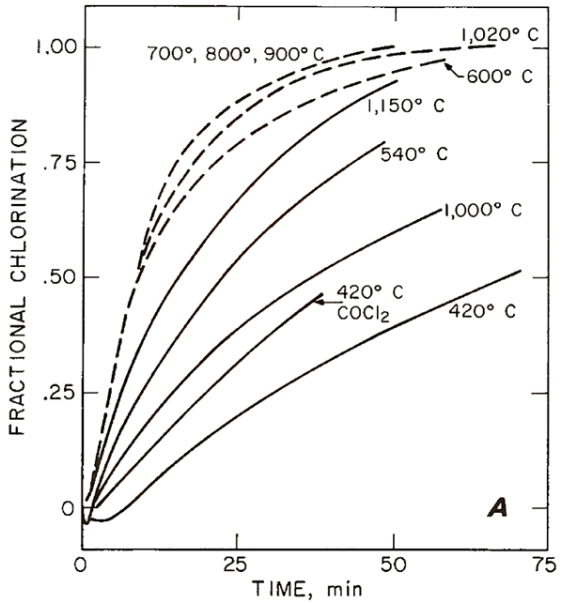

Figure 3.5: Chlorination of γ-alumina with CO/Cl_2=1. Solid lines are for 9.7 mm particles; broken lines are for 0.125 mm particles.

3.5 Possible Side Reactions

As discussed earlier, although the discussed reaction rates in section 3.4 (as the best available estimation) have been used, the simulations are based on the pure γ-alumina data with no impurities, and this means there is only one defined reaction in the simulations. Nevertheless, in a real-life case, the alumina used in this process has some impurities (as a primary advantage of this process discussion section 1). Table 3.4 gives some extra information about the real alumina, which will be used as the project's main feed.

Table 3.4: γ-Alumina impurities in percent[9]

	Impurities	**%**
1	Na_2O	0.39
2	SiO_2	0.012
3	Fe_2O_3	0.017
4	ZnO	0.0005
5	CaO	0.005
6	TiO_2	0.007
7	P_2O_5	0.0005
8	MnO	0.0005
9	V_2O_5	0.0005
10	Ga_2O_3	0.009
11	K2O	0.001
12	CuO	0.0005
13	NiO	0.0005
14	Cr_2O_3	0.0005
	Gibbsite (Al-OH_3) (bulk)	0.15
15	Gibbsite (-45µm)	0.2
	Gibbsite (+150µm)	0.23
	Alpha alumina (bulk)	1.6
16	Alpha alumina (-45µm)	4.7
	Alpha alumina (+150µm)	0.6
	Total	**7.9245**

From 7.9245% total impurities, α-alumina with 6.9% is dominating, and approximately 87 percent of impurities belong to this. Al-OH_3 with 0.38%, Na_2O with 0.39%, Fe_2O_3 with 0.017% and SiO_2 with 0.012% are leading after α-alumina (by 12.5% of total impurities). The rest are just about 0.05 % of total impurities.

These can highly affect on reaction rate by creating many side reactions. Some of them can be faster than the primary reaction, and some others can be slower. In continuation, some important side reactions are given.

Starting with α-alumina, the reaction stoichiometry is the same as the reaction for γ-alumina (reaction 3.14).

$$\alpha\text{-}Al_2O_3\,(s) + 3Cl_2\,(g) + 3CO\,(g) \rightarrow 2AlCl_3\,(g) + 3CO_2\,(g) \qquad (3.14)$$

[9] Given by SINTEF

Nevertheless, as discussed in section 3.3, by type transformation of the alumina, their physical properties change. As [47] reported, the reaction rate and activation energy of the α-alumina in a carbo-chlorination reaction is much lower than the γ type. In the range 800-900℃, the activation energy is 32±2.5 kJ/mole. In general,

$$r_{exp} = K\left(P_{cl_2}\right)^m (P_{CO})^n \tag{3.17}$$

where, P_x is the partial pressure of component x, *m* and *n* are reaction orders, K is the reaction constant, and r_{exp} is an experimentally calculated reaction rate. Table 3.5 give calculated *m* and *n* in different temperatures.

Table 3.5: Reaction orders in different temperatures

	Reaction Temperatures (℃)				
	800	**835**	**870**	**910**	**950**
m	0.71	0.60	0.59	0.56	0.48
n	0.77	0.72	0.66	0.65	0.65

The rate expression for the particular case under experiment considerations can be written as,

$$r_{exp} = \tilde{k}\left(P_{cl_2}\right)(P_{CO}) \tag{3.18}$$

where, $\tilde{k}$ is the apparent rate constant in $gg^{-1}min^{-1}atm^{-2}$. Table 3.6 shows the different values for the apparent rate constant,

Table 3.6: Values of $\tilde{k}$ obtained by regression analysis of r_{exp} vs $\left(P_{cl_2}\right)(P_{CO})$ results

T (℃)	800	835	870	910	950
$\tilde{k}$	0.0234	0.0256	0.0281	0.0313	0.0368
$ln\tilde{k}$	-3.755	-3.665	-3.572	-3.464	-3.302
10000/T	9.3197	9.0253	8.8479	8.4531	8.1766

In the IR study of alumina chlorination [48], it is reported that the Boudouard reaction caused a reduction in CO while simultaneously increasing CO under stationary conditions. Carbon deposition on almost all surfaces causes this heterogeneous reaction in a temperature between 650-1000 K.

$$2CO \rightleftarrows C + CO_2 \tag{3.19}$$

The Boudouard reaction gives the possibility of following side reactions [49],

$$Al_2O_3 + 3C + 3CO \rightarrow 2AlCl_3 + 3CO \tag{3.20}$$

$$SiO_2 + 2C + 2CO \rightarrow SiCl_4 + 2CO \tag{3.21}$$

$$CaO + C + CO \rightarrow CaCl_2 + CO \tag{3.22}$$

$$Fe_2O_3 + 3C + 3CO \rightarrow Fe_2Cl_6 + 3CO \tag{3.23}$$

$$TiO_2 + 2C + 2CO \rightarrow TiCl_4 + 2CO \tag{3.24}$$

In the temperature range investigated, all of the considered reactions were thermodynamically feasible. At 800°C, the order of reaction rates for the oxides in the carbo-chlorination reaction are as followings [49]:

$$Fe_2O_3 \geq Al_2O_3 \geq CaO \geq TiO_2 \geq SiO_2 \tag{3.25}$$

The pulse method revealed a simultaneous consumption of Cl_2 and formation of O_2 above 500 K [50]. Bulk-phase reactions that result in the release of oxygen, such as the reaction below, which are thermodynamically extremely disfavored,

$$Al_2O_3\ (s) + 3Cl_2\ (g) \rightarrow 2AlCl_3\ (g) + 3/2O_2\ (g) \tag{3.26}$$

$$Al_2O_3\ (s) + Cl_2\ (g) \rightarrow 2AlOCl\ (g) + 1/2O_2\ (g) \tag{3.27}$$

Above 700 K, with and without carbon, Fe2O3 chlorination is feasible [51],

$$Fe_2O_3\ (s) + Cl_2\ (g) \rightarrow 2/3FeCl_3\ (g) + 1/2O_2\ (g) \tag{3.28}$$

$$Fe_2O_3\ (s) + Cl_2\ (g) \rightarrow 2/3\ FeCl_3\ (g) + 1/2CO_2\ (g) \tag{3.29}$$

$$Fe_2O_3\ (s) + 3Cl_2\ (g) + 3CO\ (g) \rightarrow Fe_2Cl_6\ (g) + 3CO_2\ (g) \tag{3.30}$$

Bauxite chlorination in the presence of silicon tetrachloride acts as an alumina's chlorinating agent [51]:

$$2\ Al_2O_3\ (s) + 3SiCl_4\ (g) \rightarrow 4AlCl_3\ (g) + 3SiO_2\ (g) \tag{3.31}$$

4 Barracuda Virtual Reactor

4.1 Computational Fluid Dynamics

4.1.1 What is and why use CFD

The study of processes involving fluid flow, heat transfer, and related phenomena such as chemical reactions using computer-based simulation is known as computational fluid dynamics, or CFD. The method is very versatile, with applications in both the industrial and non-industrial sectors.

The study of fluid flows using numerical solution methods is known as Computational Fluid Dynamics (CFD). Aerodynamics and hydrodynamics are two engineering disciplines where CFD analyses are commonly used to achieve quantities such as lift and drag, as well as field properties such as pressures and velocities. Scientific rules in the form of partial differential equations are used in fluid mechanics. These laws are translated into algebraic equations by advanced CFD solvers, which can then be numerically solved.

These analyses have a high potential for saving time in the design process and are therefore less costly and more straightforward than routine data collection testing. Furthermore, real-world experiments can only calculate a small number of quantities at a time, but in a CFD study, all desired quantities can be calculated all at once, with high spatial and temporal precision. Since CFD analyses are just a rough approximation to an actual physical solution, physical testing methods cannot be eliminated entirely. Tests can also be run for verification purposes.

Furthermore, to fluid system design, CFD has several distinct advantages over experiment-based methods [52]:

- New product lead times and costs have been significantly decreased.
- In large systems, the ability to scientific researches where performing controlled experiments is difficult or impossible.
- Ability to research processes in unsafe environments, both inside and outside of their usual performance limits (e.g., safety studies and accident scenarios)
- Unlimited level of detail of results

4.1.2 Meshing and Gridding

Gridding, also known as meshing, is one of the essential parts of the computational fluid dynamics simulation process since it determines not only the simulation time but also the precision of the study's performance. Even if a very effective solver is used, generating a fragile and low-quality mesh/ grid often results in non-physical or extremely inconsistent simulation results. Consequently, the grid generation expertise and ability are just as critical as other steps of the process. In general, a CFD simulation process consists of five main steps, which can be extended to seven in adaptive simulation processes (Figure 4.1).

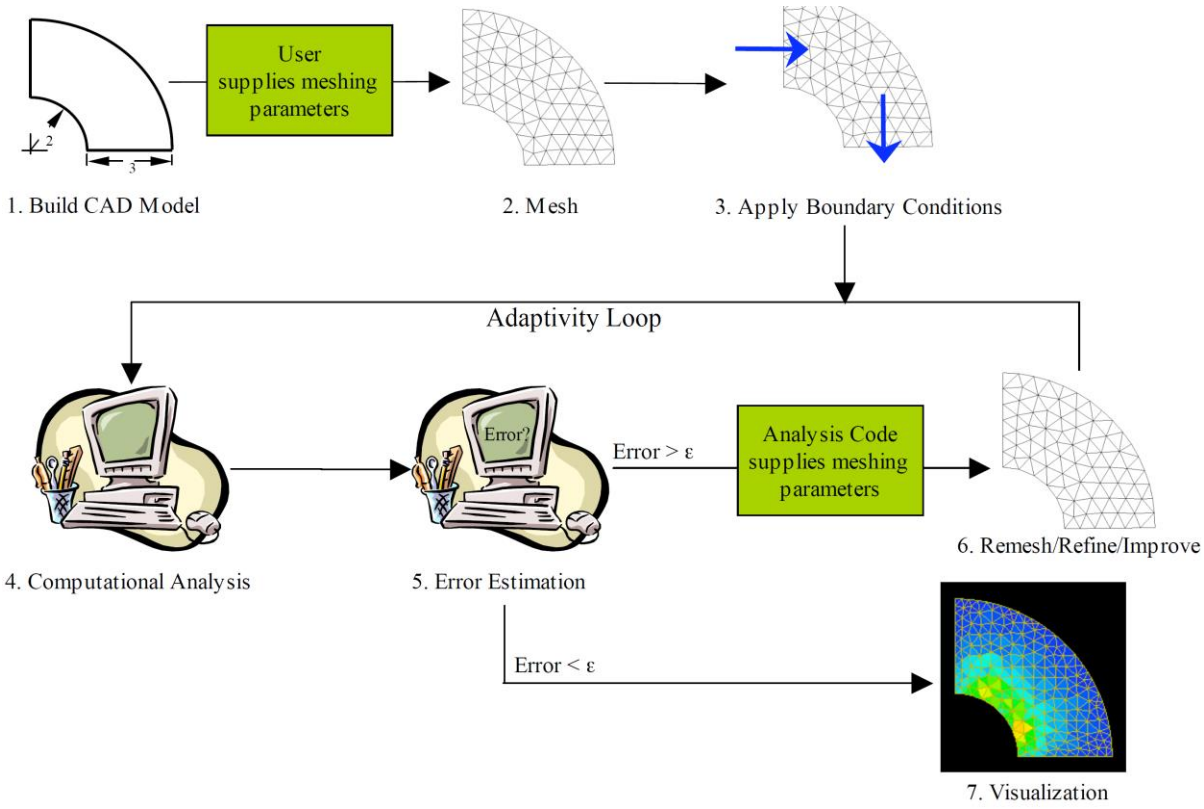

Figure 4.1: Adaptive CFD simulation Process [53]

A mesh is a method that separates a geometry into several components. The CFD solver uses these to generate control volumes. Figure 4.2 shows the main elements in this topic. The terminology of these elements are as below,

- Cell = control volume into which domain is broken up.
- Node = grid point.
- Cell center = center of a cell.
- Edge = boundary of a face.
- Face = boundary of a cell.
- Zone = grouping of nodes, faces, cells
- Domain = group of node, face, and cell zones.

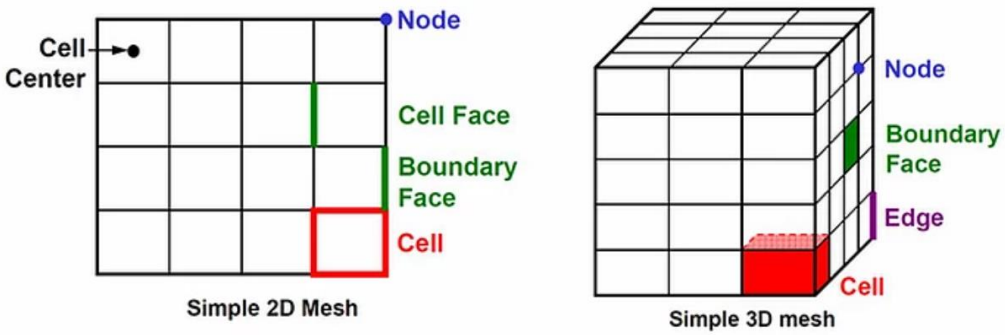

Figure 4.2: Illustration of mesh elements in 2D and 3D models[10]

[10] https://www.manchestercfd.co.uk/

There are two main types of gridding, Cartesian and Curvilinear. Grid lines of the Cartesian are often parallel to the coordinate axes. Coordinate surfaces are curved to fit boundaries in the Curvilinear (Figure 4.3).

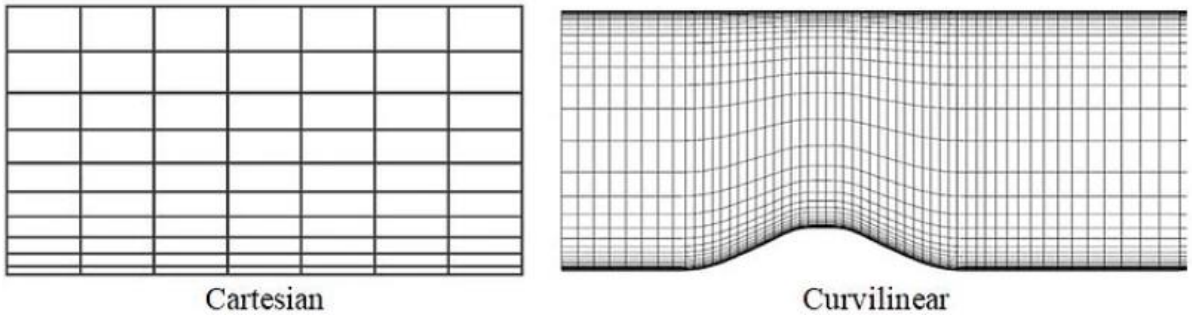

Figure 4.3: Main Types of gridding

4.2 Barracuda Virtual Reactor

Barracuda® technology is based on 3D Multiphase Particle-in-Cell (3D-MP-PIC), a patented computational technique for CFD simulation of gas-particle flows that includes close fluid-particle coupling as well as careful consideration of thermal physics and reaction chemistry. This technique was created by CPFD Software and allows for the simulation of gas-particle flows of any amount of discrete particulate solids and particle size distributions, resulting in a realistic simulated view inside a fluidized reactor. [54]

4.2.1 3D Multiphase Particle-in-Cell Approach

For dense particle flows, a three-dimensional, multiphase particle-in-cell approach is presented. The computational technique uses a continuum model to solve the governing equations of the fluid phase and a Lagrangian model to solve the governing equations of the particle phase. Through mapping particle properties to an Eulerian grid and then mapping back-calculated stress tensors to particle positions, the difficulties associated with estimating inter-particle interactions with dense particle flows with volume fractions above 5% have been removed. A robust sub-grid particle normal stress model for isolated particles that eliminates the need for an implicit measurement of normal particle stress on the grid has been presented. The properties of interpolation operators that provide compact support, conservatism, and a quick solution for a broad particle population are defined. With no numerical diffusion from the Lagrangian particle equations, the solution scheme allows for distributions of particle forms, sizes, and mass. The fluid momentum and pressure equations are indirectly solved, resulting in a stable solution. [55]

4.2.1.1 Governing Equations

There are two approaches to this, the Continuum and the Particulate Phase. For a fluid with no interphase mass transfer, the continuity equation is [55]:

$$\frac{\partial \theta_f}{\partial t} + \nabla.\left(\theta_f u_f\right) = 0 \tag{4.1}$$

Where θ_f is the fluid volume fraction (voidage) and u_f is the fluid velocity.

The momentum equation for the fluid will be as equation 4.2.

$$\frac{\partial\left(\theta_f u_f\right)}{\partial t} + \nabla.\left(\theta_f u_f u_f\right) = -\frac{1}{\rho_f}\nabla P - \frac{1}{\rho_f}\mathrm{F} + \mathrm{g}\theta_f \tag{4.2}$$

Where the F is the rate of momentum exchange per volume between the fluid and particle phases, fluid and particle phases are also isothermal, and the fluid phase is incompressible. The momentum equation discussed here ignores viscous molecular diffusion in the fluid, but the interphase drag power, F, keep the viscous drag between particles and fluid. The consequence of ignoring the laminar fluid viscous terms on dense particle flow is usually marginal, and laminar terms can be conveniently included in the fluid equation set. There are currently no suitable models

for dense particle flow, which is the fascinating turbulent flow. Gas movement around near pack particles creates small sub-grid eddies and dissipation, while high density and scale particles behave as large eddies of momentum transfer. Furthermore, particles coating walls with particle sizes of the same order or larger than the viscous sublayer complicate momentum transfer at walls. The turbulent dense particle flow is not addressed in this equation. However, discrete particle to fluid momentum transfer (a turbulent closure model for sub-grid momentum transfer between particles and fluid) yields low Reynolds numbers (based on particle diameter) and is a good predictor of dense particle flows over a wide range of gas flow. [55]

In the Particulate Phase, the particle probability distribution function $\emptyset\,(X, u_p, \rho_p, \Omega_p, t)$ is used to define the dynamics of the particle process, where X is the particle position, u_p is the particle velocity, ρ_p is the particle density, and Ω_p is the particle volume. For the time being, it is thought that each particle's mass remains stable over time (i.e., no mass transfer between particles or to the fluid), although particles may vary in size and density. By solving a Liouville equation [56] for the particle distribution function, the time evolution of $\emptyset$ is obtained.

$$\frac{\partial \emptyset}{\partial t} + \nabla.\left(\emptyset\, u_p\right) + \nabla_{u_p}.(\emptyset A) = 0 \tag{4.3}$$

where ∇_u is the divergence operator with respect to velocity. Using the definition from [57], the discrete particle acceleration, A, can be defined as,

$$A = D_p\left(u_f - u_p\right) - \left(\frac{1}{\rho_p}\nabla P + \frac{1}{\theta_p \rho_p}\tau\right) + \mathrm{g} \tag{4.4}$$

where the terms describe acceleration due to aerodynamic drag, pressure gradient, interparticle stress gradient, and gravity, respectively. At x and t in the interval $\left(u_p, u_p + du_p\right)$, $\left(\rho_p, \rho_p + d\rho_p\right)$, and $\left(\Omega_p, \Omega_p + d\Omega_p\right)$ the probability function integrated over velocity and mass gives the probable number of particles per unit volume. The particle volume fraction is calculated using the particle distribution function and is defined as follows,

$$\theta_p = \iiint \emptyset \Omega_p d\Omega_p d\rho_p du_p \tag{4.5}$$

In the Eulerian momentum equation, the interphase momentum transfer function per volume is,

$$F = \iiint \emptyset \Omega_p \rho_p \left[D_p\left(u_f - u_p\right) - \frac{1}{\rho_p}\nabla P\right] d\Omega_p d\rho_p du_p \tag{4.6}$$

By taking the moments of equation (4.3), the Eulerian governing equations for the particle process can be obtained. The particle conservation equations are obtained by multiplying equation (4.3) by $\Omega_p \rho_p$ and $\Omega_p \rho_p u_p$. Moreover, integrating over particle mass, volume, and velocity coordinates. The equation for particle continuity will be as follow,

$$\frac{\partial\left(\overline{\theta_p \rho_p}\right)}{\partial t} + \nabla.\left(\overline{\theta_p \rho_p}\;\overline{u_p}\right) = 0 \tag{4.7}$$

and the particle momentum equation can be derived as [55],

$$\begin{aligned} &\frac{\partial\left(\overline{\theta_p \rho_p}\;\overline{u_p}\right)}{\partial t} + \nabla.\left(\overline{\theta_p \rho_p}\;\overline{u_p}\;\overline{u_p}\right) \\ &\qquad = -\theta_p \nabla P - \nabla \tau_p + \overline{\theta_p \rho_p}\; g + \iiint \emptyset \Omega_p \rho_p \left[D_p\left(u_f - u_p\right)\right] d\Omega_p d\rho_p du_p \\ &\qquad - \nabla.\left[\iiint \emptyset \Omega_p \rho_p \left[\left(u_p - \overline{u_p}\right)\left(u_p - \overline{u_p}\right)\right] d\Omega_p d\rho_p du_p\right] \end{aligned} \tag{4.8}$$

where, the mean particle velocity $\overline{u_p}$ is given by the equation (4.9),

$$\overline{u_p} = \frac{1}{\overline{\theta_p \rho_p}} \iiint \emptyset \Omega_p \rho_p u_p d\Omega_p d\rho_p du_p \tag{4.9}$$

where the term $\overline{\theta_p \rho_p}$ can be calculated by,

$$\overline{u_p} = \iiint \emptyset \Omega_p \rho_p d\Omega_p d\rho_p du_p \quad (4.10)$$

It is essential to remind that $\theta_f + \theta_p = 1$

4.2.2 Chemistry

In fluidized bed reactors, typical chemistry can be separated into two categories: homogeneous reactions, which occur solely in the fluid phase, and heterogeneous reactions, including a solid as a reactant, product, or catalyst. The heterogeneous reactions can be divided into deposition reactions, consumption reactions, catalytic reactions, and solid reactions.

Homogeneous reaction (fluid phase): This reaction occurs in the fluid phase and includes reactants and products from the fluid phase. The reaction rate can be influenced by the reactant concentrations in the fluid phase, as well as temperature and other fluid properties.
Deposition reaction: This is a heterogeneous reaction that occurs at the particle's surface and results in the formation of at least one solid substance from fluid phase reactants. The reaction rate is influenced by particle surface size, particle temperature, and reactant concentrations in the fluid phase.
Consumption reaction: This is a heterogeneous reaction that takes place at a particle's surface and results in fluid phase products from at least one solid reactant. The mass of the solid reactant, particle temperature, and the concentration of any fluid phase reactants can influence the reaction rate.
Catalytic reaction: The presence of a solid component (catalyst) is needed for the reaction to occur in this heterogeneous reaction of fluid-phase reactants and materials. Although the reaction rate is likely to be influenced by the mass or surface area of the current catalyst, the catalyst would not be absorbed or formed due to the reaction. The reaction rate can also be influenced by the concentrations or temperatures of the reactants in the fluid phase.
Solid reaction ("solids producing solids"): A heterogeneous reaction involves both solid reactants and solid products and happens at the particle surface or within the particle volume. The mass of solid reactants, concentrations of fluid phase reactants, and particle or fluid temperatures all influence reaction rates. This method of the process includes the adsorption of a gas onto a solid sorbent. In a fluidized bed, alumina chlorination is a heterogeneous consumption reaction.

4.2.2.1 Approaches for calculating chemistry

Within a model, Barracuda® offers two methods for measuring chemical reactions. The first method is average volume chemistry, which calculates the reaction at the cell level (Eulerian). As a result, volume average chemistry works well for homogeneous and catalytic reactions and occurs mainly in the fluid phase. Although average volume chemistry can be used for other heterogeneous reactions, it is not recommended because all solids-dependence is dependent on cell level averages of particle properties rather than individual particle properties. Discrete particle chemistry is the favored method for most heterogeneous reactions. Specific computational particle temperature, mass, and other properties are used to measure discrete particle chemistry at each computational particle (Lagrangian) within the model. Although this method has a marginally higher computational cost, the benefit of the model's improved resolution often outweighs this cost. Discrete particle chemistry cannot be used to model a homogeneous reaction. [54]

4.2.2.2 Selecting the rate coefficient Type

Multiple Types of rate coefficients are available in Barracuda® to accommodate the wide range of possible reaction dependencies. Among these, the Arrhenius rate is used.

Arrhenius Rate: This form is the most often used rate coefficient form since it allows for temperature, pressure, fluid density, and fluid volume fraction to be calculated through the C_0, C_1, C_2, C_3, and C_4 constants in equations 4.11) and (4.12). For converting certain rate expressions to a discrete chemistry form, the discrete chemistry form often contains the additional N_p/V dependency via the C_5 constant (discussed in 5.2.2.3). The term exp (E/T+E0), E (the activation temperature term), does not contain a universal gas constant, R, in the denominator.

$$\text{Volume average:} \quad k = C_0 T^{C1} P^{C2} \rho_f^{C3} \theta_f^{C4} exp(-E/T+E0) \quad (4.11)$$

$$\text{Discrete:} \qquad k=C_0\,T^{C1}\,P^{C2}\,\rho_f{}^{C3}\,\theta_f{}^{C4}(Np/V)^{C5}\,exp(-E/T+E0) \tag{4.12}$$

So, it has already been mentioned that it is necessary to use discrete chemistry. According to section 3.4, the only available parameters for this equation are C_0 (pre-exponential factor) and E (activation energy/R). Other parameters such as C_1, C_2, and C_3, common in both equations, are zero. The only parameters that have been calculated by conversion rule are C_4 and C_5. [54]

4.2.2.3 Conversion between volume-average and discrete chemistry

Often, rate expressions are calculated depending on the volume of gas present and state that a certain amount of material per volume of gas would be consumed, produced, or otherwise transformed per time division. The cell volume is divided into different control volumes for each particle in the cell to derive equations for this conversion. If N_p is the number of particles in a cell with volume V_{cell}, then the control volume for each particle is $v_{cp}= V_{cell}/N_p$. [54]

Using this control volume, the mass and area density around each discrete particle becomes,

$$\rho_{pv} = m_p/v_{cp} = m_pN_p/V_{cell} \quad and \quad A_s = A_p/v_{cp} = A_pN_p/V_{cell} \tag{4.13}$$

where, ρ_{pv} is the equivalent volume-average solids density, m_p is the particle's mass, A_s is the equivalent volume average area density, and A_p is the particle's surface area. Similarly, for a volume-average particle reaction with a gas phase basis occurring in the cell, r, the reaction rate on the particle itself is calculated as,

$$r_d = r_{va}\theta_f v_{cp} = r_{va}\theta_f\,V_{cell}/N_p \quad \text{or} \quad r_{va} = r_d\theta_f{}^{-1}N_p/V_{cell} \tag{4.14}$$

In this project, the Arrhenius form of the reaction rate for volume-average simulation;

$$r_{va} = C_0\,exp\left(\frac{-E}{T}\right) \tag{4.15}$$

A volume-average reaction rate can be converted to a discrete particle reaction by substituting the relationships in (4.4) and (4.5).

$$\frac{r_d\theta_f{}^{-1}N_p}{V_{cell}} = C_0\exp\left(\frac{-E}{T}\right) \tag{4.16}$$

$$r_d = C_0\,\theta_f\left(\frac{V_{cell}}{N_p}\right)exp\left(\frac{-E}{T}\right) \tag{4.17}$$

This means comparing the equation (4.12) with (4.17) shows that C_4 =1 and C_5 = -1.

4.2.2.4 Shrinking core model

To accomplish more precise simulation, the shrinking core model can be enabled and used (can only apply to discrete reactions). The first-order reaction rate, gas transport from non-reacting material to the core, and gas transport to the boundary layer all influence the reaction rate. Each particle has a history, and a "fresh" particle can react more quickly than an "old" particle. In the following, the principal calculation of this model is given. As seen, many parameters (Figure 4.4) are involved in this calculation, but the software asks about the particle diffusion coefficient.

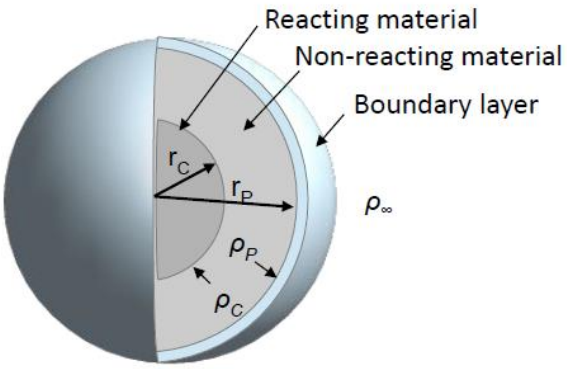

Figure 4.4: Shrinking Core model diagram [54]

$$\rho_c = \frac{\rho_\infty}{k_R\left(\frac{1}{k_R}+\frac{1}{k_D}+\frac{1}{k_B}\right)} \tag{4.18}$$

$$k_D = \frac{4\pi D_{m,s}}{r_p{}^{-1} - r_c{}^{-1}} \tag{4.19}$$

$$r_c = \left(\frac{3m_s}{4\pi\rho_s}\right)^{\frac{1}{3}} \tag{4.20}$$

4.2.3 Thermal Modeling

In addition to the particle-fluid dynamics, a model may be set up to be isothermal, in which the temperature is considered to be constant throughout, or thermal, in which heat transfer and energy balance calculations are determined in addition to the particle-fluid dynamics.

Isothermal flow: Since heat transfer equations cannot be solved, selecting the isothermal flow for the model assumes constant temperature for all fluids and particles in the system, allowing the simulation to run faster. If an isothermal model is used, the isothermal flow temperature must be entered in the isothermal flow text box.

Thermal flow: Barracuda® can quantify temperature gradients within the model due to initial particle and fluid temperatures, boundary state temperatures, thermal walls, or chemical reactions if Thermal flow is chosen. If a thermal model is used, the user must also enter the following information in the relevant fields:

- Thermal properties of all base materials
- Heat transfer coefficients
- Initial fluid temperatures in the model
- Initial particle temperatures in the model
- Boundary condition temperatures

In a reacting fluidized bed, there are several different kinds of heat transfer mechanisms, and Barracuda® handles the following heat transfer modes [54],

1. Convective fluid-to-wall heat transfer

1.1. Lean-phase heat transfer

1.2. Dense-phase heat transfer

2. Fluid-to-particle heat transfer

3. Radiation

3.1. P-1 model for thermal radiation

3.2. Wall to Particle radiation

4.2.3.1 Convective fluid-to-wall heat transfer (W/m²K)

The local fluid-wall heat transfer coefficient, h_{fw}, is a combination of contributions from a lean gas phase heat transfer coefficient, h_l, and a dense particle phase's coefficient, h_d. The fluid-to-wall heat transfer coefficient is weighted by the function f_d which is the fraction of contact time by the dense particle phase. The time fraction of dense phase contact, f_d is a function of the particle volume fraction at the wall, θ_p, and the close pack value fraction, θ_{cp}.

$$h_{fw} = h_l + f_d h_d \quad , \quad f_d = 1 - e^{-10(\theta_p/\theta_{cp})} \tag{4.21}$$

The general form of the lean phase heat transfer coefficient is,

$$h_l = \left(\left(c_0 Re_L^{n_1} Pr^{n_2} + c_1 \right) \frac{k_f}{L} + c_2 \right) \tag{4.22}$$

where, c_0, c_1, c_2, n_1, and n_2 are adjustable model parameters, k_f is the thermal conductivity of the fluid, and L is the cell length. The Reynolds number and Prandtl number are defined as,

$$Re_L = \frac{\rho_f U_f L}{\mu_f} \quad , \quad Pr = \frac{\mu_f c_{p,f}}{k_f} \tag{4.23}$$

where, ρ_f is the fluid density, U_f is the fluid velocity, μ_f is the fluid viscosity and $c_{p,f}$ is the fluid heat capacity. In this simulation, because of having no information about these coefficients, the following default lean phase heat transfer coefficient is based on the correlation of Douglas and Churchill [58] have been used.

(c_0 = 0.46, c_1 = 3.66, c_2 = 0.0, n_1 = 0.5, and n_2 = 0.33)

The general form of the dense phase heat transfer coefficient is as below,

$$h_d = \left(c_0 Re_L^{n_1} \right) \frac{k_f}{d_p} \tag{4.24}$$

where, d_p is the particle diameter. In this case, the particle Reynolds number is defined as,

$$Re_L = \frac{\rho_f U_f d_p}{\mu_f} \tag{4.25}$$

In this simulation, because of having no information about these coefficients, the following default dense phase heat transfer coefficient values [58] have been used.

(c_0 = 0.525, n_1 = 0.75)

4.2.3.2 Fluid-to-particle heat transfer (W/m²K)

Heat transfer between the fluid and particle phases is modeled by the fluid-to-particle heat transfer coefficient. The fluid-to-particle heat transfer coefficient has the same general form:

$$h_l = \left(\left(c_0 Re_p^{n_1} Pr^{0.33} + c_1 \right) \frac{k_f}{d_p} + c_2 \right) \tag{4.26}$$

The Reynolds number and Prandtl number are defined as,

$$Re_L = \frac{\rho_f |U_f - U_p| d_p}{\mu_f} \quad , \quad Pr = \frac{\mu_f c_{p,f}}{k_f} \tag{4.27}$$

where, U_f is the fluid velocity, U_p is the particle velocity.

The particle Nusselt number, Nu_p in fluidized beds, is typically lower than the Nusselt number for a single sphere when the Reynolds number is less than 20. Theoretically, a single sphere in a quiescent fluid will have a value of Nu_p =2.0, representing the limit of conductive heat transfer. However, in a fluidized bed, the bubbling phenomenon will cause the observed magnitude of Nu_p to be lower than 2.0. Low Reynolds numbers correspond to beds of fine particles (small d_p and U_p), wherein bubbles tend to be clouded with entrained particles. This diminishes the efficiency of particle-gas contact below represented by idealized plug flow, resulting in reduced values of Nu_p. The "bubbles" become relatively cloudless as particle diameter increases (coarse particle beds), and gas-particle interaction improves. Barracuda® uses a correlation for fluid-to-particle heat transfer coefficient dependent on McAdams' correlation to capture fluid-to-particle heat transfer in a fluidized bed. [59].

(c_0 = 0.37, c_1 = 0.1, c_2 = 0.0, and n_1 = 0.6)

Turton and Levenspiel's experimental results on particle-fluid heat transfer coefficient in fluidized beds with small particles agree with this correlation. [26].

4.2.3.3 Radiation model

P-1 radiation model: where thermal radiation between particles, particles and fluid, particles and thermal walls, and fluid and thermal walls is taken into account. The incident radiation transfer equation in the P-1 radiation model is:

$$\nabla.(\Gamma \nabla G) + 4\left(an^2 \sigma T^4 + E_p\right) - \left(a - a_p\right) G = 0 \tag{4.28}$$

The Marshak boundary condition is used for the radiative heat flux at the thermal wall by defining a thermal wall boundary condition., q_w:

$$-q_w = \Gamma_w \left(\frac{\partial G}{\partial n} \right) = \frac{\varepsilon_w}{2(2 - \varepsilon_w)} (4\sigma T_w^4 - G_w) \tag{4.29}$$

$$\Gamma = \frac{1}{3\left(a + a_p + \sigma_f + \sigma_p\right)} \tag{4.30}$$

Fluid mixture properties are averaged from components by the following mixing rule:

$$a = \sum_{i=1}^{nf} y_{f_i} a_{f_i} \tag{4.31}$$

The equivalent particle absorption coefficient is:

$$a_p = \sum_{i=1}^{np} \varepsilon_{pi} \frac{A_{pri}}{V} \tag{4.32}$$

The equivalent fluid scattering coefficient is:

$$\sigma_f = \sum_{i=1}^{nf} y_{f_i} \sigma_{f_i} \tag{4.33}$$

The equivalent particle scattering factor is:

$$\sigma_p = \sum_{i=1}^{nf} (1 - \sigma_{pi})(1 - \varepsilon_{pi}) \frac{A_{pi}}{V} \tag{4.34}$$

The refractive index of the fluid mixture, *n*, is calculated as:

$$\frac{n^2 - 1}{n^2 + 2} = \sum_{i=1}^{nf} x_{f_i} \frac{{n_{f_i}}^2 - 1}{{n_{f_i}}^2 + 2} \tag{4.35}$$

The equivalent emission of the particles is:

$$E_p = \sum_{i=1}^{nf} \varepsilon_{pi} A_{pi} \frac{\sigma {T_{pi}}^4}{V} \tag{4.36}$$

The heat source, or sink, due to radiation, q_r is:

$$-\nabla . q_r = \nabla . (\Gamma \nabla G) = (a - a_p) G - 4\left(a n^2 \sigma T^4 + E_p\right) \tag{4.37}$$

The heat source is integrated into the fluid and particle energy equations to account for radiation's contribution.

Wall to Particle Radiation: The model, which is only used under thermal wall boundary conditions, only considers radiation between a thermal wall and the particle phase and ignores radiative heat transfer between particles, walls, or the wall and fluid. The radiation between a thermal wall cell and nearby particles, q_{wp}, is calculated as,

$$q_{wp} = A_w F_{wp} \varepsilon_{wp} \sigma \left({T_w}^4 - {\bar{T}_p}^4\right) \tag{4.38}$$

$$\varepsilon_{wp} = \left(\frac{1}{\bar{\varepsilon}_p} + \frac{1}{\varepsilon_w} - 1\right) \tag{4.39}$$

4.2.4 Drag Models

In Virtual Reactor, the drag model calculates the force exerted on a particle, F_p, by the model's fluid. In Virtual Reactor can use the drag models mentioned below,

- Constant Drag
- Stokes
- Wen-Yu
- Ergun
- WenYu-Ergun
- Turton-Levenspiel
- Richardson, Davidson, and Harrison
- Haider-Levenspiel
- EMMS-Yang-2004
- Non-spherical Ganser
- Non-spherical Haider-Levenspiel

All drag models calculate a force acting on a particle, F_p as a function of the fluid and particle properties and flow conditions. For all models below, the force on the particle is a function of the mass of the particle m_p, fluid velocity u_f, the particle velocity u_p, and the drag function $\acute{D}$.

$$F_p = m_p \acute{D}(u_f - u_p) \tag{4.40}$$

In many of the models, the drag function is dependent on the fluid conditions, the drag coefficient C_d, and the Reynolds number *Re*. For purposes of calculating particle drag, the Reynolds number is calculated as

$$Re = \frac{2\rho_f r_p |u_f - u_p|}{\mu_f} \tag{4.41}$$

where ρ_f is the fluid density, r_p is the particle radius, and μ_f is the fluid viscosity. In many models, the drag function $\acute{D}$ is related to the drag coefficient by:

$$\acute{D} = \frac{3}{8} C_d \frac{\rho_f |u_f - u_p|}{r_p \rho_p} \tag{4.42}$$

Constant drag

The constant drag model calculates the force on the particle using (4.40). The drag function *D* is specified by the Constant value entered in the Drag Model Selection dialog box.

Stokes drag

The Stokes drag model is based upon an analytical calculation for the drag force acting on a single particle at creeping flow, typically $Re < 0.1$ [60]. Using equations (4.40) and (4.42) and when $C_d = 24/Re$, the Stokes drag The Stokes drag can be written as follow,

$$F_p = 6\pi\mu_f r_p (u_f - u_p) \tag{4.43}$$

Wen-Yu drag model

The Wen-Yu model in Barracuda® is based on single-particle drag models plus a dependence on the fluid volume fraction θ_f to account for the particle packing. In the Wen-Yu model [61] and [62], the particle force and drag function are calculated by equations (4.40) and (4.42). The drag coefficient C_d is a function of the Reynolds number Re according to the following set of conditions:

$$C_d = \begin{cases} \frac{24}{Re}{\theta_f}^{-2.65} & Re < 0.5 \\ \frac{24}{Re}{\theta_f}^{-2.65}(1 + 0.15Re^{0.687}) & 0.5 \le Re \le 1000 \\ 0.44{\theta_f}^{-2.65} & Re > 1000 \end{cases} \tag{4.44}$$

Ergun drag

The Ergun Drag model was developed from dense bed data and is therefore only valid for those systems [63]. In the Ergun drag model, the particle drag force is calculated by (4.40), and the drag function is given by

$$D = 0.5\left(\frac{180\theta_p}{\theta_f Re} + 2\right)\frac{\rho_f |u_f - u_p|}{r_p \rho_p} \tag{4.45}$$

Wen-Yu/Ergun blend

Since the Wen and Yu correlation [61] is appropriate for more dilute systems and the Ergun relationship [64] is appropriate at higher packing fractions, [65] proposed a drag function blending both the Wen-Yu and Ergun functions. In Barracuda®, the particle force is calculated using equation (4.17) in which the drag function is calculated as,

$$D = \begin{cases} D_1 & \theta_p < 0.75\theta_{cp} \\ (D_2 - D_1)\left(\dfrac{\theta_p - 0.75\theta_{cp}}{0.85\theta_{cp} - 0.75\theta_{cp}}\right) & 0.75\theta_{cp} \le \theta_p \le 0.85\theta_{cp} \\ D_2 & \theta_p > 0.85\theta_{cp} \end{cases} \quad (4.46)$$

where:

θ_p is the particle volume fraction

θ_{cp} is the particle volume fraction at close pack[11]

D_1 is the Wen and Yu drag function defined in (4.44)

D_2 is the Ergun drag function defined in (4.45)

Turton and Levenspiel

The Turton and Levenspiel model in Barracuda® uses the single-particle drag function of [66] to depend on the fluid volume fraction [61]. The Turton and Levenspiel model calculates the drag force on a particle using (4.40) and (4.42). The Turton and Levenspiel drag coefficient is

$$C_d = \frac{24}{Re}(1 + 0.173Re^{0.657})\theta_f{}^{-2.65} \frac{0.413}{1 + 16300Re^{-1.09}}\theta_f{}^{-2.65} \quad (4.)$$

Richardson, Davidson, and Harrison

The Richardson, Davidson and Harrison model in Barracuda® uses the single-particle drag function [67]. The drag force on a particle is calculated with (4.40) and (4.42), where the drag coefficient is calculated as,

$$C_d = \begin{cases} \dfrac{24}{Re} & Re < 0.2 \\ \dfrac{24}{Re} + 10.56Re^{-0.313} & 0.2 \le Re \le 500 \\ 0.44 & Re > 500 \end{cases} \quad (4.48)$$

Haider-Levenspiel

The Haider-Levenspiel drag model in Barracuda® is from [68].

$$D = \frac{9}{2}\frac{\mu_f}{r_p{}^2\rho_p} f_h \quad (4.49)$$

$$f_h = 1 + 0.14017Re^{0.6529} + \frac{0.19197Re^2}{Re + 2682.5} \quad (4.50)$$

EMMS-Yang-2004

The EMMS-Yang-2004 drag model in Barracuda® is based on [69] and [70]. The EMMS-Yang-2004 model constants were generated for the following conditions based on the Li and Kwauk experiment.

[11] The close pack volume fraction specifies the maximum volume fraction of particles when they are packed randomly.

- Air at atmospheric conditions
- 54-micron mono-sized particles
- The particle density of 930 *kg/m³*
- Fluid Superficial Velocity of 1.52 *m/s*
- Solids Flux of 14.3 *h*

$$D = \frac{9}{2}\frac{\mu_f}{{r_p}^2 \rho_p} f_e \tag{4.51}$$

$$C_d = \begin{cases} \dfrac{1}{18\theta_f}\left(150\dfrac{\theta_p}{\theta_f} + 1.74Re\right) & \theta_f < 0.74 \\ (1 + 0.15Re^{0.687})\ \omega & \theta_f \geq 0.74\ and\ Re < 1000 \\ 0.44\ \dfrac{Re}{24}\omega & \theta_f \geq 0.74\ and\ Re \geq 1000 \end{cases} \tag{4.52}$$

$$\omega = \begin{cases} -0.576 + \dfrac{0.0214}{4\left(\theta_f - 0.7463\right)^2 + 0.0044} & 0.74 \leq \theta_f < 0.82 \\ -0.0101 + \dfrac{0.0038}{4\left(\theta_f - 0.7789\right)^2 + 0.0040} & 0.82 < \theta_f \leq 0.97 \\ -31.8295 + 32.8295\ \theta_f & 0.97 < \theta_f \leq 1 \end{cases} \tag{4.53}$$

Non-spherical Ganser

The Non-spherical Ganser model in Barracuda® uses the single-particle non-spherical drag model of Ganser [71] with the dependence on the fluid volume fraction of [61]. The Non-spherical Ganser model calculates the drag force on a particle using (4.40) and (4.42). The drag coefficient C_d is calculated as,

$$C_d = {\theta_f}^{-2.65} K_2 \left[\frac{24}{ReK_1K_2}(1 + 0.1118(ReK_1K_2)^{0.6567}) + \frac{0.43056}{1 + \dfrac{3305}{ReK_1K_2}}\right] \tag{4.54}$$

and the isometric shape constants K_1 and K_2 are defined as

$$K_1 = \frac{3}{1 + 2\varphi^{-0.5}} \quad , \quad K_2 = 10^{1.8148(-log\varphi)^{0.5743}} \tag{4.55}$$

Non-spherical Haider-Levenspiel

The Non-spherical Haider-Levenspiel model in Barracuda® uses the single-particle non-spherical drag model of Haider and Levenspiel [71] with the dependence on the fluid volume fraction of [61]. The Non-spherical Haider-Levenspiel model calculates the drag force on a particle using (4.40) and (4.42). The drag coefficient C_d is calculated as,

$$C_d = {\theta_f}^{-2.65}\left[\frac{24}{Re}\left[1 + 8.1716\exp(-4.0655\varphi)\ Re^{(0.0964 + 0.5565\varphi)}\right] + \frac{73.6896\exp(-5.0748\varphi)\ Re}{Re + 5.378\exp(6.2122\varphi)}\right] \tag{4.56}$$

5 Design Considerations

5.1 Overall Design Criteria

The project goals to design a fluidized bed reactor for the pure γ-alumina chlorination in the presence of equimolar carbon monoxide and chlorine gas mixture under the isothermal condition at 700℃. The reactor should be designed for handling 0.6 kg/s of alumina feed. There are no specified limitations for the reactor dimensions or the geometry. However, it is recommended to minimize the use of internals (specifically for cooling and solid circulation). Moreover, because of some technical considerations, such as the possibility of having a considerable percentage of α-alumina in the feed, it is also suggested not to use circulation. However, designing a cyclone for solid separation in the outlet is preferable. It is important to note that the inlet pressure boundary conditions were not provided at the beginning of the project, and it is specified later during the project. Based on the overall process simulations of the main project, SINTEF has revised the pressure boundary conditions, and then those input data in the CFD simulations from the current study is revised accordingly. Having the experience of the group project [16] on the topic, in the following, the main design factors and considerations are discussed.

Circulation System: Although the preliminary project ended up having a turbulent regime and using internal circulation, considering the highly corrosive environment inside the reactor and the existence of α-alumina impurity in the system, which is not favorable, it lead to avoid the use of circulation added to the fluidized bed reactor.

Gas-Solid Separator: Although one of the project's main goals is to minimize the solid escape from the system, an external high-efficiency cyclone with an efficiency of 99% will be designed to handle maximum solid carryover. The cyclone is designed for half of the inlet solid flow rate to the reactor (0.01-0.3 kg/s). The other design parameters such as pressure, fluid properties, and average particle size will be calculated from simulations.

Regime and Bed Type: Based on discussed considerations, the reactor should be designed for the bubbling regime. A free bubbling bed with no internal baffles is recommended to use. To have a smaller bubble size and lower rise velocity, the superficial velocity is chosen in a range close to the minimum bubbling velocity.

Bed Aspect Ratio (H/D): The bed height (H) to the bed diameter (D) ratio is known as the bed aspect ratio (H/D), which is one of the most crucial factors for reactor design calculations. The superficial gas velocity by matching the required fluidization regime is used to determine the bed diameter. The bed is generally called a tall or deep bed if the aspect ratio is more significant than unity. On the other side, a shallow bed has an aspect ratio of one or less than one. In the fluidization literature, the precise aspect ratio that marks the transition between a deep and shallow fluidized bed has yet to be determined [72].

To have better hydrodynamics in the bed, it has been avoided using a shallow bed. The minimum aspect ratio has been about unity as a safe value [26]. In this project, the effect of several bed aspect ratios (2.5, 2, 1.5, 1, and 0.5) will be studied, and finally, the best ratio to achieve the best hydrodynamics will be chosen.

Reactor Diameter: Based on the carbon monoxide and chlorine mixture's stoichiometry and physical properties, the needed volumetric flow rate of the fluid at the inlet to handle 0.6 kg/s of solid can be calculated easily. On the other hand, the range for the fluid's superficial velocity is chosen before to be very close to minimum bubbling velocity (Regime and Bed Type), which can be calculated too [16].

Reactor Height: The height of a fluidized bed reactor can be divided into dense and lean phases. Solids lose density as they rise in height. The lean process's height (or freeboard) can be separated into two zones, with the lower section known as the transport disengaging height (TDH). If there is no secondary reaction in the freeboard region, the reactor outlet can be located on top of TDH or above. Otherwise, it can be done by reducing the freeboard and adding a more efficient cyclone to the system. Both dense phase and TDH can be calculated for a bubbling regime [26].

Heat Transfer: As discussed in section 3, published literature confirms that the best and optimum temperature for the alumina chlorination process is in the range 650-850℃ (most preferably 700℃). In general, there are two methods for CFD thermal simulations, isothermal and non-isothermal. The first method, which is always the first step, keeps the control volume constant. Although this is a huge assumption that is far from the actual case, it helps to study and modify easily to get the best base model. After the continuation of further studies, the thermal

model can be simulated. The main goal of the present study is to touch the project objectives under isothermal conditions at 700℃. If the simulation's result is promising, a thermal model can be defined and simulated to study the system's heat transfer.

Operating Pressure: These parameters highly affect hydrodynamics by influencing fluid's physical properties. There is no specific pressure in the system because the pressure at the bottom and top of the reactor is not identical, and there is a pressure drop to overcome the bed height of the reactor. The Upstream pressure is the bottleneck to define a pressure for the system. It is enough to calculate the needed pressure at the reactor's bottom by choosing a pressure for the fluidized bed outlet. Depending on how the flow boundary at the inlet is defined, this pressure can be calculated automatically by the software or defined manually.

Gas Distributor: The distribution mechanism in the gas inlet of the fluidized bed reactor significantly affects hydrodynamics. For example, it can contribute to channeling in the bed or change the bubble size or regime in the bed. At the first step, a uniform and flat distribution throughout the whole inlet area will be used. In the next step, to be more realistic, a grid plate or sparger should be considered as a uniform distributing system. If necessary, the non-uniform distribution of changing the distribution's geometry (from flat to a 3D geometry) can be considered for the final step.

Alumina: As mentioned in section 3.2, there are many types of alumina with different properties. In this study, pure γ-alumina has been taken into account, and the effect of impurities listed in Table 3.4 is neglected. Each powder has many characteristic properties which affect the fluidized bed system. Among these, some have a significant effect that is given in Table 5.1. Parameters properties such as particle size distribution (Appendix C) and bulk density are available. Other parameters should be found or estimated as accurately as possible.

Reactor Geometry: A simple cylindrical reactor with a uniform circular cross-section has been used for the first step. The reactor's optimum dimensions should be chosen by changing the bed aspect ratio, superficial velocity, and reactor height. In the second step, an exit geometry should be selected (between smooth and abrupt). As discussed in section 2.2.1.4, the former seems the best choice because the reactor will end up with a cyclone, and on the other hand, this geometry has no severe impact on the reactor's desirable flow regime. In the third step, any change in the reactor geometry can be applied to achieve lower particle escape and desirable hydrodynamics.

Reaction kinetics: The project aims to simulate the single overall reaction (3.14) in Barracuda. It is agreed that the reaction kinetics, including Arrhenius equation parameters, can be used from the published work [45]. However, the side reactions, as reviewed in section 3.5, are neglected. In further studies, the effect of dominating impurities such as γ-alumina can be taken into account.

Solid Feeder: The current fluidized bed is a continuous reactor that alumina is fed to the reactor with a feeding rate of 0.6 kg/s. In general, the powder can be transported mechanically or pneumatically (or air-assisted). The screw feeder, as an example of a mechanical conveyor or pneumatic conveying system, can be used in the design. In this project, it is considered that the powder is injected pneumatically using CO_2. Another critical point is the location and direction of the injection. In some cases, particles' downward movement positively affects the reaction (For example, alumina chlorination in fluidized bed [40]). However, taking the other considerations, such as possible particle outflow into account, placing the particle injection at the bottom side-wall of the reactor beneficial.

Construction Material: Although this project does not directly consider the materials, reactor design is affected by general considerations. The fluidized bed's typical design uses a carbon steel shell lined with particular alumina refractory (this can also be applied to the cyclone). This means no inserts are allowed to handle the generated heat in the system. So, in future studies, the possibility of cooling the reactor can be investigated.

Erosion: There are three primary sources for erosion in a fluidized bed, temperature, chemical, and solid particles. All the internal surfaces that contact a corrosive or very high-temperature fluid are in danger of erosion. On the other hand, in higher velocities, solid particles can cause erosion, and usually, it is associated with transitional and directional changes in the system. For example, most erosions occur in the internal cyclone wall or near the elbow of bent pipes. In the present project, a particular type of alumina refractory is considered as a reactor lining to protect the reactor against very high temperatures and chemical corrosion. Although alumina particles are highly abrasive [73], this effect may be minimal because of the shallow velocity in the system. As a further study, erosion of the cyclone can be studied.

Drag Model: The force acting on a particle by the flow of fluid around it is determined by the particle's drag model. The Barracuda® provides a range of predefined drag models that the WenYu-Ergun blended drag model could be more suitable for the current study. Since the Wen and Yu correlation is appropriate for more dilute systems and the Ergun relationship is appropriate at higher packing fractions, proposed a drag function blending both the Wen-Yu and Ergun functions.

5.2 Design Basis

5.2.1 Alumina

As discussed in the previous section, several essential parameters have been defined in the software (the more accurate parameters, the more realistic result). Table 5.1 gives some information about the availability of these parameters in this project.

Table 5.1: Status of alumina parameters in the simulation

Parameter	Accurate Data[12]	Direct Effects on	Used-values and Sources
Particle size	Available	Hydrodynamics, Reaction	Appendix C (given by SINTEF)
Sphericity	Not Available	Hydrodynamics	0.7 (suggested by SINTEF + experimental)
Emissivity	Not Available	Reaction, Heat Transfer	0.75 (based on SINTEF best practice)
Envelope Density	Not Available	Hydrodynamics	2100 kg/m^3 (based on SINTEF best practice)
Bulk Density	Available	Hydrodynamics	0.98 (given by SINTEF)
Diffusion coefficient	Not Available	Reaction	2.2E-06 cm^2/s [74], [75]
Void Fraction	Not Available	Hydrodynamics	0.46 (based on Barracuda best practice)

5.2.1.1 Alumina Particle Size

Figure 5.1 illustrates the particle size distribution of a typical alumina sample. As seen, the average particle size is around 100 microns. There is no need to define the average particle size to Barracuda®, but for theoretical calculations, it is needed. The calculated average particle size with the method introduced in [26] is 98 microns.

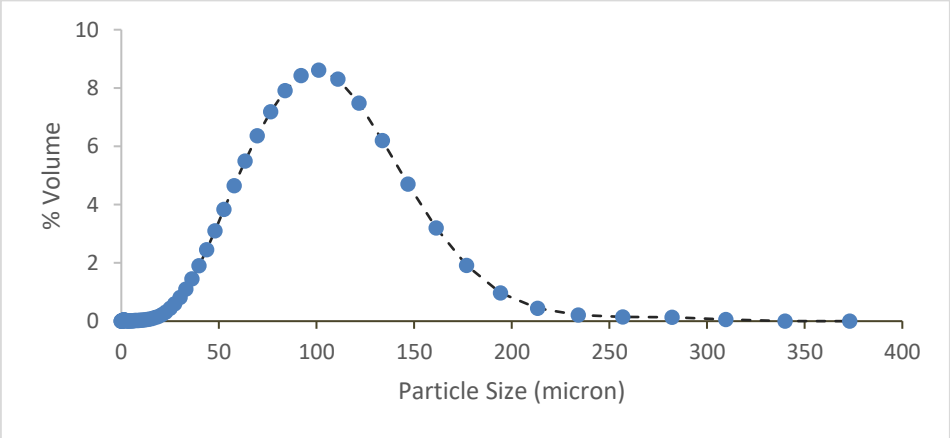

Figure 5.1: Particle size distribution of the alumina sample

[12] In powder technology, mostly there is no accurate data and here it means the data that is acceptable by all or calculated in laboratory.

5.2.1.2 Alumina Sphericity

A measurement of how much a particle is close to a sphere is called sphericity. The sphericity (ψ) of a particle can be described as the fraction of the surface area of an equal-volume sphere to the actual surface area of the particle [76].

$$\psi = \frac{\pi^{1/3}\left(6V_p\right)^{2/3}}{A_{po}} \tag{5.1}$$

where, V_p is the particle volume, and A_{po} is the overall surface area of that particle. For complete sphere, that value becomes unity, so it can be concluded that always $0 < \psi \leq 1$. Sphericity must not be mistaken with roundness. In Figure 5.2, an approximation of each is given.

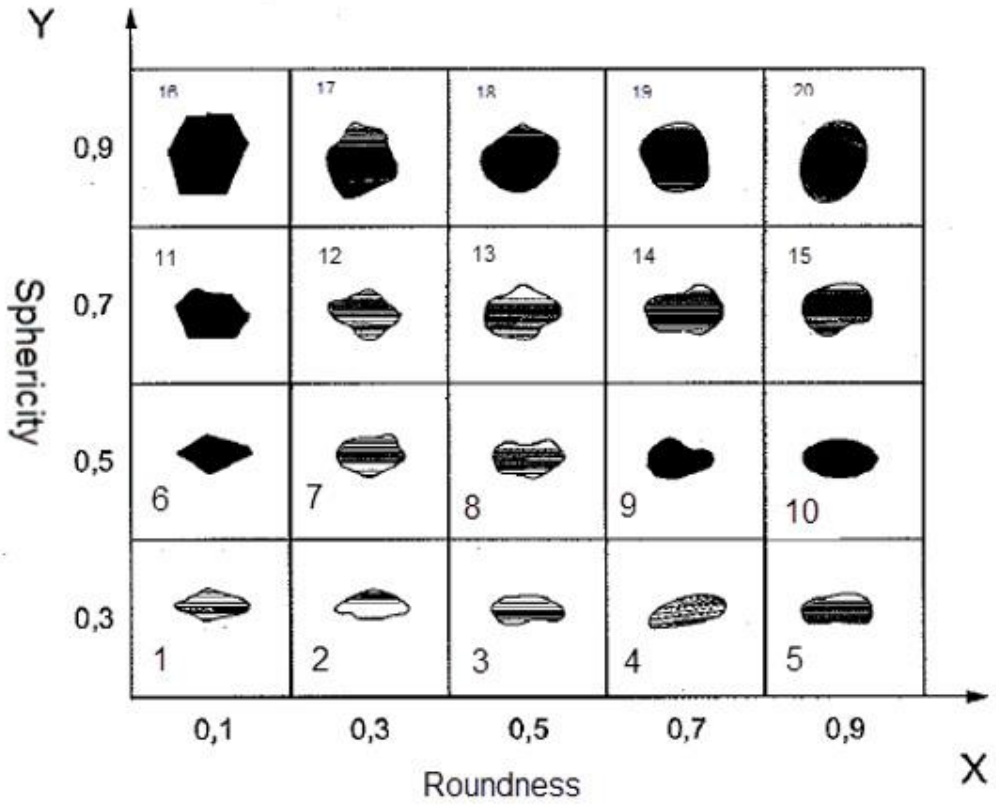

Figure 5.2: An approximation of sphericity and roundness of a particle [77]

Nevertheless, practically, these parameters cannot be calculated easily and need special measuring apparatus and procedures. On the other hand, the literature gives a different value for alumina sphericity (between 0.3 – 0.9). To get closer to the acceptable range, an experiment has been done using a microscope[13] (Figure 5.3).

[13] Nikon smz745T

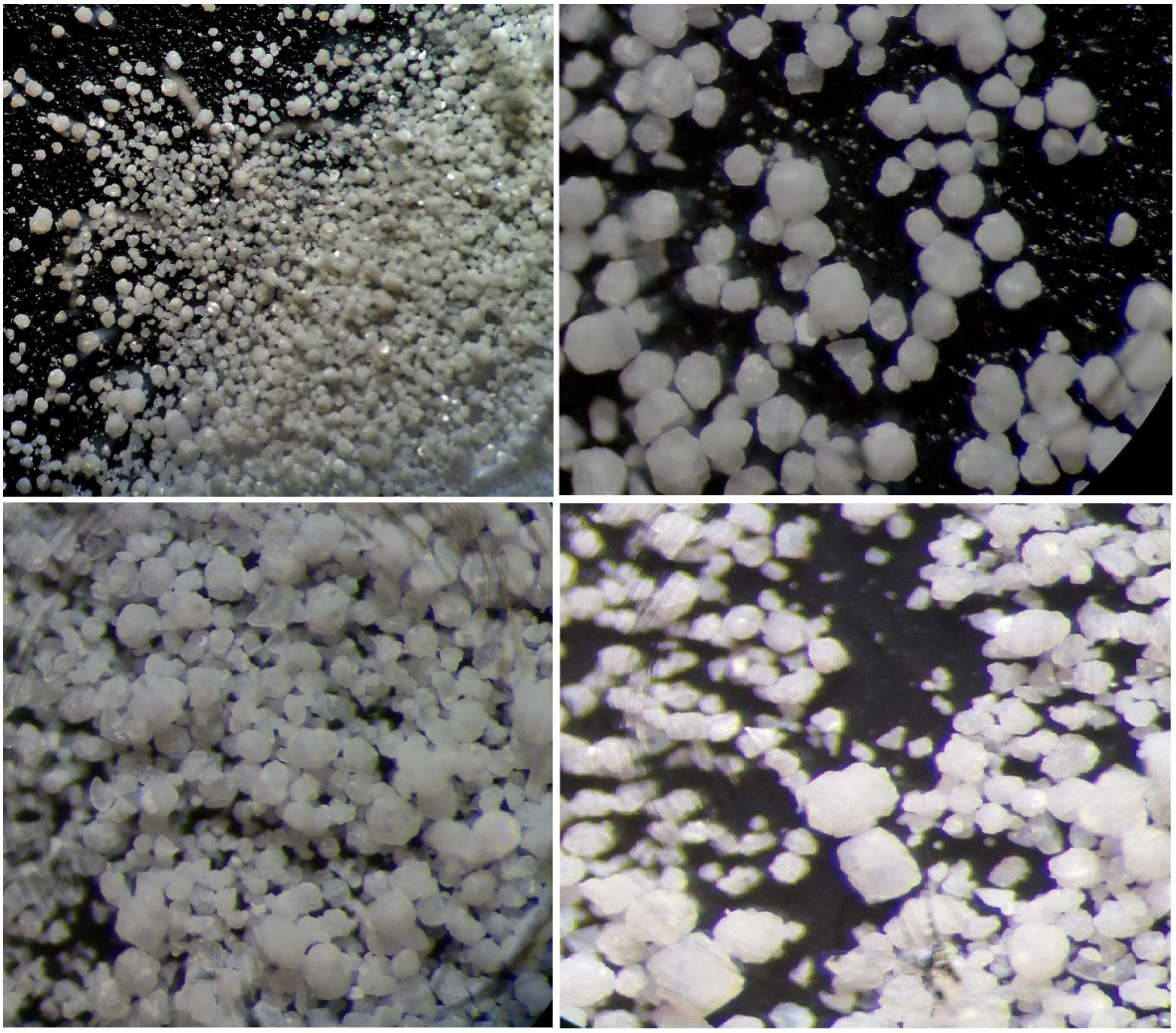

Figure 5.3: Alumina sample under the microscope[14]

Two main observations of this experiment:

1. Although the sampling procedure has not been followed for taking the sample, this shows a considerable amount of cracked particles (by attrition), which might be created during the process.
2. The complete particles (mostly bigger ones) have a sphericity of more than 0.7 and near 0.9. Nevertheless, most of the small particles have sphericity less than 0.5. (using Figure 5.2)

All in all, 0.9 for the average sphericity of this alumina is somewhat optimistic, and finally, 0.7 has been chosen.

5.2.1.3 Alumina Void Fraction

Void Fraction (ϑ_{cp}) is a measure of the empty spaces in a powder and a fraction of empty spaces' volume over the total volume between 0 and 1[15]. In Barracuda®, solid volume fraction, θ_{cp} which in the definition is 1-ϑ_{cp} is defined as equation (5.2),

$$\theta_{cp} = {}^{\rho_b}/_{\rho_p} \tag{5.2}$$

[14] University of South-Eastern Norway, combustion laboratory

[15] Theoretically it cannot be zero but one is possible

Where, ρ_b is the bulk density of the particle and ρ_p is the particle density. In general, the interaction between a particle and fluid is strongly dependent on particle density. There are four definitions of particle density commonly used: actual density, skeletal density, envelope density, and bulk density [78] based on the volume defined in Figure 5.4.

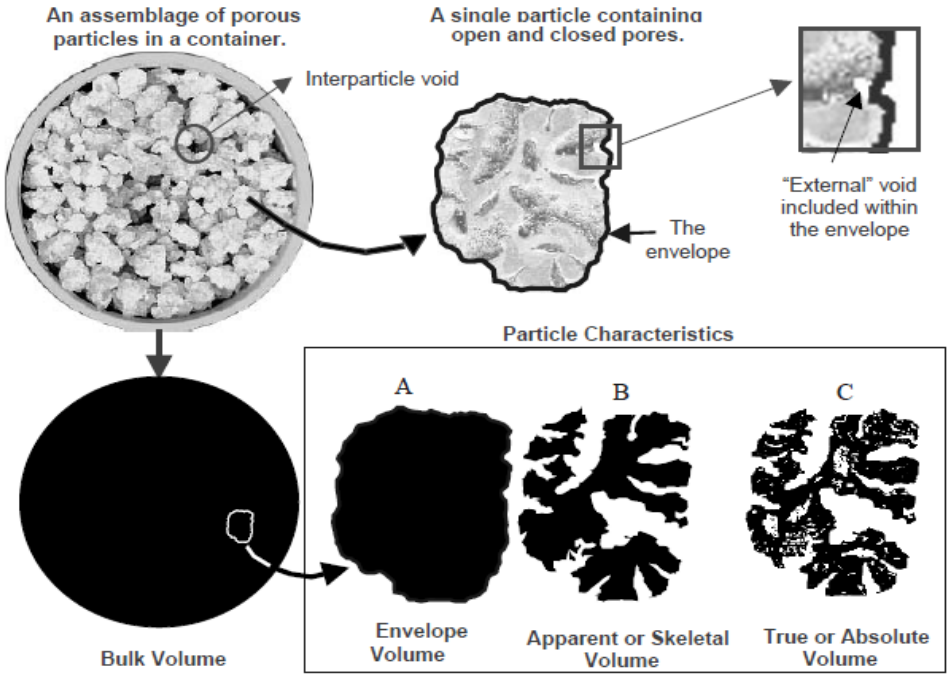

Figure 5.4 different particle volume definitions [78]

- **True density:** Which also called True particle density, is the mass of a particle divided by its volume, excluding open pores and closed pores.
- **Skeletal density: "**The ratio of the mass of discrete pieces of solid material to the sum of the volumes of the solid material in pieces and closed (or blind) pores within the pieces (ASTM D3766 [79])."
- **Envelope density:** "The ratio of the mass of a particle to the sum of the volumes of the solid in each piece and the voids within each piece, that is, within close-fitting imaginary envelopes surrounding each piece (ASTM D3766 [79]) or the ratio of the mass of a particle to the envelope volume of the particle."[78]
- **Bulk density:** The apparent powder density under defined conditions. (1) The mass of the particles divided by the volume they occupy that includes the space between the particles (ASTM D5004 [80]) and (2) the ratio of the mass of a collection of discrete pieces of solid material to the sum of the volumes of the solids in each piece, the voids within the pieces, and the voids among the pieces of the particular collection (ASTM D3766 [79]).

With the definitions above, in this case, equation (5.3) can be written as [54],

$$\theta_{cp} = \frac{\text{Alumina Bulk Density}}{\text{Alumina Envelope Density}} \tag{5.3}$$

1- Sensitivity analysis of the parameters [16] in designing a fluidized bed shows that this parameter has the highest sensitivity among all parameters. Thus, finding a value as accurate as possible helps to have more reliable results. To achieve this goal, here are several significant challenges,

2- In definition, there are several bulk densities, such as loose or vibrated bulk densities. (Although a value for each is available (980 and 1190 kg/m3, respectively), which one should be considered in equation (5.3)?

3- Although the value for the sample's envelope density is given (2100 kg/m3), measuring these kinds of values always has numerous errors.

To find an answer to these, a simple experiment has been done (Figure 5.5). Ten cubic centimeters (cc) of the sample have been measured accurately(error ± 0.0001 *g*). By subtracting the graduated cylinder's weight, the sample's weight has been measured, 11.7168 *g*, equal to 1172 kg/m^3. The calculated void fraction with both given vibrated bulk density and measured one is (Table 5.2),

Table 5.2: Calculating solid volume fraction by different methods

Bulk Density (kg/m^3)	Solid Volume Fraction
1190	0.566
980	0.466
1172	0.558

Comparing these results with Barracuda's best practice guideline ("typical values for close pack volume fraction range from 0.56 to 0.64."), shows that 0.56 is the best choice as the solid volume fraction.

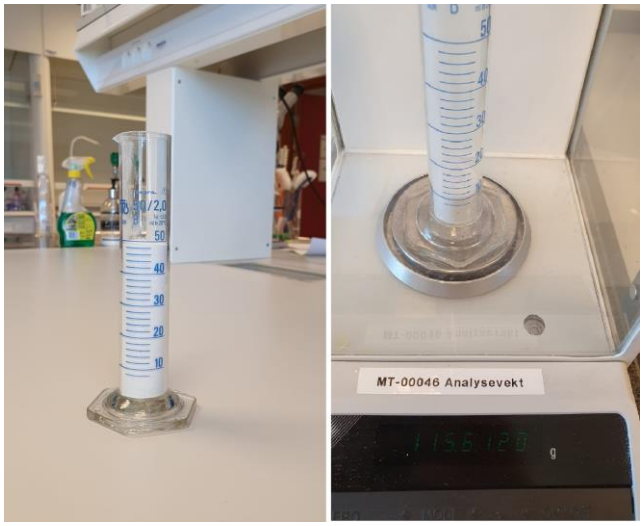

Figure 5.5: Weight measurement of 10 cm^3 vibrated sample

5.2.2 Reaction Kinetics

The optimum temperature for the reaction is about 700℃. Figure 3.3 shows that the specific initial reaction rate, *r* in equation (4.5), is 277.6 ($mgg^{-1}min^{-1}$)[16]. It is agreed with the industrial partner to use this value for the reaction rate, based on the facts that the listed initial reaction rate in the study belongs to the control of the system at time zero. As the reaction proceeds, the batch reactor's conditions change, and the data becomes more uncertain. Hence the initial rate is the more accurate one. A fluidized bed reactor is a continuous system known to easily reach the steady-state with the steady input parameters.

Barracuda® calculates reaction kinetics based on the Arrhenius law (see equation 5.4) and inserting the reaction rate and activation energy from [44]

[16] $mgg^{-1}min^{-1}$= (change in weight of alumina)/[(weight of alumina at time zero).time]

$$4625\ (\frac{1}{s}) = C_0 \exp\left(\frac{-23\ (\frac{kJ}{mole})}{8.3145T}\right) \tag{5.4}$$

So, the pre-exponential factor (C_0) is manually calculated as 79367 s^{-1} and used in Barracuda® calculations.

Note: As seen in chapter 3, the reaction with these parameters is rapid. To study the effect of bed aspect ratio, lower pre-exponential factor and higher activation energy have been used. This means that there are three kinds of safety factors regarding the defined reaction in the simulations.

1. These values are based on an experiment with much bigger particles and lower pressure. This means that theoretically, the current case is faster than the experiment.
2. There were three different stages of activation energy for different ranges of temperature [44]. A second design safety factor, the lowest, has been chosen.
3. As the last design safety factor, the lower pre-exponential factor has been defined.

5.2.3 Gas-Solid separator

A circulating fluidized bed output is heavily influenced by gas-solid separation. Separators are used for two different functions in two different locations of a CFB plant [81]. To minimize particulate emissions from the boiler plant, baghouses and electrostatic precipitators are used at the relatively cold downstream (although ESP can be used for high temperatures as well). In contrast, cyclone or impingement separators are used inside the CFB boiler loop to help in the recirculation of hot solids across the circulating fluidized bed loop. This helps to keep the special hydrodynamic condition in the riser.

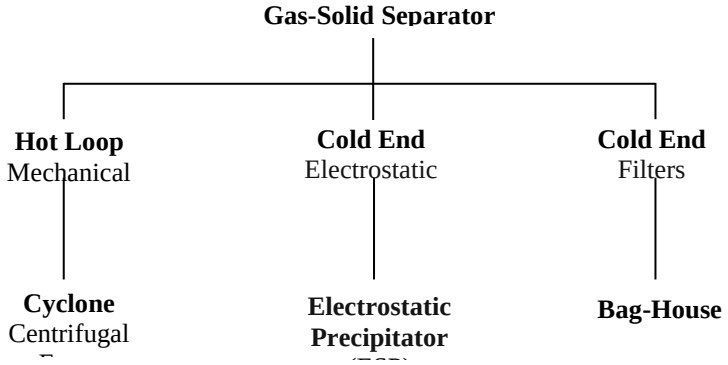

Figure 5.6: General classification of the gas-solid separation units

One of the following forces has been used to isolate solids from the gas flow. External forces such as electrostatic, gravity, and/or magnetic and internal forces such as diffusion, inertial, and/or centrifugal. In a CFB, the separation equipment can be generally defined as follows (Figure 5.6).

The size of the particles defines the separation efficiency of most gas-solid separators (Figure 5.7).

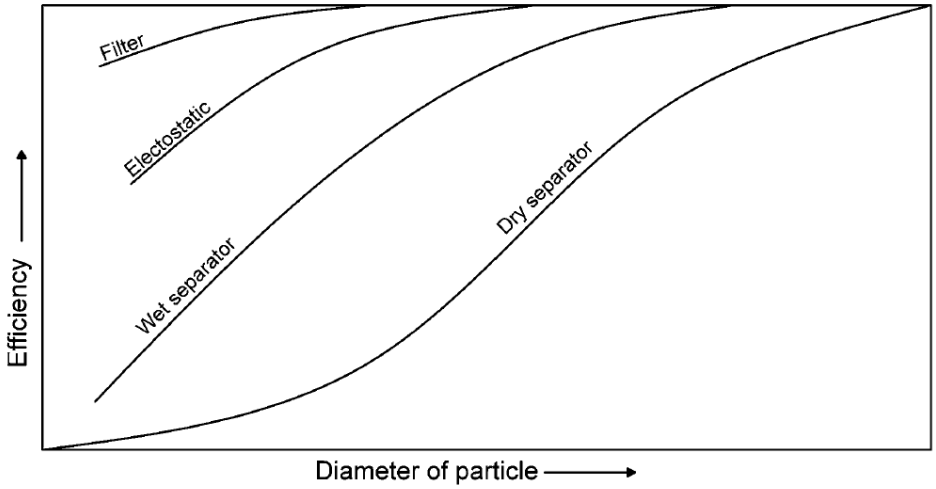

Figure 5.7: Separation characteristics of different solid separation methods [82]

5.2.3.1 Cyclones Overview

In general, cyclones are the most common kind of mechanical separator. This basic system has very high efficiency with a very low-pressure drop, which is the most advantage. A cyclone is a device that separates solid particles from a fluid by centrifugal force and works simply by the kinetic energy of the incoming mixture (flow stream) and the geometry of the cyclone. Particle (in fluid) velocity and residence time are two main factors in cyclone design. A typical cyclone scheme is shown in Figure 5.8.

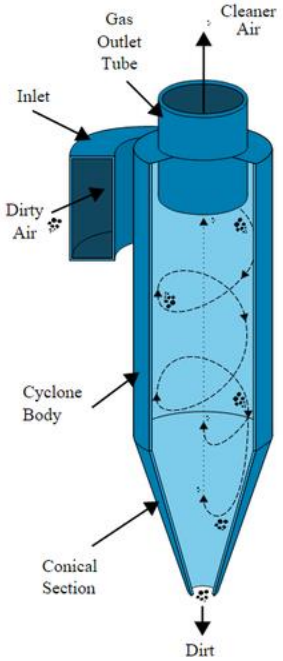

Figure 5.8: Components of a vertical axis tangential entry cyclone [82]

Because of the cyclone's cylindrical form and the gas's tangential entrance, the gas-solid suspension flows in two concentric vortices around the cyclone. The outer vortex is heading downward, while the central vortex is moving upward. Solids, which have a higher density than flue gas, exit the outer vortex and pass against the wall due to centrifugal force. The comparatively clean gas rises through the inner vortex and leaves through a vertical exit on the cyclone's top. [81]
There are different classifications for cyclones regarding inlet design (Figure 5.9) and arrangement (Figure 5.10).

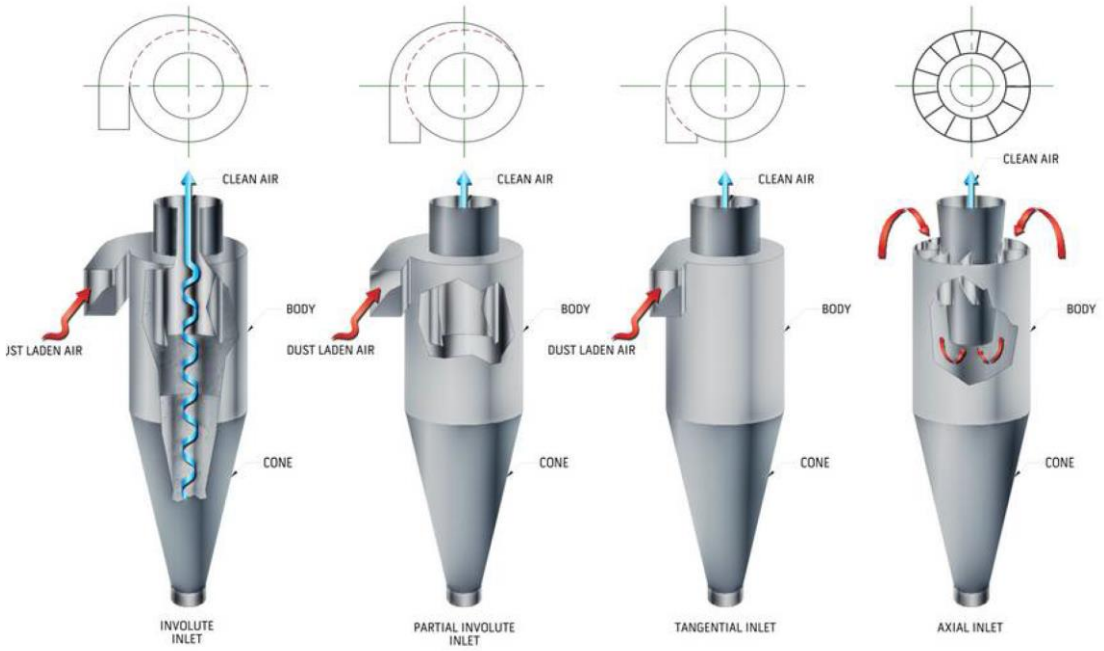

Figure 5.9: Different styles of cyclones (Inlet designs) [83]

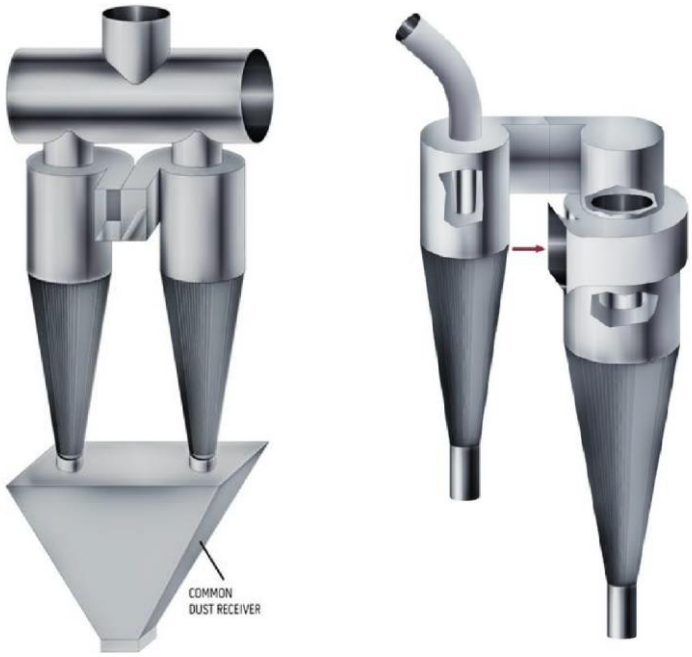

Figure 5.10: Arrangement of a cyclone, parallel (left) and series (right) [83]

There are many parameters' which effects cyclone efficiency. Table 5.3 shows the effect of design and process parameters on cyclone’s efficiency [84].

Table 5.3: Effect of parameters on the efficiency of a cyclone [84]

Parameter	If the parameter increases, the cyclone's efficiency will:
Particle size	Increase
Particle density	Increase
Dust loading	Increase*
Inlet gas velocity	Increase*
Cyclone body diameter	Decrease
The ratio of cyclone body length to diameter	Increase
The smoothness of cyclone's inner wall	Increase
Gas viscosity	Decrease
Gas density	Decrease
Gas inlet duct area	Decrease
Gas exit pipe diameter	Decrease

* These parameters can only increase to a certain point, then it will be decreased.

5.2.3.2 Cyclone Design

Figure 5.11 and Table 5.4give information about how a cyclone's geometrical parameters are related to the diameter (*D*). This means, in any way, by finding the diameter, the whole dimensions of the geometry will be found, respectively.

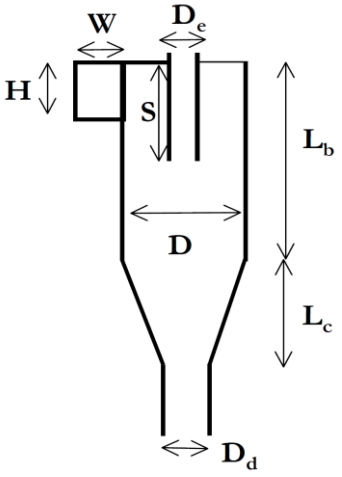

Figure 5.11: Lapple cyclone design lengths [82]

Table 5.4: Relationship between cyclone's geometry parameters and the diameter

	Description	High efficiency	Conventional	High throughput
H / D	Height of inlet	0.44 ~ 0.50	0.5	0.75 ~ 0.8

W / D	Width of inlet	0.20 ~ 0.21	0.2	0.375 ~ 0.35
D_e / D	Diameter of gas exit	0.40 ~ 0.50	0.5	0.75
S / D	Length of vortex finder	0.5	0.625 ~ 0.6	0.875 ~0.85
L_b / D	Length of body	1.5 ~1.4	2.0 ~ 1.75	1.5 ~1.7
L_c / D	Length of cone	2.5	2	2.5 ~2.0
D_d / D	Diameter of dust outlet	0.375 ~ 0.4	0.25 ~ 0.4	0.375 ~ 0.4

Steps to calculate the cyclone's dimensions:

1- Choosing an efficiency and finding d_{50} from the equation below,

$$\eta = \frac{1}{1 + \left(\frac{d_{50}}{d_p}\right)^2} \tag{5.5}$$

Where, η is the cyclone's efficiency, d_p is the average particle diameter and d_{50} is the cut point or separation size when the efficiency of a cyclone is 50%.

2- Replacing the parameters in the equation below with d_{50},

$$d_{50} = \sqrt{\frac{9\mu_f W}{2\pi\vartheta_{f.in}(\rho_p - \rho_f)N_A}} \tag{5.6}$$

where, $N_A = \frac{L_b + 0.5L_c}{H}$, $L_b = 1.5D$, $L_c = 2.5D$, $\vartheta_{f.in} = \frac{\dot{V}_{f.in}}{HW}$, $H = 0.44D$, $W = 0.2\,D$.

$$d_{50} = \sqrt{\frac{9\,\mu_f(0.2D)}{2\pi\frac{\dot{V}_{f.in}}{(0.44D)(0.2\,D)}(\rho_p - \rho_f)\frac{1.5D + 0.5(2.5D)}{0.44D}}} \tag{5.7}$$

3- Finding *D* from the equation above,

$$D = \left(247.916087\frac{\dot{V}_{f.in}(\rho_p - \rho_f){d_{50}}^2}{\mu_f}\right)^{\frac{1}{3}} \tag{5.8}$$

Now, all the other cyclone dimensional parameters can be easily be calculated.

4- Another critical factor in cyclone design is pressure drop which can be calculated by using the following equation.

$$\Delta P = \frac{1}{2}\frac{\rho_{gas}{\vartheta_{f.in}}^2 KHW}{{D_e}^2} \tag{5.9}$$

where, for the constant K, the value 12 ~ 18 is suggested (K=16 as recommended value [84])

5- And for the last step, calculating solid concentration in the cyclone outlet,

$$C_{s.out} = (1-\eta)\frac{\dot{m}_{p.in}(P_{f.in} - \Delta P)}{\dot{V}_{f.in}P_{f.in}} \tag{5.10}$$

where, $C_{s.out}$ is the concentration of the particles leaving the cyclone, $P_{f.in}$ is the pressure at the cyclone's inlet, $\dot{m}_{p.in}$ is the mass flow rate of solid particles at the inlet, and $\dot{V}_{f.in}$ is the volumetric flow rate of the flow at the inlet.

5.2.4 Reactor Dimensions

5.2.4.1 Reactor Diameter

To calculate the reactor diameter, the volumetric flow rate and superficial velocity (u_{sf}) of the fluid at the inlet are needed. The first one can be derived from mass flow rate, and the range for the second one can be selected by considering the flow regime, which is close to minimum bubbling velocity.

Volumetric flow rate: From the stoichiometry and mass balance (section), the needed mass flow rate of gas ($\dot{m}_f$) can be calculated in this case equals to 1.745 *kg/s* [16]. By using the equation (5.11) volumetric flow rate of fluid ($\dot{V}_f$) at specific pressure and temperature can be calculated.

$$\dot{V}_f = \frac{\dot{m}_f}{\rho_f} \tag{5.11}$$

where, ρ_f is the fluid density at the inlet.

Minimum bubbling velocity: the superficial velocity at which the bubbles first appear can be calculated by a set of equations. Equations (5.12) which can be used for Geldart group A[17], is an alternative to calculate minimum bubbling velocity [26].

$$u_{mb} = u_{mf}\frac{2300\rho_f^{0.13}{\mu_f}^{0.52}\ e^{0.72P_{45\mu m}}}{d_p^{0.8}\left(\rho_p - \rho_f\right)^{0.93}} \tag{5.12}$$

Where, u_{mf} is the minimum fluidization velocity which can be calculated by solving the following quadratic equation [26].

$$\frac{1.75}{\varepsilon_{mf}^3\ \emptyset_s}\left(\frac{d_p\ u_{mf}\ \rho_g}{\mu}\right)^2 + \frac{150-(1-\varepsilon_{mf})}{\varepsilon_{mf}^3\ \emptyset_s^2}\left(\frac{d_p\ u_{mf}\ \rho_g}{\mu}\right) = \frac{d_p^3\ \rho_g\ (\rho_s - \rho_g)g}{\mu^2} \tag{5.13}$$

Now, the reactor diameter (D_{FBR}) can be simply calculated using the following equation,

$$D_{FBR} = \left(\frac{4\dot{V}_f}{u_{sf}\pi}\right)^{\frac{1}{2}} \tag{5.14}$$

[17] The current sample belongs to this.

Based on the study in the group project [16] and calculated superficial velocity at a selected pressure, 3.88 meters is calculated to be used in the very first generation of the model.

5.2.4.2 Reactor Height

As discussed earlier in overall design considerations, the height of a fluidized bed reactor can be divided into two parts: the dense and lean phases (Figure 5.12).

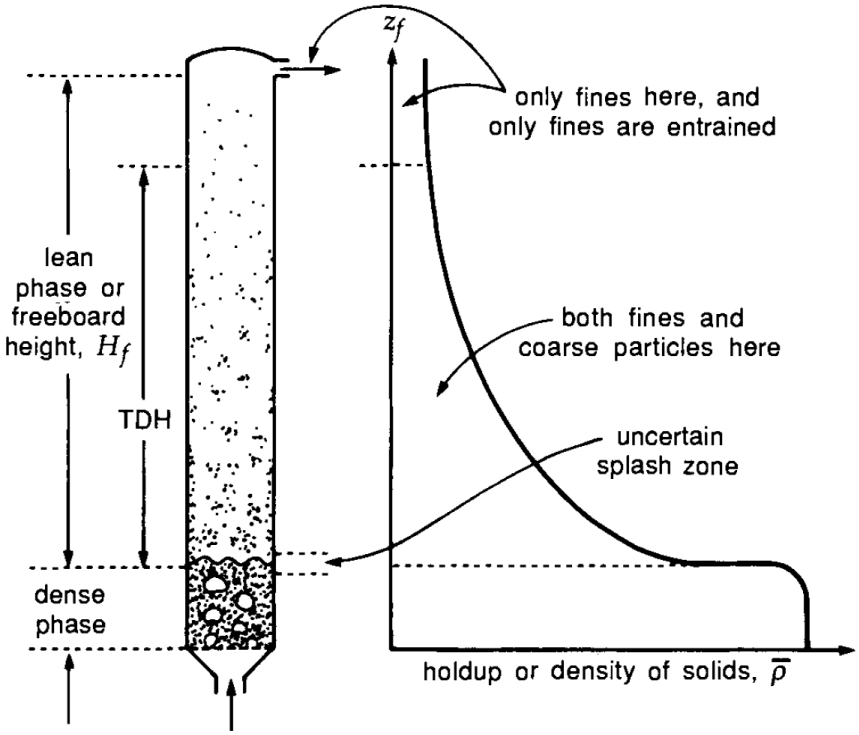

Figure 5.12: Main parts in a fluidized bed height [26]

Because of the complex behavior of particles, the calculation of a precise height is almost impossible. Although some theoretical approaches give fairly good estimations [26] to achieve more accurate height, these have been modified by simulation.

Using the procedure introduced during the student group project [16], the initial calculated height for H/D=1 will be used in the model's first generation.

However, different H/D ratios are further investigated and discussed in section 6.2.1.

Cylindrical FB reactors inherited several weak points. According to Yang and Keairns [82], the effect of the expanded cross-section at the top of the reactor and related hydrodynamics were investigated. The experiment has

concluded that this expanded section can effectively reduce the slugging. Therefore, it may have a positive effect to reduce the particle outflow. Figure 5.13 illustrates the schematic view of their reactor[18].

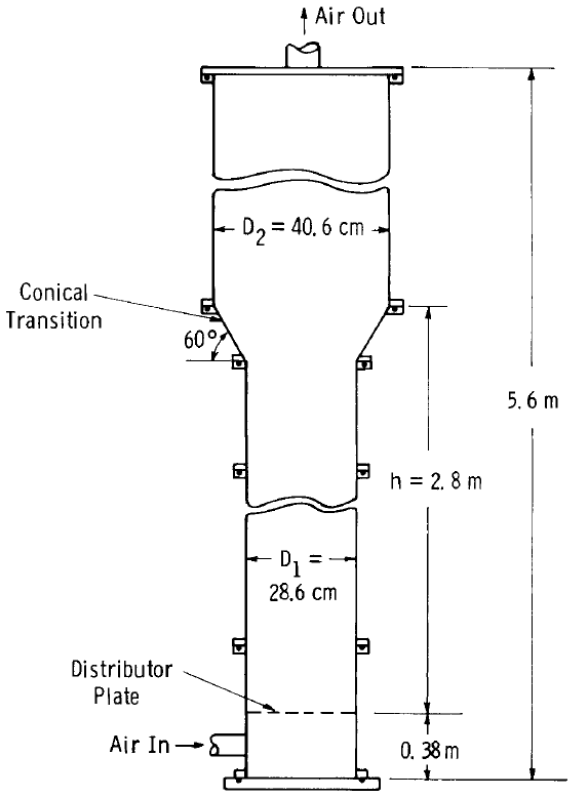

Figure 5.13 Schematic of the semicircular Plexiglas column.[85]

5.2.5 Gas Distributor

The design of the fluidized bed gas distributors has a significant impact on hydrodynamics and its efficiency [86]. Therefore, before going further, it is crucial to be familiar with different types of gas distribution mechanisms and their characteristics, and their effect on hydrodynamics.

5.2.5.1 Types of Gas distributors

Ideal Distributor

As an ideal situation, ceramic or metal porous plate distributors (or some other materials such as filters or a thin layer of particles) are used in most small-scale fluidization applications because of their high enough flow resistance to ensure a uniform gas delivery across the bed. Despite this significant advantage, there are some drawback as below [26],

- Higher operating cost because of higher pressure drop and higher pumping power.
- Impractical for large-scale applications due to lack of structural strength.
- Higher cost for some cases built with special materials.
- Low thermal resistivity
- Possibility of clogging by fine particles

[18] This geometry has also proposed by SINTEF.

Multi-orifice Plates

Multi-orifice (or Perforated) plate distributors are common in the industry because they are inexpensive and straightforward to make. Some basic types of this distributor are shown in Figure 5.14. The lack of rigidity in this design is one of its disadvantages. Large plates deflect unpredictably under heavy loads, necessitating support reinforcement. Furthermore, gas leakage at the bed perimeter is likely during thermal expansion. Orifices in perforated plate distributors can be as small as 1 to 2 *mm* in small laboratory beds and as large as 50 *mm* in large Fluid Catalytic Cracking (FCC) units with solid-entrained gases. [26]

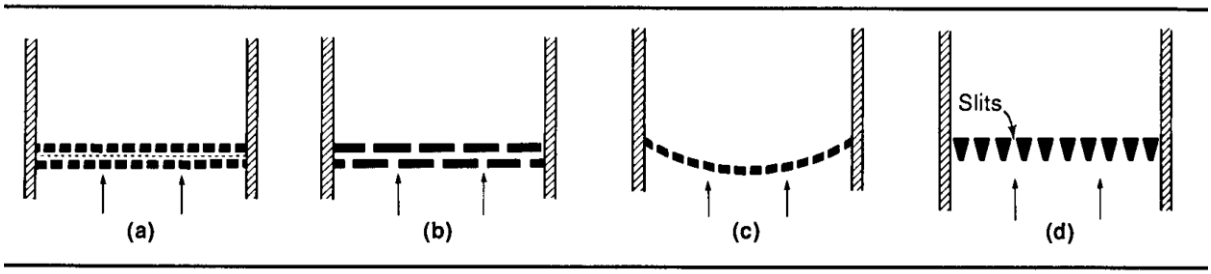

Figure 5.14: Types of the multi-orifice distributor [26]. (a) sandwiching multi-orifice plates; (b) staggered multi-orifice plates; (c) dished multi-orifice plate; (d) grate bars.

Tuyere Distributor

Under extreme operating conditions, such as high temperature or an extremely reactive atmosphere, perforated plate distributors are ineffective. In these cases, Tuyere designs (Figure 5.15) are used. While type (a) allows for good gas distribution above each filter, particles will settle between adjacent tuyeres. Additionally, extra care must be taken to ensure that the incoming gas does not contain any filter-clogging content. Other cases are commonly employed to save solids from dropping into the distributor. Particles are convenient to settle and sinter on the distributor plate itself in all designs. To reduce this effect, several designs have been suggested and implemented [26].

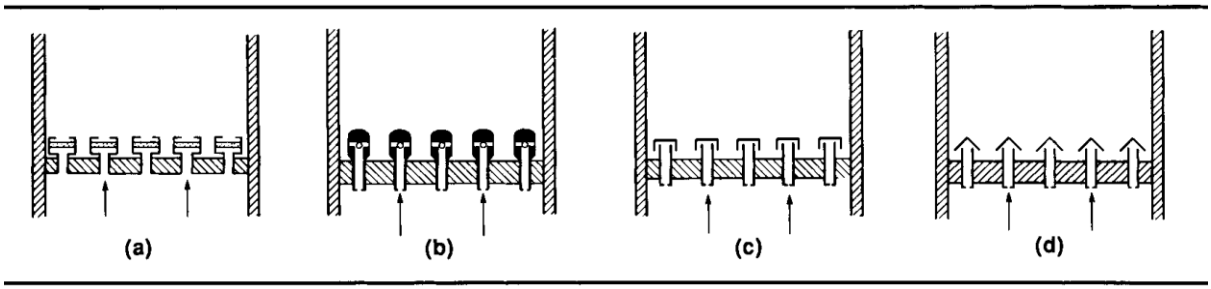

Figure 5.15: Types of Tuyere distributors [26]. a) Porous type, b) nozzle type, c) bubble cap type, d) slit nozzle type

Pipe Grids (Sparger)

Internals, such as correctly positioned heat exchanger tubing, have been shown to significantly increase gas-solid contacting by splitting up growing bubbles or gross solid circulation. Practically, the proper internal design will increase fluidization efficiency to the point that high-resistance distributors are no longer needed. In such situations, a pipe grid or sparger, such as the one seen in Figure 5.16, may be all that is required to inject reactant gas.

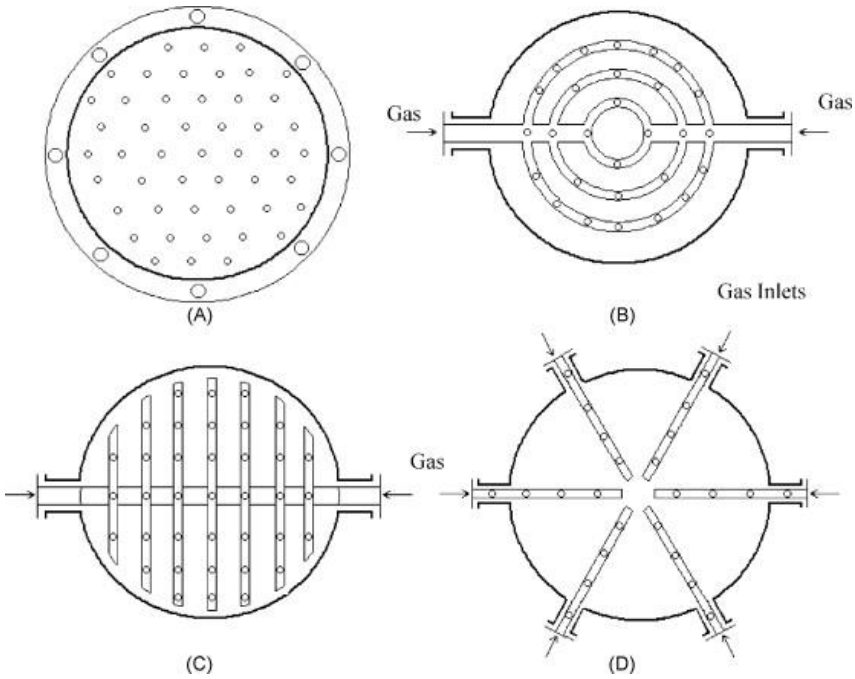

Figure 5.16: Different types of sparger for bubbling fluidized bed. (a) sieve plate sparger, (b) multiple ring sparger, (c) spider, and (d) pipe sparger [87].

5.2.5.2 Region above Distributor

The gas-solid contacting just above the distributor has gotten much interest because contacting is effective here, and this can have a significant impact on the performance of processes such as quick heat transfer, mass transfer, and reaction. Here is a graphical description of some distributors' behavior in their immediate vicinity (Figure 5.17 -6.19). [26]

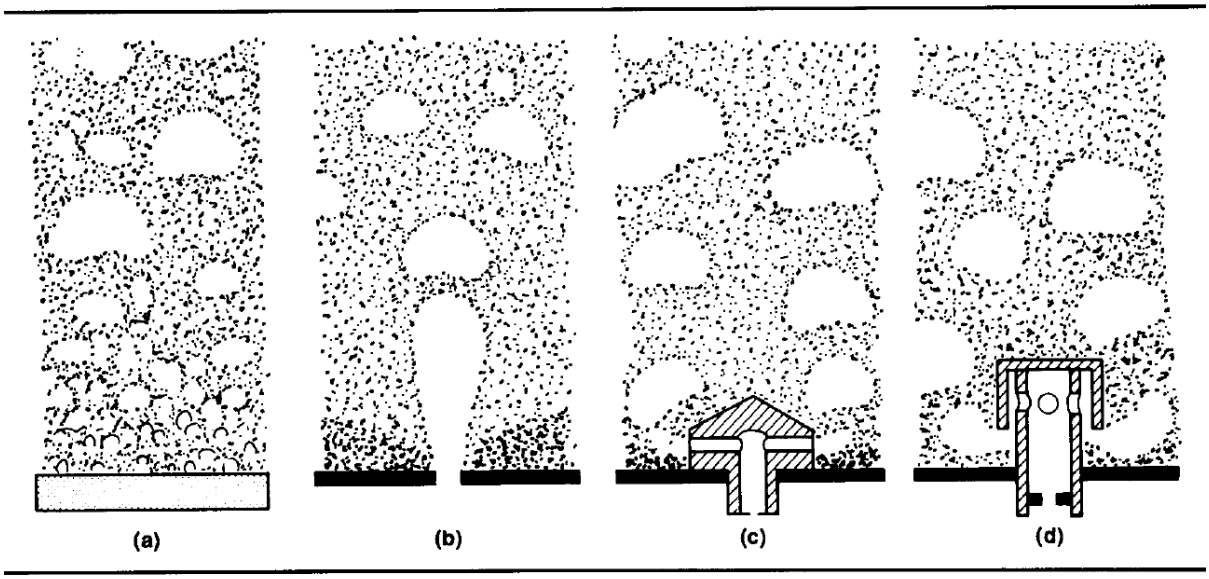

Figure 5.17: Bubble's behavior just immediately above distributor [26]; (a) porous plate; (b) perforated plate; (c) nozzle-type Tuyere; (d) bubble cap Tuyere.

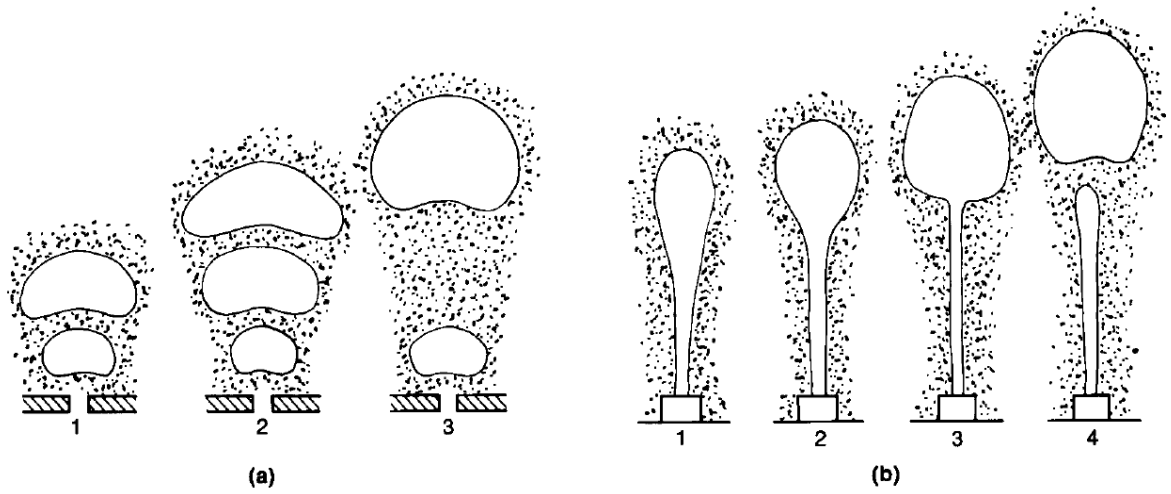

Figure 5.18: Just above a single orifice into an incipiently fluidized bed, two types of bubble formation [26]. a) low gas velocity, b) high gas velocity

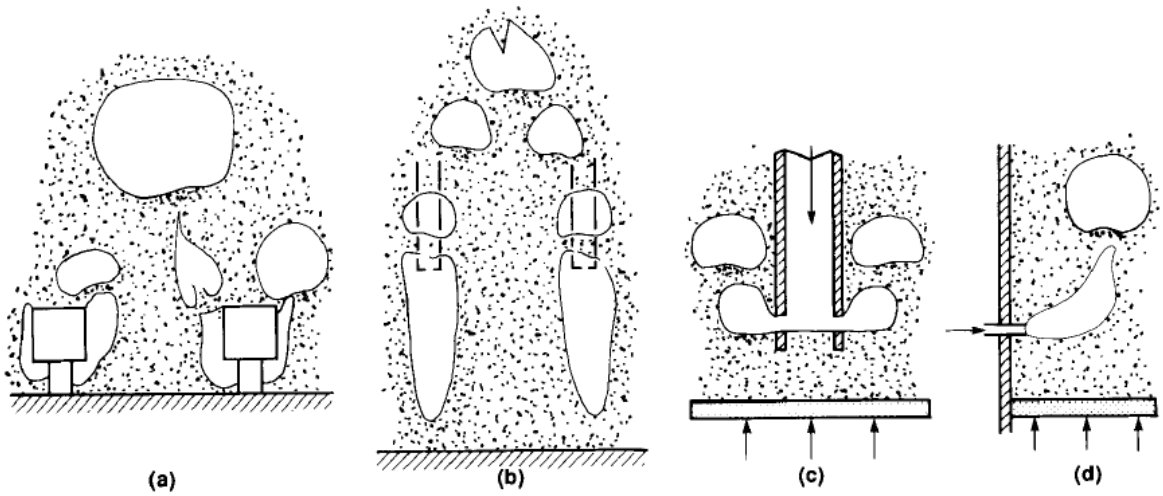

Figure 5.19: Downward and horizontal injection into a fluidized bed [26]. a) bubble cap Tuyere, b) high-velocity sparger, c) low-velocity slotted pipe, and d) high-velocity vessel wall.

5.2.5.3 Design Strategy

Considering all of this information, the simulations will be started with an ideal distributor with uniform flow. Then, depending on the hydrodynamics, needed changes will be applied.

6 CPFD simulation and the development of the reactor design

In this chapter, the way that the final reactor has been designed will be reviewed. For better understanding, it is decided to discuss results immediately after each simulation and give insight into what the problem is and how it can be solved. As discussed earlier, this project has been started with the decision about the regime inside the reactor. Although the design in the previously done group project [16] was a circulating fluidized bed (fast fluidized bed) with a turbulent regime, considering the practical disadvantages of such a system, all these simulations have been modeled in a bubbling regime which seems to be the best alternative for alumina chlorination. The present study includes six different development stages (generations), as shown in Figure 6.1, which starts from an iso-thermal simulation of the simple cylindrical geometry to a thermal study of complex geometry. At the end and as extra work, the effect of impurity in the alumina will be studied.

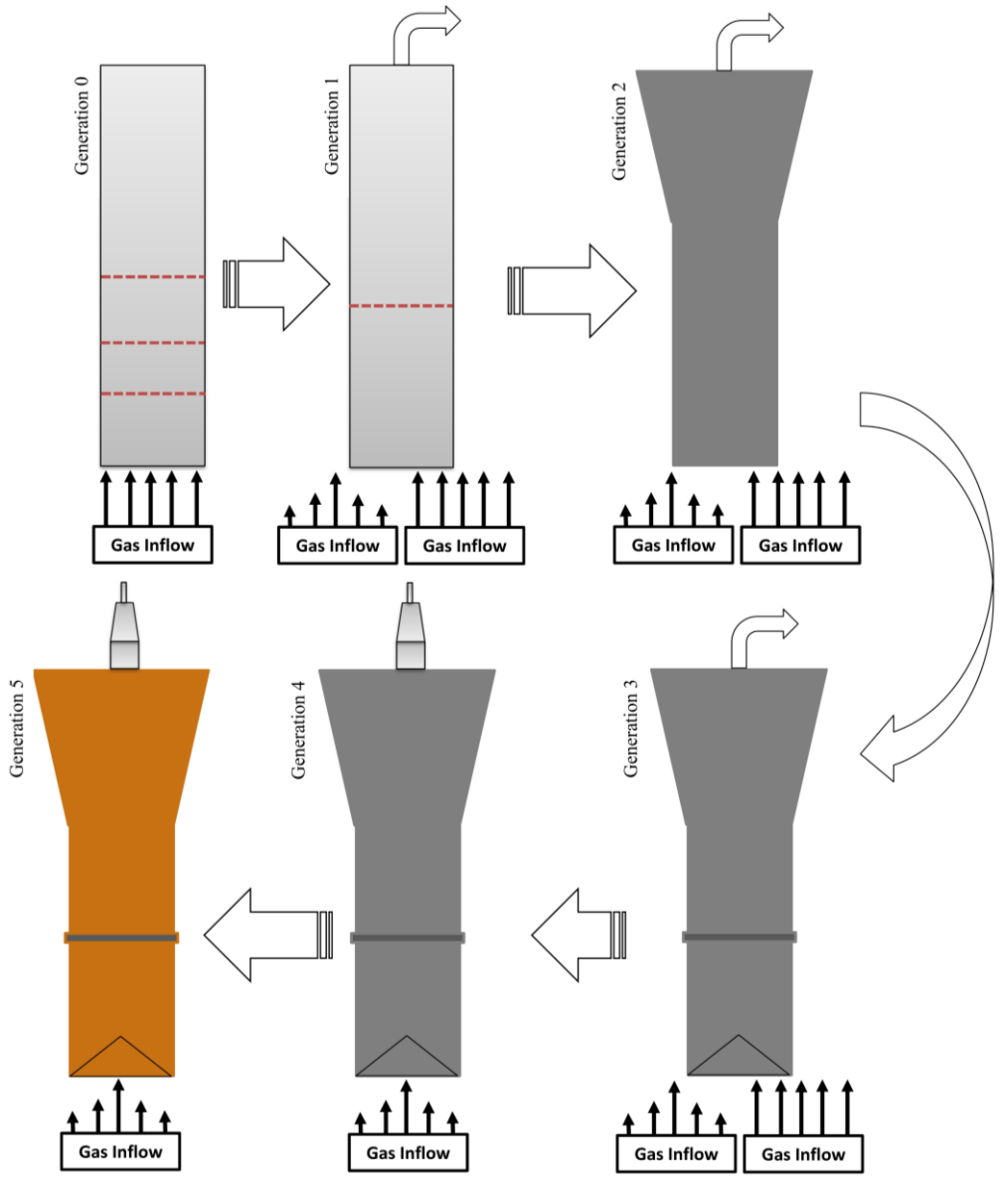

Figure 6.1 Reactor generations diagram (v.0 – v.5)

To continue, in the next section, the simulation procedure in barracuda which is same in all the cases, will be reviewed once. Then, for each generation, specific considerations and results will be discussed separately.

6.1 Simulation Steps in Barracuda®

In general, the Barracuda® Virtual Reactor is a powerful engineering tool for simulating, optimizing, and designing particle-fluid systems. A successful model setup can be used in different simulations with slight modifications to investigate different operating conditions, feed materials, or geometry designs. Therefore, it is essential when setting up a model to know what kind of output data is required, how the data will be analyzed, and what modifications will possibly be made in the future. In Barracuda, two types of inputs should be set, simulation and post-processing parameters. The first one is any information that needs to be calculated, and the second is to set up the Barracuda® interface to report those data helpfully. This section covers a brief introduction to simulation parameters. The steps (in order) to define a model are as follows.

1- Setup Grid

This step is one of the most critical steps in CFD. The Barracuda® grid is generated based on two user inputs: a CAD file and a set of grid line locations. A good grid has the following characteristics [54]:

Accuracy: The grid accurately represents essential aspects of the model. External concrete walls and flexible borders, as well as solid internal elements like cyclones, tube bundles, and distributors, fall under this category. X, y, and z grid lines at suitable positions within the model domain are needed to ensure adequate representation of these elements.

Resolution: The model needs enough resolution to calculate the particle-fluid dynamics accurately. The precision with which the fluid flow can be measured is determined by the number of grid lines used in the model, particularly in regions with significant pressure, velocity, temperature, or composition gradients.

Uniformity: In Barracuda®, uniformity of the cell sizes is vital for producing a stable and efficient simulation. Transitioning from thin, high-resolution cells to more extensive, lower-resolution cells can be done progressively.

The number of cells: It is often desirable to keep the number of cells in a grid at a minimum while maintaining the grid's accuracy, resolution, and uniformity. Increasing the number of cells in the model increases the computing requirements and the calculation time of a simulation as well. Often, the best grid is one that produces the best answer in the shortest amount of time.

For example, Figure 6.2 shows a uniformly meshed reactor. It is essential to double-check the grid's cell count and uniformity before and after making changes. Daily grid checks can aid in creating a grid that is designed for both speed and reliability.

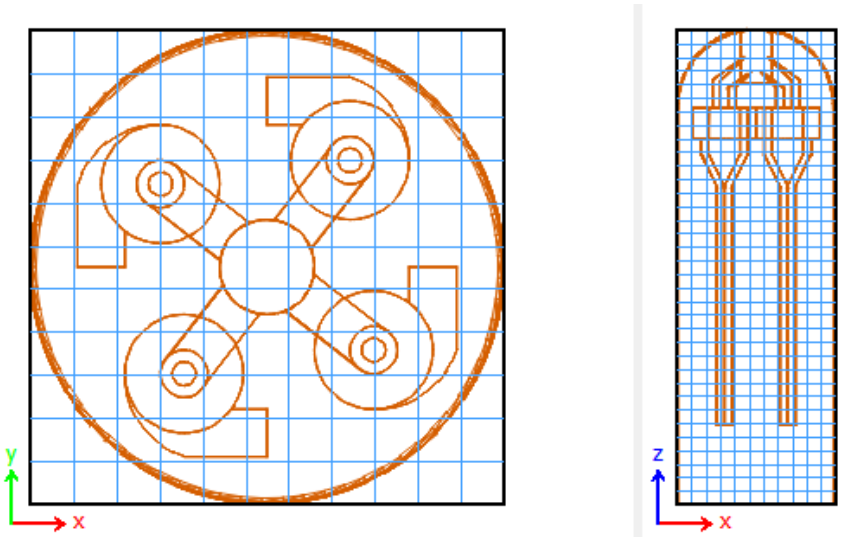

Figure 6.2 Circulating fluidized bed with four parallel cyclones meshing using 5000 cells

Grid utility is a useful option for plotting the cell spacing the check the quality of the generated mesh. Virtual Reactor analyzes the current set of grid lines and generates a grid check plot, as seen in Figure 6.3 when the "Check Grid" button at the top of the "Setup Grid window" is clicked. The grid check plot shows the model's cell spacing normalized by the smallest cell spacing in each direction. On the x-axis, the i, j, and k coordinates enable the user to define any non-uniformity regions. When using the "Check Grid" utility, the following guidelines are recommended [54]:

- The scale of neighboring cells should be identical. n each linear direction, the maximal growth between neighboring cells should be limited to 25%.
- The y-axis of the plot indicates that the maximum cell size difference between the smallest and largest cells in the model should be limited to 5. At this value, the story displays a line with a “High Aspect Ratio.” At 10, a “Severe Aspect Ratio” line is shown; the Normalized x, y, and z lines can never surpass this value.

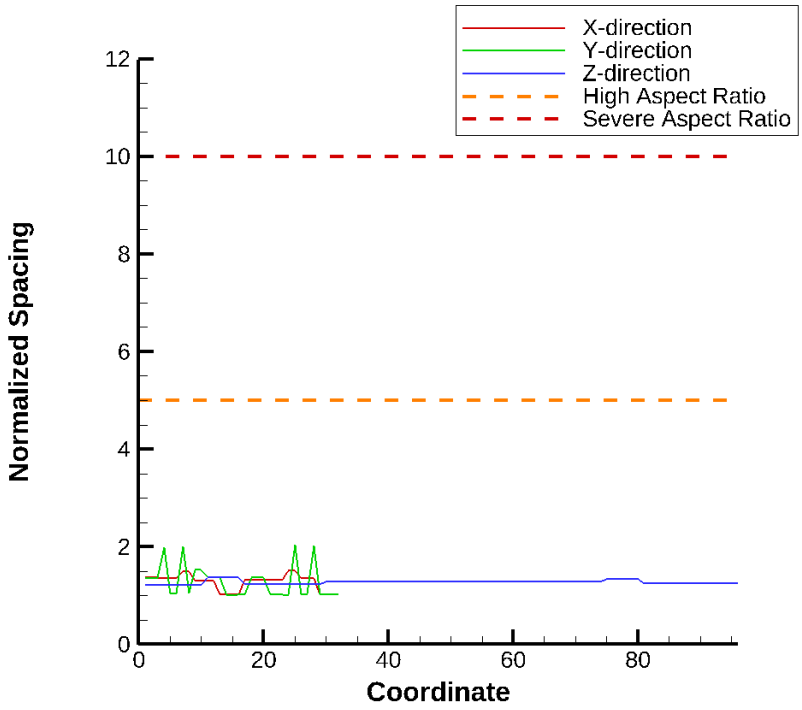

Figure 6.3 Check grid output showing the normalized spacing of cells in all directions [54]

2- Global Setting

In Global Settings (Figure 6.4), parameters that apply to the entire model are specified in this section. These include the gravity vector, the global thermal settings, and how chemistry is initialized. In this setting, it can be decided to simulate a model under iso-thermal or non-uniform thermal conditions. In the present study, all the reactor generations except the last one are simulated iso-thermally.

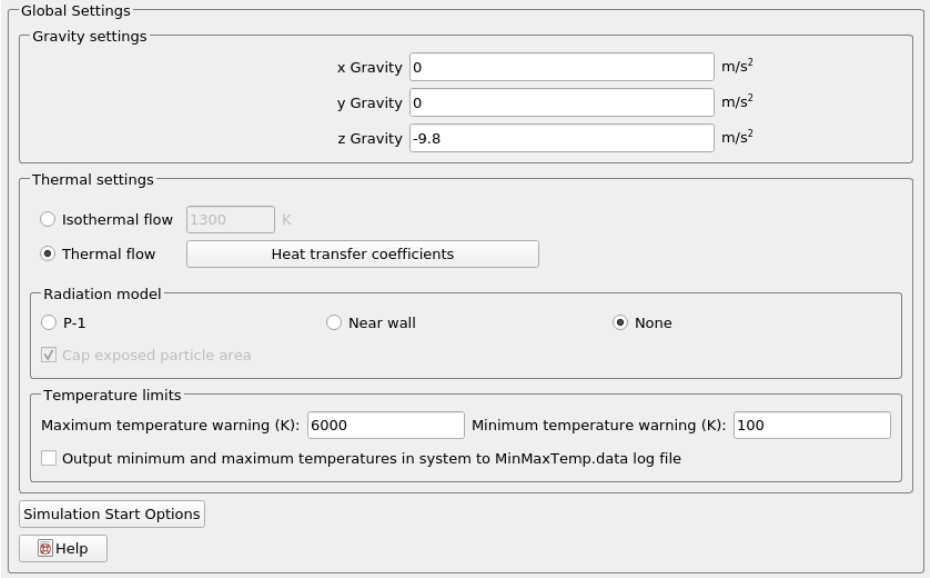

Figure 6.4 Global setting window

3- Base Material

In this section, all materials (gas, liquid, or solid) used in any part of the model, as well as their thermal and physical properties, can be defined. Although Barracuda® includes a property library of many commonly used gas, solid, and liquid materials used in the model, it needs to define the parameters manually in many cases. To do this, some properties, such as shown in Figure 6.5, have been defined (in the term of 4th order functions). In the present study, AlCl3 was not in the database and has been defined manually. Appendix A provides the information about the base materials in the present study.

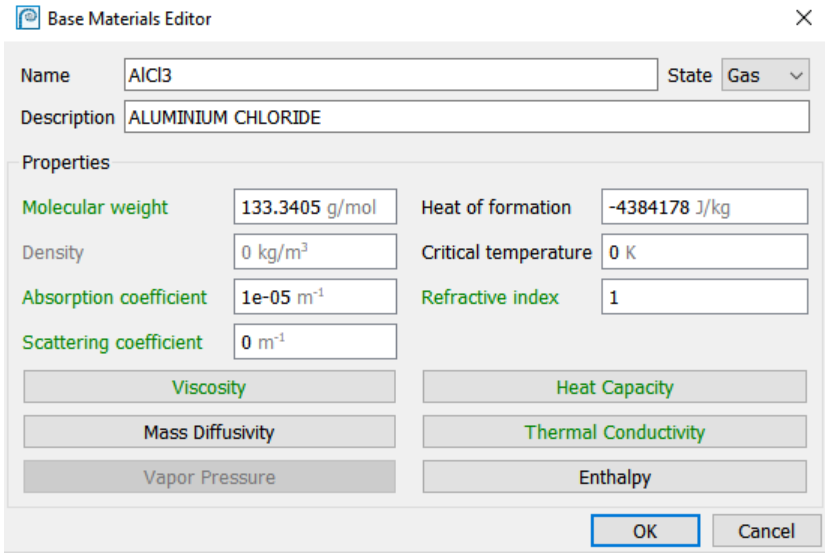

Figure 6.5 Aluminum chloride's material editor window

4- Particles

In the "Particles" section (Figure 6.6), the needed information about the particles to be simulated is specified. This information includes particle size, solid, liquid, and volatile material components, particle packing, and the models for particle drag, collisions, and interactions. All of these parameters highly affects the hydrodynamic of the model and have been defined carefully.

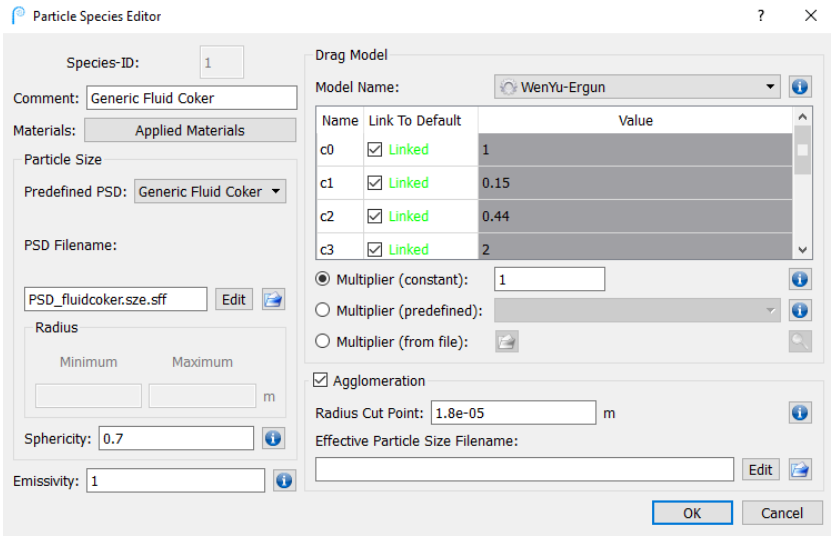

Figure 6.6 Particle Species Editor

5- Initial Conditions

The Initial Conditions (IC) define the state and composition of the fluid and particles in the model domain at the simulation start. The initial pressure, temperature, velocity, and composition of Fluid ICs (Figure 6.7-left) must all be defined. Although the model can have several initial conditions (ICs) distributed within the domain, it must be ensured that an initial condition is defined for each cell within the domain. The number of particles, temperature, and particle species must all be defined for Particle ICs (Figure 6.7- right). It is optional to define particle ICs in the system (a simulation can start with the domain void of solids).

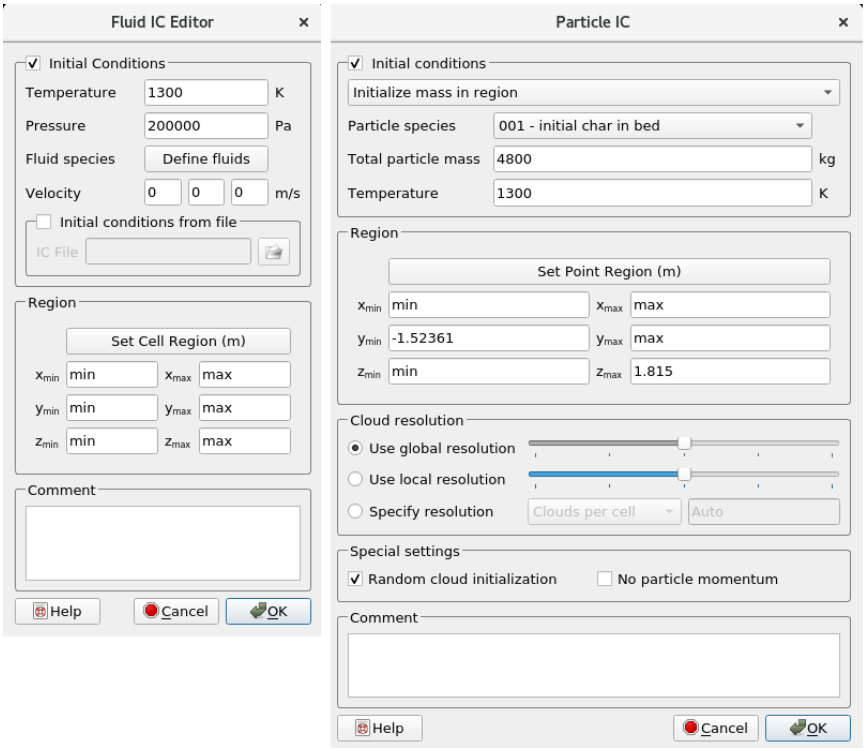

Figure 6.7 left) Fluid ICs dialog box, right) Particle ICs dialog box.

6- Boundary Condition

This section is another most essential setting in simulation. Boundary conditions define how fluids, particles, and energy can enter or exit a model. This section of Barracuda® manages various boundary conditions, such as the inflow and outflow of material from the domain, the temperature of solid walls, and the use of Eulerian-Lagrangian tracers to track fluid movement during simulation. A wall is any item in the simulation domain that does not have a pressure BC or a flow BC attached to it. By default, walls are considered adiabatic, with no heat transfer into or out of the domain at the wall; adding a Thermal Wall BC changes this behavior.

Pressure BC creates a pressure-controlled gap in the domain from which fluid and particles can flow in and out. A pressure BC is typically used as a fluid source, but it may also be used for fluid inflow and as a particle feed spot (Figure 6.8).

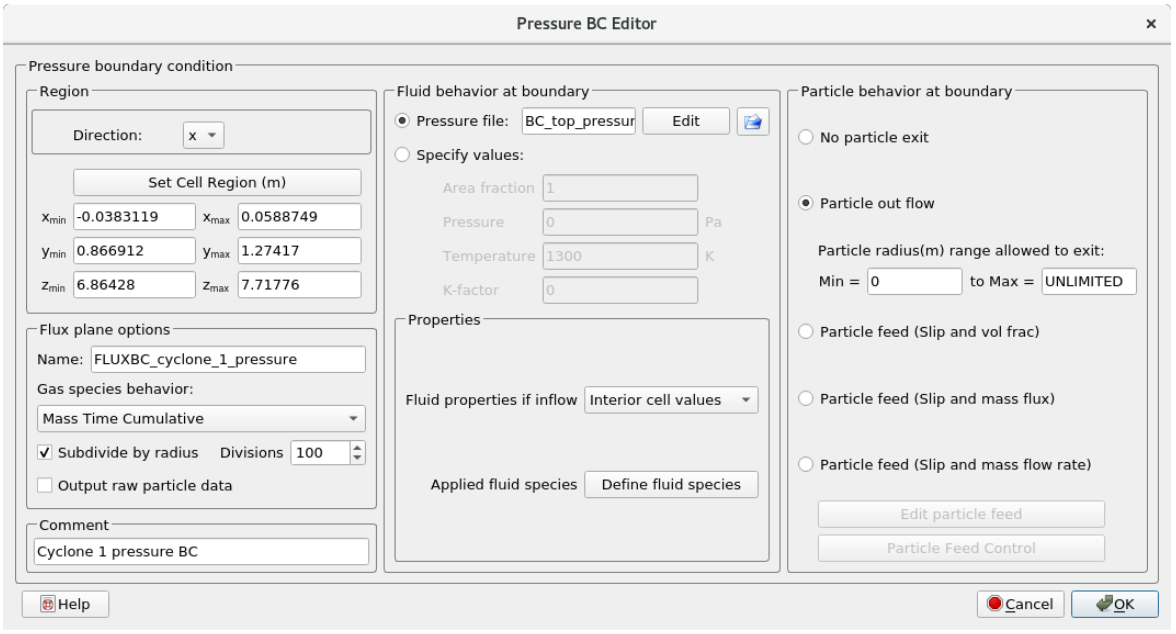

Figure 6.8 Pressure BCs Dialog showing sample pressure BC

Flow BC creates an opening in the domain from which a specific mass rate of fluid will enter or exit the domain. A flow BC is typically used as a fluid inlet with an optional particle feed but can also serve as a fluid and particle outlet. When a flow BC acts as an outlet, the fluid is drawn from the simulation domain at the specified rate. (Figure 6.9)

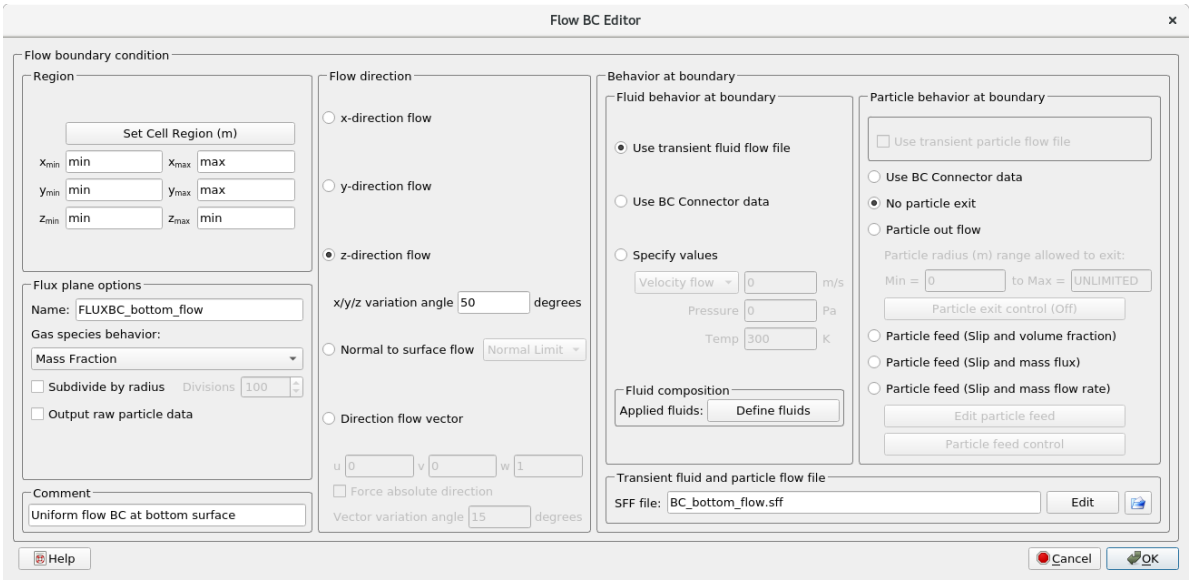

Figure 6.9 Flow BC Dialog with a sample inlet flow BC

Injection BC An injection BC defines a point source of fluid, particles, or Lagrangian tracers into the domain. The injection point can be at any location within the domain, making injection BCs an important tool for adding nozzles, distributor shrouds, or other inlets that cannot be easily captured by the grid. (Figure 6.10)

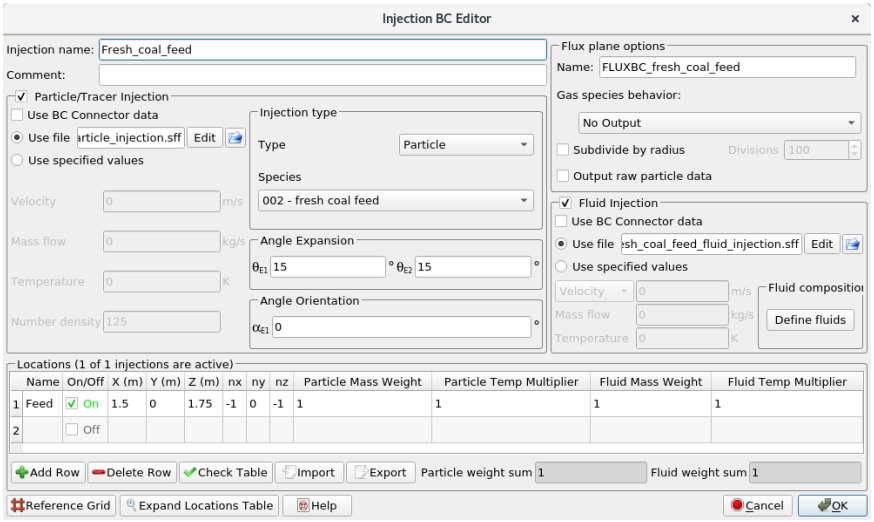

Figure 6.10 Injection Specifications Dialog showing the sample specification of both particle and fluid injection

BC Thermal Wall is a solid boundary that is heated to a specific temperature and then transfers heat from the wall to the domain at the rates defined by the fluid-to-wall heat transfer mode and radiative heat transfer mode. (has been discussed in detail in section 4.2.3).

7- Chemistry

This section, which is covered in depth in Chapter 3, impacts all aspects of a fluidized bed's behavior, so it is critical in terms of chemical reactions and particle-fluid dynamics/heat transfer while using Barracuda®. Chemical reactions can be closely combined with particle-fluid dynamics and heat transfer within the bed, depending on the system under consideration. For example, a reaction that generates or consumes gases from solids will result in a change in gas volume, which will cause the fluidization regime of the reactor. Conversely, the reaction rate and reactant availability will be a strong function of the gas mixing produced by the fluidization regime. Both temperature-dependent reaction rate expressions and the exothermicity or endothermicity of a reaction are strongly coupled to the temperatures in the bed and its thermal models. When the chemical reactions within the

system are considered, a fluidized bed model is also even more practical. Rate coefficient properties are entered in the "Rate Coefficient Dialog", shown in Figure 6.11. This dialog appears when a new rate coefficient is added or an existing rate coefficient is edited. Although both volume-average and discrete rate coefficients are described using the same dialog, some of the solid units can change depending on the rate coefficient type.

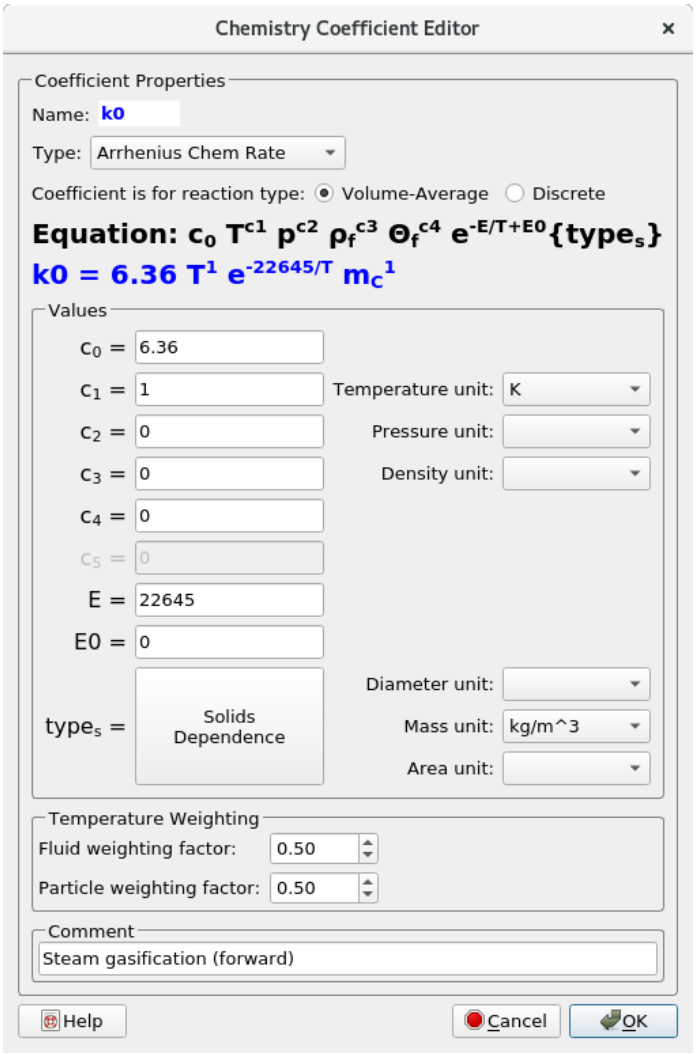

Figure 6.11 Rate Coefficient Dialog

There are some other settings in Barracuda, but for this case, just these seven settings have been used. For easy tracking of the simulations, a sheet called simulation sheet (Table 6.1) has been prepared for each simulation listed in Appendix B.

Table 6.1 Simulation sheet template

Simulation Sheet No.:

Simulation Duration:

Setup Grid	**Number of Cells:**					**Overall Dimention:** H x W x L (m)
Global Setting	**Iso-Thermal:**				(K)	
	Thermal:					**Geometry**
	Radiation model:	P-1	Near Wall	None		
Base Materials	**Base Solid (s):**					
	Base Fluid(s):					
Particles	**Close-Pack Volume Fraction:**					
	Volatile:					
	Envelope Density:				(kg/m3)	
	Bulk Density:				(kg/m3)	
	Size Distribution:					
	Sphericity:					
	Emissivity:					
	Drag Model:					
	Agglomeration:	Yes	No			
	Radius Cut Point:				(micron)	
Fluid ICs	**Initial Pressure:**				(Pa)	
	Initial Temperature:				(K)	
	Initial Fluids:					
Particle ICS	**Bed Aspect Ratio:**					
	Solid Volume Fraction:					
Pressure BCs	**Pressure :**				(Pa)	
	Temperature:				(K)	
	Particle outflow:	Yes	No			
Flow BCs	**Flow Type:**	Mass Flow	Velocity Flow			
	Pressure:				(Pa)	
	Temperature:				(K)	
Reaction	**Coefficient Properties:**	Volume-Average	Discrete			
	Pre-exponential Factor:				(1/s)	
	Activation Energy:				(Kj/mole)	
	Shrinking Core Model:	On	Off			
	Diffusion Coefficient:				(cm2/s)	

6.2 Model Development

6.2.1 Generation 0

This is the initial stage to deals with the alumina chlorination fluidized bed reactor. The primary aid is simulating the reaction under an isothermal condition for a simple cylindrical reactor and study the effect of different bed aspect ratios (H/D) on the reaction and hydrodynamics of the system.

Simulation Objectives:

- Set the simulation (v.0) based on the simulation sheet 01 and 02 (Appendix B).
- To apply different H/Ds (2.5, 1.5, 1, 0.75, 0.5).
- To apply different superficial velocities (or pressures).
- Plot the Cl2 concentration in the outlet for all cases.
- Plot the particle outflow for all cases.
- Plot the particle outflow vs. bed height.

As the first step, a cylinder based on the given dimensions for this task has been built in Autodesk Inventor®. Setting up the grids, 25000 uniform cells have been selected (Figure 6.12). In this simulation (v.0.1), other parameters have been set based on the simulation sheet 01 (Appendix B).

Figure 6.12 Meshed simple cylindrical reactor v.0

For output data, several flux planes have been defined at different levels in the reactor. Each flux plane gives some information such as total fluid and mass flow rates as well as the flow rate of each species (Figure 6.13). To study and track Cl_2 concentration through the reactor, the information in 5 data points in each level has been averaged.

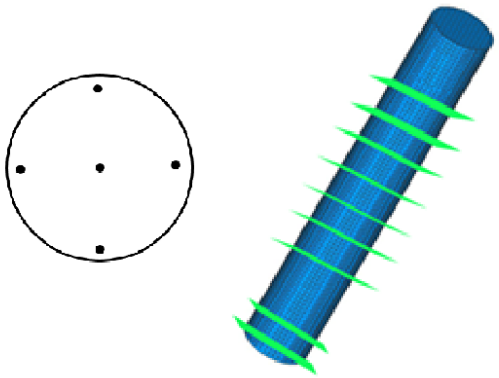

Figure 6.13 Data points (right) and Flux Planes (left).

6.2.1.1 Result and Discussion

The simulation has started with H/D=1 and five different superficial velocities (0.05, 0.1, 0.12, 0.15, 0.2 m/s) have been tested. To have each of these velocities, the pressure has been adjusted respectively in the flow BCs setting. Each simulation has a duration of at least 1200 seconds to reach the pseudo steady-state. Figure 6.14 shows the particle's distribution through the reactor at the steady-state.

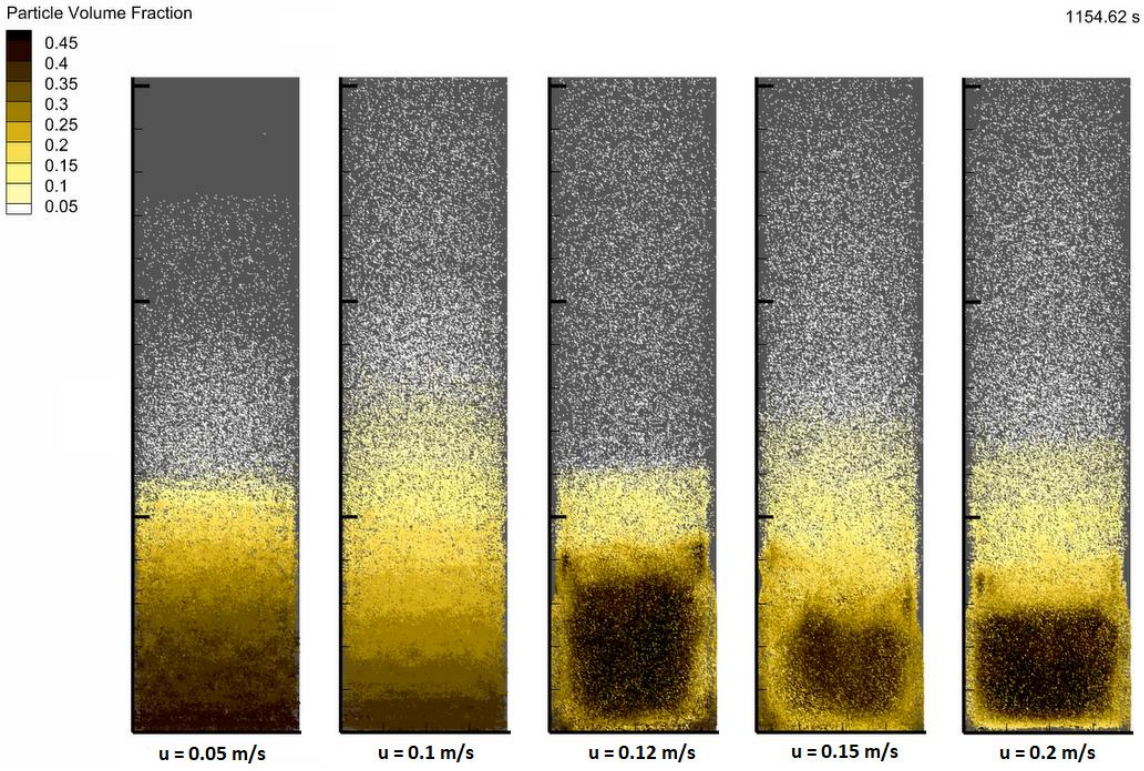

Figure 6.14 Particle distribution through the reactor in different velocities (H/D=1)

The Cl_2 concentration and particle outflow in the outlet are plotted for each case in steady-state. In all cases, when the system reaches the pseudo steady-state, the Cl_2 concentration (Figure 6.15) lies on 0.0001 mole/m3 or below. Particle escape in all cases has considerable value except in the case with the lowest velocity (Figure 6.16).

These graphs clearly show that:

- Although it is negligible, when the superficial velocity of a fluid increases (or the inlet pressure decreases), the Cl_2 concentration increases slightly.
- The time needed to reach the steady-state for lower velocities may be longer. It has been noted that this effect is not an issue for long-run applications.

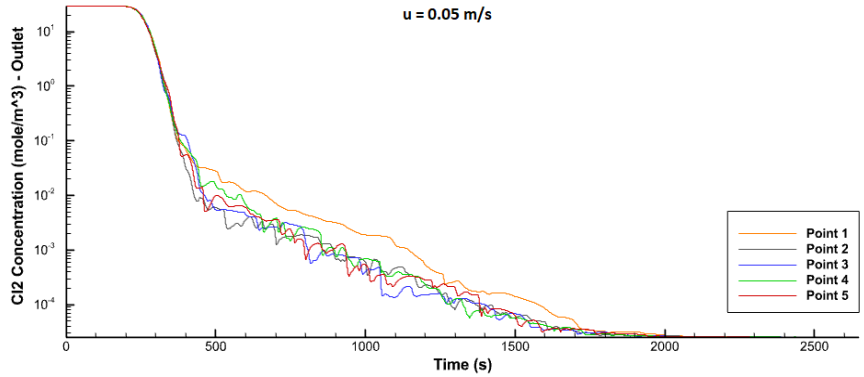
u = 0.05 m/s
Cl2 Concentration (mole/m^3) - Outlet
Time (s)
Point 1
Point 2
Point 3
Point 4
Point 5

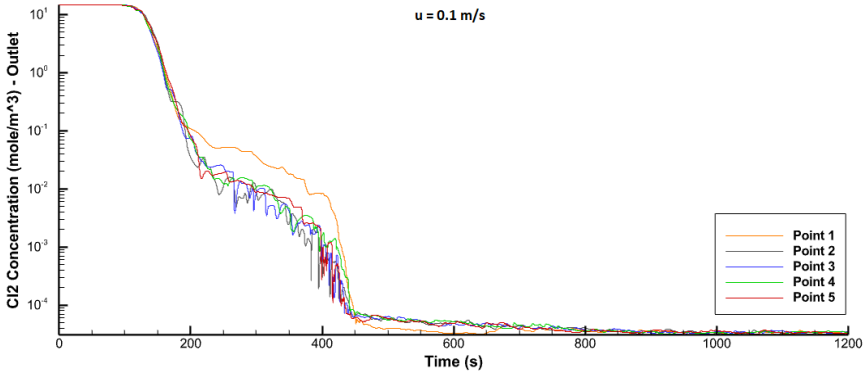
u = 0.1 m/s
Cl2 Concentration (mole/m^3) - Outlet
Time (s)
Point 1
Point 2
Point 3
Point 4
Point 5

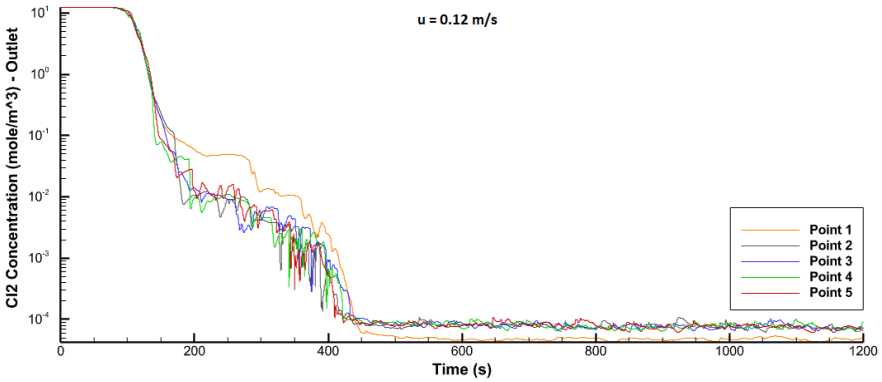
u = 0.12 m/s
Cl2 Concentration (mole/m^3) - Outlet
Time (s)
Point 1
Point 2
Point 3
Point 4
Point 5

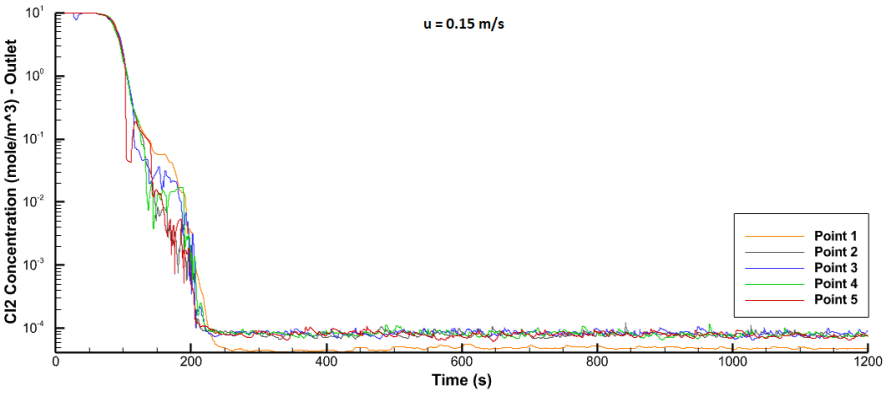
u = 0.15 m/s
Cl2 Concentration (mole/m^3) - Outlet
Time (s)
Point 1
Point 2
Point 3
Point 4
Point 5

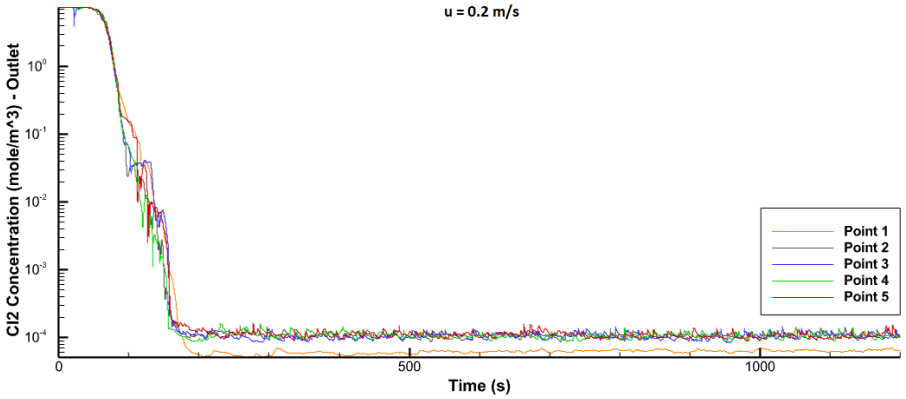

Figure 6.15 Cl_2 concentration in different superficial velocities (H/D=1)

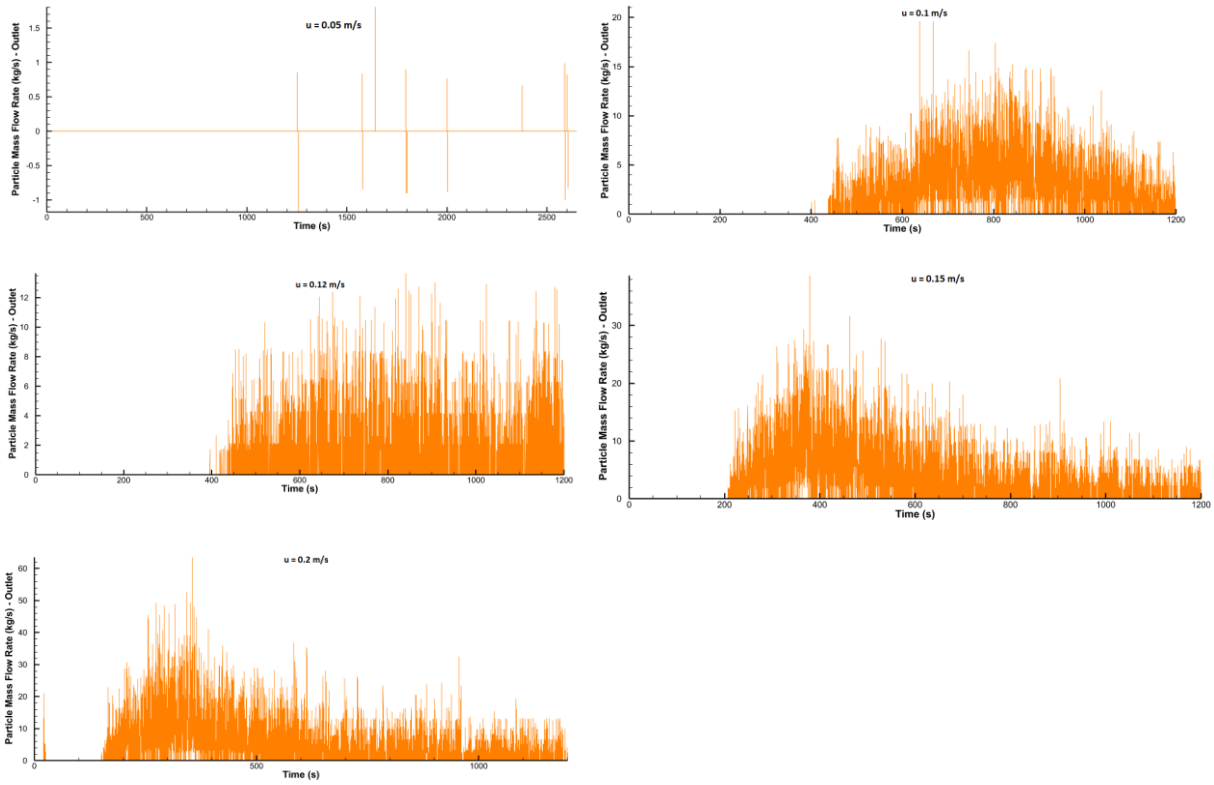

Figure 6.16 Particle outflow in different superficial velocities (H/D=1)

The figure above indicated that almost no particle outflow had been observed when the velocity is the lowest. This means that with this velocity, the drag force is not enough for particle escape, or it needs much more time to see the effect. By increasing the velocity, the particle escape increases.

Similarly, for other bed aspect ratios (2.5, 2, 1.5, 0.75, 0.5, 0.25), the graph related to the Cl_2 concentration and particle escape at the outlet is given in Figure 6.17- Figure 6.22.

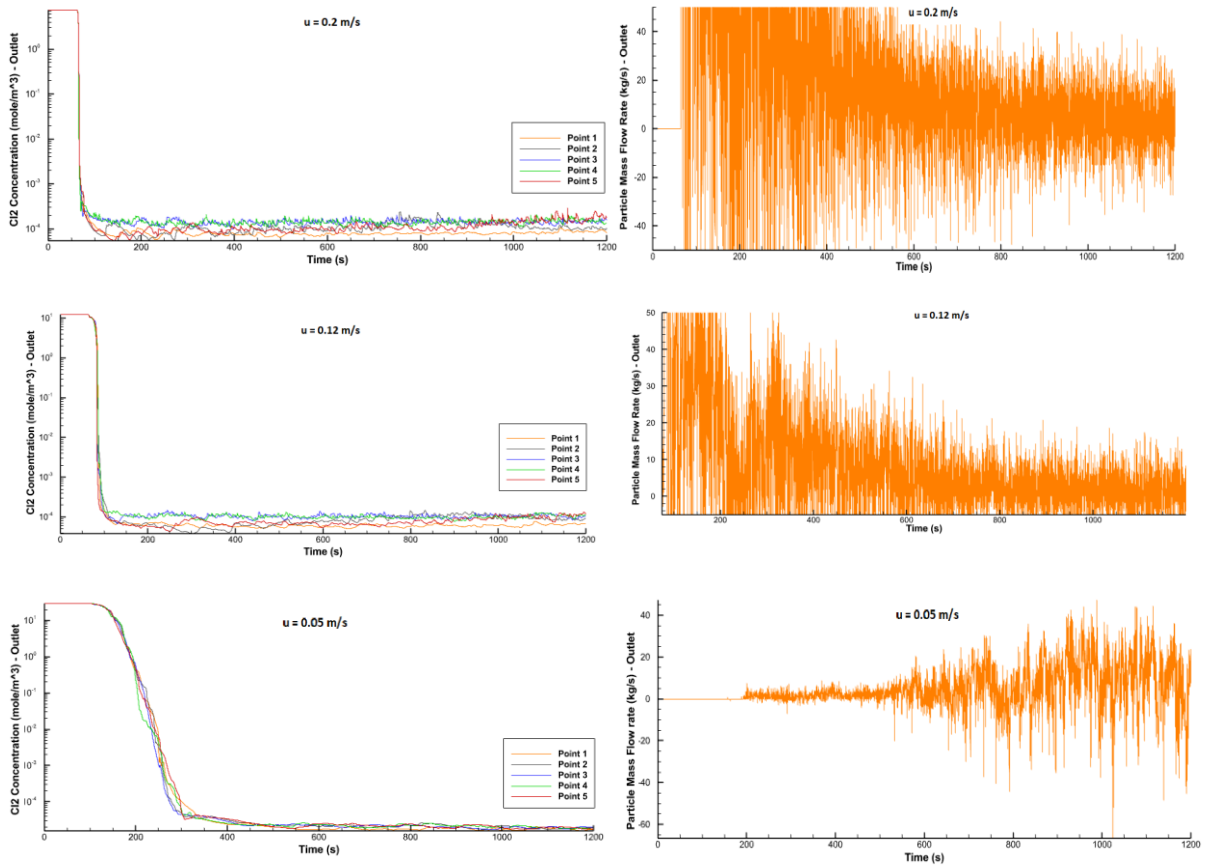

Figure 6.17 Particle outflow and Cl_2 concentration in different superficial velocities (H/D=2.5)

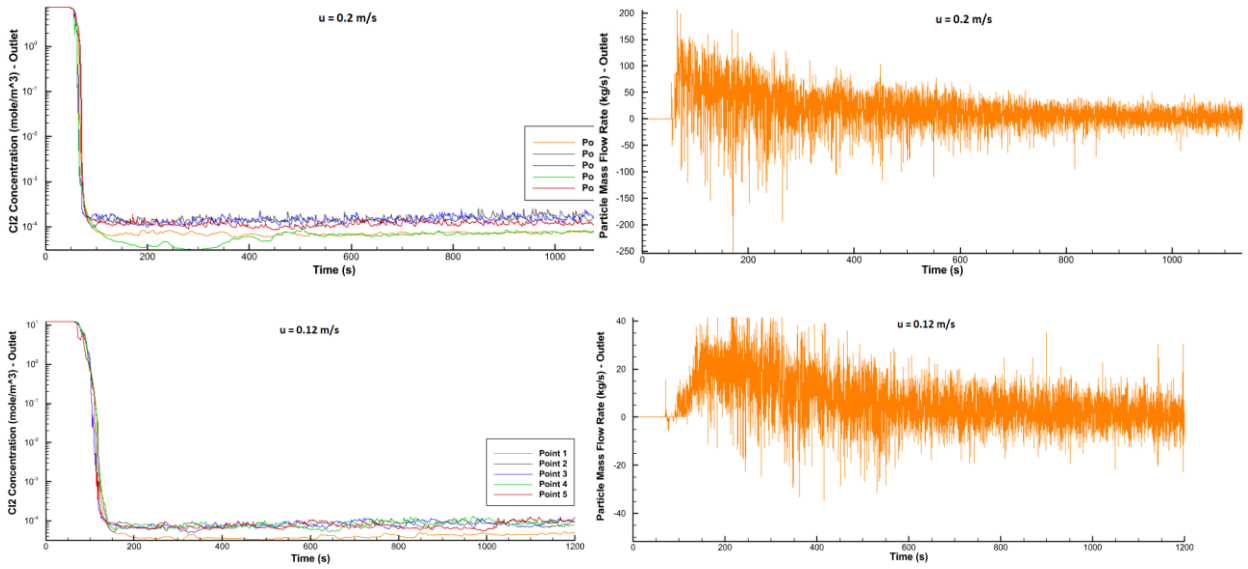

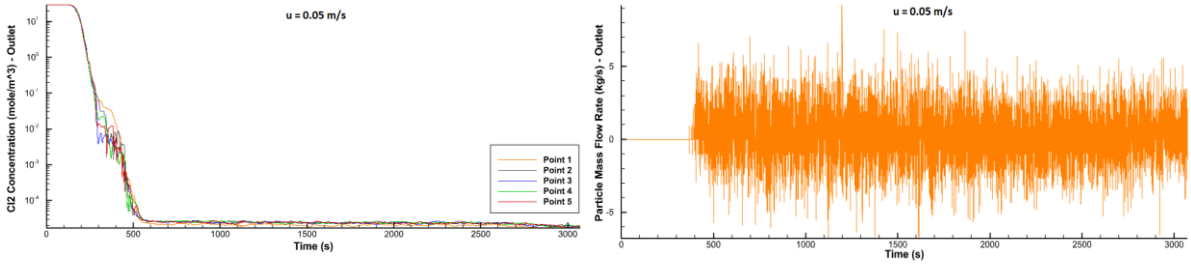

Figure 6.18 Particle outflow and Cl_2 concentration in different superficial velocities (H/D=2)

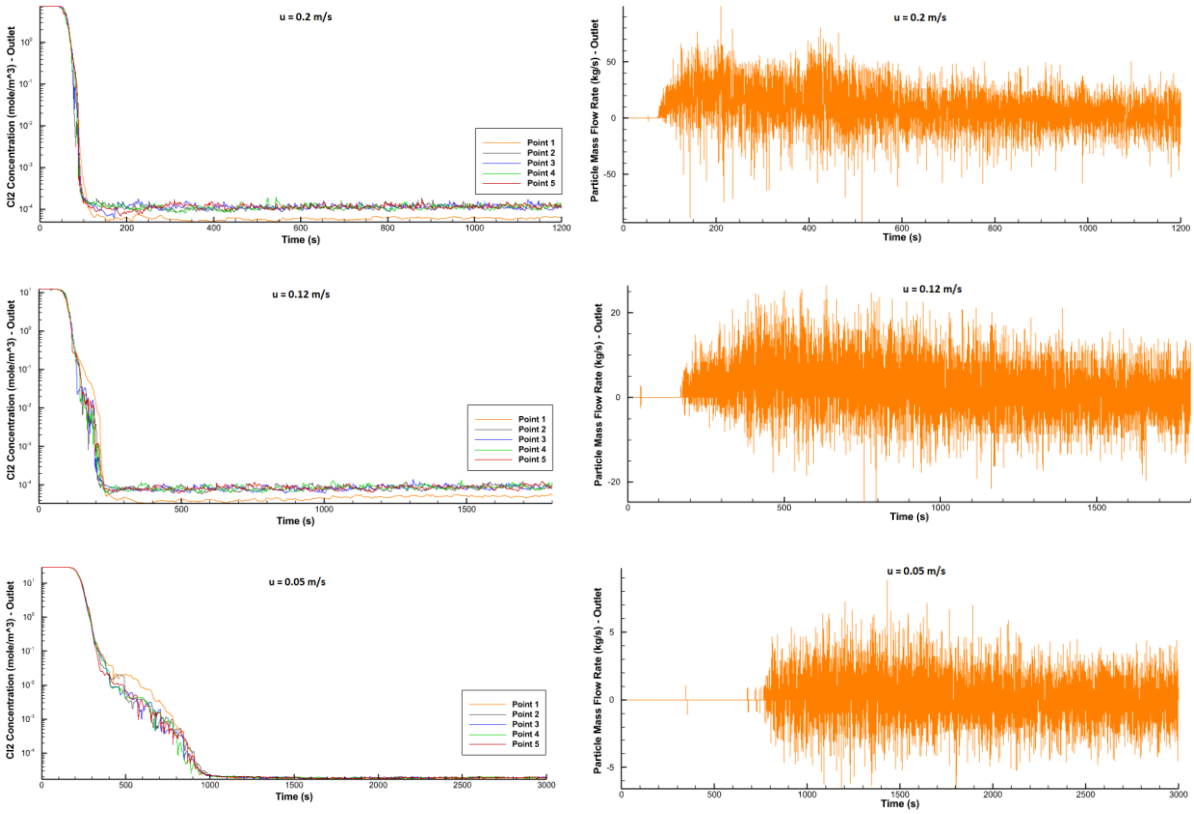

Figure 6.19 Particle outflow and Cl_2 concentration in different superficial velocities (H/D=1.5)

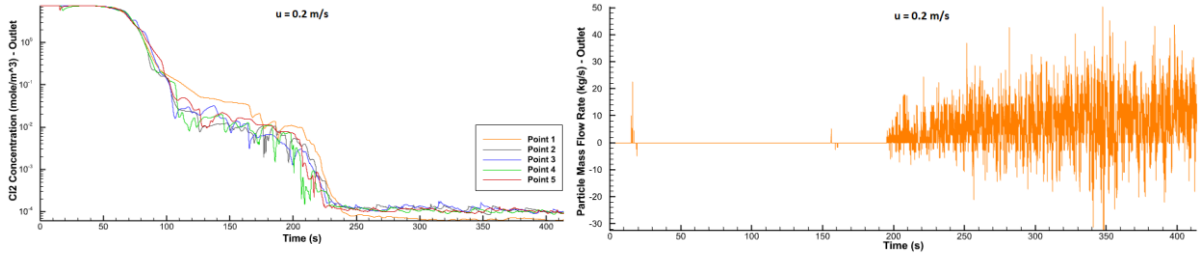

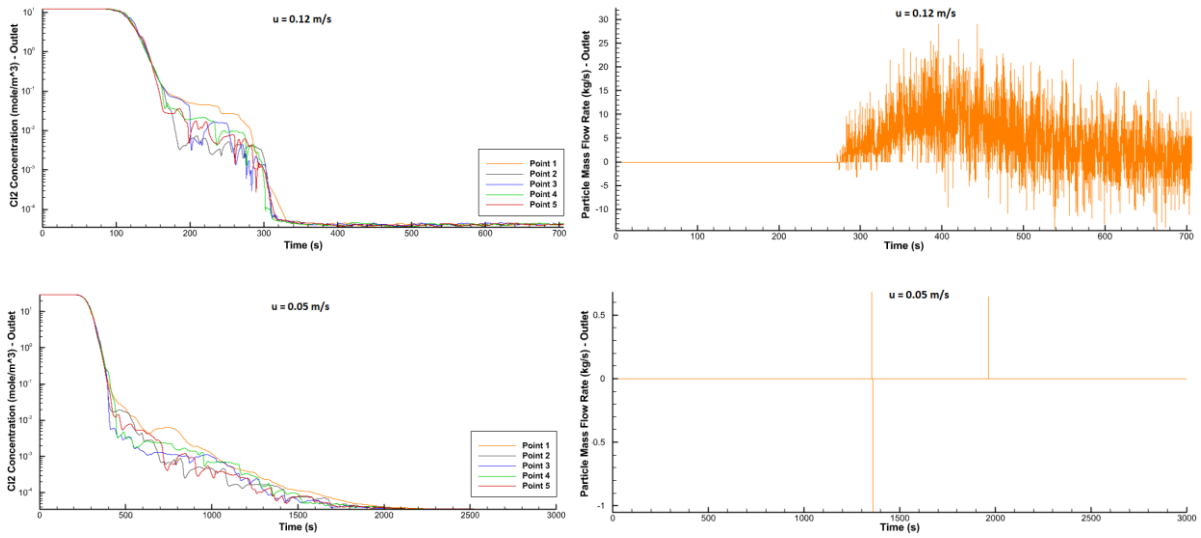

Figure 6.20 Particle outflow and Cl2 concentration in different superficial velocities (H/D=0.75)

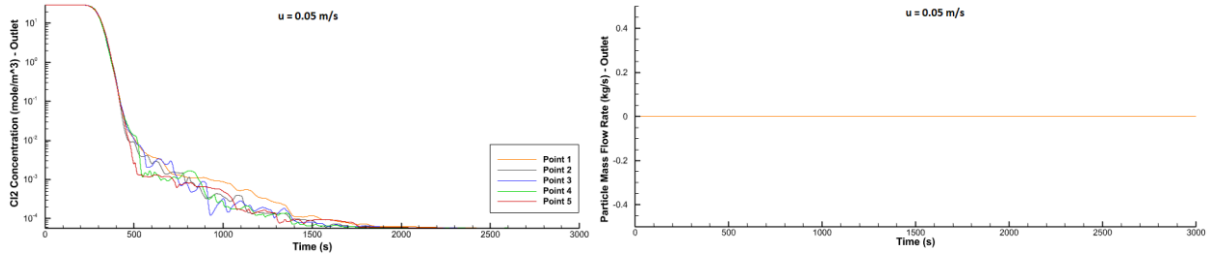

Figure 6.21 Particle outflow and Cl_2 concentration when u=0.05 m/s (H/D=0.75)

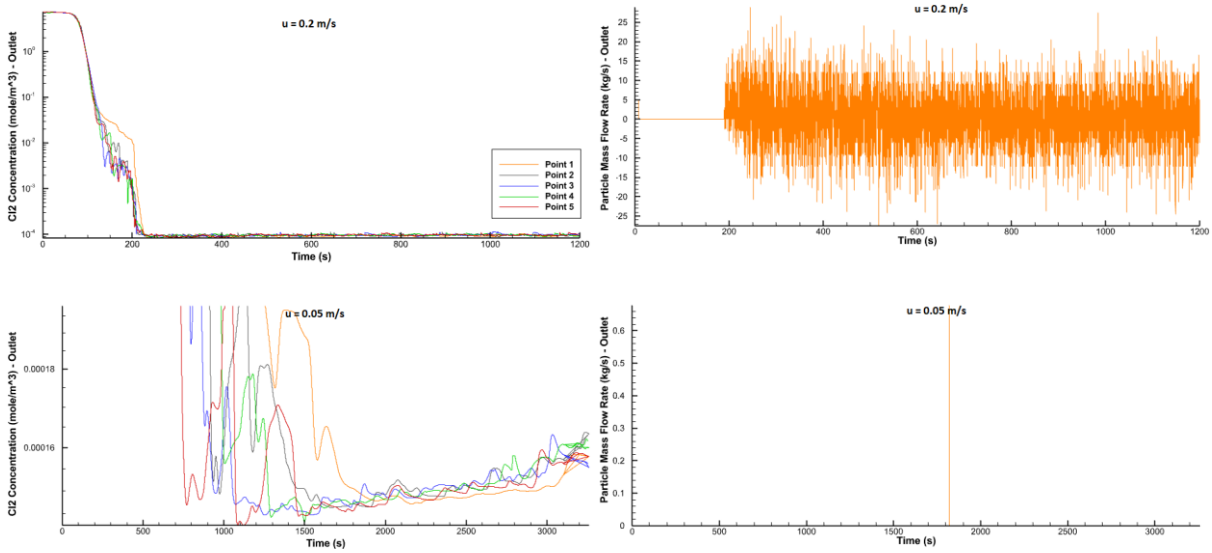

Figure 6.22 Particle outflow and Cl_2 concentration in different superficial velocities (H/D=0.25)

Table 6.2 Cl_2 concentration (mg/l) at the outlet for different bed aspect ratios

H/D	0.2 m/s	0.12 m/s	0.05 m/s
2.5	0.014	0.011	0.002
2	0.011	0.014	0.001
1.5	0.011	0.007	0.001
1	0.011	0.007	0.001
0.75	0.009	0.004	0.001
0.25	0.007	-	0.011

Table 6.2 gives the average Cl_2 concentration at the outlet for different bed aspect ratios. Change in the fluid's velocity from high to low (or low to high for pressure) leads to higher conversion and less Cl_2 chlorine at the outlet. The above graphs show that when the fluid's superficial velocity through the reactor is slower, the particle outflow is less. As the result of this observation, it is desirable to have the highest possible pressure and lowest velocity in the system, but always the overall process has its considerations. At this step, the outlet pressure has been given by the project description. Therefore, based on simulation sheet 02 (Appendix B), the following simulations (v.0.2) have been done. Figure 6.23 shows the particle distribution through the rector at the steady-state.

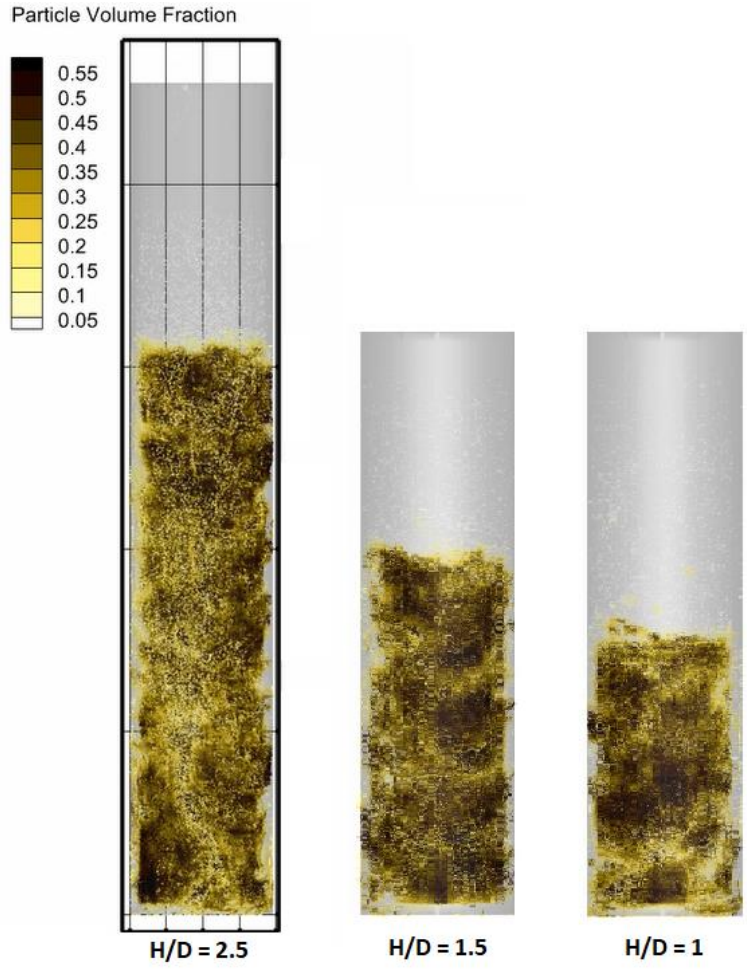

Figure 6.23 Particle distribution through the reactor at the pseudo steady-state (v.0.2)

The following graphs (Figure 6.24-Figure 6.27) present the chlorine concentration and particle outflow at the outlet of the reactors with the bed aspect ratio of 2.5, 1.5, 1, and 0.5 are given.

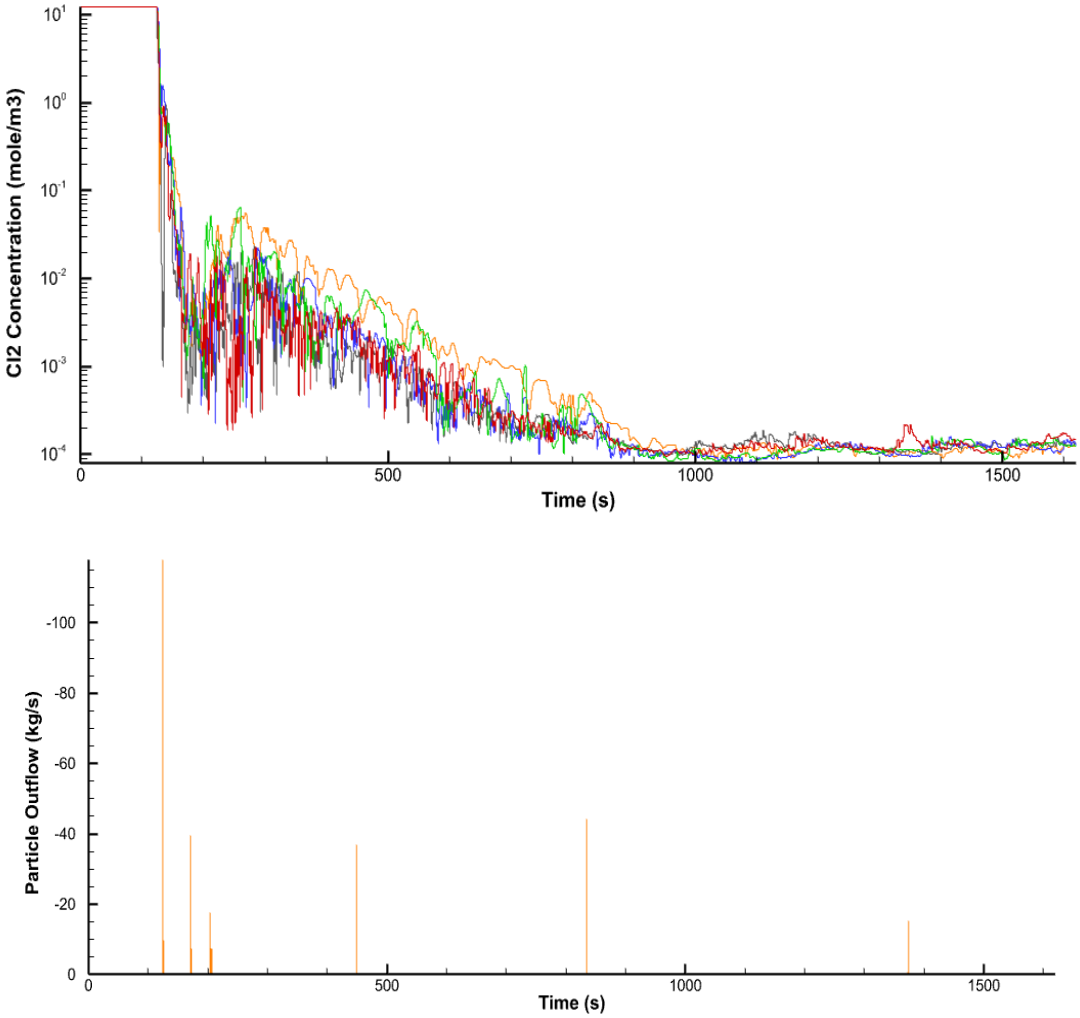

Figure 6.24 Particle outflow and Cl_2 concentration (H/D=2.5)

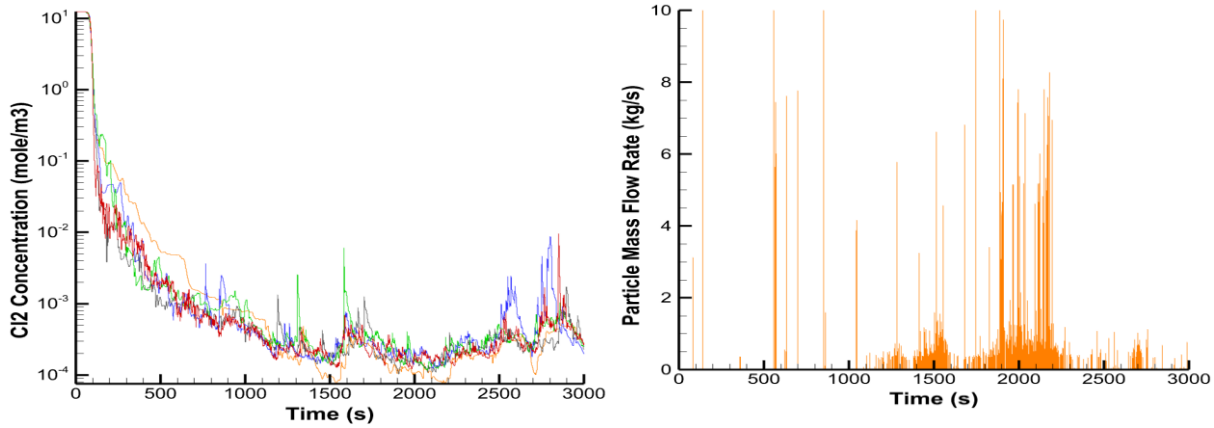

Figure 6.25 Particle outflow and Cl_2 concentration (H/D=1.5)

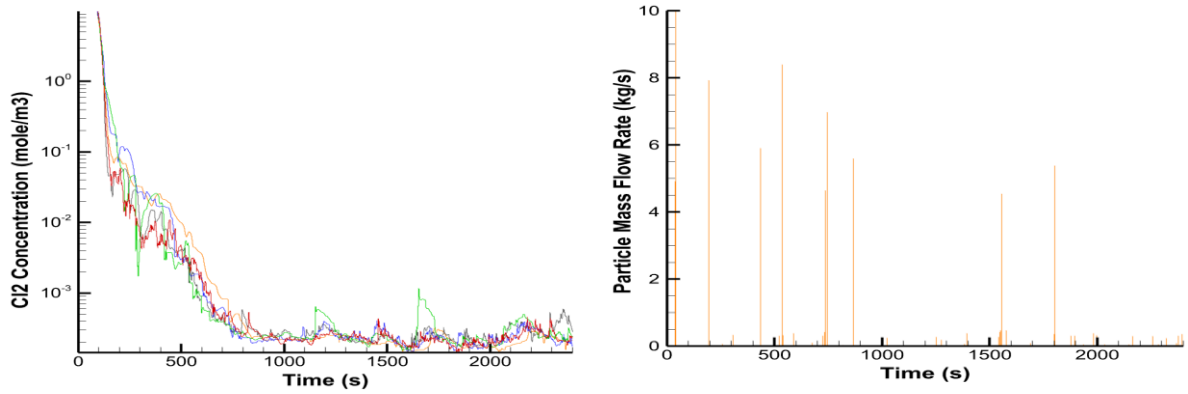

Figure 6.26 Particle outflow and Cl_2 concentration (H/D=1)

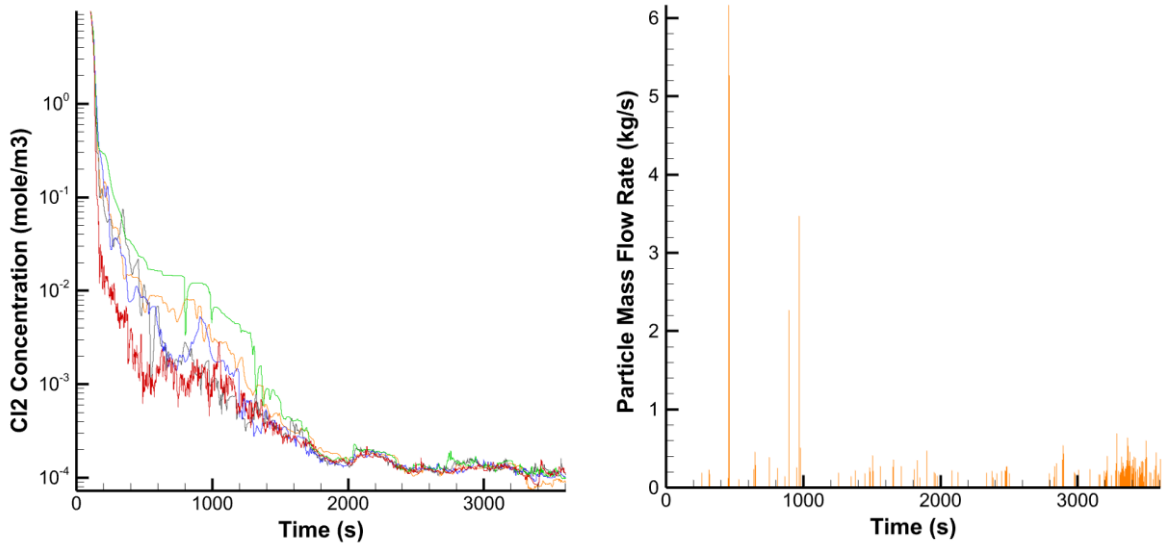

Figure 6.27 Particle outflow and Cl_2 concentration (H/D=0.5)

6.2.1.2 Conclusion

Almost all the Cl_2 are consumed within the first meter of the reactor, which means the current range of bed and reactor height may not be an issue in the actual chlorination process. However, the H/D value inherits a vital role for good hydrodynamics of the reactor. Selecting the reactor specification for good hydrodynamics of the gas-solid fluidized bed reactor is very important.

Too low H/D can cause channeling, and it may reduce the reaction efficiency. As a result, Cl_2 concentration at the reactor outlet may increase. Even a tiny amount of Cl_2 at the outlet could cause problems if there is not a purification process on Cl_2. Simultaneously, too high H/D may increase energy consumption due to the increased pressure drop of the reactor.

Considering all factors such as hydrodynamics, change in Cl_2 concentration over height, and particle outflow, suitable H/D is found as around 2. In this case, the minimum reactor height could be calculated.

6.2.2 1st Generation

Based on the results from the previous section, a bed aspect ratio and overall reactor dimensions have been selected. In addition to a simple cylindrical reactor, as discussed in the overall design criteria (section 5.1), a smooth exit will be added to the system.

Simulation Objectives:

- Set the simulation (v.1) based on the simulation sheet 03 and 04 (Appendix B).
- Change the method of computing the average concentration or mass flow from average data points to data planes which is more accurate and realistic.
- Add a smooth exit to the top of the reactor.
- Plot the Cl2 concentration through the reactor height.
- Calculate the particle outflow.

As the first step, a geometry based on the given dimensions has been built in Autodesk Inventor®. Setting up the grids, 25000 uniform cells have been selected (Figure 6.28). In this simulation (v.1.0), all other needed parameters have been set based on the simulation sheet 03 (Appendix B).

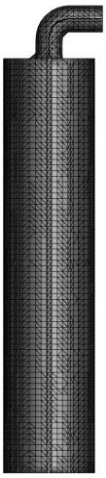

Figure 6.28 Meshed simple cylindrical reactor v.1

For output data, the flux plane and data point are defined as before (Figure 6.29).

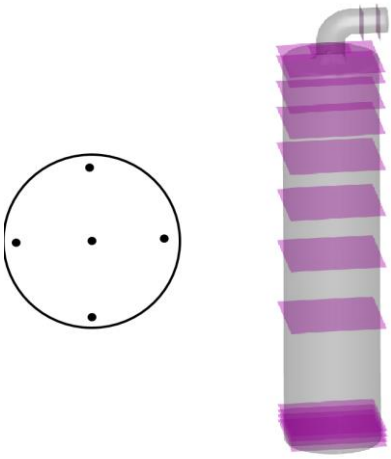

Figure 6.29 Data points (right) and flux planes (left).

6.2.2.1 Result and Discussion

As mentioned in section 6.2.1, to average the data at each level height, the average data from five data points (in the same plane) has been used. As seen in Figure 6.30, the distribution of the chlorine concentration or solid mass flow is not uniformly distributed, and averaging by selecting five random data points was not an accurate method.

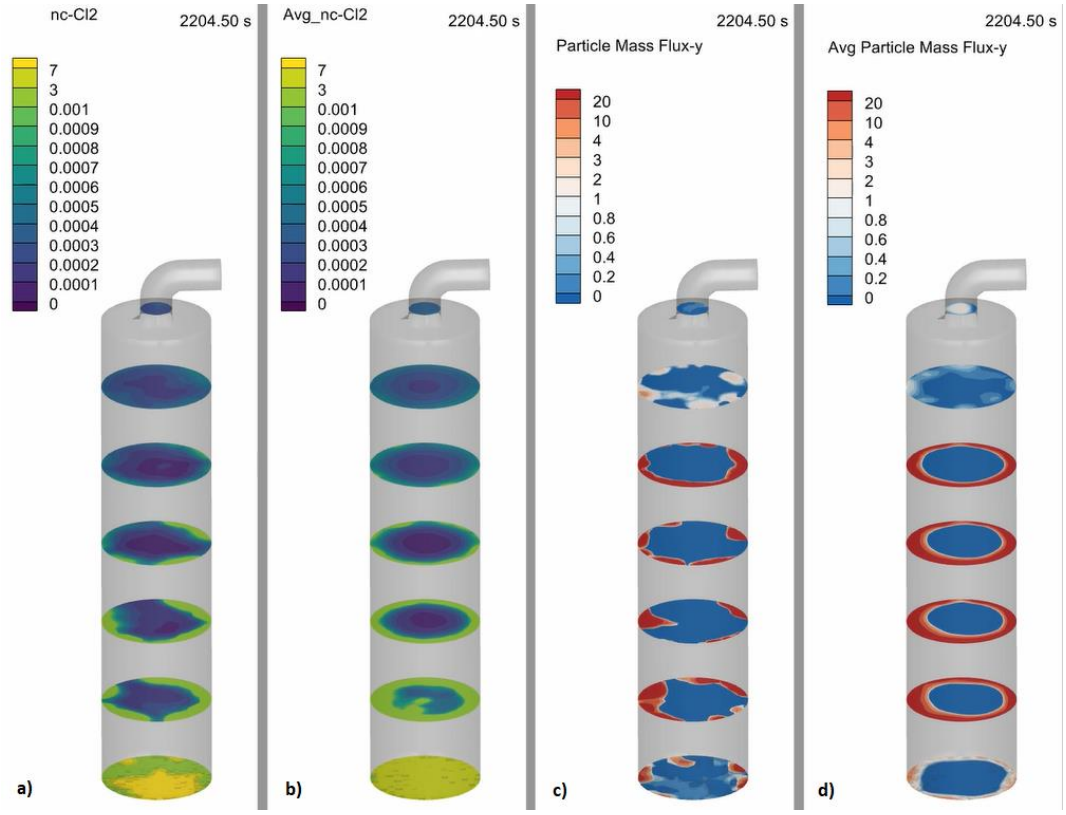

Figure 6.30 Cl_2 concentration (mole/m^3) and particle mass flux (kg/sm^2) in different heights when the inflow is uniform a) Cl_2 concentration at the specific time, b) Average Cl_2 concentration in the last 300 seconds, c) Particle mass flux at the specific time, and d) Average particle mass flux in the last 300 seconds.

Figure 6.30 has been built using the recorded data from each cell in that plane, such as Figure 6.31.

			4.60E-04	4.82E-04	4.91E-04	4.81E-04	4.65E-04	4.49E-04	4.12E-04	3.64E-04	3.25E-04	2.90E-04	2.60E-04			
		4.36E-04	5.10E-04	5.92E-04	6.34E-04	6.31E-04	5.94E-04	5.61E-04	4.94E-04	4.26E-04	3.73E-04	3.26E-04	2.75E-04	2.47E-04		
	3.67E-04	4.52E-04	5.64E-04	6.31E-04	6.76E-04	6.64E-04	5.95E-04	5.29E-04	4.61E-04	4.07E-04	3.72E-04	3.42E-04	3.03E-04	2.61E-04	2.24E-04	
2.91E-04	3.47E-04	4.35E-04	5.13E-04	5.45E-04	5.90E-04	5.98E-04	5.15E-04	4.38E-04	3.85E-04	3.46E-04	3.32E-04	3.46E-04	3.27E-04	2.77E-04	2.26E-04	1.96E-04
2.59E-04	3.06E-04	3.57E-04	3.94E-04	4.10E-04	4.40E-04	4.45E-04	3.95E-04	3.49E-04	3.19E-04	2.99E-04	2.90E-04	3.28E-04	3.21E-04	2.62E-04	2.13E-04	1.82E-04
2.25E-04	2.53E-04	2.76E-04	2.96E-04	3.07E-04	3.20E-04	3.20E-04	2.98E-04	2.81E-04	2.70E-04	2.60E-04	2.55E-04	2.77E-04	2.68E-04	2.24E-04	1.85E-04	1.59E-04
1.96E-04	2.12E-04	2.17E-04	2.27E-04	2.35E-04	2.50E-04	2.57E-04	2.60E-04	2.55E-04	2.51E-04	2.43E-04	2.32E-04	2.24E-04	2.00E-04	1.74E-04	1.53E-04	1.37E-04
1.72E-04	1.80E-04	1.78E-04	1.81E-04	1.90E-04	2.11E-04	2.35E-04	2.55E-04	2.58E-04	2.48E-04	2.35E-04	2.12E-04	1.84E-04	1.56E-04	1.34E-04	1.25E-04	1.16E-04
1.56E-04	1.59E-04	1.58E-04	1.58E-04	1.66E-04	1.84E-04	2.09E-04	2.29E-04	2.40E-04	2.31E-04	2.11E-04	1.83E-04	1.55E-04	1.28E-04	1.12E-04	1.05E-04	1.00E-04
1.42E-04	1.45E-04	1.46E-04	1.46E-04	1.49E-04	1.60E-04	1.76E-04	1.94E-04	2.05E-04	1.95E-04	1.74E-04	1.51E-04	1.29E-04	1.08E-04	9.57E-05	9.06E-05	8.86E-05
1.36E-04	1.41E-04	1.40E-04	1.40E-04	1.42E-04	1.46E-04	1.53E-04	1.61E-04	1.65E-04	1.55E-04	1.39E-04	1.22E-04	1.08E-04	9.48E-05	8.59E-05	8.32E-05	8.37E-05
1.34E-04	1.38E-04	1.37E-04	1.37E-04	1.39E-04	1.37E-04	1.37E-04	1.36E-04	1.31E-04	1.20E-04	1.08E-04	9.88E-05	9.00E-05	8.23E-05	7.74E-05	7.84E-05	8.31E-05
1.34E-04	1.36E-04	1.38E-04	1.38E-04	1.39E-04	1.35E-04	1.28E-04	1.21E-04	1.09E-04	9.53E-05	8.62E-05	8.06E-05	7.55E-05	7.15E-05	7.13E-05	7.71E-05	8.55E-05
1.32E-04	1.34E-04	1.37E-04	1.38E-04	1.36E-04	1.30E-04	1.23E-04	1.10E-04	9.13E-05	7.67E-05	6.93E-05	6.52E-05	6.35E-05	6.35E-05	6.80E-05	7.98E-05	8.75E-05
0.00E+00	1.27E-04	1.25E-04	1.24E-04	1.24E-04	1.19E-04	1.09E-04	9.32E-05	7.25E-05	5.73E-05	5.15E-05	5.00E-05	5.15E-05	5.58E-05	6.41E-05	7.52E-05	0.00E+00
	0.00E+00	0.00E+00	1.16E-04	1.10E-04	1.04E-04	9.29E-05	7.66E-05	5.93E-05	4.83E-05	4.56E-05	4.66E-05	4.86E-05	5.21E-05	0.00E+00	0.00E+00	
		0.00E+00	0.00E+00	0.00E+00	9.08E-05	7.97E-05	6.56E-05	5.27E-05	4.61E-05	4.55E-05	4.57E-05	0.00E+00	0.00E+00	0.00E+00		
			0.00E+00	0.00E+00	0.00E+00	0.00E+00	0.00E+00	0.00E+00	0.00E+00	0.00E+00	0.00E+00	0.00E+00	0.00E+00			

Figure 6.31 Recorded average data for Cl_2 concentration in the last 300 seconds of the simulation (at 2 meters from the bottom of the reactor)

Figures 6.30b and 6.30d give more information about hydrodynamics inside the reactor. The green and the red ring near the wall emphasize the escape of fluid homogenously near the wall. This means the central area of the reactor builds more resistance, and fluid can escape through a tiny space near the wall, and when there is a lower area to escape, a higher speed will be seen, which is not favorable for the process.

Previously, a uniform injection through the bottom of the reactor has been used. A non-uniform pattern (Figure 6.32) with higher velocity in the middle and gradually decrease to the outer side (by keeping the overall fluid's mass flow rate the same as before) is used as a possible way to solve the channeling problem.

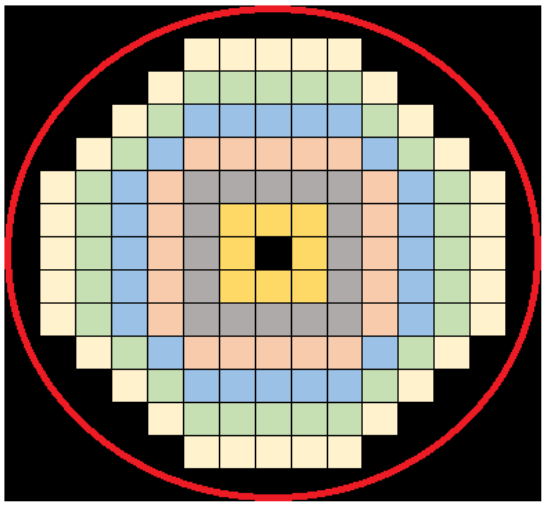

Figure 6.32 Defining non-uniform ring injection in Barracuda®

Figure 6.32 shows the cross-sectional reactor area in red and six rings with different mass flow rates (Figure 6.33). The black areas have no flow.

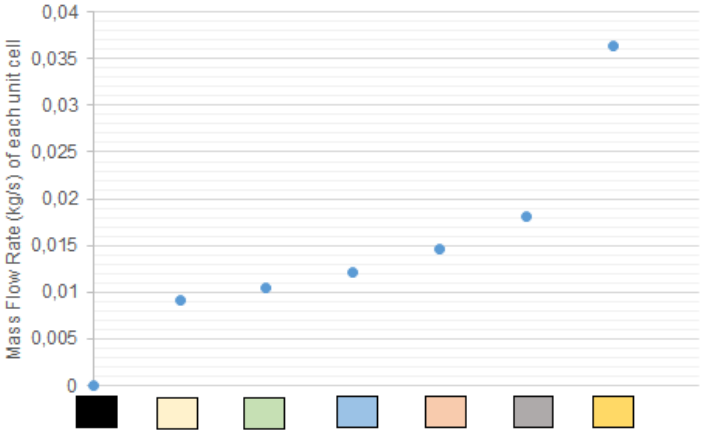

Figure 6.33 Mass flow rate of each unit cell in Barracuda®

As expected, by changing the inflow pattern, no significant change in Cl_2 consumption has occurred (very fast reaction). Table 6.3 gives the average Cl_2 concentration in different heights through the reactor for both uniform and non-uniform patterns.

The levels start from the bottom (level 0), and there are 15 levels distributed uniformly. As it clear, after the first meter of the reactor, the conversion is almost complete, and the Cl_2 concentration is reasonably constant. This low value confirms the very fast reaction.

Table 6.3 Average Cl_2 concentration in different heights of the reactor.

Uniform Inflow Pattern			Non-uniform Inflow Pattern		
level	mole/m3	mg/l	level	mole/m3	mg/l
0	4.08	289.27	0	0.92	65.23
1	0.132742	9.41	1	0.1825	12.94
2	0.005003	0.35	2	0.008254	0.59
3	0.000817	0.06	3	0.001989	0.14
4	0.000683	0.05	4	0.000564	0.04
5	0.000478	0.03	5	0.004726	0.34
6	0.000438	0.03	6	0.000328	0.02
7	0.000350	0.02	7	0.000302	0.02
8	0.000350	0.02	8	0.000314	0.02
9	0.000326	0.02	9	0.000501	0.04
10	0.000280	0.02	10	0.000598	0.04
11	0.000377	0.03	11	0.000495	0.04
12	0.000373	0.03	12	0.000410	0.03
13	0.000394	0.03	13	0.000404	0.03
14	0.000337	0.02	14	0.000357	0.03
15	0.000319	0.02	15	0.000372	0.03
16	0.000363	0.03	16	0.000395	0.03

Comparing both hydrodynamics (Figure 6.30 and Figure 6.34), it can be observed that the non-uniform pattern has a positive effect on the hydrodynamics, but still, fluid can escape through the wall but from one side.

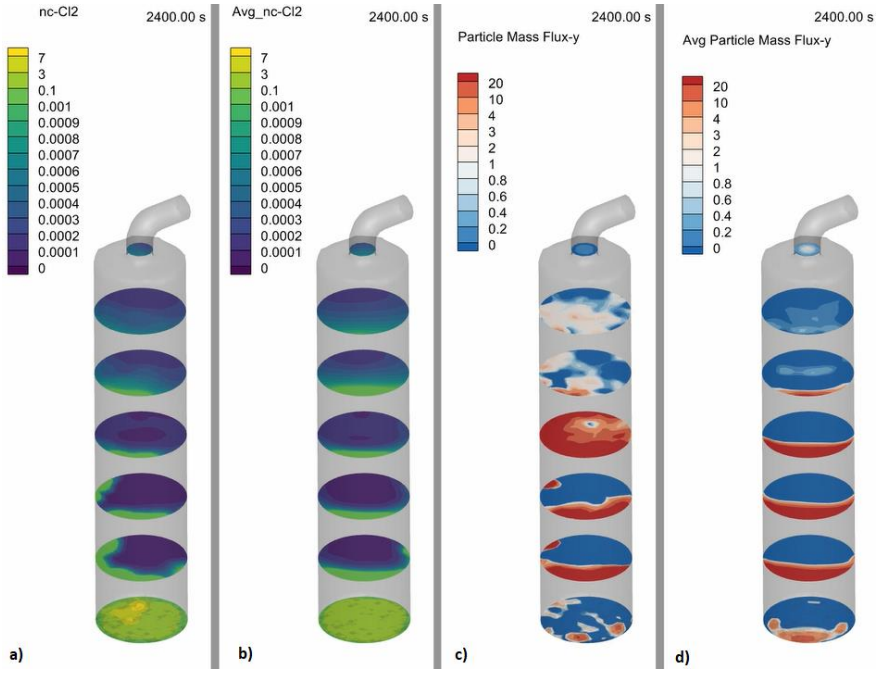

Figure 6.34 Cl_2 concentration (mole/m^3) and particle mass flux (kg/sm^2) in different heights when the inflow is non-uniform a) Cl_2 concentration at the specific time, b) Average Cl_2 concentration in the last 300 seconds, c) Particle mass flux at the specific time, and d) Average particle mass flux in the last 300 seconds.

However, considering the particle outflow, the situation is not good according to the Cl_2 concentration. As seen in Figure 6.35, a considerable amount of particles are leaving the reactor. For uniform inflow, the average particle

outflow at the pseudo steady state is about 0.38 kg/s which is almost 0.63% of the particle inflow, which is too high. This value for the non-uniform inflow is even higher and almost the same as particle inflow which is 0.6 kg/s.

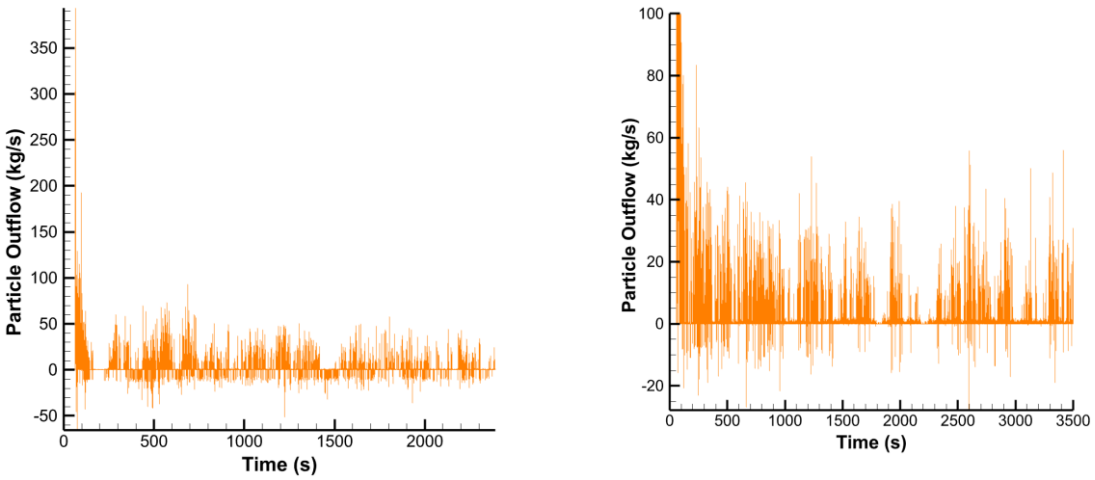

Figure 6.35 Particle outflow (kg/s) with uniform inflow (left), and non-uniform inflow (right).

This amount of particle escape is not acceptable and can be reduced by increasing the reactor diameter (or reducing the superficial velocity in the reactor). In the new simulation (v.1.1), the bed aspect ratio is kept as same as before at 2, but the bed height is increased (because of increase in reactor diameter), and as a result, the reactor height should be revised (simulation sheet 04 – Appendix B).

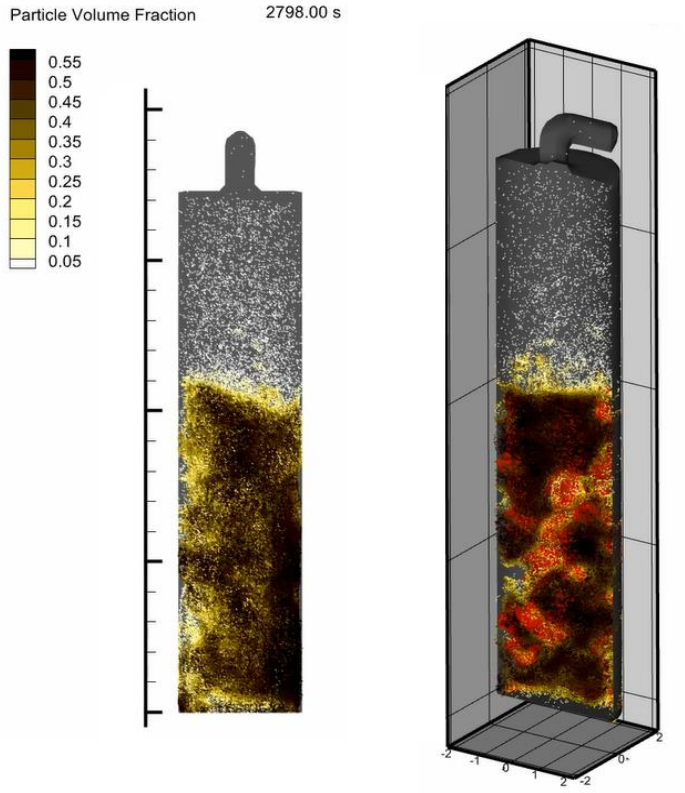

Figure 6.36 Channeling in the bed (reactor v.1.1)

Similarly, as before, chlorine concentration has no significant change because of the very fast reaction. Nevertheless, the particle outflow has increased to 0.67 kg/s (with non-uniform inflow) which is almost two times

the first case. Although the velocity has been reduced, a negative impact has been observed. One reason could be channeling inside the bed. Figure 6.36 illustrates the bed condition and particle distribution inside the reactor. Channeling and fluid escape can be found near the wall (left) and through the bed (right).

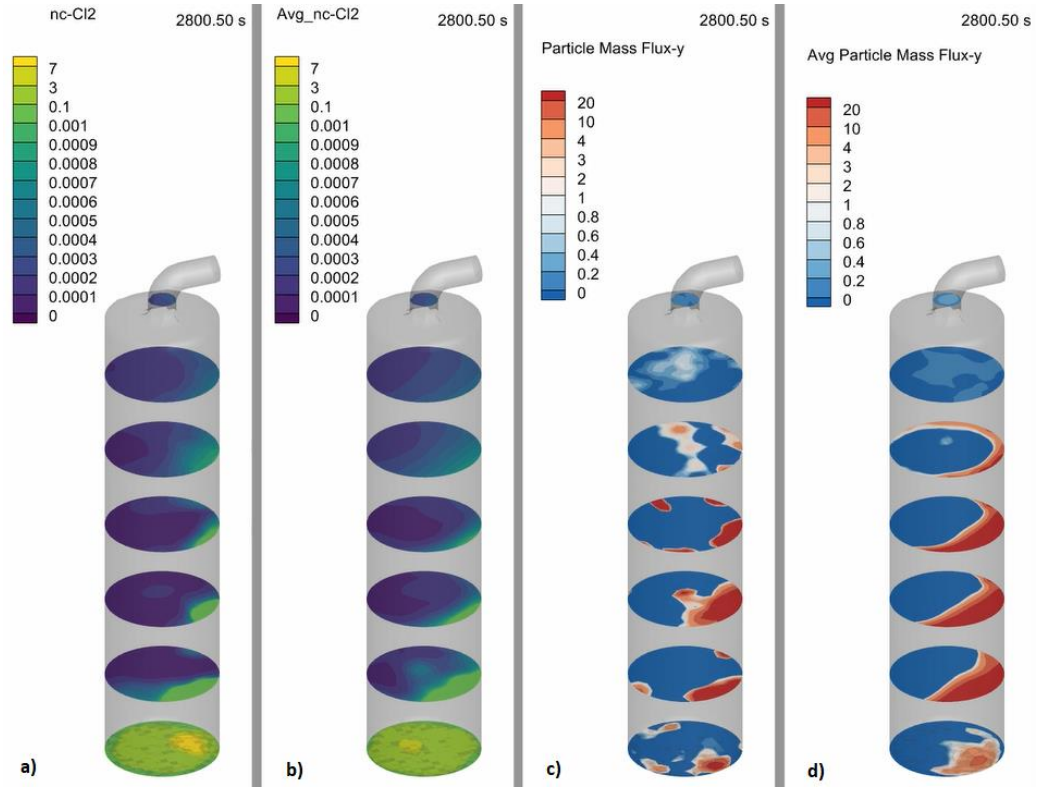

Figure 6.37 Cl_2 concentration (mole/m^3) and particle mass flux (kg/sm^2) in different heights when the inflow is non-uniform a) Cl_2 concentration at the specific time, b) Average Cl_2 concentration in the last 300 seconds, c) Particle mass flux at the specific time, and d) Average particle mass flux in the last 300 seconds.

Figure 6.37 shows a better conversion rate for the Cl_2, and the chlorine concentration is lower than previous models, but still a considerable amount of fluid escape through the reactor wall.

6.2.2.2 Conclusion

In this series of simulations for a simple cylindrical geometry with a smooth exit at the top, the effect of fluid's uniform and non-uniform inflow pattern and superficial velocity on the Cl_2 concentration and particle outflow have been investigated. The simulations still confirm that conversion becomes almost complete in all simulations in the first meter of the reactor. However, there is a severe challenge in particle outflow from the reactor. Not only the change in the pattern of the feed gas but also the reduction of the fluid's superficial velocity had no positive effect on the escape of particles.

In channeling, the fluid's velocity in the channel becomes much higher than the inlet velocity and makes the cut size of the outflowing particles bigger. In this situation, there will be more particle escape. A possible solution to this problem can be to reduce the fluid speed above the dense phase by changing the reactor's geometry, and this is studied in the next generation of the reactor.

6.3 Model Optimization

6.3.1 2nd Generation

As it is concluded in the first generation of the reactor, one possible solution to reduce a considerable amount of particle escape is to change the hydrodynamics above the dense phase and make the superficial velocity of the fluid slower. This can be done by changing the geometry from a simple cylindrical reactor to the reactor shown in Figure 6.38.

Simulation Objectives:

- Set the simulation (v.2) based on the simulation sheet 05 and 06 (Appendix B).
- Modify the particle sphericity based on the latest experiments.
- Suggest a geometry to tackle the challenges observed in previous generations.
- Apply both uniform and non-uniform inflow patterns.
- Study of the hydrodynamics, chlorine concentration, and particle outflow in all cases.

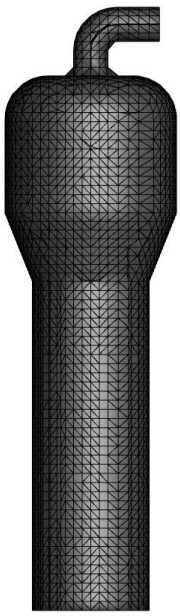

Figure 6.38 Geometry of 2nd generation reactor

To compare the results with the 1st generation reactor, the simulations are based on both reactors with the same overall height and diameter and the exit. The only change is that the reactor's diameter in the region above the dense phase is bigger than the main body. Also, same as before, the effect of change in the pattern of inflow from uniform to non-uniform will be studied. The first simulation (v.2.1) is based on the simulation sheet 05.

6.3.1.1 Simulation and Discussion

As seen in Figure 6.39, the dense bed height in the case with the uniform flow is higher than the other, and dense beds have a considerable amount of solid rigid regions. Comparing Figure 6.40 and Figure 6.41 shows that, same as before, there is a fluid escape in both cases.

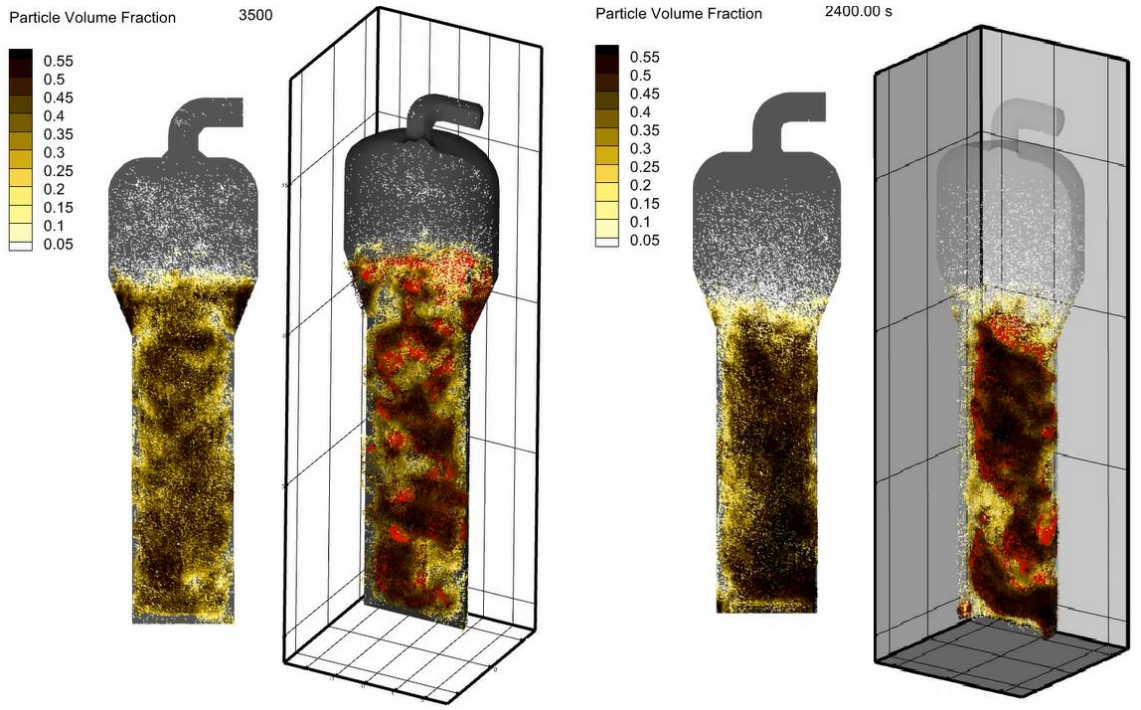

Figure 6.39 Particle distribution through the reactor with the uniform flow (left), non-uniform flow (right).

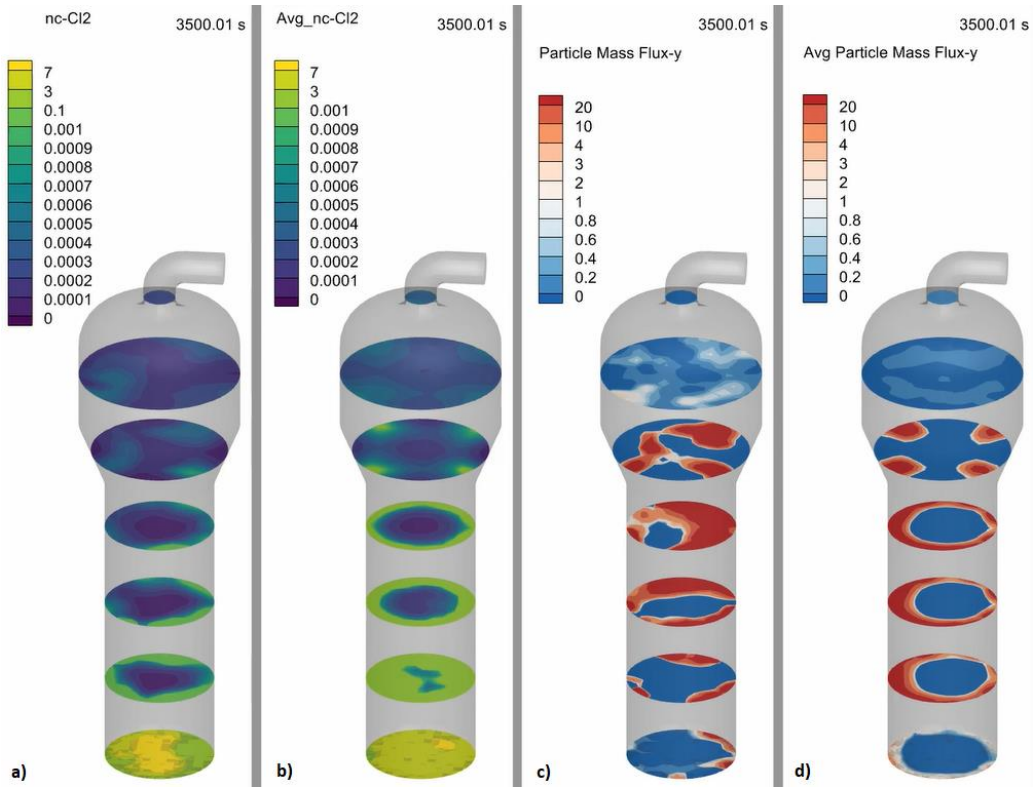

Figure 6.40 Cl_2 concentration (mole/m^3) and particle mass flux (kg/sm^2) in different heights when the inflow is uniform, a) Cl_2 concentration at the specific time, b) Average Cl_2 concentration in the last 300 seconds, c) Particle mass flux at the specific time, and d) Average particle mass flux in the last 300 seconds.

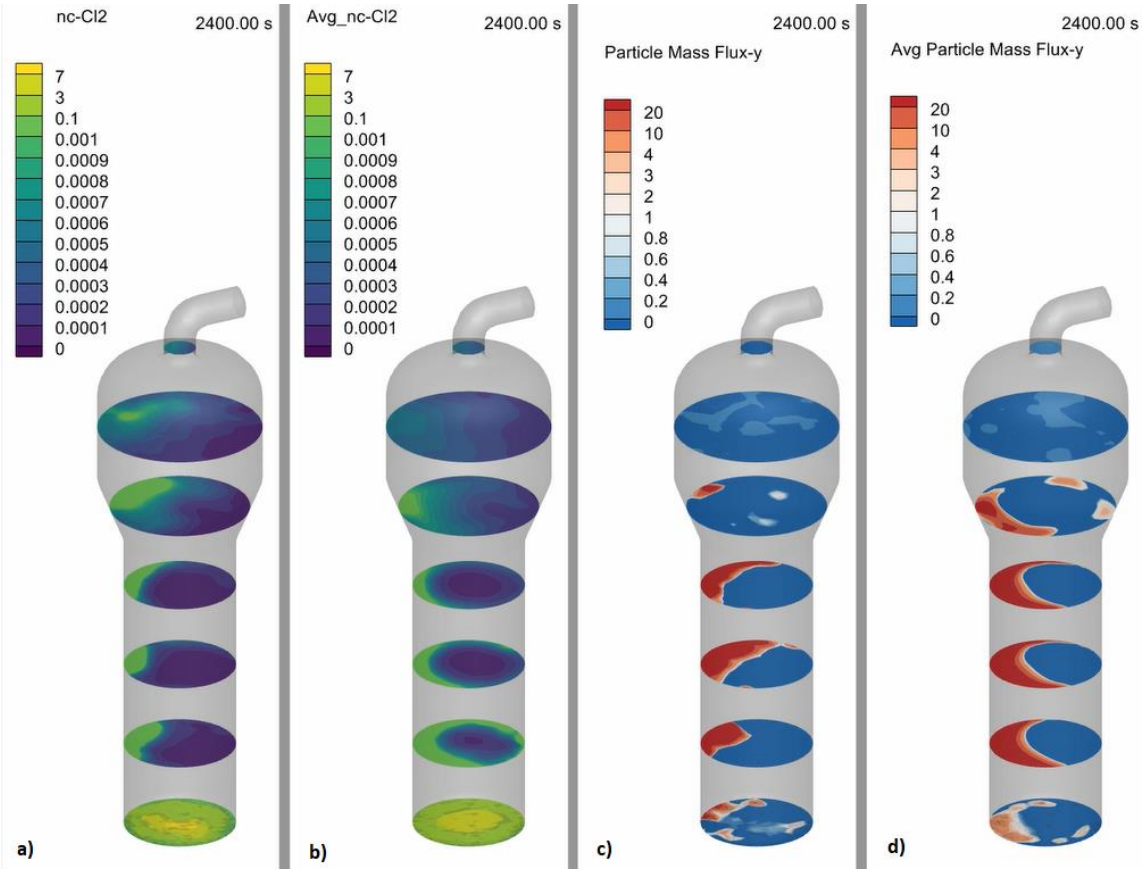

Figure 6.41 Cl_2 concentration (mole/m^3) and particle mass flux (kg/sm^2) in different heights when the inflow is non-uniform, a) Cl_2 concentration at the specific time, b) Average Cl_2 concentration in the last 300 seconds, c) Particle mass flux at the specific time, and d) Average particle mass flux in the last 300 seconds.

Up to this point, the result was the same as before, but when it comes to particle escape, a considerable difference is observed. In the first case with the uniform pattern, the average solid outflow has dropped to 0.115 kg/s, which is almost 20 percent of the particle inflow to the reactor. This value has fallen to 0.0004 kg/s in the same period by changing the gas feeding pattern, which is just 0.07% of the inflow. Although this is a small value, the mass of particles leaving the reactor, in the long run, can be enormous and not cost-effective.

In the next step (simulation v.2.2, simulation sheet 06), by changing the dimensions like generation v.1.2, the particle outflow even becomes lower and falls to 0.0002 kg/s which is around 0.02% of the inflow (Figure 6.42).

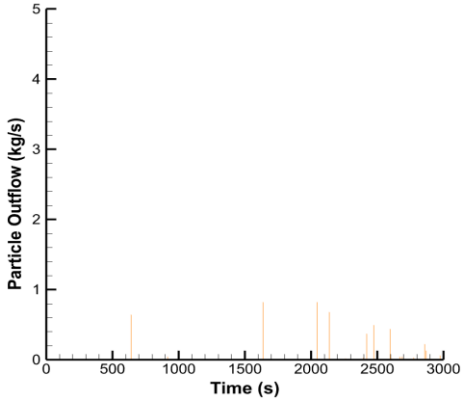

Figure 6.42 Particle outflow (kg/s) in reactor v.2.2

Figure 6.43 and Figure 6.44 illustrate the particle distribution through the reactor and the chlorine concentration and particle flow information at different levels.

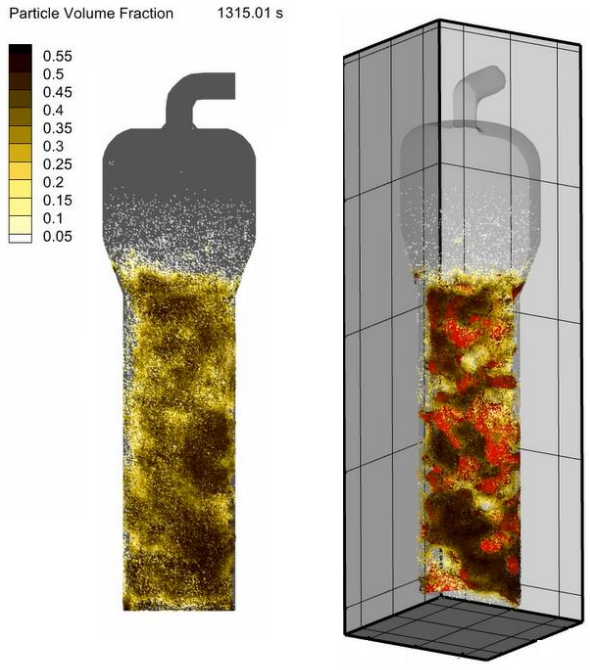

Figure 6.43 Particle distribution through the reactor v.2.2

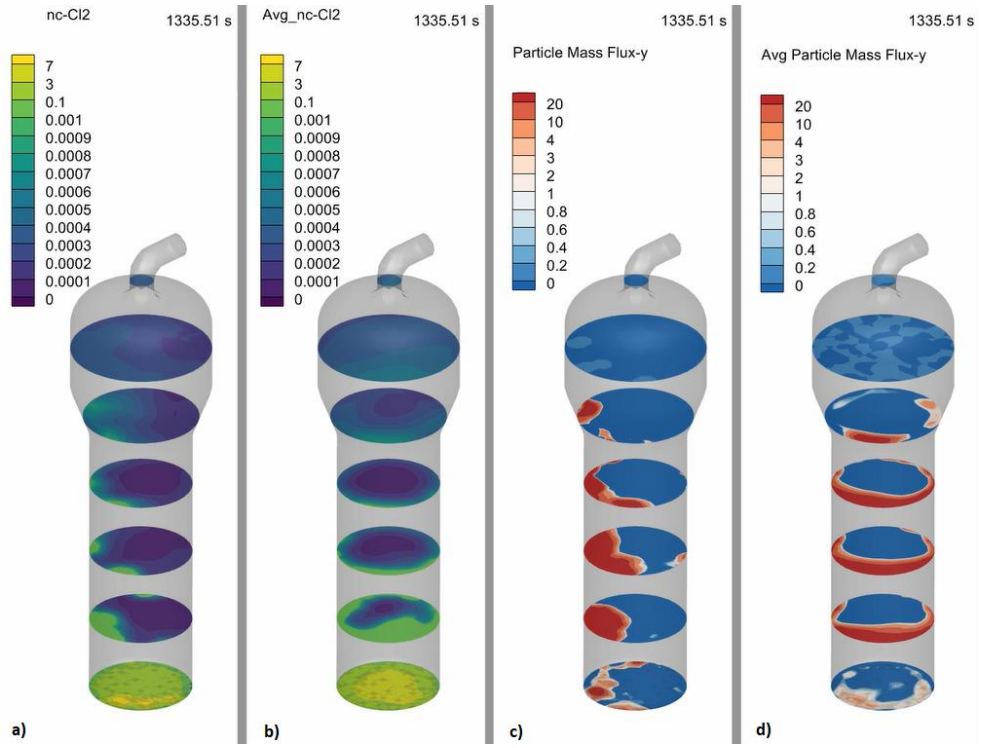

Figure 6.44 Cl_2 concentration (mole/m^3) and particle mass flux (kg/sm^2) in different heights when the inflow is non-uniform, a) Cl_2 concentration at the specific time, b) Average Cl_2 concentration in the last 300 seconds, c) Particle mass flux at the specific time, and d) Average particle mass flux in the last 300 seconds.

6.3.1.2 Conclusion

By changing the reactor's geometry, it increases the cross-sectional area of the reactor. Because of that, the superficial velocity of the fluid decreases, and generated drag forces on the particles are not strong enough to exit the particles. On the other hand, changing the inflow pattern from a uniform distribution to a non-uniform decreases the particle outflow significantly. It is essential to consider that although a tiny particle flow rate has been reported at a steady state. However, the simulation time should be increase as much as possible to have more accurate data.

Besides these advantages, the current generation of reactor model suffers from the possibility of high agglomeration and caking phenomena (on sidewalls), and it seems the slope and height of the middle region of the reactor affect this. On the other hand, although the non-uniform pattern has shown remarkable results, the hydrodynamics of the reactor can still be improved. In the next generation, to achieve better hydrodynamics and minimizing the channeling effect, not only the slope and height of the conic region of the reactor can be modified, but also some changes in other parts of the reactor are studied.

6.3.2 3rd Generation

As concluded in the 2nd generation of the reactor, the geometry with a bigger top showed an outstanding result regarding particle outflow, but the hydrodynamics inside the reactor still needs more improvement. In the present study, the effect of two changes in geometry will be investigated. The first change is using a conical non-uniform distributor at the bottom of the reactor, and the second is adding two lines of the internal ring to the main body of the reactor. To do this, several simulations based on the geometry of the 2nd generation have been set as below.

Simulation Objectives:

- Set a simulation (v.3.1) based on the simulation sheet 06[19] by adding a non-uniform conical distributor.
- Set a simulation (v.3.2) based on the simulation sheet 06 by adding two internal rings with flat and uniform distribution.
- Set a simulation (v.3.3) based on the simulation sheet 06 by adding two internal rings with the non-uniform flat distribution.
- Set a simulation (v.3.4) based on simulation sheet 06 by adding two internal rings and a non-uniform conical distributor.
- Modifying the geometry by changing the transient section angel.
- Study of the hydrodynamics, chlorine concentration, and particle outflow in all cases.

Theoretically, using a non-uniform flow conical geometry helps circulate the particles in the dense bed more effectively, and the internal rings disturb the escape of the fluid near the wall by creating more resistance. Figure 6.45 shows a schematic of these systems. In the present study, it will be investigated that how much of these changes are effective in the current reactor design.

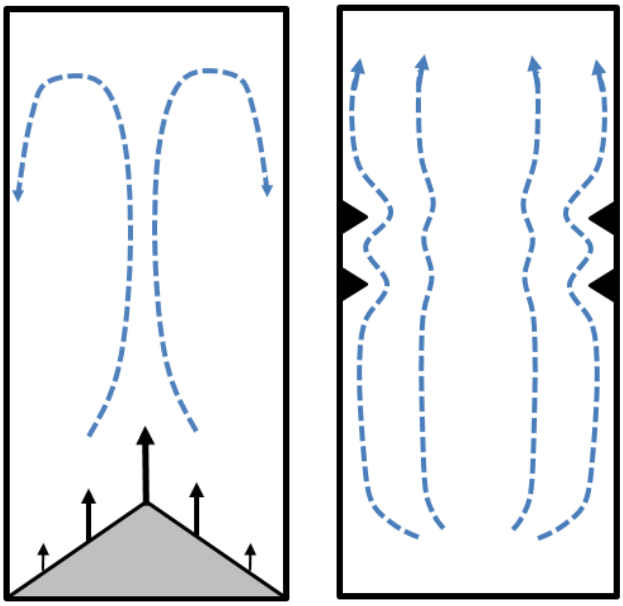

Figure 6.45 Non-uniform conical distributor (left) and Internal rings (right)

The simulations start with the reactor with non-uniform conical distribution (v.3.1). In the same manner, as before, it starts with adding and meshing the geometry. Figure 6.46 shows the geometry of this reactor. All other parameters and settings have been kept the same as simulation v.2.2 (simulation sheet 06).

[19] is given in Appendix B

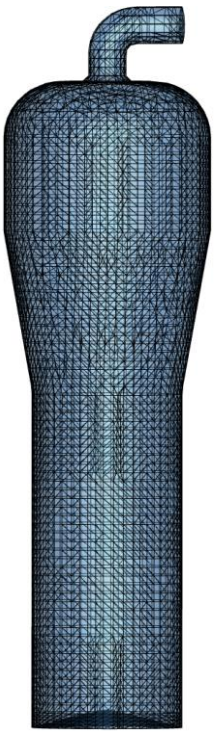

Figure 6.46 Geometry of reactor v.3.1

6.3.2.1 Results and Discussion

As seen in Figure 6.47, fluid movement is closer to the center of the reactor instead of escaping through the wall, and this is due to having the non-uniform flow pattern with conical geometry instead of a flat distributor.

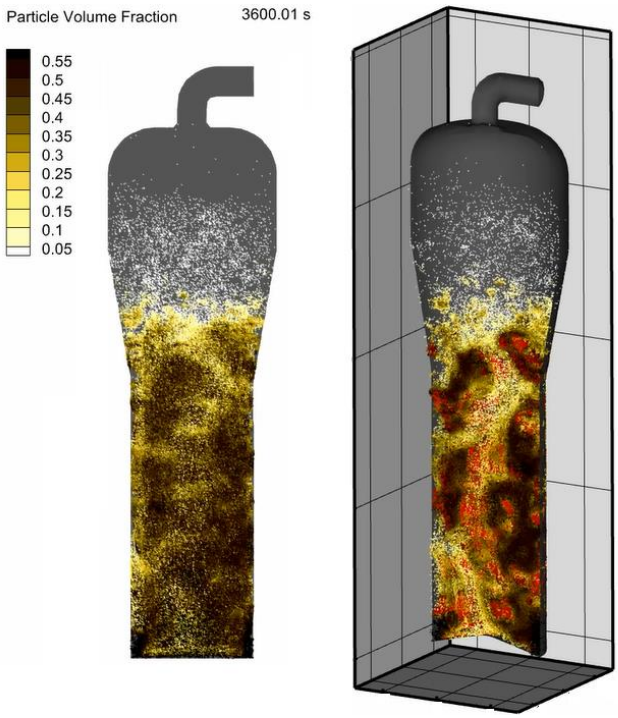

Figure 6.47 Particle distribution through the reactor v.3.1

Figure 6.48 gives more precise data about the overall movement of the fluid inside the reactor. This regime is much better than before because in all previous models, even in the fifth level, there was considerable flow, but in this model, it is up to the fourth level. On the other hand, the red area, which belongs to high solid flux, is much smaller and homogeneous in this regime. Now, let see what has happened to the particle outflow. The average results show that the particle outflow from the reactor is even lower than before. The value is about 0.0001 kg/s which is almost negligible.

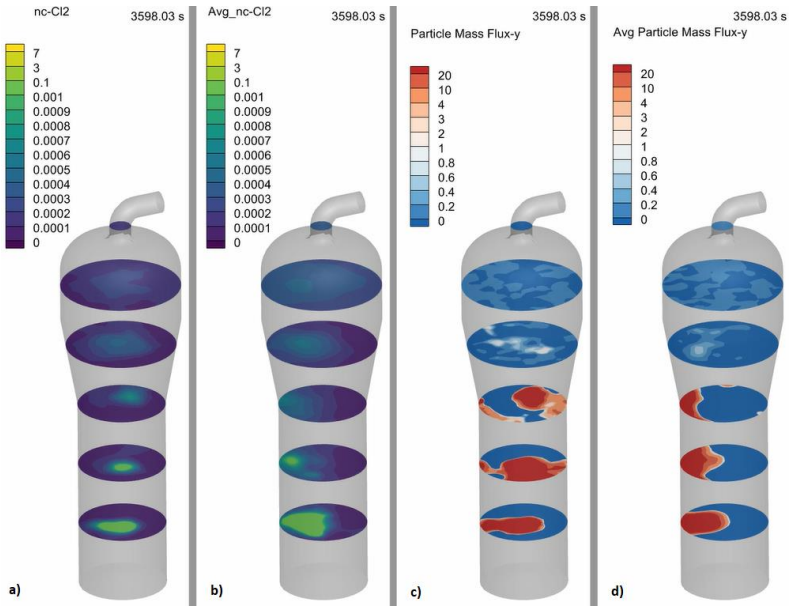

Figure 6.48 Cl_2 concentration (mole/m^3) and particle mass flux (kg/sm^2) in different heights when the distribution is non-uniform with conical geometry, a) Cl_2 concentration at the specific time, b) Average Cl_2 concentration in the last 300 seconds, c) Particle mass flux at the specific time, and d) Average particle mass flux in the last 300 seconds.

Now, it is time for the second step, studying the effect of the ring on the hydrodynamics inside the reactor. As mentioned in the simulation objectives, this simulation includes two different cases. The first one is a ringed reactor with uniform and flat distribution (v.3.2), and the second one is a reactor with a non-uniform flat distribution system (v.3.3).

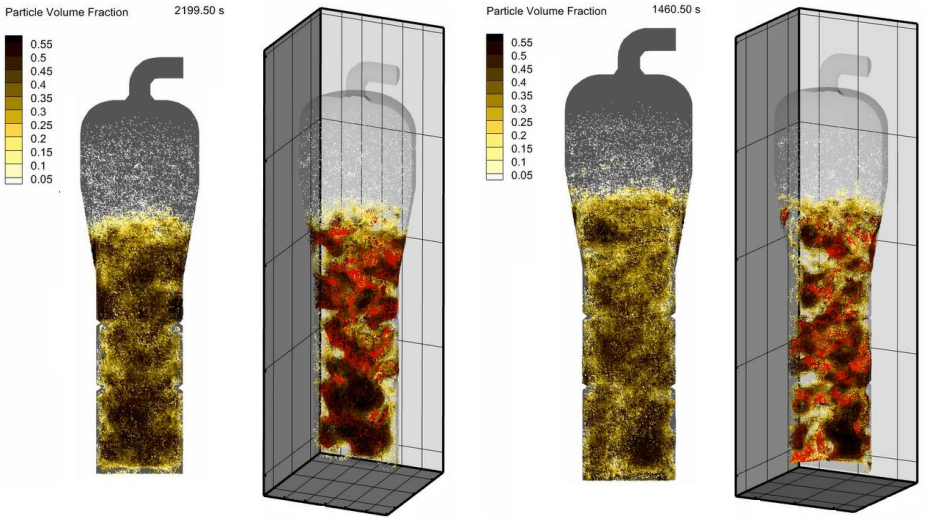

Figure 6.49 Particle distribution through the reactor v.3.2 with uniform flat distribution (left), and non-uniform flat distribution v.3.3 (right)

Taking Figures 6.50 and 6.51 into account, it can be observed that this change seems to have no positive effect on the escape of fluid through the reactor wall.

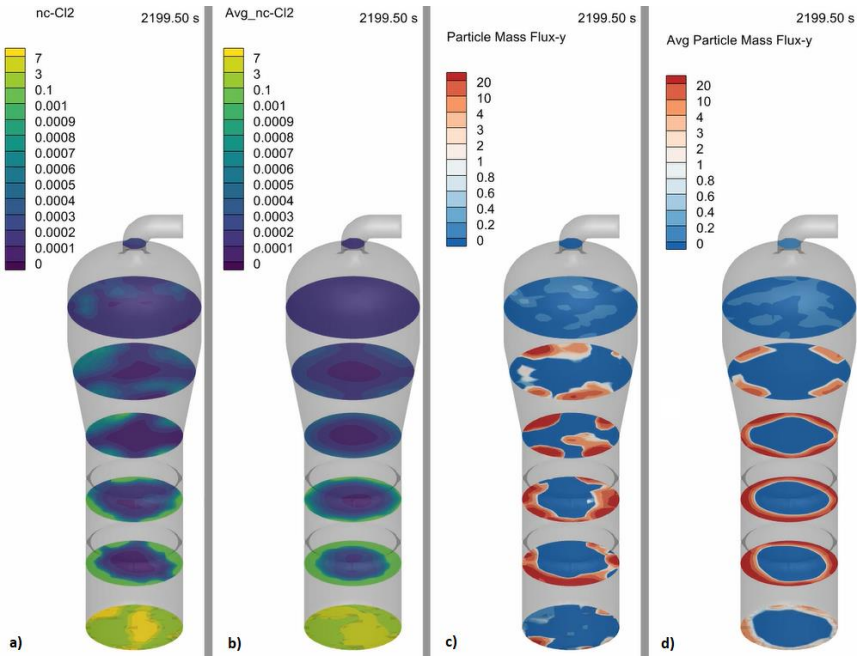

Figure 6.50 Cl_2 concentration (mole/m^3) and particle mass flux (kg/sm^2) in different heights when the distribution is flat-uniform (v.32), a) Cl_2 concentration at the specific time, b) Average Cl_2 concentration in the last 300 seconds, c) Particle mass flux at the specific time, and d) Average particle mass flux in the last 300 seconds.

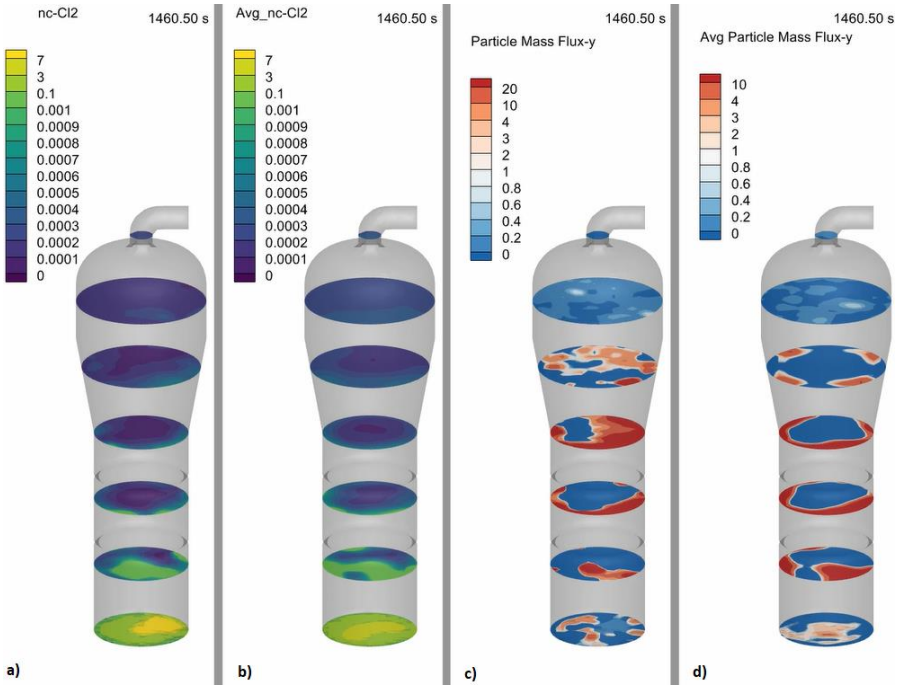

Figure 6.51 Cl_2 concentration (mole/m^3) and particle mass flux (kg/sm^2) in different heights when the distribution is flat and non-uniform (v.3.3), a) Cl_2 concentration at the specific time, b) Average Cl_2 concentration in the last 300 seconds, c) Particle mass flux at the specific time, and d) Average particle mass flux in the last 300 seconds.

In the last attempt (reactor v.3.4), both changes are applied to the geometry simultaneously (Figure 6.52) based on simulation sheet 06.

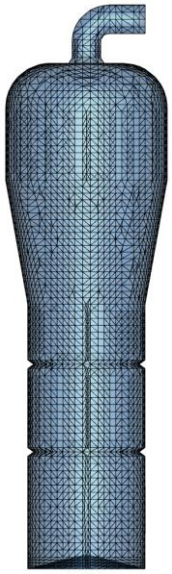

Figure 6.52 Geometry of the reactor (v.3.4)

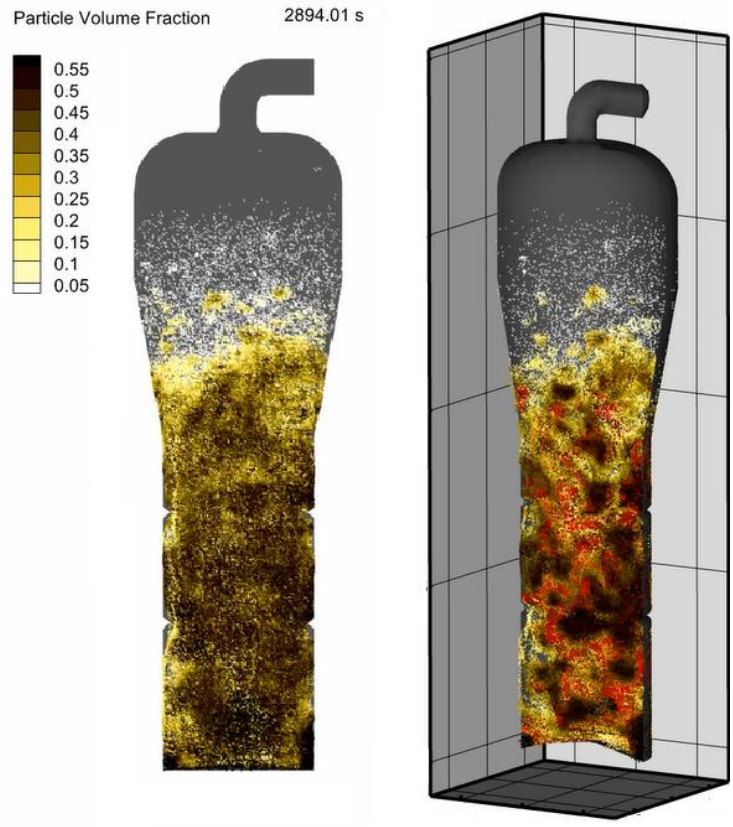

Figure 6.53 Particle distribution through the reactor v.3.4

The hydrodynamics in Figure 6.53 shows that the fluid escape through the wall is the minimum compared to previous models and the internal rings are working as expected.

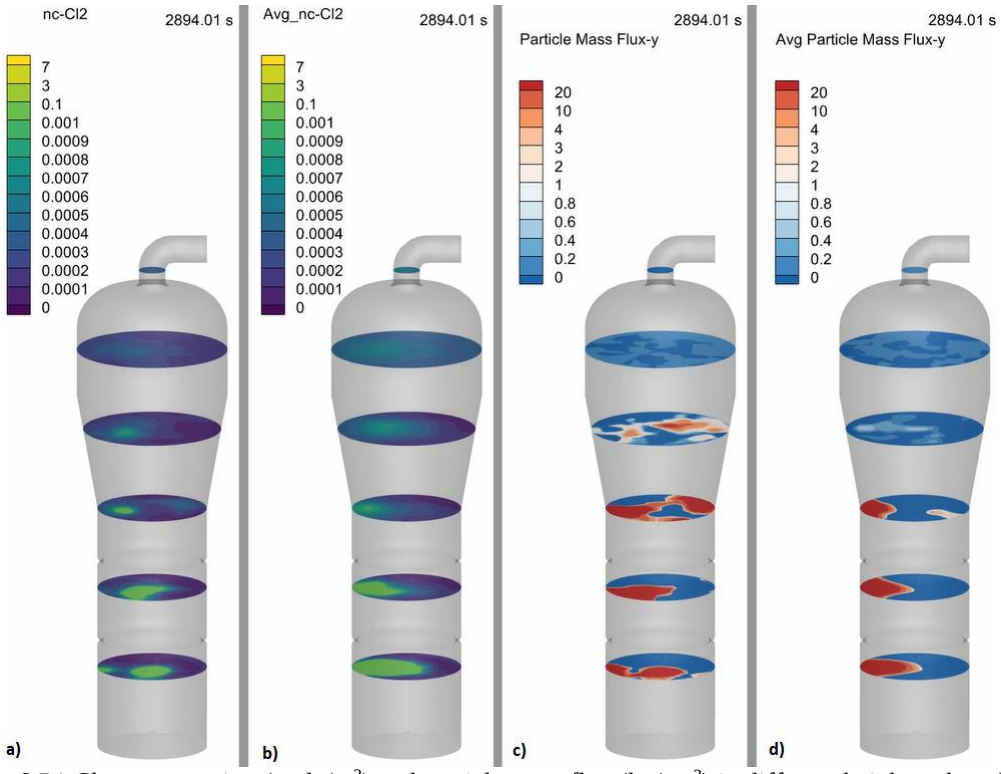

Figure 6.54 Cl_2 concentration (mole/m^3) and particle mass flux (kg/sm^2) in different heights when the distribution is non-uniform with conical geometry, and the main body has two internal rings, a) Cl_2 concentration at the specific time, b) Average Cl_2 concentration in the last 300 seconds, c) Particle mass flux at the specific time, and d) Average particle mass flux in the last 300 seconds.

Compared with old generations, the reactor shows a remarkable performance to reduce the particle outflow (0.0002 kg/s), which the lowest among all generations. On the other hand, Figure 6.53 and 6.54 confirm better hydrodynamics because the red/green areas with the higher fluxes are minimum in this reactor.

6.3.2.2 Conclusion

In comparison with generation 2, the change in slope of the middle part of the reactor and modifying the heights led to minimizing the agglomeration effect in the top area of the reactor and particle escape from the reactor. On the other hand, adding the internal rings and conical distributor simultaneously significantly affected particle outflow and hydrodynamics inside the reactor. The rings change the direction, and the conical distributor helps to avoid escaping the fluid through the wall.

6.4 Complete Model with Cyclone

In the previous simulation, the optimization in geometry let to reach better hydrodynamics and minimum particle outflow. As mentioned earlier, this low particle scape (almost negligible), however, may change in the very long run in the real system. Therefore, to prevent any particle escape from the reactor, a separation unit (cyclone) is added. Among the mechanisms discussed in section 0, the cyclone is the best solution in this case. Following the procedure in section 5.2.3.2 and applying the boundary condition, the dimensions of the cyclone have been calculated (simulation sheet 07 - Appendix B).

Simulation Objectives:

- Design the complete geometry (reactor and cyclone) based on the cyclone's calculated dimensions.
- Simulate (v.4) the cyclone based on simulation sheet 07.
- Calculate the proficiency and compare it with the nominal one.
- Study the particle size distributions in boundaries.
- Study the pressure drop in the system.

As seen in Figure 6.55, there is a significant difference in size between the reactor and the cyclone. This is because of a relatively low superficial velocity in the system, and the information in Table 5.3 confirms this.

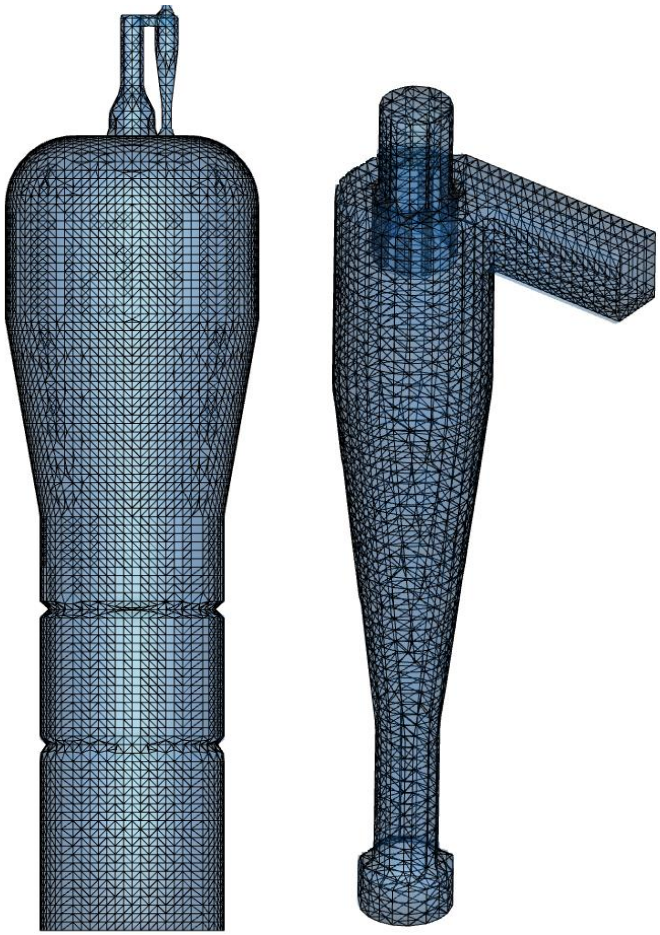

Figure 6.55 Cyclone (right), Assembled cyclone on top of the reactor v.4 (left)

6.4.1 Simulation and Discussion

Figure 6.56 gives the information about particle mass flow rate (kg/s) in the inlet. The mass inflow to the system has been assumed half of the particle inflow to the reactor, which is 0.3 kg/s. Barracuda® assumes this value as an average and applies the dynamic inflow with the average of 0.3 kg/s.

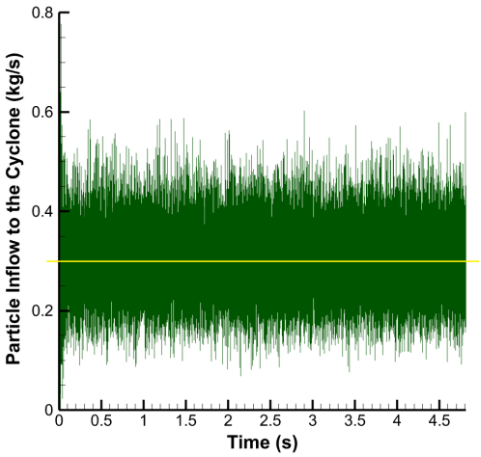

Figure 6.56 The mass flow pattern set to enter the cyclone (kg/s)

Figure 6.57 shows a snapshot of the cyclone simulation. As it clear, most of the particles leave the system from the bottom. The average cyclone efficiency can be calculated by dividing the average particle mass flow rates between the bottom and the inlet.

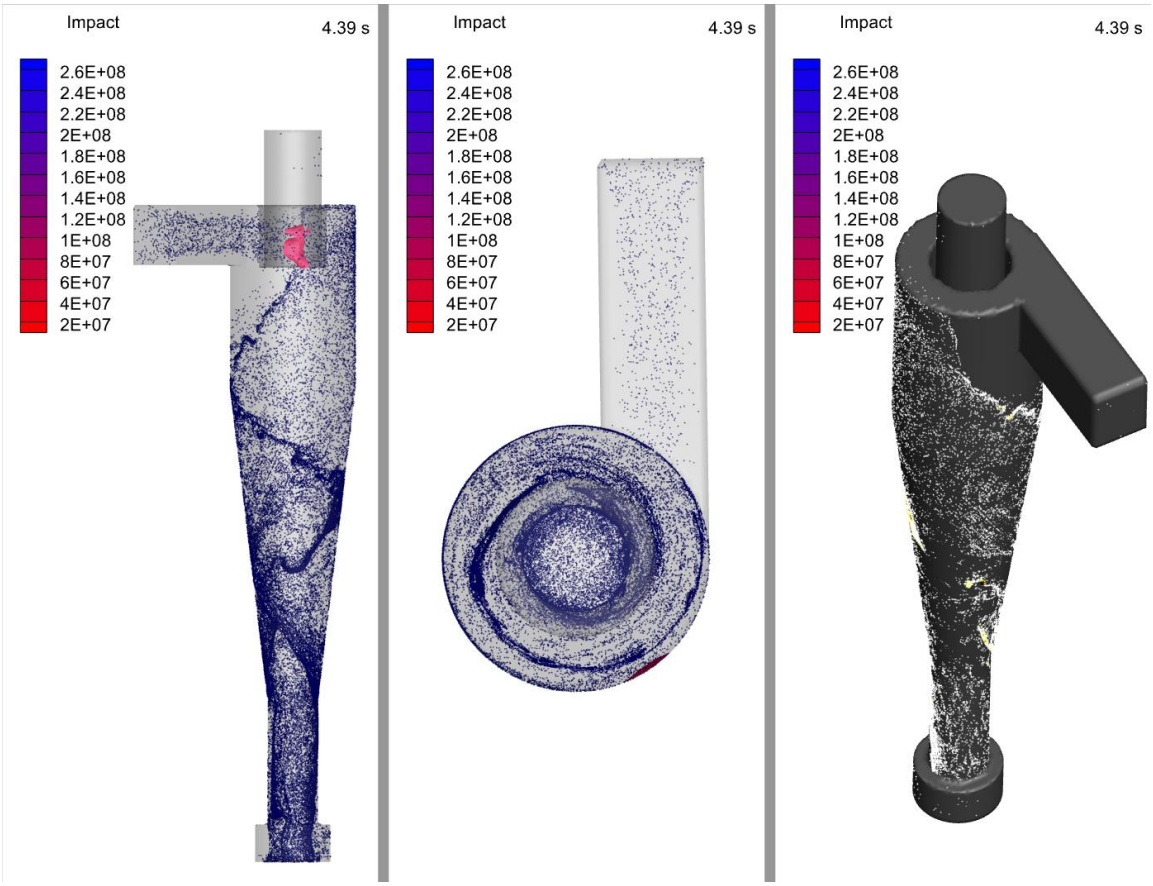

Figure 6.57 Particle movement inside the cyclone

Figures 6.58 and 6.59 show the particle outflow from the cyclone's bottom and top (with an average of 0.28597 and 0.008284 kg/s), respectively. This gives the average cyclone efficiency about 97.2%. While the design was based on the high-efficiency cyclone with 0.99% of efficiency. (The negative values show the direction of the flow to the outside of the system)

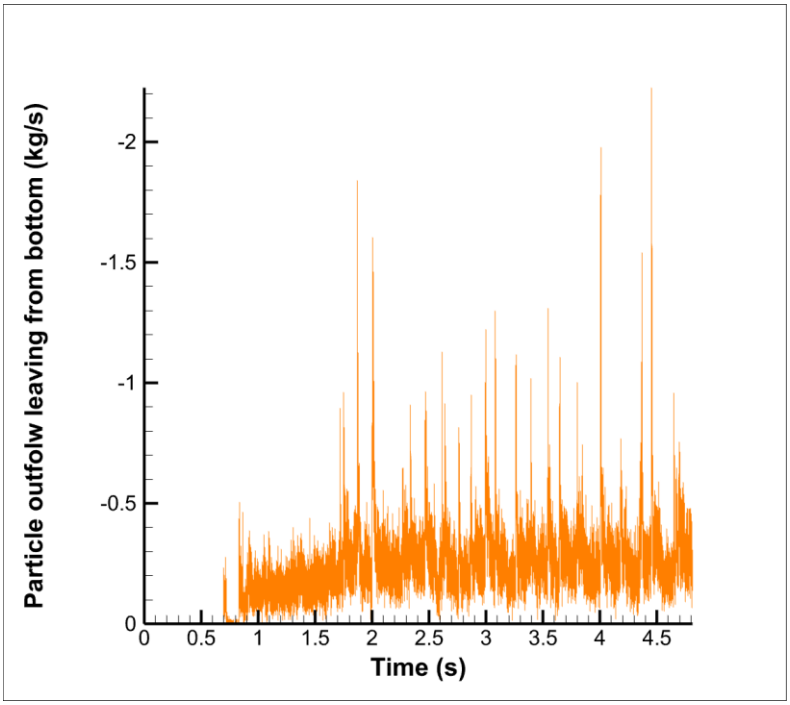

Figure 6.58 Mass flow rate (kg/s) of the particles leaving the system from the bottom (separated)

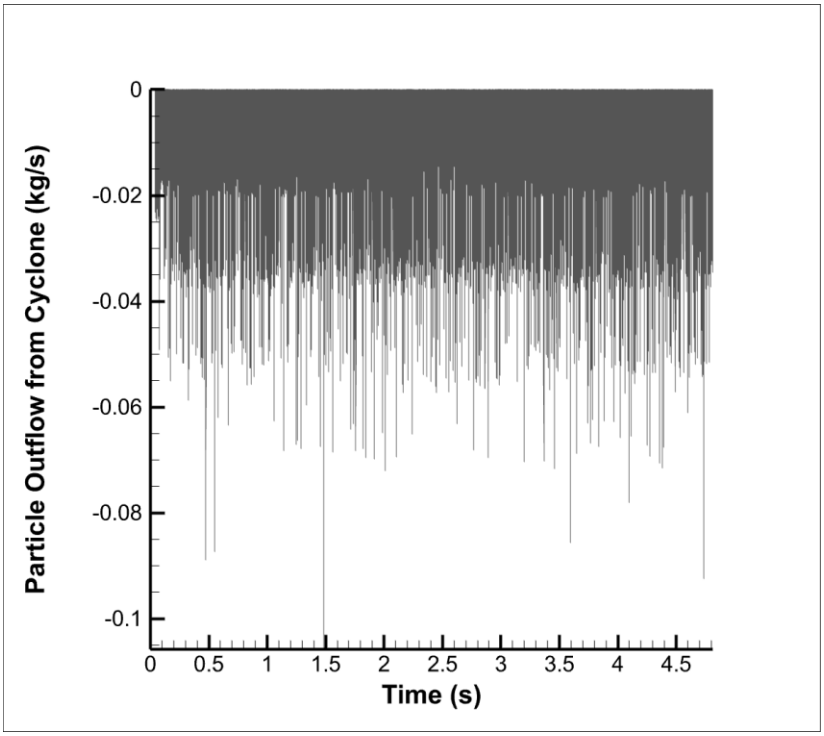

Figure 6.59 Mass flow rate (kg/s) of the particles leaving the system from the top (escaped)

Base on the information from previous simulations, the size distribution of leaving particles is as Figure 6.60. The minimum and maximum particle radiuses are 0.2 and 12.5 microns, respectively. The rage has been divided into 20 intervals uniformly.

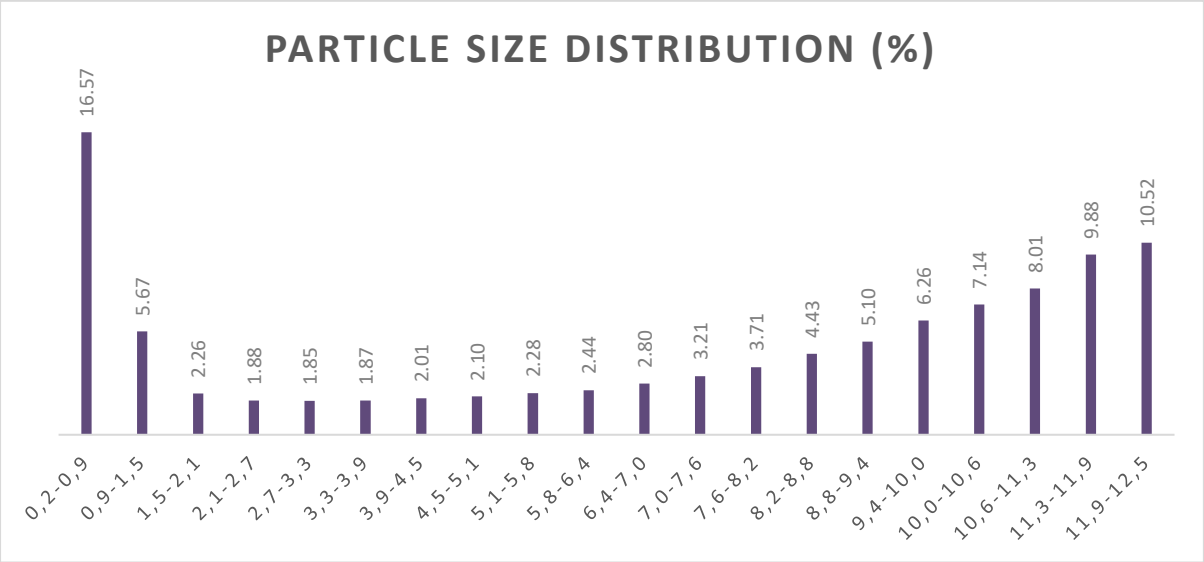

Figure 6.60 Particle size distribution (defined in the inlet)

The particle size distribution in the outlet and top of the reactor is based on Figure 6.61. As expected, almost all bigger particles were captured and left from the bottom, and very fine particles (the radios below 1 micron) can escape from the top. These particles can be captured by other units such as filters or ESPs. Figure 6.62 illustrated the distribution of the captured particles.

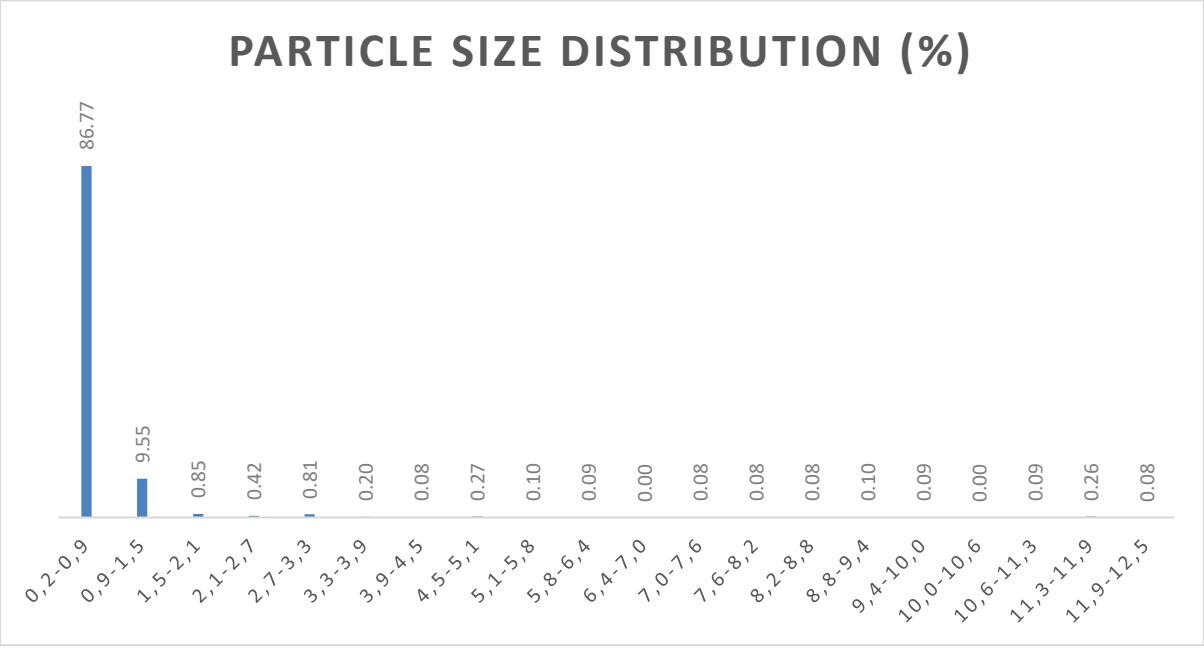

Figure 6.61 Particle size distribution (escaped from the top of the cyclone)

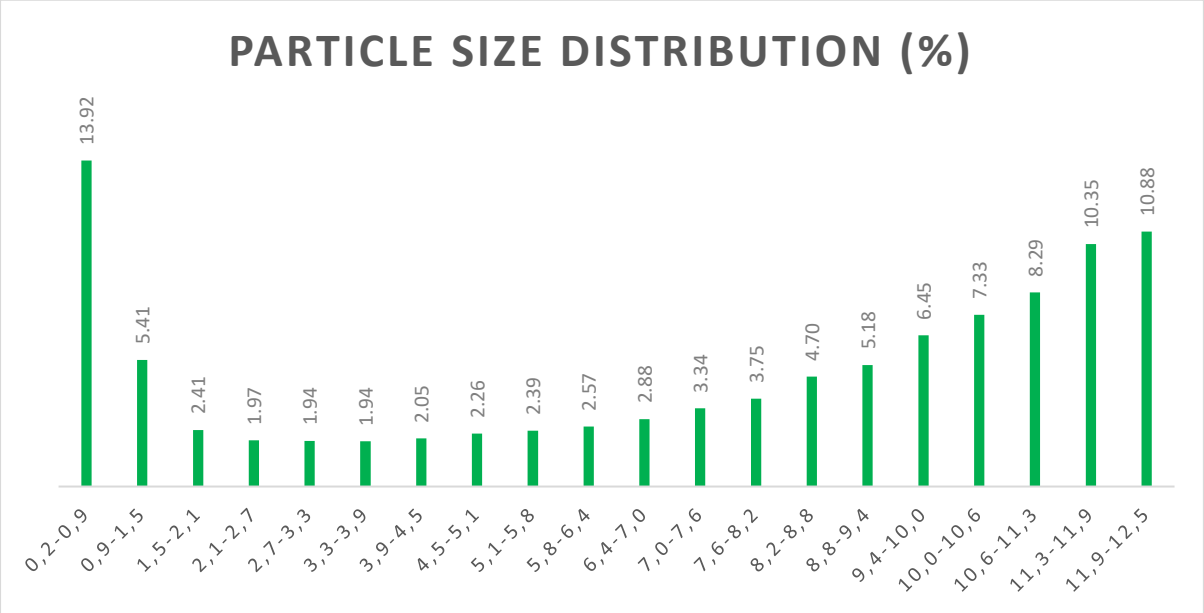

Figure 6.62 Particle size distribution (captured and leaving from bottom)

In simulation v.4, the particle duty entered into the system has been set to 0.3 kg/s. However, what happens if this rate changes? According to Table 5.3, by increasing the particle duty, the cyclone's efficiency will increase, and after a certain point it will start to drop. By investigating this with the CPFD simulation, the following results have been observed (Table 6.4).

Table 6.4 Cyclone efficiency in different particle concentrations

Particle duty Kg/s	Particle Escape kg/s	Efficiency %
0.01	0.000441	95.6
0.05	0.002676	94.6
0.1	0.005447	94.6
0.2	0.007239	96.4
0.3	0.008284	97.2
0.4	0.011694	97.1

6.4.2 Conclusion

Because of the low superficial velocity in the reactor, the size of the cyclone is considerably smaller than the reactor. Although the initial geometry calculation of the design was based on 99% efficiency, Barracuda® simulation shows that the efficiency would be slightly lower (around 97%). This is due to assuming the 0.3 kg/s inflow of particles.

By increasing the solid feeding rate, the efficiency of the cyclone increasing up to a certain point and then starting to decrease again. This does not mean that the higher particle duty is better because when there is lower particle inflow, the particle escape will be less in practice. Therefore, the effort to minimize the particle outflow was utterly efficient.

6.5 Thermal Model

The current simulation work aims to study heat transfer between reactive materials in an industrial FBR reactor (dedicated for alumina chlorination) and its wall. To maintain the pseudo steady state, the heat produced from exothermic reactions must be transferred outside the reactor (cooling). Further investigations are done on temperature gradient and its variations through the height of the reactor.

Simulation Objectives:

- Simulate the reactor v.5 (simulation sheet 08-Appendix B) under thermal condition.
- Find the good physical and chemical properties of base materials.
- Study the heat transfer gradient through the reactor.
- Study all heat transfer mechanisms.
- Compare the result with Gibbs reactor calculations in Aspen Plus®

All needed parameters have been set according to the equations in section 4.2.3. All the base material properties used in the simulations are given in Appendix A.

6.5.1 Simulation and Discussion

In Barracuda®, the thermal wall of a model applies a user-defined temperature to the reactor wall. Energy can be transferred in and out of the model via the reactor wall depending on the temperature in between the wall and the fluid near the wall.

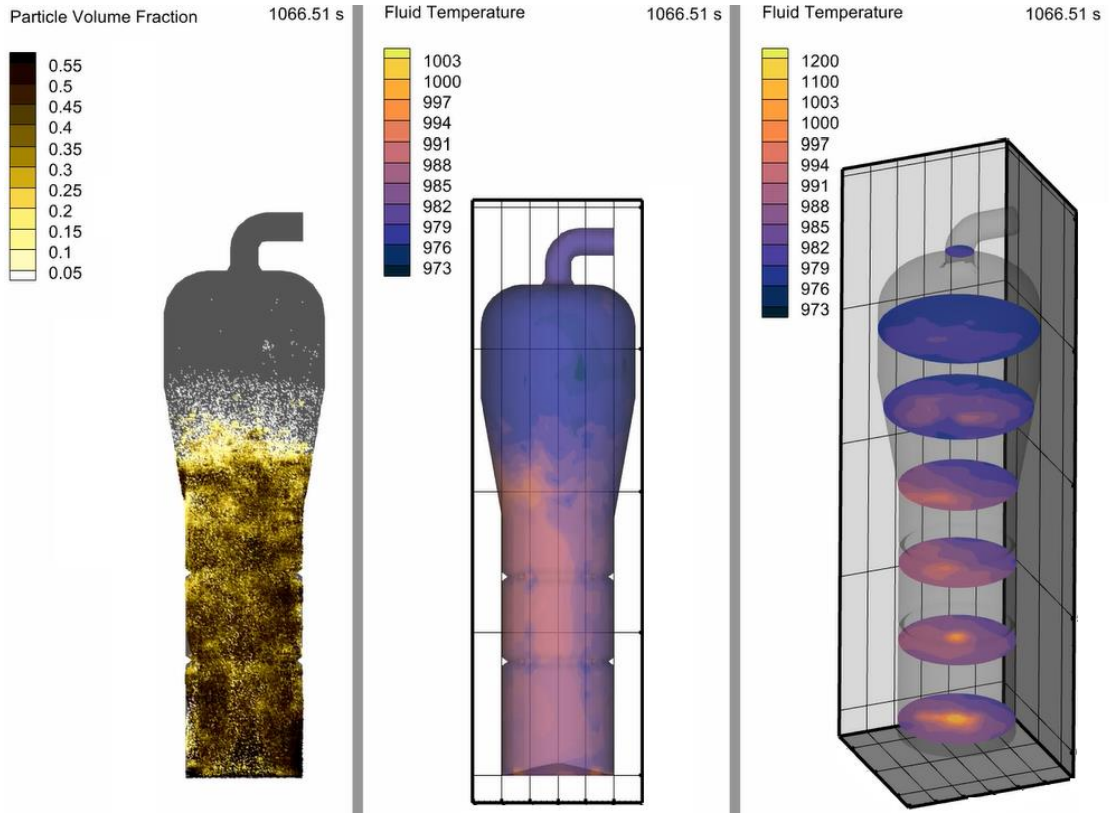

Figure 6.63 Particle and heat distribution through the reactor v.5

In the current alumina chlorination reactor, the operational temperature is maintained at around 700℃. Although thermal wall boundary condition keeps the wall temperature 700℃, the temperature inside the reactor, even at pseudo steady-state, is not constant (see Figure 6.63).

The average cooling required for the reactor to maintain steady thermal conditions (at 700℃) is about 1.82 MW (Figure 6.64). Theoretically, this heat transfer cannot be distributed uniformly through the reactor because almost all the reaction occurs at the bottom of the reactor, and all the heat should be generated there. The reactor wall has been divided into seven sections to see how the heat duty distribution through the reactor is. Figure 6.65 and Figure 6.66 show two different heat transfer mechanisms in all sections separately (convective and radiation, respectively).

Figure 6.64 Total heat transfer to the environment

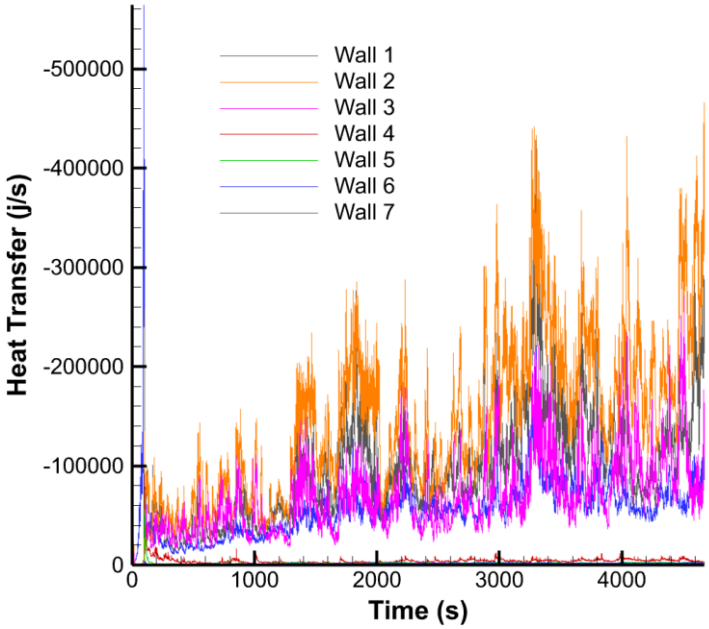

Figure 6.65 Convective Heat transfer in different walls

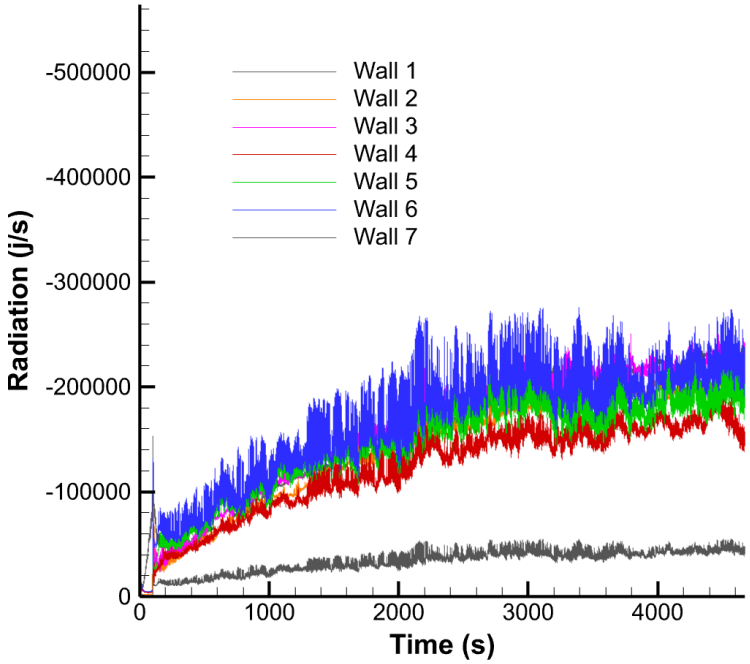

Figure 6.66 Radiation in different walls

Most of the heat transfer from inside the reactor to the wall belongs to the radiation. As seen in Figure 6.67, neglecting wall 7 (because of low surface area compared with other walls), the heat transferred to all the walls by radiation are almost the same, but in convective heat transfer, in the last three sections, the heat transfer is negligible. Taking both heat transfer mechanisms into account, the overall heat transfer is highest in the third section of the reactor.

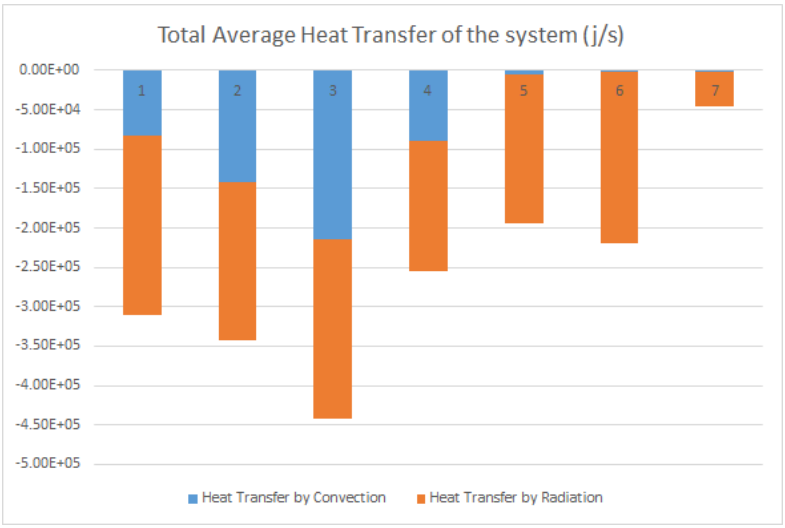

Figure 6.67 Both Heat transfer mechanisms in wall 1-7

At pseudo steady state, the total heat transfer to the system is about 1.74 MW which, in comparison with Gibbs reactor simulation in Aspen Plus, is in an acceptable range. Figure 6.68 shows the calculated heat duty of this reaction in the Gibbs reactor simulation. 1.62 KW has been handled to keep the reactor isothermal. Without using any heat exchangers, this duty jumps the reactor temperature up above 1420°C, which is relatively high for this process.

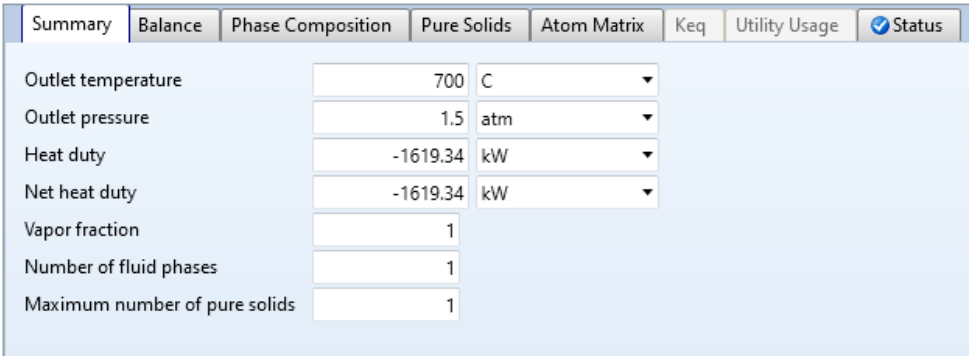

Figure 6.68 Heat duty of the reaction using Gibbs reactor in Aspen Plus®

6.5.2 Conclusions

Design an exothermic reactor with an efficient heat transfer performance is probably the most critical task from an engineering point of view. The efficiency of the reaction is highly affected by temperature. The Gibbs reactor simulation in Aspen Plus® validates the heat transfer calculated in thermal analysis by CPFD simulation. At the steady-state, the reactor temperature range is 700-780℃.

6.6 Extended model applying impure alumina

As discussed in section 3.2, alumina is one of the most widely used pure chemicals on the market today, with annual production totaling millions of tons of highly pure alumina. A large portion of this output is used to make aluminum, but a growing amount is used in ceramics, refractories, catalysts, and other various products. In nature and different thermal conditions, alumina is found in different phases. These phases can be transformed into each other in different temperatures. Among these, γ-alumina is used in the chlorination process in the aluminum production industry because of the higher reaction rates. α-Alumina has outstanding mechanical properties and superb thermal properties at high temperatures; polycrystalline α-alumina is used as a structural ceramic. As a result, this type has much lower reaction rates in the chlorination process. In the previous studies, the chlorination of the pure γ-alumina has been taken into account. The given alumina composition (see section 3.5) shows almost 7 percent of the sample in α-alumina. The present study aims to study the reaction conversion and composition of leaving particles with the CPFD simulation in the presence of α-alumina. To do this, considerable amount of particle outflow is needed. Hence, reactor v.2 with a uniform inflow pattern and the particle outflow of 0.115 kg/s has been chosen between different reactor generations. (see section 6.3.1.2)

Simulation Objectives:

- Simulate reactor v.6 based on the simulation sheet 06 (Appendix B).
- Defining the α-Alumina with same size distribution as γ-alumina with envelope mass density of 2600 kg/m^3 (which is higher than the γ-alumina's mass density)
- Changing the 7 percent of the initial bed to α-Alumina
- Dedicating the 7 percent of particle inflow to α-Alumina
- Defining the proper reaction rates regarding α-Alumina
- Study the bed's hydrodynamics
- Study the composition of the particles escaping the reactor.

6.6.1 Simulation and Discussion

The reaction rate has been set using the information in sections 3.4 and 3.5. The chlorination reaction for α-alumina is much slower than the γ-alumina. On the other hand, because of their different densities, the behavior of them may be different. The different components in the initial bed have been defined as Figure 6.69.

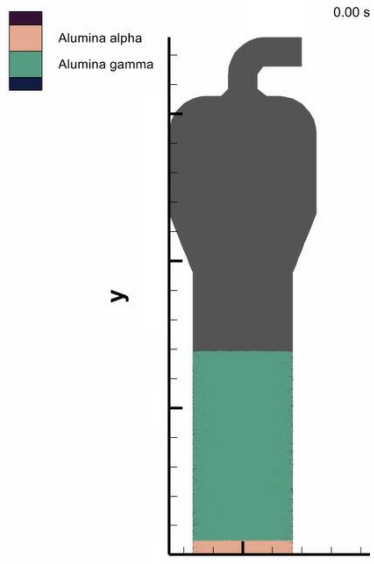

Figure 6.69 Alpha and gamma-alumina in the initial bed

Figure 6.70 shows the alpha and gamma-alumina particle distribution through the reactor. However, because of the densification, α-alumina is relatively heavier than the γ-alumina; in steady-state, it has been distributed homogeneously.

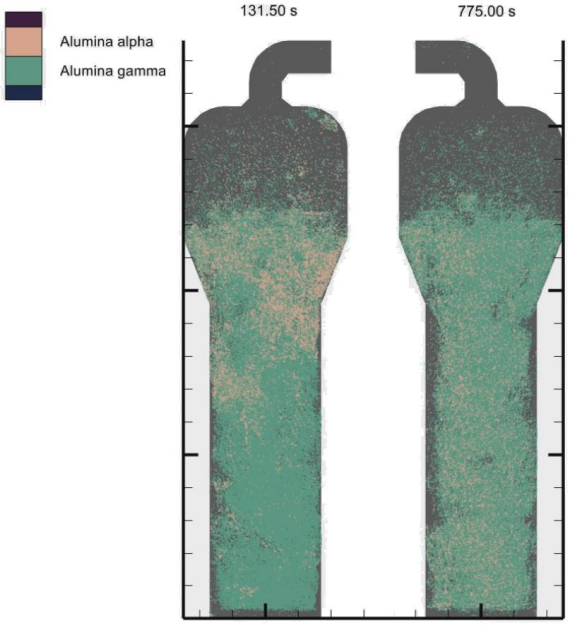

Figure 6.70 Different types of alumina particle's distribution after fluidization (left) in steady-state (right)

Relevant data of the particle outflow is given in Figure 4.2. The average escaping rate of α-alumina particles has been recorded as 6 g/s. In comparison, the corresponding value for γ-alumina is observed as 150 g/s. This clearly confirms that the α-alumina may not easily leave the system because of the higher density.

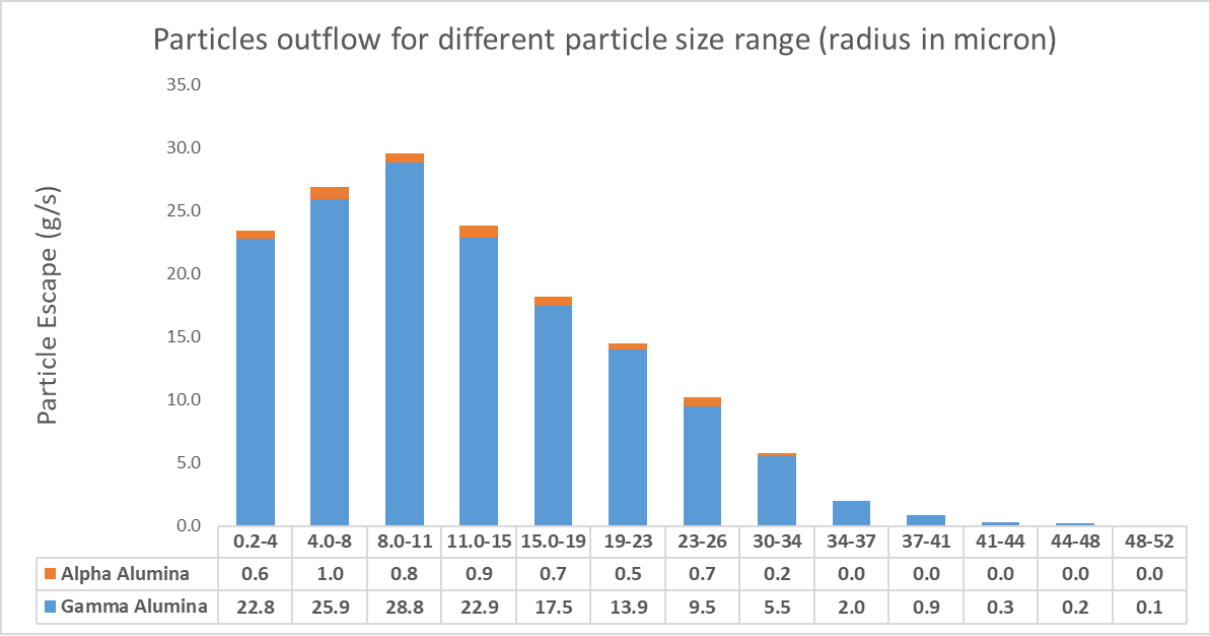

	0.2-4	4.0-8	8.0-11	11.0-15	15.0-19	19-23	23-26	30-34	34-37	37-41	41-44	44-48	48-52
Alpha Alumina	0.6	1.0	0.8	0.9	0.7	0.5	0.7	0.2	0.0	0.0	0.0	0.0	0.0
Gamma Alumina	22.8	25.9	28.8	22.9	17.5	13.9	9.5	5.5	2.0	0.9	0.3	0.2	0.1

Figure 6.71 Total heat transfer to the environment

Figures 6.71 and 6.72 show the size distribution of the different alumina components leaving the reactor.

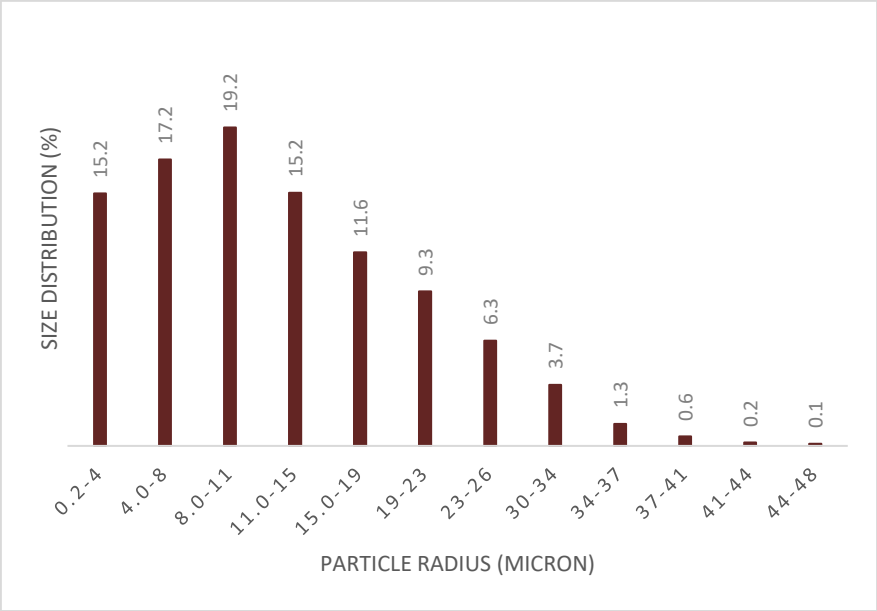

Figure 6.72 γ-Alumina size distribution in the outlet

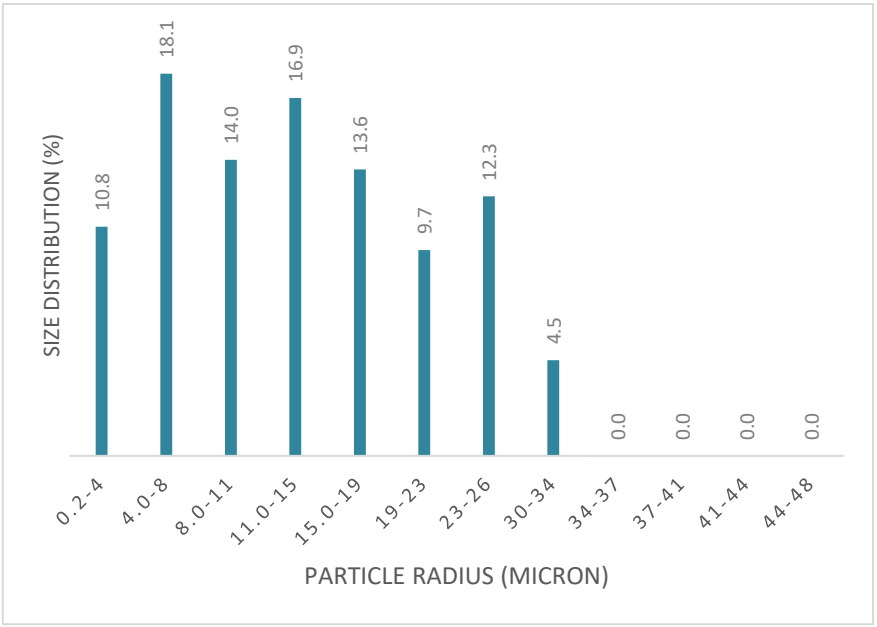

Figure 6.73 α-Alumina size distribution in the outlet

These figures above show that the α-alumina's cut size is smaller than γ-alumina, and this is physically correct because the mass density of γ-alumina is higher than the other component.

6.6.2 Conclusions

The results show that the alumina impurity does not affect the chlorination reaction itself. The overall particle outflow has become slightly higher in the case of pure γ-alumina. Almost only 3 percent of the total particle outflow belongs to α-alumina, and consequently, in the long run, that may cause α-alumina accumulation in the reactor, which is not favorable. In the operating temperature, the reaction rate of α-alumina is much slower, and the accumulation of α-alumina will affect the overall reaction negatively. As remedies, adding a circulation path or speeding up the fluid inside the reactor to a certain point may be helpful, which can be investigated in future works.

7 Conclusion and Future works

The aluminum market expects to grow in the coming years, which means a significant carbon emission. The current dominated method for aluminum production (Hall-Héroult) has already reached its lowest energy consumption and carbon footprint, but still, it is very high. After years, with the help of advanced technologies, it seems the possible alternative methods (specifically, alumina chlorination) become more feasible and practical. The aluminum production using alumina chlorination not only uses much lower energy (direct impact to have lower carbon footprint) but also has some other advantages, such possibility of using alumina with impurities which have an indirect impact on carbon footprint.

The alumina chlorination reaction (exothermic) is taking place in a bubbling fluidized bed reactor. Because of the very high corrosivity of the chlorine and aluminum chloride in very high temperatures, the reactor has no internals for cooling or circulation of particles, making the design more challenging. There were two main parameters studied in the design: chlorine concentration as representative of the reaction conversion rate and particle escape from the system, which should be minimized. Due to the nature of this quick reaction, almost in all cases, the reaction reached the complete conversion. Nevertheless, reducing the particle outflow and having better hydrodynamics inside the bed were the main challenges. The present study includes six different development stages, which start from an iso-thermal simulation of the simple cylindrical geometry to a more sophisticated thermal study of complex geometry. Step by step, by changing the reactor's geometry and gas's inflow pattern, the optimum performance has been achieved.

In the first stage (reactor generation 0), a simple cylindrical reactor has been simulated to study the effect of bed aspect ratio on the hydrodynamics and the reaction. Almost all the Cl_2 are consumed within the first meter of the reactor, which means the current range of bed and reactor height may not be an issue in the actual chlorination process. However, the H/D value inherits a vital role for good hydrodynamics of the reactor. Selecting the reactor specification for good hydrodynamics of the gas-solid fluidized bed reactor is very important.
Too low H/D can cause channeling, and it may reduce the reaction efficiency. As a result, Cl_2 concentration at the reactor outlet may increase. Even a tiny amount of Cl_2 at the outlet could cause problems if there is not a purification process on Cl_2. Simultaneously, too high H/D may increase energy consumption due to the increased pressure drop of the reactor. Considering all factors such as hydrodynamics, change in Cl_2 concentration over height, and particle outflow, suitable H/D is found as around 2. In this case, the minimum reactor height has been calculated and used in the following stages.

In the second stage, a smooth exit has been added to the top of the reactor with the height calculated in the previous stage. In this series of simulations, the effect of fluid's uniform and non-uniform inflow pattern and superficial velocity on the Cl2 concentration and particle outflow have been investigated. The simulations still confirm that conversion becomes almost complete all simulations in all simulations in the first meter of the reactor. However, there is a severe challenge in particle outflow from the reactor. Not only the change in the pattern of the feed gas but also the reduction of the fluid's superficial velocity and had no positive effect on the escape of particles. In channeling, the fluid's velocity in the channel becomes much higher than the inlet velocity and makes the cut size of the outflowing particles larger. In this situation, there will be more particle escape. A possible solution to this problem can be to reduce the superficial fluid velocity above the dense phase by changing the reactor's geometry, and this is studied in the next generation of the reactor.

In the third stage, changing the reactor's geometry (extended top section) increases the cross-sectional area of the reactor. Because of that, the superficial velocity of the fluid decreases, and generated drag forces on the particles are not strong enough to exit the particles. On the other hand, changing the inflow pattern from the uniform distribution to the non-uniform decreases the particle outflow significantly. It is essential to consider that although a tiny particle flow rate has been reported at the steady state. However, the simulation time should be increase as much as possible to have more accurate data. Besides these advantages, the current generation of reactor model suffers from the possibility of high agglomeration and caking phenomena (on sidewalls), and it seems the slope and height of the middle region of the reactor affect this. On the other hand, although the non-uniform pattern has shown remarkable results, the hydrodynamics of the reactor can still be improved. In the next generation, to achieve better hydrodynamics and minimizing the channeling effect, not only the slope and height of the conic region of the reactor can be modified, but also some changes in other parts of the reactor are studied.

In the fourth stage, some significant changes have been applied to the geometry. Compared with the third stage, the change in slope of the middle part of the reactor (transient section) and modifying the heights led to minimizing

the agglomeration effect and caking phenomenon in the top area of particle escape from the reactor. On the other hand, adding the internal rings and conical distributor simultaneously significantly affected particle outflow and hydrodynamics inside the reactor. The rings change the flow direction inside the bed, and the conical distributor helps avoid escaping the fluid through the wall. The best hydrodynamics and the minimum particle escape have been achieved by this geometry and non-uniform pattern of the inlet gas.

It is time to add a separation unit (high-efficiency cyclone) to the system in the fifth stage. Because of the low superficial velocity in the reactor, the size of the cyclone is considerably smaller than the reactor. Although the initial geometry calculation of the design was based on 99% efficiency, Barracuda® simulation shows that the efficiency would be slightly lower (around 97%). This is due to assuming the 0.3 kg/s inflow of particles. By increasing the solid feeding rate, the efficiency of the cyclone increasing up to a certain point and then starting to decrease again. This does not mean that the higher particle duty is better because when there is lower particle inflow, the particle escape will be less in practice. Therefore, the effort to minimize the particle outflow was utterly efficient.

In the sixth stage, instead of an isothermal condition, the model has been simulated under thermal conditions, including convective and radiative heat transfer mechanisms to calculate and design the needed cooling system. Design an exothermic reactor with an efficient heat transfer performance is probably the most critical task from an engineering point of view. The efficiency of the reaction is highly affected by temperature. The Gibbs reactor simulation in Aspen Plus® validates the heat transfer calculated in thermal analysis by CPFD simulation. At the steady-state, the reactor temperature range is 700-780℃.

In the seventh and last stage, the reaction conversion and composition of leaving particles with the CPFD simulation in the presence of seven percent α-alumina impurity have been studied. The results show that the alumina impurity does not affect the chlorination reaction itself. The overall particle outflow has become slightly higher in the case of pure γ-alumina. Almost only 3 percent of the total particle outflow belongs to α-alumina, and consequently, in the long run, that may cause α-alumina accumulation in the reactor, which is not favorable. In the operating temperature, the reaction rate of α-alumina is much slower, and the accumulation of α-alumina will affect the overall reaction negatively. As remedies, adding a circulation path or speeding up the fluid inside the reactor to a certain point may be helpful, which can be investigated in future works.

It is important to note that, CFD model has no opportunity to validate against the experiments, and there is not much information available, specifically on possible side reactions that can affect the performance. Because of these reasons, the worst-case scenario is considered to achieve a more reliable result in the current study. Using much lower reaction rates than the reported ones in the literature, using a high enough bed aspect ratio (although the lower ratios also showed a good result), or assuming higher particle outflow in cyclone design are examples of these scenarios. On the other hand, in any possible cases, the CPFD simulation results have been compared with other software to verify the results as possible.

Suggested Future Studies

Up to this point, many optimizations have been applied to the model to achieve a real situation. To have a more realistic model, the following suggestions are recommended to study in the future. Most of them have been kicked off during the current study:

- Heat transfer optimization to minimize the needed heat transfer.
- Designing and modeling the optimum fluid distribution system.
- Applying more impurities to the alumina sample.
- Defining possible side reactions as possible.
- Study of the necessity of having circulation to avoid α-alumina accumulation in the reactor
- Finding the optimum superficial velocity to prevent α–alumina accumulation in the reactor.
- Size optimization of the reactor.
- Finding the optimum circulation/separation design

References

[1] (04.27.2021). *Aluminum Statistics and Information*. Available: https://www.usgs.gov/centers/nmic/aluminum-statistics-and-information

[2] "Mapping resource prices: the past and the future," Rotterdam.

[3] *The Aluminum Effect, A Enique Metal With Unique Properties*. Available: https://european-aluminium.eu/about-aluminium/the-aluminium-effect/

[4] *Adoption of the Paris Agreement*, U. Nation, 2015.

[5] C. Clemence. (2019). *Leaders Emerge In The Aluminium Industry's Race To Zero Carbon*. Available: https://aluminiuminsider.com/leaders-emerge-in-the-aluminium-industrys-race-to-zero-carbon/

[6] *Aluminum Market*. Available: https://www.fortunebusinessinsights.com/

[7] S. B. Kunal Ahuja. (2021). *Global Aluminum Market size worth over USD 210 Billion by 2027*. Available: https://www.gminsights.com/pressrelease/aluminum-market

[8] A. Kovács, C. J. W. Breward, K. E. Einarsrud, S. A. Halvorsen, E. Nordgård-Hansen, E. Manger, *et al.*, "A heat and mass transfer problem for the dissolution of an alumina particle in a cryolite bath," *International Journal of Heat and Mass Transfer*, vol. 162, p. 120232, 2020/12/01/ 2020.

[9] S. Prasad, "Studies on the Hall-Heroult Aluminum Electrowinning Process," *Journal of the Brazilian Chemical Society*, vol. 11, 05/01 2000.

[10] J. Thonstad, *Aluminum Electrolysis - Fundamentals of the Hall-Heroult Process*. Germany at Breuerdruck, Dusseldorf: Aluminium-Verlag Marketing & Kommunikation GmbH, 2001.

[11] "Energy Conservation: S. 2176, a bill to provide for a National Fuels and Energy Conservation Policy, to establish an office of Energy Conservation," Interior, Ed., ed: U.S. Government Printing Office, 1973, p. 1315.

[12] I. Arthur D. Little, "Survey of potential processes for the manufacture of aluminium," Cambridge, MA (USA), United States, Technical Report ANL/OEPM-79-4, 1979.

[13] B. Øye. (2019). *Could the chloride process replace the Hall-Héroult process in aluminium production?* Available: https://blog.sintef.com/

[14] *Hall-Heroult Centennial*. United States of America: TMS (The Minerals, Metals & Materials Society), 2002.

[15] J. E. Wanvik. (2000, 3.27.2021). *Norwegian anorthosites and their industrial uses, with emphasis on the massifs of the Inner Sogn-Voss area in western Norway*. Available: https://www.ngu.no/filearchive/102/Bulletin436_11.pdf

[16] O. A. Z. Barahmand, L. Salcido, E. Rustad, "CPFD Simulation and Modeling of the Industrial Alumina Chlorination Reactor," University of South-Eastern Norway, Norway, Group Project Report2020.

[17] K. Grjotheim and B. Welch, "Impact of Alternative Processes for Aluminium Production on Energy Requirements," in *Essential Readings in Light Metals: Volume 2 Aluminum Reduction Technology*, G. Bearne, M. Dupuis, and G. Tarcy, Eds., ed Cham: Springer International Publishing, 2016, pp. 1049-1055.

[18] H. S. Ray, *Introduction to Melts: Molten Salts, Slags and Glasses*: Allied Publisher Pvt. Limited, 2006.

[19] Yalamanchili K. Rao; Mohamad K. Soleiman, "Alumina Chlorination," United-States Patent, 1986.

[20] J. R. H. Elmer, "Method for extracting heat from a chamber containing a molten salt," United-States Patent, 1979.

[21] *Circulating Fluidized Beds*: BLACKIE ACADEMIC &. PROFESSIONAL, 1997.

[22] J. L. Sinclair and R. Jackson, "Gas-particle flow in a vertical pipe with particle-particle interactions," *AIChE Journal*, vol. 35, pp. 1473-1486, 1989/09/01 1989.

[23] E. U. Hartge, D. Rensner, and J. Werther, "SOLIDS CONCENTRATION AND VELOCITY PATTERNS IN CIRCULATING FLUIDIZED BEDS," in *Circulating Fluidized Bed Technology*, P. Basu and J. F. Large, Eds., ed: Pergamon, 1988, pp. 165-180.

[24] W. Zhang, Y. Tung, and F. Johnsson, "Radial voidage profiles in fast fluidized beds of different diameters," *Chemical Engineering Science,* vol. 46, pp. 3045-3052, 1991/01/01/ 1991.

[25] F. J. Anders Svensson, Bo G Leckner, "Fluid-dynamics of the bottom bed of circulating fluidized bed boilers," *Proc of the 12th International Conference on Fluidized-Bed Combustion,* vol. 2, pp. 887-897, 1993.

[26] D. Kunii and O. Levenspiel, "Fluidization Engineering," Second Edition ed Boston: Butterworth-Heinemann, 1991, p. 497.

[27] M. Kruse and J. Werther, "2D gas and solids flow prediction in circulating fluidized beds based on suction probe and pressure profile measurements," *Chemical Engineering and Processing: Process Intensification,* vol. 34, pp. 185-203, 1995/06/01/ 1995.

[28] Y. L. Yang, Y. Jin, Z. Q. Yu, and Z. W. Wang, "Investigation on slip velocity distributions in the riser of dilute circulating fluidized bed," *Powder Technology,* vol. 73, pp. 67-73, 1992/11/15/ 1992.

[29] M. Rhodes, H. Mineo, and T. Hirama, "Particle motion at the wall of a circulating fluidized bed," *Powder Technology*, vol. 70, pp. 207-214, 1992/06/01/ 1992.

[30] R. C. Senior and C. Brereton, "Modelling of circulating fluidised-bed solids flow and distribution," *Chemical Engineering Science,* vol. 47, pp. 281-296, 1992/02/01/ 1992.

[31] J. R. G. C. Brereton, "End effects in circulating fluidized bed hydrodynamics," *Proc. 4th Int. Conf. on Cirulating Fluidized Beds,* pp. 169-174, 1993.

[32] A. W. Nienow, "Fluidization of dissimilar materials," *Fluidization,* pp. 357-381, 1985 1985.

[33] D. R. Bai, "Residence Time Distributions of Gas and Solids in a Circulating Fluidized Bed," *Fluidization,* vol. VII, pp. 195-202, 1992 1992.

[34] B. Nauman, *Handbook of Chemical Reactor Design, Optimization, and Scaleup*, First ed.: McGraw-Hill Professional, 2001.

[35] B. Lie, "Title," unpublished|.

[36] J. Beckmann, *A history of inventions, discoveries, and origins*, 4th ed. vol. 2, 1946.

[37] R. L. D. Beauchamp, *Preparation of Anhydrous Aluminum Chloride*: University of Michigan Library, 1969.

[38] L. K. A. Russell, and W. E. Haupin, "Production of aluminum," United State Patent US3725222A, 1973.

[39] C. M. K. Wefers, *Oxides and hydroxides of aluminum* vol. 19. Pittsburgh: Alcoa Laboratories, 1987.

[40] N. A. Gokcen, "Rates of chlorination of aluminous resource," United State1983.

[41] I. Bertóti, A. Tóth, T. Székely, and I. S. Pap, "Kinetics of γ-alumina chlorination by phosgene," *Thermochimica Acta,* vol. 44, pp. 325-331, 1981/04/01/ 1981.

[42] H. P. M. H. P. Alder, and W. Richarz, "Kinetic Study of the Alumina Chlorination.," *Light Metals,* vol. 1, pp. 219-232, 1977.

[43] W. D. J. Hille, "Production of Anhydrous Aluminum Chloride from Y-alumina in a Fluidized Bed," *Angewandte Chemie,* vol. 72, pp. 850-855, 1960.

[44] A. Tóth, I. Bertóti, and T. Székely, "Kinetics of γ-alumina chlorination by carbon monoxide and chlorine," *Thermochimica Acta,* vol. 52, pp. 211-215, 1982/01/16/ 1982.

[45] D. Milne, "The Chlorination of Alumina and Bauxite with Chlorine and Carbon Monoxide," *Proc Australas Inst Min Metall,* vol. 260, pp. 23-31, 12/01 1976.

[46] H. Y. Sohn, J. Szekely, and J. Evans, *Gas–Solid Reactions*, 1976.

[47] M. Soleiman and Y. Rao, "Kinetics and Mechanism of Chlorination of Alumina Grains with He–CO–Cl2 Gas Mixtures—I. Experimental," *Canadian Metallurgical Quarterly,* vol. 26, pp. 207-215, 07/01 1987.

[48] M. Rohner, V. Sharma, and W. Richarz, "IR Study of Chlorination of Alumina Employing Mixtures of Gaseous Chlorine and Carbon Monoxide," *Chemical Engineering & Technology - CHEM ENG TECHNOL*, vol. 12, pp. 27-32, 02/01 1989.

[49] L. Wang, T.-A. Zhang, G.-Z. Lv, Z. Dou, W.-G. Zhang, and L.-P. Niu, "Carbochlorination Kinetics of High-Alumina Fly Ash," *JOM*, vol. 71, 09/28 2018.

[50] F. Réti, I. Bertóti, G. Mink, and T. Székely, "Surface reactions of chlorine with Y-alumina," *Reactivity of Solids*, vol. 3, pp. 329-336, 1987/08/01/ 1987.

[51] B. Øye, "Carbochlorination routes in production of Al," SINTEF Industry, Norway2018.

[52] H. K. V. a. W. MALALASEKERA, *An introduction to computational fluid dynamics, The finite volume method*: Longman Group Ltd, 1995.

[53] "Geometry Modeling & Grid Generation," S. University, Ed., ed, 2007, p. 132.

[54] (2021, 12.04.2021). *Barracuda Virtual Reactor User Manual*. Available: https://cpfd-software.com/user-manual/index

[55] D. M. Snider, "An Incompressible Three-Dimensional Multiphase Particle-in-Cell Model for Dense Particle Flows," *Journal of Computational Physics*, vol. 170, pp. 523-549, 2001/07/01/ 2001.

[56] A. W. Ed. Forman, *Combustion Theory*, Second ed.: The Benjamin/Cummings Publishing Company, Inc, 1985.

[57] M. J. Andrews and P. J. O'Rourke, "The multiphase particle-in-cell (MP-PIC) method for dense particulate flows," *International Journal of Multiphase Flow*, vol. 22, pp. 379-402, 1996/04/01/ 1996.

[58] W.-C. Yang, "Handbook of Fluidization and Fluid–Particle System," *China Particuology*, vol. 1, pp. 137-137, 07/01 2003.

[59] L.-S. F. L. S. Fan, Chao Zhu, *Principles of Gas-Solid Flows* vol. 1. New York: Cambridge University Press,, 1989.

[60] F. White, *Viscous Fluid Flow*, 3rd ed. New York: McGraw-Hill, 1991.

[61] C. Wen and Y. Yu, "Mechanics of Fluidization," *Chemical Engineering Progress Symposium Series*, vol. 62, pp. 100-111, 01/01 1966.

[62] M. K. Patel, K. Pericleous, and M. Cross, "NUMERICAL MODELLING OF CIRCULATING FLUIDIZED BEDS," *International Journal of Computational Fluid Dynamics*, vol. 1, pp. 161-176, 1993/01/01 1993.

[63] R. Beetstra, M. A. van der Hoef, and J. A. M. Kuipers, "Drag force of intermediate Reynolds number flow past mono- and bidisperse arrays of spheres," *AIChE Journal*, vol. 53, pp. 489-501, 2007/02/01 2007.

[64] S. Ergun and A. A. Orning, "Fluid Flow through Randomly Packed Columns and Fluidized Beds," *Industrial & Engineering Chemistry*, vol. 41, pp. 1179-1184, 1949/06/01 1949.

[65] D. Gidaspow, *Multiphase Flow and Fluidization: Continuum and Kinetic Theory Description*: Elsevier Science Publishing Co. Inc, 1994.

[66] R. Turton and O. Levenspiel, "A short note on the drag correlation for spheres," *Powder Technology*, vol. 47, pp. 83-86, 1986/03/01/ 1986.

[67] D. H. J. F. Davidson, *Fluidization*, First ed. New York: Academic Press, 1971.

[68] A. Haider and O. Levenspiel, "Drag coefficient and terminal velocity of spherical and nonspherical particles," *Powder Technology*, vol. 58, pp. 63-70, 1989/05/01/ 1989.

[69] N. Yang, W. Wang, W. Ge, L. Wang, and J. Li, "Simulation of Heterogeneous Structure in a Circulating Fluidized-Bed Riser by Combining the Two-Fluid Model with the EMMS Approach," *Industrial & Engineering Chemistry Research*, vol. 43, pp. 5548-5561, 2004/09/01 2004.

[70] J. L. M. Kwauk, *Particle-fluid two-phase flow : the energy-minimization multi-scale method*. Beijing Metallurgical Industry Press, 1994.

[71] R. P. Chhabra, L. Agarwal, and N. K. Sinha, "Drag on non-spherical particles: an evaluation of available methods," *Powder Technology*, vol. 101, pp. 288-295, 1999/03/01/ 1999.

[72] D. Sathiyamoorthy and M. Horio, "On the influence of aspect ratio and distributor in gas fluidized beds," *Chemical Engineering Journal*, vol. 93, pp. 151-161, 2003/06/15/ 2003.

[73] I. B. Haugland, O. Kjos, A. Røyset, P. E. Vullum, T. A. Aarhaug, and M. Halstensen, "Alumina Scale Composition and Growth Rate in Distribution Pipes," in *Light Metals 2019*, Cham, 2019, pp. 697-706.

[74] E. J. Frazer and J. Thonstad, "Alumina Solubility and Diffusion Coefficient of the Dissolved Alumina Species in Low-Temperature Fluoride Electrolytes," *Metallurgical and Materials Transactions B*, vol. 41, pp. 543-548, 2010/06/01 2010.

[75] A. R. Gaddipati and W. D. Scott, "Surface mass transport of alumina," *Journal of Materials Science*, vol. 21, pp. 419-423, 1986/02/01 1986.

[76] D. Wang and L. S. Fan, "Particle characterization and behavior relevant to fluidized bed combustion and gasification systems," in *Fluidized Bed Technologies for Near-Zero Emission Combustion and Gasification*, F. Scala, Ed., ed: Woodhead Publishing, 2013, pp. 42-76.

[77] F. Liang, M. Sayed, G. Al-Muntasheri, F. Chang, and L. Li, "A Comprehensive Review on Proppant Technologies," *Petroleum*, vol. 2, 11/01 2015.

[78] (05.05.2021). *What is density? how to distinguish different density definitions?* Available: https://www.cementscience.com/

[79] "Standard Terminology Relating to Catalysts and Catalysis," ed. West Conshohocken, PA: ASTM International, 2018.

[80] "Standard Test Method for Real Density of Calcined Petroleum Coke by Xylene Displacement," ed. West Conshohocken, PA: ASTM International, 2017.

[81] P. Basu, *Circulating fluidized bed boilers: Design, operation and maintenance*, 2015.

[82] J. H. Bethel Afework, Kailyn Stenhouse, Jason Donev. (2018, 04.27.2021). *Cyclone separator*. Available: https://energyeducation.ca/encyclopedia/Cyclone_separator

[83] *High-Efficiency Cyclone Features*. (04.27.2021). Available: https://www.heumannenviro.com/high-efficiency-cyclone-features/

[84] F. C. A. C. David Cooper, *Air Pollution Control: A Design Approach* 4th ed.: Waveland Pr Inc, 2010.

[85] W. C. Yang and D. L. Keairns, "The effect of an expanded section on slugging," *AIChE Journal*, vol. 26, pp. 144-148, 1980/01/01 1980.

[86] W. Bauer and J. Werther, "THE ROLE OF GAS DISTRIBUTION IN FLUIDIZED BED CHEMICAL REACTOR DESIGN†," *Chemical Engineering Communications*, vol. 18, pp. 137-147, 1982/10/01 1982.

[87] A. V. Kulkarni, S. V. Badgandi, and J. B. Joshi, "Design of ring and spider-type spargers for bubble column reactor: Experimental measurements and CFD simulation of flow and weeping," *Chemical Engineering Research and Design*, vol. 87, pp. 1612-1630, 2009/12/01/ 2009.

Appendixes

Appendix A: Base Material Properties

Appendix B: Simulation Sheets

Appendix C: Barracuda® Summary Info

Appendix D: Submitted papers to SIMS conference 2021

Appendix G: Task Description

Appendix A: Base Material Properties

Base Material Data (Al_2O_3)

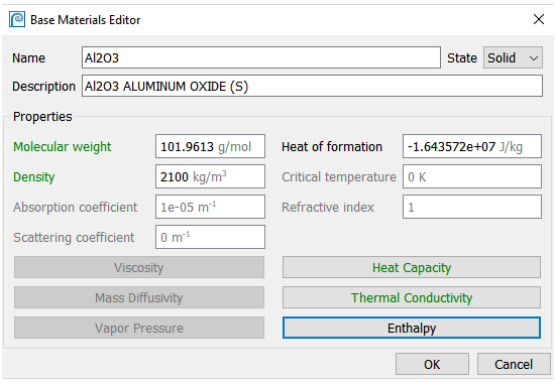

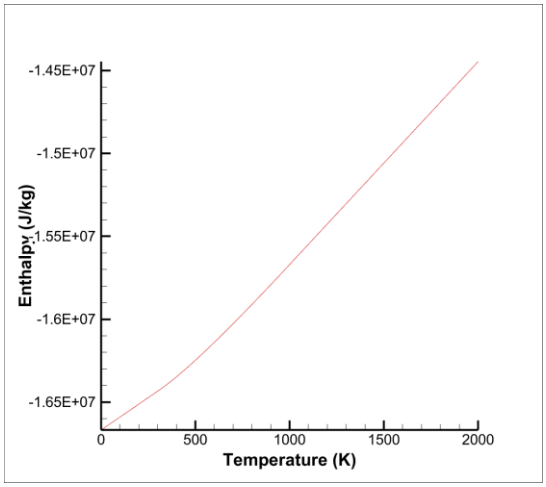

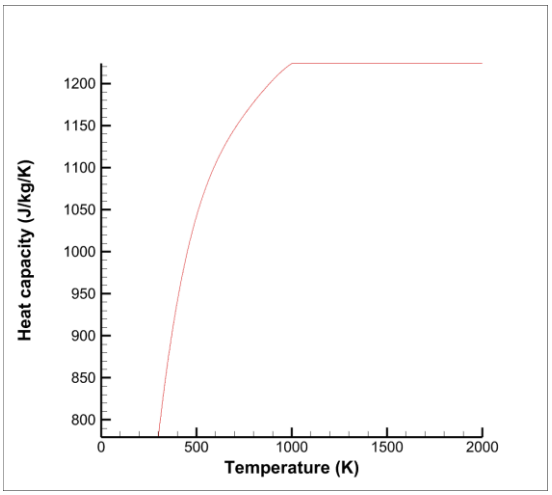

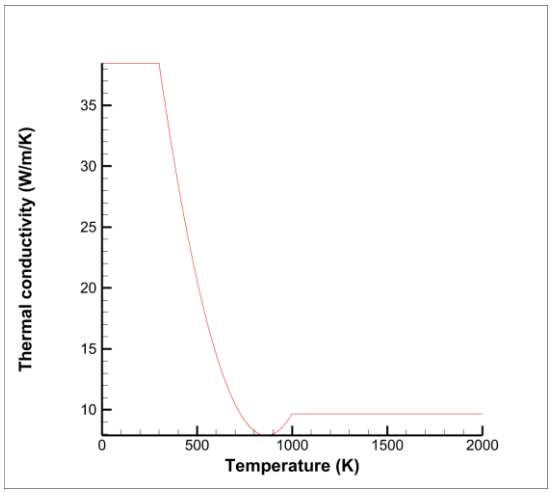

Appendix A (Continued)

Base Material Data ($AlCl_3$)

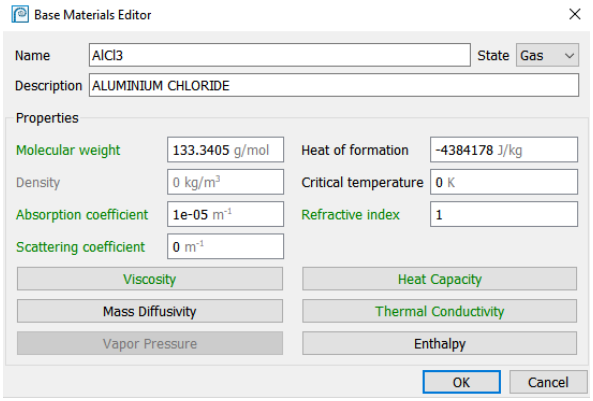

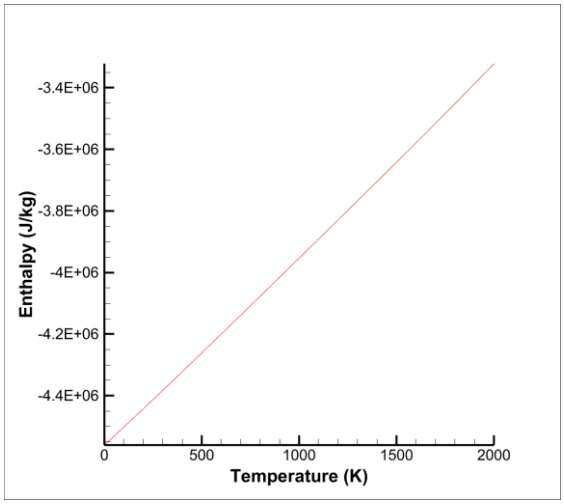

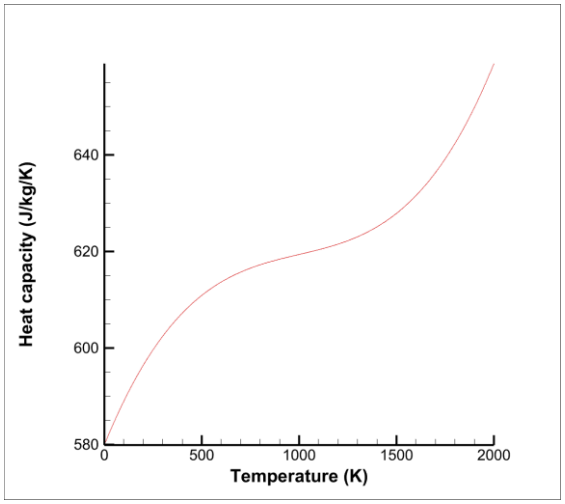

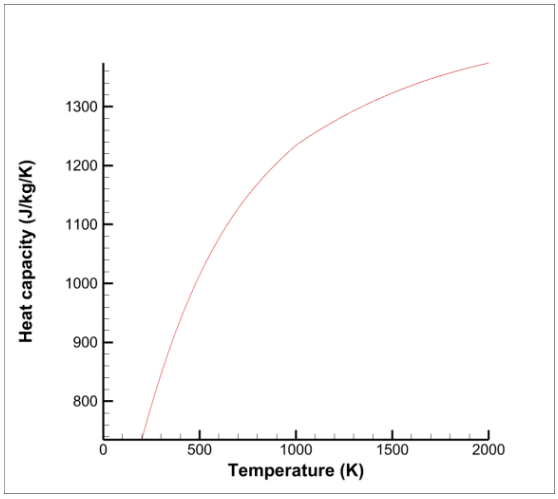

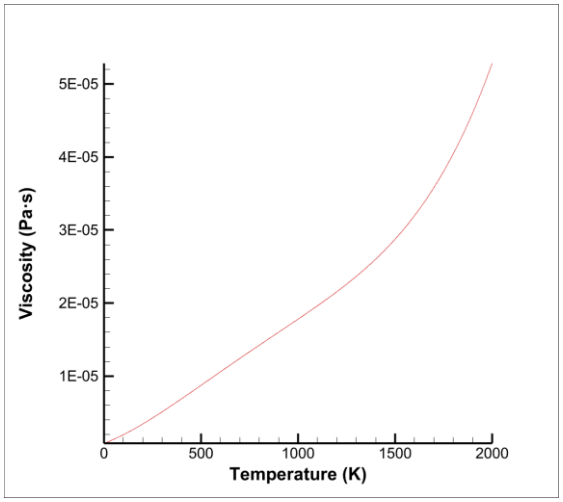

Appendix A (Continued)

Base Material Data (CO_2)

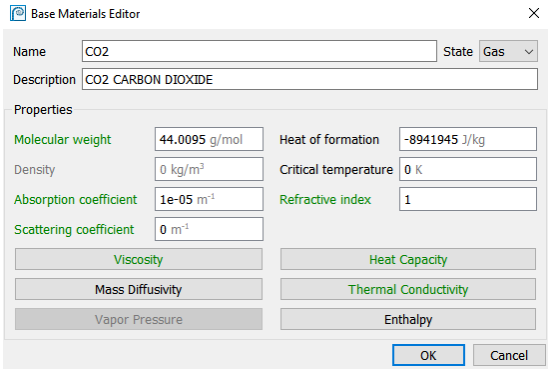

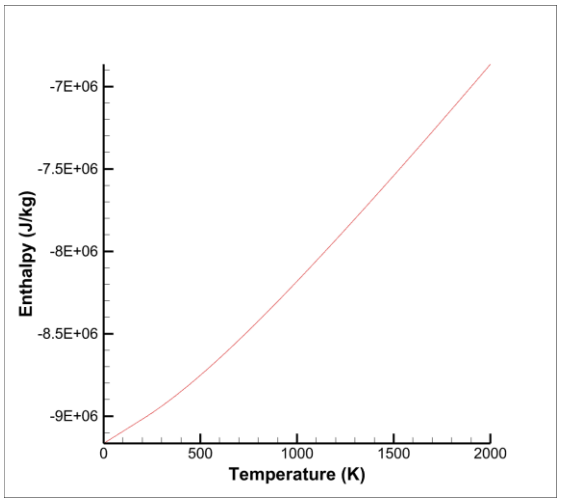

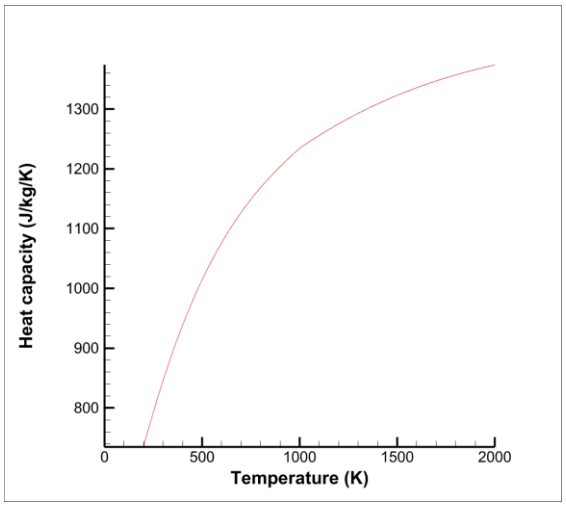

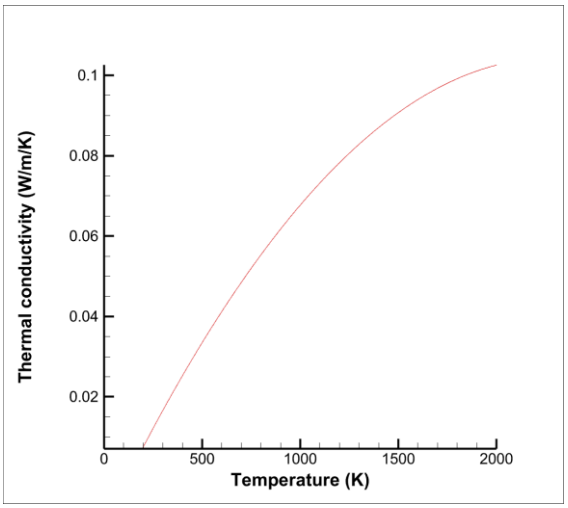

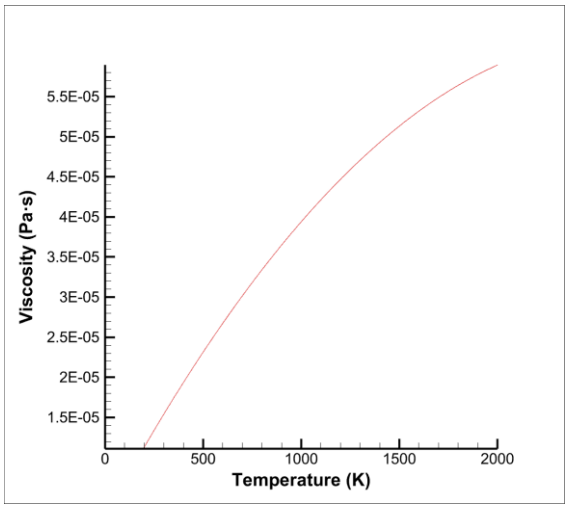

Appendix A (Continued)

Base Material Data (CO)

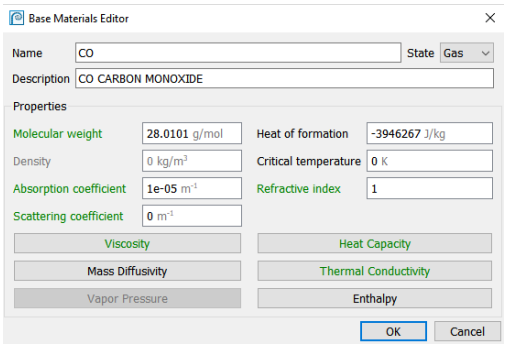

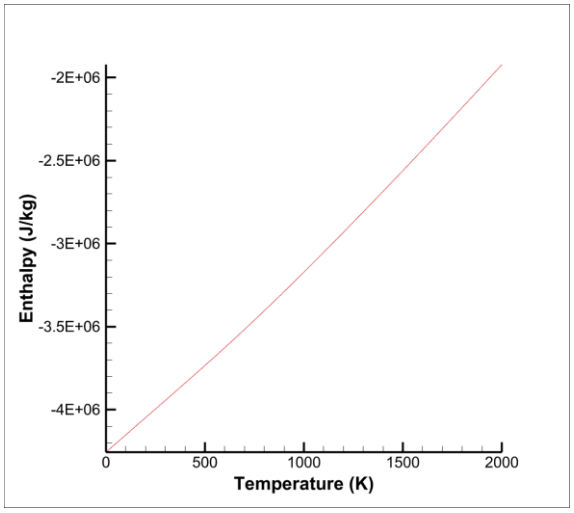

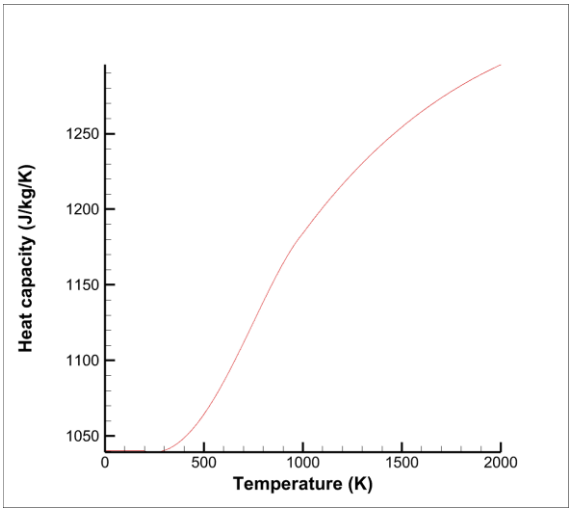

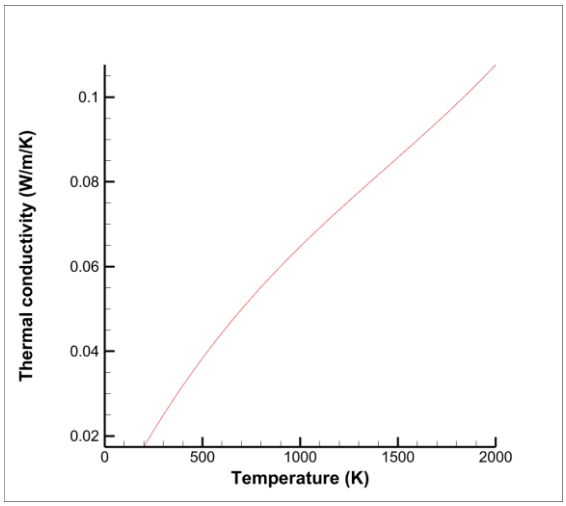

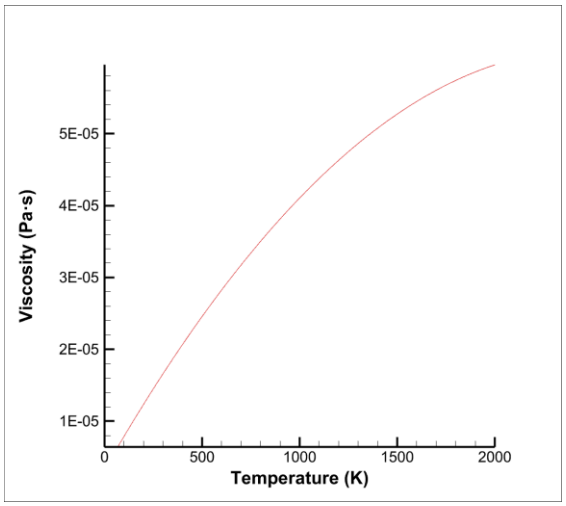

Appendix A (Continued)

Base Material Data (Cl_2)

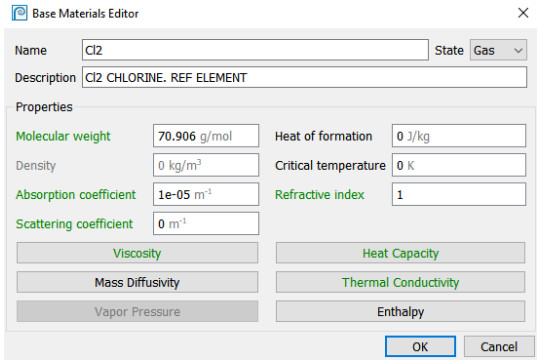

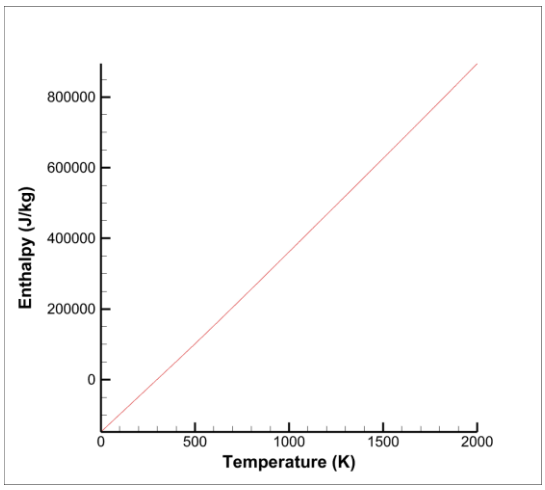

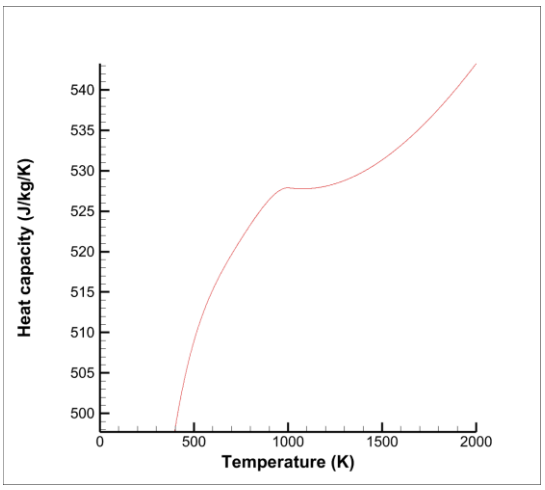

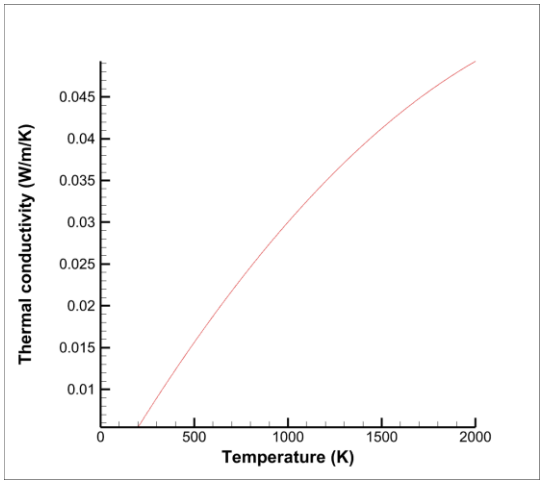

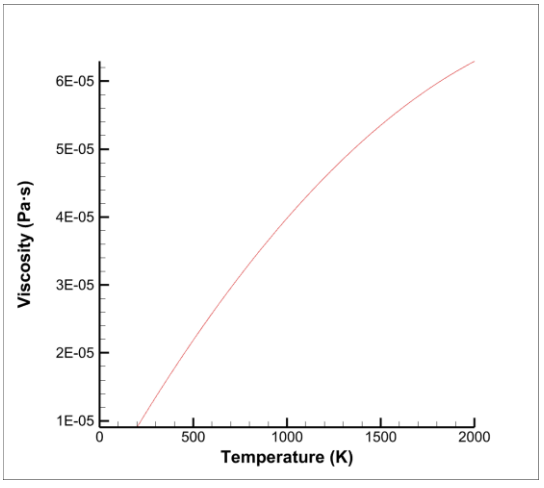

Appendix B: Simulation Sheets

Simulation Sheet 01

Appendix B (Continued)

Simulation Sheet 02

Appendix B (Continued)

Simulation Sheet 03

Appendix B (Continued)

Simulation Sheet 04

Appendix B (Continued)

Simulation Sheet 05

Appendix B (Continued)

Simulation Sheet 06

Appendix B (Continued)

Simulation Sheet 07

Appendix B (Continued)

Simulation Sheet 08

Appendix C: Barracuda® Summary Info[20] (based on reactor v.5)

```
#
# Barracuda® release  20.1.0
# Solver version    20.1.0.x025
# Build date        2021-03-07 14:24:56 Mountain Standard Time
# Solver run command: cpfd.x.17.exe Cylinder 17.2 4.prj

Error opening existing shared memory file.

Using shared memory data exchange

Input project file is from series 17. Input control version 40
GridGenerated: 2018-11-15 15:02:10 Mountain Standard Time
Check: Small area fraction relative to opposite neighbor area fraction
Number face area fractions <  1.00e-03 is 58. Max area fraction removed =  1.00e-04. Set A=0.

Number of non-CV with walls = 0

Number of CV cells = 4002
Sum volume of CV cells =  6.67366e+01 m^3
Min volume of CV cells =  8.84658e-03 m^3
Max volume of CV cells =  1.83742e-02 m^3
Ave volume of CV cells =  1.66758e-02 m^3
Ave length of CV cells =  2.55483e-01 m
Max model dimension    =  1.50000e+01 m
Model bounding volume  =  8.63222e+01 m^3

*******************************************
Number of real cells: 4002
*******************************************

Fluid mixture property averaging method: mole-based

Particle distribution based on mass average or volume average, from Al2O3 average particle size
distribution.sff
   i   dm[i]/M   r[i] (micron)
  --- --------- ---------
    0 0.000000 0.248000
    1 0.000003 0.272500
    2 0.000040 0.299000
    3 0.000150 0.328000
    4 0.000340 0.360500
    5 0.000590 0.395500
    6 0.000880 0.434000
    7 0.001200 0.476500
    8 0.001600 0.523500
```

[20] Particle size distribution can be found here

9 0.002000 0.574500
10 0.002400 0.630500
11 0.002700 0.692500
12 0.003100 0.760000
13 0.003400 0.834000
14 0.003800 0.916000
15 0.004100 1.005500
16 0.004300 1.103500
17 0.004600 1.211500
18 0.004800 1.330000
19 0.005000 1.460000
20 0.005100 1.602500
21 0.005300 1.759500
22 0.005400 1.931500
23 0.005600 2.120000
24 0.005700 2.327500
25 0.005900 2.555000
26 0.006000 2.805000
27 0.006200 3.079000
28 0.006400 3.380000
29 0.006600 3.710500
30 0.006800 4.073500
31 0.007100 4.471500
32 0.007400 4.908500
33 0.007700 5.390000
34 0.008100 5.915000
35 0.008600 6.495000
36 0.009200 7.130000
37 0.009900 7.825000
38 0.010700 8.590000
39 0.011900 9.430000
40 0.013500 10.350000
41 0.015700 11.365000
42 0.018800 12.475000
43 0.023200 13.695000
44 0.029200 15.035000
45 0.037400 16.505000
46 0.048400 18.120000
47 0.062900 19.890000
48 0.081900 21.835000
49 0.106000 23.970000
50 0.137000 26.310000
51 0.176000 28.885000
52 0.222000 31.705000
53 0.277000 34.805000
54 0.341000 38.210000
55 0.413000 41.945000
56 0.492000 46.045000
57 0.576000 50.550000
58 0.662000 55.500000
59 0.745000 60.900000
60 0.820000 66.850000

```
   61 0.882000 73.400000
   62 0.929000 80.600000
   63 0.961000 88.450000
   64 0.990000 97.100000
   65 0.994000 117.050000
   66 0.997000 128.450000
   67 0.998000 141.050000
   68 0.999000 154.800000
   69 0.999900 169.950000
   70 1.000000 186.550000

Particle species  1. Particle density =  3958.00 kg/m3
        Solid mass / vol =  3958.00 (kg/m3) Mass fraction solid     =     1.00
       Liquid mass / vol =     0.00 (kg/m3) Mass fraction liquid    =     0.00
    Non-solid mass / vol =     0.00 (kg/m3) Mass fraction non-solid =     0.00

   Al2O3            Solid     Density= 3958.00 kg/m3 Y(particle)= 1.00000 Y(solids)  = 1.00000 Mass/particle
vol= 3958.000 kg/m3. Volume/particle vol= 1.000000


--------- -------- -------- --------  ----------  ------------

Pressure BC 0 with normal to z-surface
  flux name   FLUXBC_P_Outlet
  cell range  i:0-10 j:58-59 k:0-10
  xyz region  x:1.081350e-03-2.398919e+00  y:1.485450e+01-1.500000e+01  z:0.000000e+00-2.400000e+00
  Area fraction = 1.000000e+00
  Flow surface area =  7.71279253e-01 m^2
  x-BC area =  0.00000000e+00 m^2
  y-BC area =  0.00000000e+00 m^2
  z-BC area =  7.71279253e-01 m^2

--------- -------- -------- --------  ----------  ------------

Warning: Flow BC <1>. 'Subdivide by radius' has no effect when used concurrently with 'No particle exit'.

Flow BC 0 with normal to y-surface
  flux name   FLUXBC_F_In
  cell range  i:1-9 j:1-1 k:1-9
  xyz region  x:1.081350e-03-2.398919e+00  y:0.000000e+00-1.383510e-01  z:0.000000e+00-2.400000e+00
  Area fraction = 1.000000e+00
  Flow surface area =  4.44910944e+00 m^2
  x-BC area =  0.00000000e+00 m^2
  y-BC area =  4.44910944e+00 m^2
  z-BC area =  0.00000000e+00 m^2



Concentration in rate equations
[] = mole concentration   {} mass concentration
```

Heat of reaction partition between fluid and particles for volume-averaged chemistry is Manual
Rate coefficients

Volume average k0 = 2666 * exp(-2825/T)

Check continuity stoichiometric equation

Equations are consistent within 0.001

Stoichiometric equations

0: Al2O3 + 3 CO + 3 Cl2 => 2 AlCl3 + 3 CO2

Stoichiometric matrix

0: Al2O3(S)
1: AlCl3(G)
2: CO(G)
3: CO2(G)
4: Cl2(G)

	0	1	2	3	4	
0:	-1.000	2.000	-3.000	3.000	-3.000	hf=-1.179e+08 (Exothermic)

Stoichiometric rate equations (all materials)
---

0 d[Al2O3]/dt = -R00

1 d[AlCl3]/dt = 2 R00

2 d[CO]/dt = -3 R00

3 d[CO2]/dt = 3 R00

4 d[Cl2]/dt = -3 R00

Stoichiometric rates

R00 = (k0 * [CO(G)]^0.500 * [Cl2(G)]^0.500)

Rates after conversion based on concentration type
==========

Rate coefficients

Volume average k0 = 2666 * exp(-2825/T)

Stoichiometric rates

R00 = (k0 * {CO(G)}^0.500 * {Cl2(G)}^0.500)

Implicit rate equations (kmol/m^3/s)

0: d{Al2O3(S)}/dt = - 0.001 { (k0 * {CO(G)}^0.500 * {Cl2(G)}^0.500) }

1: d{AlCl3(G)}/dt = 0.002 { (k0 * {CO(G)}^0.500 * {Cl2(G)}^0.500) }

2: d{CO(G)}/dt = - 0.003 { (k0 * {CO(G)}^0.500 * {Cl2(G)}^0.500) }

3: d{CO2(G)}/dt = 0.003 { (k0 * {CO(G)}^0.500 * {Cl2(G)}^0.500) }

4: d{Cl2(G)}/dt = - 0.003 { (k0 * {CO(G)}^0.500 * {Cl2(G)}^0.500) }

Checking continuity. The test will use:
Mass concentration all species = 1 kg/m^3
Temperature fluid = 1000.000000 K
Pressure = 101000.000000 Pa
Temperature solid = 1000.000000 K
Volume fraction solids[0] = 0.400000
Surface area solids[0] = 0.001000
Mean rad[0] = 0.000020
Total volume fraction solids = 0.400000
Total surface area solids = 0.001000
Volume = 0.000100
Mean radius = 0.000020
Fluid density = 1.000000 kg/m^3
Solid massPerVol = 3958.000000 kg/m^3

Rate coefficients for implicit rate equations
k0 = 1.58117e+02

Al2O3 = -1.61218e+01 kg/s-m^3
AlCl3 = 4.21666e+01 kg/s-m^3
CO = -1.32866e+01 kg/s-m^3
CO2 = 2.08759e+01 kg/s-m^3
Cl2 = -3.36343e+01 kg/s-m^3

Sum of equations = -1.26494e-04 kg/s-m^3

Appendix D: Submitted Short papers to SIMS 2021

Design of a medium-scale circulating fluidized bed reactor for chlorination of processed aluminum oxide

CPFD modeling of the hydrodynamics and reaction kinetics of alumina chlorination in an industrial fluidized bed reactor

CPFD simulations on a chlorination fluidized bed reactor for aluminum production an optimization study

Study of the thermal performance of an industrial alumina chlorination reactor using CPFD simulation

Sensitivity and uncertainty analysis in a fluidized bed reactor modeling

The effect of impurities on γ-Alumina chlorination in a fluidized bed reactor: A CPFD study

Design of a medium-scale circulating fluidized bed reactor for chlorination of processed aluminum oxide

Zahir Barahmand[a,1], Omid Aghaabbasi[a], Jose Luis Salcido[a], Emmy Kristine L. Rustad[a], Chameera Jayarathna[b], Chandana Ratnayake[a,b]
a University of South-Eastern Norway, Porsgrunn, Norway, [1]zbarahmand@gmail.com
b SINTEF Tel-Tek, SINTEF Industry, Porsgrunn, Norway

Abstract:

Fluidization is a well-established and widely used technology in the process industry. The production stability and the large effective contact area between the active substances, resulting in high mass and heat transfer between the phases, are some of the main advantages of fluidization. However, this technology has not yet been developed for alumina chlorination as a standard solution on an industrial scale. Although the design of a circulating fluidized bed reactor is complex, it is advantageous to simulate the process compared to running experiments on a lab scale. The Computational Particle-Fluid Dynamic (CPFD) simulation lays a foundation for studying the given reaction process.

The reaction between the solid alumina particles and the gaseous chlorine and carbon monoxide results in the products (aluminum chloride and carbon dioxide). The project aims to design a circulating fluidized bed reactor by simulating the process in Barracuda®. Simulations with a simple geometry contributed to a better understanding of the reaction process. The simulation results are compared with values from both a theoretical approach and parallel simulations in Aspen Plus®. The comparison revealed that the results from Barracuda® Virtual Reactor, such as product flow rate, are within a reasonable range of what could be expected. The promising preliminary results imply that CPFD is a promising approach for future research on the design, optimization, and implementation of the industrial alumina chlorination process.

Keywords:
CPFD Simulation, Alumina Chlorination, Circulating Fluidized Bed Reactor (CFBR), Reactor Design, Barracuda

Zahir Barahmand*, Omid Aghaabasi, Emmy Kristine L. Rustad, Jose Luis Salcido, Chameera Jayarathna, Chandana Ratnayake

Designing of a medium-scale circulating fluidized bed reactor for chlorination of processed aluminum oxide

Keywords: CPFD Simulation, Alumina Chlorination, Circulating Fluidized Bed Reactor (CFBR), Reactor Design, Barracuda, Fast fluidized bed

***Corresponding Author:**
Zahir Barahmand, University of South-Eastern Norway, E-mail: zbarahmand@gmail.com

Co-Authors:
Omid Aghaabbasi, University of South-Eastern Norway, Norway, E-mail: 230755@student.usn.no
Emmy Kristine L. Rustad, University of South-Eastern Norway, Norway, E-mail: 162430@student.usn.no
Jose Luis Salcido, University of South-Eastern Norway, Norway, E-mail: 230754@student.usn.no
Chameera Jayarathna, SINTEF Tel-Tek, SINTEF Industry E-mail: chameera.jayarathna@sintef.no
Chandana Ratnayake, University of South-Eastern Norway, & SINTEF Tel-Tek, SINTEF Industry E-mail: chandana.ratnayake@sintef.no

1 Background

Producing aluminum from bauxite is mainly done by extraction in a Bayer process and converting it to pure alumina by an electrochemical process, namely Hall-Héroult [1]. This process has a considerable power consumption, and it is advantageous to evaluate an alternative process. The challenge lies in finding a proper and economical solution, considering the complexity of reducing alumina carbothermic. Alcoa® proposed a two-step solution that converts alumina to aluminum chloride ($AlCl_3$) in a fluidized bed and then reduces it to aluminum metal by electrolysis [2].

The fluidized bed technology has a wide range of applications in the process industry. The upward flow of a fluid through a bed of solid particles is a technique that results in an efficient heat and mass transfer and generally offers the process a stable production. Due to the complexity of the flow pattern and the flow hydro-dynamics within the gas-solid multiphase, the challenge of using a fluidized bed reactor rests in the design.

2 Aims

The current work aims to design a medium-scale chlorination reactor for producing a stream of $AlCl_3$ that may later be converted into pure aluminum. The basic geometry and the size of the reactor specifications are figured out for suitable hydrodynamics based on the available gas-solid fluidization theories. The design and operation of the reactor are evaluated and analyzed by the CFD simulations for actual operating and process conditions.

As the first step of the study, a Circulating Fluidized Bed Reactor (CFBR) preliminary mechanical design is completed using SOLIDWORKS®. The reactor model is then simulated/optimized with CFD software called Barracuda® Virtual Reactor version 17.4.

However, alumina chlorination is an aggressive exothermic reaction that occurs at higher temperatures (~700℃), and the products are highly corrosive. Therefore the specification of material and the cooling system are essential parts of the design process. However, these are not considered within the scope of the current study.

3 Materials and methods

The base model consists of simple geometry (cylindrical shape) without implementing the chlorination reaction. The simulation results are compared with values from both a theoretical approach and simulations in Aspen Plus®. CFD simulations without reaction reduce the computation time and are good enough to figure out the reactor's specification for good hydrodynamics at the bubbling bed fluidization regime. Final reaction rates and boundary conditions have been applied into complex geometry shown in Figure 3.1.

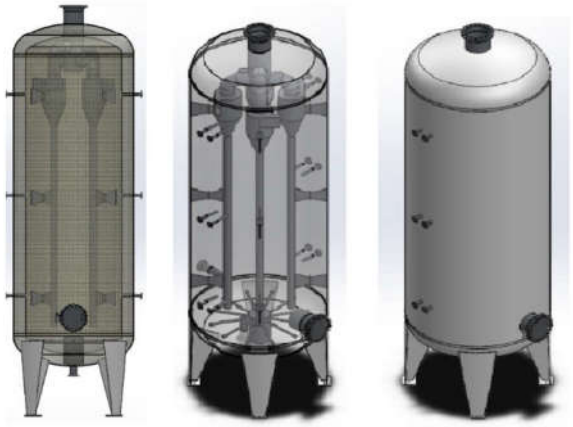

Figure 3.1: Reactor general assembly

4 Results

The alumina chlorination is an exothermic and fast reaction. Due to the low reaction time, the residence time for particles could be lower as well. The reactor has been designed based on the turbulent regime (fast fluidization) with four internal cyclones (Figure 4.1).

Based on the transient barracuda simulations, the reactor is predicted to be stabilized in around two minutes of operational time. Figure 4.2 shows the variation of the $AlCl_3$ and CO_2 produced at the reactor based on the reaction (1).

$$Al_2O_3 + 3Cl_2 + 3CO \rightarrow 2AlCl_3 + 3CO_2 \qquad (1)$$

Based on the reaction stoichiometry, the mole fraction of produced aluminum chloride and carbon dioxide at steady-state should be 2:3, equivalent to 2:1 mass fraction. At the steady-state, the average mass flow rate of $AlCl_3$ and CO_2 have been calculated as 0.381 m/s and 0.188 m/s, respectively.

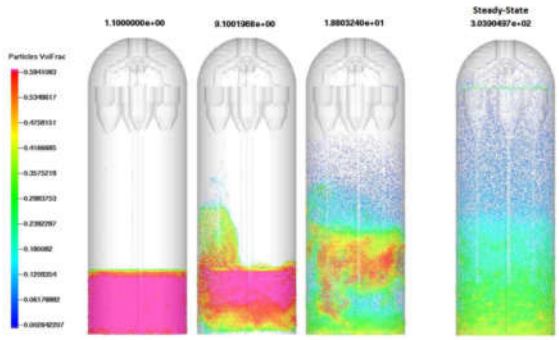

Figure 4.1: Simulated alumina chlorination reactor

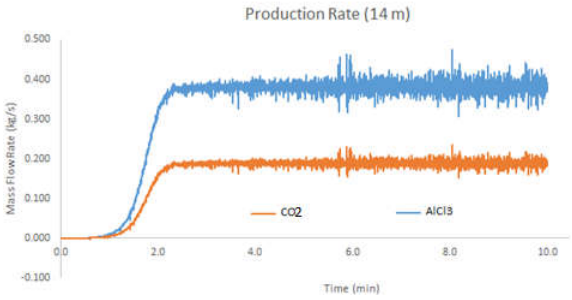

Figure 4.2: Product's mass flow rate at the outlet

Table 4.1: Comparing the component outflow by different methods

Component	Mass Flow Rates (kg/s)		
	CFD Simulation (Barracuda®)	Theoretical	Process simulations (Aspen Plus®)
$AlCl_3$	0.381	0.314	0.313
CO_2	0.188	0.155	0.155
CO	0.00145	0	0.00021
Cl_2	5×10^{-7}	0	0.00055

The chlorination product composition in the outlet has been calculated and compared with the results based on theoretical manual calculation, process simulations (Aspen Plus®), and CFD simulations (see Table 4.1).

5 Conclusions and future development

The study results have been evaluated and imply that this can be a practical solution for industrial aluminum production with lower environmental effects as CO_2 produced from the process can be separated straightforwardly after the crystallization of $AlCl_3$. It can be concluded that the results suggest continuing the work and research towards implementing a real-life industrial-scale reactor. It is crucial to validate the CFD simulation data with a lab-scale experimental unit as future work. However, the results have been verified within the considered design parameters with theoretical methods and Aspen Plus® simulations.

References

[1] S. Prasad, "Studies on the Hall-Heroult Aluminum Electrowinning Process," *Journal of the Brazilian Chemical Society,* vol. 11, 05/01 2000.

[2] *Hall-Heroult Centennial*. United States of America: TMS (The Minerals, Metals & Materials Society), 2002.

CPFD modeling of the hydrodynamics and reaction kinetics of alumina chlorination in an industrial fluidized bed reactor

Zahir Barahmand[a,1], Chameera Jayarathna[b], Chandana Ratnayake[a,b]
[a] University of South-Eastern Norway, Porsgrunn, Norway, [1] zbarahmand@gmail.com
[b] SINTEF Tel-Tek, SINTEF Industry, Porsgrunn, Norway

Abstract:

Aluminum is now the world's second most used metal. Since aluminum has a unique combination of appealing properties and effects, it allows for significant energy savings in many applications, such as vehicles and buildings. Although this energy-saving leads to lower CO_2 emissions, the production process of aluminum still dramatically impacts the environment.
The process used almost exclusively in the aluminum industry is the Hall-Héroult process with a considerable amount of carbon footprint with high energy consumption. As the best alternative, Alcoa's process (which is not industrialized yet) is based on the chlorination of processed aluminum oxide, reducing the traditional method's negative impacts.
In continuation of Alcoa's effort, this study aims to investigate the possibility of a new low carbon aluminum production process by designing an industrial fluidized bed reactor equipped with an external (due to high corrosion inside the reactor) gas-solid separation unit to handle a total of 0.6 kg/s of solid reactants and produce aluminum chloride as the main product. The research focuses on determining the best bed height based on the available reaction rates, determining the best reactor dimension to reduce particle outflow under isothermal conditions (700°C). Autodesk Inventor® and Barracuda® are used for 3D modeling of the reactor and CFD simulation for multiphase (solid-gas) reaction, respectively. Although results have shown that the bed aspect ratio (H/D; H- bed Height and D- bed Diameter) does not affect the reaction, it highly affects the reactor's hydrodynamics and particle outflow. The final design shows the best hydrodynamics belongs to bed aspect ratio equal to 2.

Keywords:
CPFD simulation, Bubbling regime, Fluidized bed reactor, Reactor design, Alumina Chlorination

Zahir Barahmand*, Chameera Jayarathna, Chandana Ratnayake

CPFD modeling of the hydrodynamics and reaction kinetics of alumina chlorination in an industrial fluidized bed reactor

Keywords: CPFD simulation, Bubbling regime, Fluidized bed reactor, Reactor design, Alumina Chlorination

***Corresponding Author:**
Zahir Barahmand, University of South-Eastern Norway, E-mail: zbarahmand@gmail.com

Co-Authors:
Chameera Jayarathna, SINTEF Tel-Tek, SINTEF Industry E-mail: chameera.jayarathna@sintef.no
Chandana Ratnayake, University of South-Eastern Norway, & SINTEF Tel-Tek, SINTEF Industry E-mail: chandana.ratnayake@sintef.no

1 Background

One of the aluminum industry's key targets has remained the manufacturing of aluminum with the lowest carbon footprint possible thanks to growing concern about global climate change led by the Paris agreement [1] on GHG emissions.

Alternative aluminum processing strategies have been under intense investigation due to the comparatively high energy usage and carbon footprint associated with anode consumption [2]. In continuation of this, in 1973, an innovative process was introduced by Alcoa Corporation, and it had several advantages compared to the commonly used method (Hall-Héroult) at that time.

In continuation of Alcoa's effort and based on the alumina chlorination process, the current project may create a new possibility of a new low carbon aluminum production process.

2 Aims

Until now, fluidized bed technology has been studied in a wide range of applications. Even though it is a well-known technology, designing such a reactor with ideal and realistic operating conditions continues to be a challenge without advanced numerical calculations. Not only the complexity of hydrodynamics but also the uncertain nature of the particle's behavior with their enormous influential characteristics in the fluidized bed reactor make this engineering process complex. A highly corrosive environment inside the reactor adds the design further challenges.

3 Methods

Having many advantages, the literature confirms that the bubbling regime could be the most suitable fluidization regime for many reactions [3]. The operating gas velocity should be chosen to achieve this regime in a range between minimum bubbling and terminal velocities. This method leads to pinpointing the required diameter of the reactor.

To more realistic model development in Barracuda®, the value for the particle void fraction (at minimum fluidization condition), envelope and bulk density, and solids' sphericity have been validated experimentally. In the next step, the kinetics and reaction rates have been defined.

$$Al_2O_3 + 3Cl_2 + 3CO \rightarrow 2AlCl_3 + 3CO_2 \qquad (1)$$

4 Results

It is calculated that the required superficial gas velocity is around 6 cm/s, and the required diameter of the reactor should be about 3.9 m, accordingly. The reactor height (22 m) is calculated based on the assumed bed aspect ratio (H/D) equal to 2.5 and Transport Disengaging Height (TDH) [4]. Table 4.1 shows the Cl_2 concentration at the outlet for different bed aspect ratios, and cases are varied based on the H values since the target was to find the suitable H/D value for the process.

Table 4.1: Cl2 concentration in the outlet

H/D	mole/m³
0.5	1.29E-04
1	2.67E-04
1.5	5.57E-04
2.5	1.57E-04

Figure 4.1 shows the steady-state particle volume fraction when the initial bed height is 9.7 m (H/D=2.5).

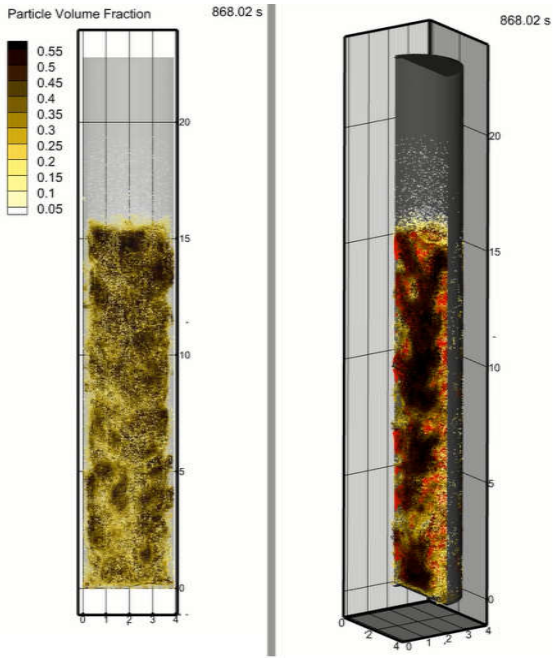

Figure 4.1: Fluidization at steady-state when H/D=2.5

In this case, Cl2 concentration in the outlet and particle outflow are given in Figures 4.2 and 4.3.

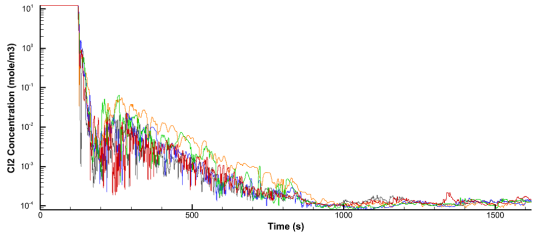

Figure 4.2: Cl2 concentration in the outlet of the reactor (H/D=2.5)

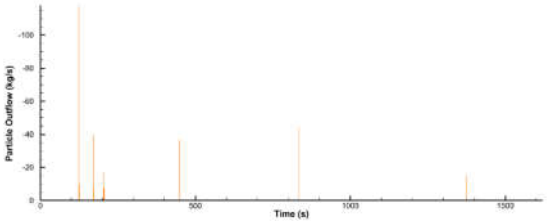

Figure 4.3: Particle outflow (H/D=2.5)

5 Conclusions and future development

Almost all the Cl_2 are consumed within the first meter of the reactor, which means the current range of bed and reactor height may not be fully activated in an actual chlorination process. However, the H/D value inherits a vital role for good hydrodynamics of the reactor. Selecting the reactor specification for good hydrodynamics of the gas-solid fluidized bed reactor is very important.

Too low H/D can cause channeling, and it may reduce the reaction efficiency. As a result, Cl_2 concentration at the reactor outlet may increase. Even a tiny amount of Cl_2 at the outlet could cause problems if there is not a purification process on Cl_2. Simultaneously, too high H/D may increase energy consumption due to the increased pressure drop of the reactor.

Considering all factors such as hydrodynamics, change in Cl_2 concentration over height, and particle outflow, the suitable H/D is found as around 2. In this case, the minimum reactor height could be calculated as 15.6m.

References

[1] UNFCCC. (2015, 15/12). *Adoption of the Paris agreement (FCCC/CP/2015/l.9/Rev.1 ed.)*. Available: http://unfccc.int/resource/docs/2015/cop21/eng/l09r01.pdf

[2] J. Thonstad, *Aluminum Electrolysis - Fundamentals of the Hall-Heroult Process*. Germany at Breuerdruck, Dusseldorf: Aluminium-Verlag Marketing & Kommunikation GmbH, 2001.

[3] N. Couto, A. Rouboa, V. Silva, E. Monteiro, and K. Bouziane, "Influence of the Biomass Gasification Processes on the Final Composition of Syngas," *Energy Procedia,* vol. 36, pp. 596-606, 2013/01/01/ 2013.

[4] D. Kunii and O. Levenspiel, "Fluidization Engineering," Second Edition ed Boston: Butterworth-Heinemann, 1991, p. 497.

CPFD simulations on a chlorination fluidized bed reactor for aluminum production: an optimization study

Zahir Barahmand[a,1], Chameera Jayarathna[b], Chandana Ratnayake[a,b]
a University of South-Eastern Norway, Porsgrunn, Norway, [1]zbrahmand@gmail.com
b SINTEF Tel-Tek, SINTEF Industry, Porsgrunn, Norway

Abstract:

The previous study on designing a fluidized bed reactor for alumina chlorination, CPFD simulation showed that the model suffers from high particle outflow and dense phase bed channeling. The present study optimizes the previous alumina chlorination fluidized bed reactor model through modified geometry, parameter modifications, and improved meshing. To optimize the performance of the reactor, complex geometry with an extended top section was combined with a regular cylindrical reactor. Besides, the gas inlet pattern was changed from an ideal uniform distribution to a non-uniform one. Besides, the reactor's inlet diameter is reduced, and the value for the particle sphericity and voidage has been updated based on experimental observations. The results show that the new reactor has a significantly lower particle outflow even with the higher inlet superficial gas velocity. The paper discusses the optimization steps and relevant changes in reactor performances in detail.

Keywords:
Optimization, fluidized bed reactor (FBR), alumina chlorination, Barracuda, CPFD simulation.

Zahir Barahmand*, Chameera Jayarathna, Chandana Ratnayake

CPFD simulations on a chlorination fluidized bed reactor for aluminum production: an optimization study

Keywords: Optimization, Fluidized bed reactor (FBR), Barracuda, Alumina Chlorination, CPFD simulation

***Corresponding Author:**
Zahir Barahmand, University of South-Eastern Norway, E-mail: zbarahmand@gmail.com

Co-Authors:
Chameera Jayarathna, SINTEF Tel-Tek, SINTEF Industry E-mail: chameera.jayarathna@sintef.no
Chandana Ratnayake, University of South-Eastern Norway, & SINTEF Tel-Tek, SINTEF Industry E-mail: chandana.ratnayake@sintef.no

1 Background

In 1889, the melted cryolite-alumina electrolysis process known as Hall-Héroult was started, and the commercial production of metallic aluminum started, and this process has been used almost exclusively in the aluminum production industry until [1]. In the electrolytic process, aluminum oxide is dissolved in molten cryolite (Na_3AlF_6) and afterward electrolytically reduced to aluminum at almost 960°C. Carbon anodes are used in the process, which is consumed during electrolysis, resulting in the formation of CO_2. Even though the manufacturers have gradually improved their performance, this process suffers from relatively high heat loss from the electrolytic cells and increased CO_2 emissions from the anodes.

In the current study alternative, aluminum processing strategies are investigated, and the smelting process combined with chlorination is identified as most convenient with potentially low greenhouse gas (GHG) emissions. Alumina chlorination with a basic fluidized bed reactor FBR is previously done by Alcoa® corporation in 1973 [2].

The present study optimizes and develops the previous study [3] on alumina chlorination in the fluidized bed reactor based on CPFD simulation that can be effectively used for aluminum production.

2 Aims

This study aims to optimize and develop the pre-designed alumina chlorination fluidized bed reactor to achieve the minimum particle outflow, improving the hydrodynamics inside the reactor by minimizing the channeling effect in the dense phase bed and modifying the highly sensitive parameters using CPFD simulations.

3 Methods

Modifications to the geometry: The reactor geometry has been changed from a regular cylindrical shape to a reactor with complex geometry (an extended cross-sectional area on top) (Figure 3.1). The resulted increase in the area leads to a drop of the fluid's superficial velocity gradually, and as a result, particles return to the bed instead of escaping through the outlet.

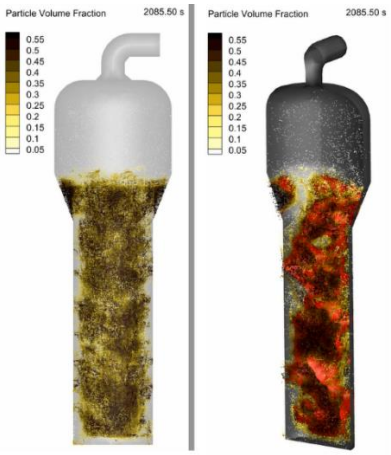

Figure 3.1: Modified geometry of chlorination reactor

Fluid Injection Pattern: Previously, a uniform injection through the bottom of the reactor was used. A non-uniform gas injection pattern (Figure 3.2) with higher velocity in the middle and gradually decreasing toward the inner walls (Figure 3.3) and solved the channeling problem.

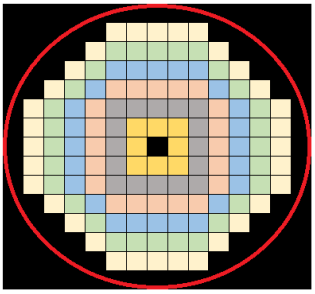

Figure 3.2: Defining non-uniform ring injection in Barracuda

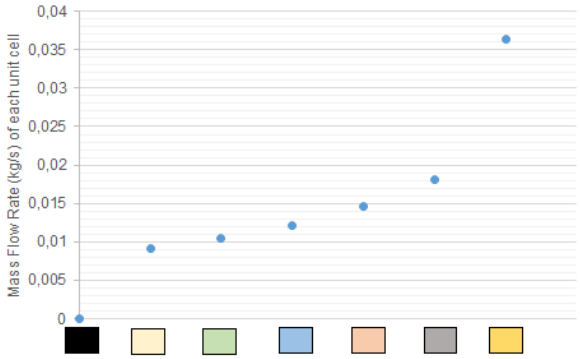

Figure 3.3: Inlet gas (CO+Cl2) mass flow rate of each cell

Particle sphericity and voidage: practically, these parameters cannot be calculated easily and need special high-tech lab instruments and procedures. The literature suggests a wide range for alumina sphericity (between 0.3 – 0.9). To get closer to the acceptable range for the sample, an experiment has been done using a microscope (Figure 3.4).

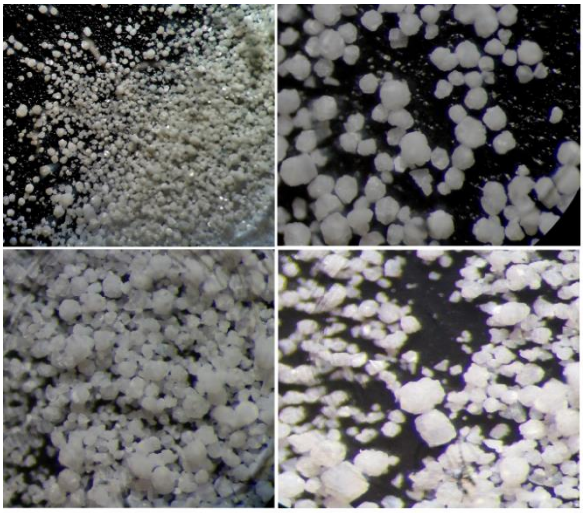

Figure 3.3: Alumina sample under the microscope[1]

4 Results

The results show that the optimized geometry has a significant effect on the particle outflow.

Table 4.1: Particle outflow (kg/s) in different cases

	Uniform Distribution	Non-Uniform Distribution
Cylindrical	0.38	0.59
New Design	0.15	0.0004

Applying a non-uniform inlet flow pattern has reduced the channeling effect, and less scape through the sidewall has been observed.

[1] Nikon smz745T

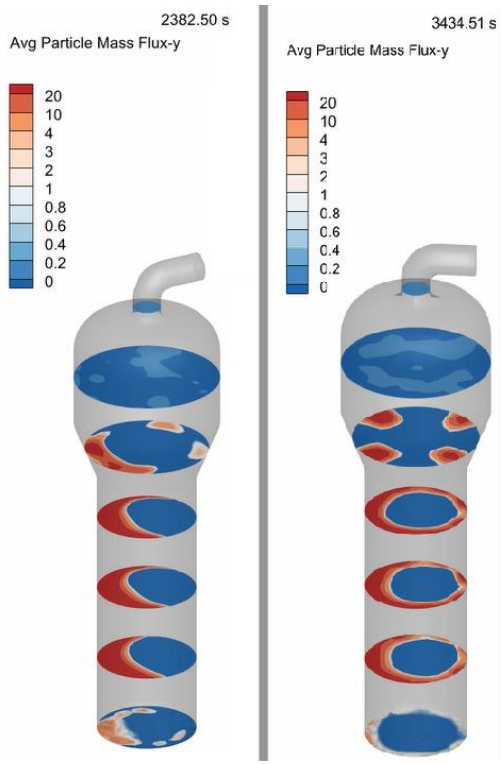

Figure 4.1: Average particle mass flux (kg/sm2) for non-uniform (left) and uniform (right) injection

5 Conclusions and future development

The modified geometry leads to minimizing the particle outflow significantly and helps the reactor's hydrodynamics. On the other hand, In contrast with simple cylindrical geometry, the non-uniform gas inflow reduces the particle outflow considerably. Combining geometrical modification and change in gas injection, the reactor has now shown quite promising performances.

References

[1] S. Prasad, "Studies on the Hall-Heroult Aluminum Electrowinning Process," *Journal of the Brazilian Chemical Society,* vol. 11, 05/01 2000.

[2] "Energy Conservation: S. 2176, a bill to provide for a National Fuels and Energy Conservation Policy, to establish an office of Energy Conservation," Interior, Ed., ed: U.S. Government Printing Office, 1973, p. 1315.

[3] Z. Barahmand, C. Jayarathna, C. Ratnayake, "CPFD modeling of the hydrodynamics and reaction kinetics of alumina chlorination in an industrial fluidized bed reactor " in *1st SIMS EUROSIM Conference on Modelling and Simulation*, Finland, 2021 (submitted).

Study of the thermal performance of an industrial alumina chlorination reactor using CPFD simulation

Zahir Barahmand[a,1], Chameera Jayarathna[b], Chandana Ratnayake[a,b]
a University of South-Eastern Norway, Porsgrunn, Norway, [1]zbarahmand@gmail.com
b SINTEF Tel-Tek, SINTEF Industry, Porsgrunn, Norway

Abstract:

As a part of the new sustainable aluminum production process under study, alumina chlorination plays a crucial role. The relevant process is an exothermic reaction in a fluidized bed reactor, where solid alumina reacts with chlorine and carbon monoxide and produces aluminum chloride as the main product of the process, besides carbon dioxide can be separated. The previous studies have assumed an isothermal condition at 700℃, which is the optimum temperature for this reaction. The reactor's temperature should be kept in the range of 650-850℃ (most preferably 700℃) because below that temperature range, the reaction rate drops and above that range, the alumina (which usually is γ-alumina) will be transferred to θ-alumina and α-alumina phases which is not desirable for the purpose.

Based on previous simulation studies (isothermal), the CPFD method has been utilized to thermal study and simulate the overall heat transfer of the system, including convective fluid to the wall, fluid to particle, and radiation heat transfer. By comparing the thermal results from Barracuda®, it is found that the needed total heat duty transferred to the environment agrees well with the Gibbs reactor simulation in Aspen Plus® ($\sim$ 1.6 MW). Radial and axial heat transfer coefficient profiles at different levels show that almost all the heat should be transferred in the lower half of the reactor, making the design more challenging. At the steady-state, the range for the fluid temperature inside the reactor has been recorded 700-780℃.

Keywords:
Heat transfer, fluidized bed reactor, alumina chlorination, exothermic reaction, Barracuda, radiation, thermal simulation, CPFD simulation

Zahir Barahmand*, Chameera Jayarathna, Chandana Ratnayake

Study of the thermal performance of industrial alumina chlorination reactor using CPFD simulation

Keywords: Heat transfer, Fluidized bed reactor, Alumina chlorination, exothermic reaction, Barracuda, radiation, thermal simulation, CPFD simulation

***Corresponding Author:**
Zahir Barahmand, University of South-Eastern Norway, Norway, E-mail: zbarahmand@gmail.com

Co-Authors:
Chameera Jayarathna, SINTEF Tel-Tek, SINTEF Industry E-mail: chameera.jayarathna@sintef.no
Chandana Ratnayake, University of South-Eastern Norway, & SINTEF Tel-Tek, SINTEF Industry E-mail: chandana.ratnayake@sintef.no

1 Background

During the last decades, fluidized bed reactors (FBR) have been used in a wide range of applications in the industry due to the inherited uniform thermal distribution through the reactor, high heat and mass transfer, and flexibility in operation in large-scale applications [1].

In FBR, several heat transfer mechanisms could be identified, such as fluid convection, solid particle conduction or convection, and radiation [2]. In the computational particle fluid dynamics (CPFD) simulation, the following mechanisms can be studied [3]:

1. Convective fluid-to-wall heat transfer
   1.1. Lean-phase heat transfer
   1.2. Dense-phase heat transfer
2. Fluid-to-particle heat transfer
3. Radiation
   3.1. P-1 model [4] for thermal radiation
   3.2. Wall to Particle radiation

2 Aims

The current simulation work aims to study heat transfer between reactive materials in an industrial FBR reactor (dedicated for alumina chlorination) and its wall. To maintain the pseudo-steady-state, the heat produced from exothermic reactions should be transferred outside the reactor (cooling). Further investigations are done on temperature gradient and its variations through the height of the reactor.

3 Methods

Based on defined heat transfer mechanisms in CPFD simulation [3], a lean gas-phase heat transfer coefficient, h_l, and a dense particle-phase heat transfer coefficient, h_d, are combined to form the local fluid-wall heat transfer coefficient, h_{fw}. The function f_d, which is the fraction of contact time by the dense particle phase, is used to weight the fluid-to-wall heat transfer coefficient. The particle volume fraction at the wall, θ_p, and the close-pack value fraction, θ_{cp}, determine the time fraction of dense phase contact, f_d.

$$h_{fw} = h_l + f_d h_d \quad (1)$$

$$f_d = 1 - e^{-10(\theta_p/\theta_{cp})} \quad (2)$$

The lean and dense phase heat transfer coefficients in general forms are given as equation (3) and (4), respectively:

$$h_l = \left(\left(c_0 Re_L^{n_1} Pr^{n_2} + c_1 \right) \frac{k_f}{L} + c_2 \right) \quad (3)$$

$$h_d = \left(c_0 Re_L^{n_1} \right) \frac{k_f}{d_p} \quad (4)$$

The Heat transfer between the fluid-solid phases can be modeled by the fluid to particle heat transfer coefficient (equation 5).

$$h_l = \left(\left(c_0 Re_p^{n_1} Pr^{0.33} + c_1 \right) \frac{k_f}{d_p} + c_2 \right) \quad (5)$$

Thermal radiation between particles and particle, fluid and thermal walls, and fluid and thermal walls is taken into account in the P-1 radiation model. The overall equation in the P-1 radiation model is:

$$\nabla . (\Gamma \nabla G) + 4\left(an^2 \sigma T^4 + E_p\right) - \left(a - a_p\right) G = 0 \quad (6)$$

4 Results

In Barracuda®, the thermal wall of a model applies a user-defined temperature to the reactor wall. Energy can be transferred in and out of the model via the reactor wall depending on the temperature in between the wall and the fluid near the wall.

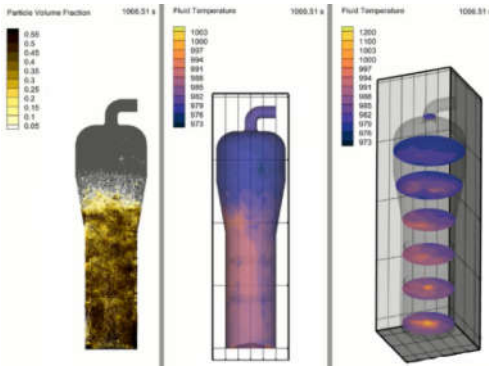

Figure 4.1: Particle and heat distribution through the reactor

In current alumina chlorination reactor, the operational temperature is maintained at around 700℃. Although thermal wall boundary condition keeps the wall temperature 700℃, the temperature inside the reactor, even at a steady-state, is not constant (see Figure 4.1).

The average cooling required for the reactor to maintain steady thermal conditions (at 700℃) is about 1.5 MW (Figure 4.2). However, this heat transfer has not been distributed uniformly through the reactor. A considerably higher fraction of reactions occurs within the lowest part of the reactor, and due to that reason, heat transfer from the lower part should be higher than the top part, theoretically. Instead of one thermal boundary, seven smaller (equal height) thermal walls have been defined to investigate this phenomenon. Confirming the above, Figure 4.3 shows that the heat transfer belongs to the last three walls (top of the reactor) are negligible.

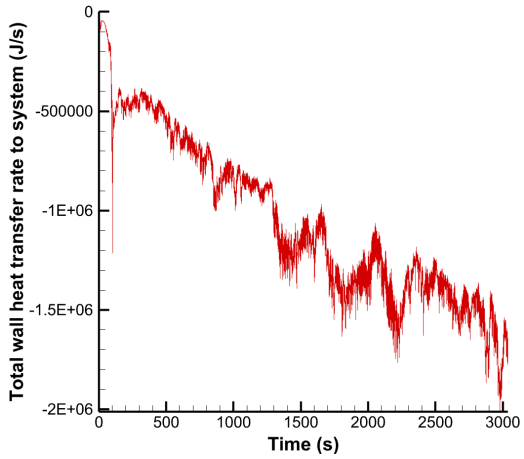

Figure 4.2: Total heat transfer to the environment

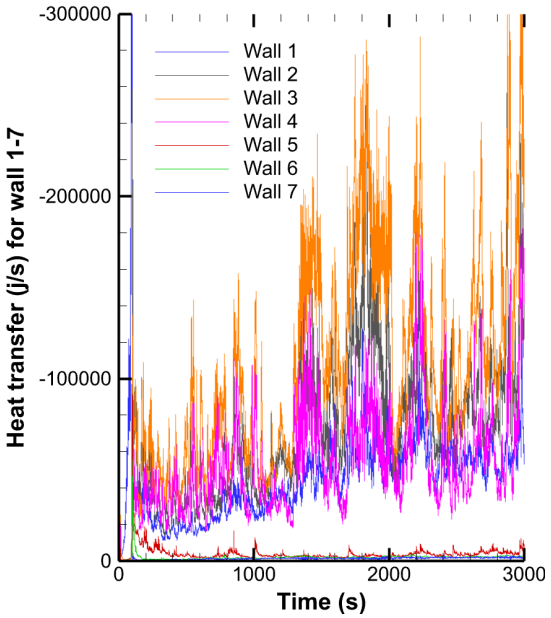

Figure 4.3: Heat transfer of different sections

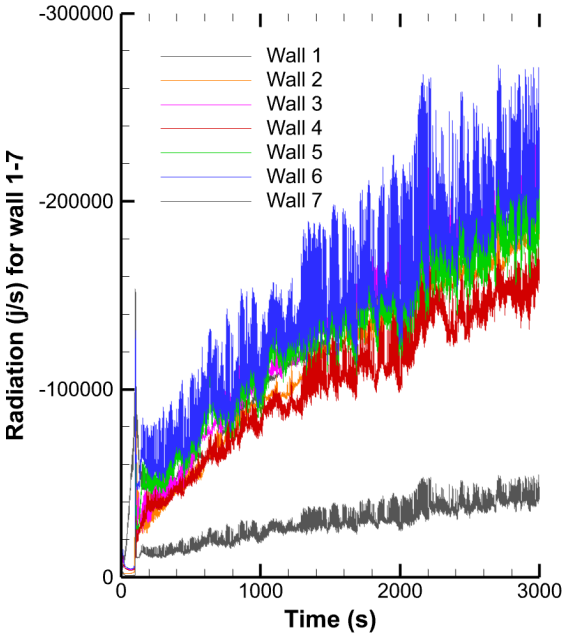

Figure 4.4: radiation of different sections

5 Conclusions and Future Developments

Design an exothermic reactor with an efficient heat transfer performance is probably the most critical task from an engineering point of view. The efficiency of the reaction is highly affected by temperature. The Gibbs reactor simulation in Aspen Plus® validates the heat transfer calculated in thermal analysis by CPFD simulation. At the steady-state, the reactor temperature range is 700-780℃.

References

[1] Y. Zhang and Q. Wei, "CPFD simulation of bed-to-wall heat transfer in a gas-solids bubbling fluidized bed with an immersed vertical tube," *Chemical Engineering and Processing: Process Intensification,* vol. 116, pp. 17-28, 2017/06/01/ 2017.

[2] B. Nauman, *Handbook of Chemical Reactor Design, Optimization, and Scaleup*, First ed.: McGraw-Hill Professional, 2001.

[3] (2021, 12.04.2021). *Barracuda Virtual Reactor User Manual*. Available: https://cpfd-software.com/user-manual/index

[4] S. Sazhin, E. Sazhina, O. Faltsi-Saravelou, and P. Wild, "The P-1 model for thermal radiation transfer: Advantages and limitations," *Fuel,* vol. 75, pp. 289-294, 02/01 1996.

Sensitivity and uncertainty analysis in a fluidized bed reactor modeling

Zahir Barahmand[a,1], Chameera Jayarathna[b], Chandana Ratnayake[a,b]
a University of South-Eastern Norway, Porsgrunn, Norway, [1]zbarahmand@gmail.com
b SINTEF Tel-Tek, SINTEF Industry, Porsgrunn, Norway

Abstract:

Such as many real applications in the world of fine powders and small particles, depending on how the method is accurate, there are uncertainties and vagueness in the parameters such as particle size, sphericity, void fraction, envelope density, etc. In some cases, there are different methods to measure a parameter, such as a particle size that depends on the method (based on length, weight, and volume); the measured value may be significantly different. Therefore, there is no crisp or certain parameter in many cases because of the fine powders' uncertain nature. On the other hand, being characteristic of the dynamic systems, physical parameters such as temperature, pressure, etc., are fluctuating but can be kept in an acceptable range, affecting the main design parameters such as fluid density and dynamic viscosity.

Most of the traditional tools and methods for simulating, modeling, and reasoning are crisp, deterministic, and precise, but these values are estimated or changing (randomly or stochastically). Several approaches can describe this phenomenon when it comes to the uncertainty that the mathematical tools are one of the best. With this method (using fuzzy set theory), linguistic variables or ranges can be converted to mathematical expressions, and consequently, instead of crisp values, these can be applied to the equations. The uncertainty analysis can be more important when the model is highly sensitive to one parameter. The sensitivity analysis has shown that the solid void fraction has the highest, and the fluid density has the lowest sensitivity.

Keywords:
Sensitivity analysis, uncertainty analysis, fluidized bed reactor, reactor design, fuzzy set theory

Zahir Barahmand*, Chameera Jayarathna, Chandana Ratnayake

Sensitivity and uncertainty analysis in a fluidized bed reactor modeling

Keywords: Sensitivity analysis, Uncertainty analysis, Fluidized bed reactor, reactor design, Fuzzy set theory

***Corresponding Author:**
Zahir Barahmand, University of South-Eastern Norway, E-mail: zbarahmand@gmail.com

Co-Authors:
Chameera Jayarathna, SINTEF Tel-Tek, E-mail: chameera.jayarathna@sintef.no
Chandana Ratnayake, University of South-Eastern Norway, & SINTEF Tel-Tek, SINTEF Industry E-mail: chandana.ratnayake@sintef.no

1 Background

In general, a solid particle in a fluid behaves in a state of uncertainty. This fact motivates to study the behavior of uncertain phenomena. Most of our traditional formal modeling, reasoning and computing tools are crisp, deterministic, and precise. In order to model uncertainty, a powerful mathematical tool is needed. In modern modeling, modelers believe that the world is not just black and white, and we have a spectral grey between them.

Many factors may cause uncertainty. The primary source of uncertainty is the lack of information. For instance, there is no precise data about particle parameters such as sphericity or envelope density in many cases. As another example, in particle size distribution, the measurement error is the most crucial factor for the uncertainty [1]. Complexity, conflicting nature of pieces of information, ambiguity, and subjective opinions are other sources.

With this method, linguistic variables or ranges can be converted into mathematical expressions, and consequently, instead of crisp or deterministic values, these can be applied to the equations. The uncertainty analysis can be more important when the model is highly sensitive to one parameter.

2 Aims

Many parameters are used to design a fluidized bed reactor, and there are uncertainties about the accuracy of these values. The present study aims to find the parameters that the model is sensitive to and, consequently, develop a mathematical solution to apply the model's uncertainties.

3 Methods

Sensitivity Analysis

This unique technique is used to define how an independent variable will impact a specific dependent variable under a given set of assumptions.

Table 3.1: Sensitivity Analysis of minimum fluidization velocity (fluid density vs. void fraction)

	Output	Input
	u_{mf}	ε_{mf}
Initial	0.00452	0.4
Secondary	0.01059	0.5
% changed	134%	25%
Sensitivity	134/25 = 5.36	

	u_{mf}	ρ_g
Initial	0.01059	0.93
Secondary	0.01059	2
% changed	0%	115%
Sensitivity	0/115 = 0	

Table 3.1 shows that, for example, the minimum fluidization velocity is not sensitive to the gas density, has low sensitivity to dynamic viscosity, is sensitive to particle size and sphericity, and highly sensitive to the void fraction. This means the void fraction should be calculated and used as accurately as possible.

Mathematical Model

For each uncertain parameter, instead of choosing a single crisp value for parameters, a function (triangular or trapezoidal) can be introduced based on fuzzy set theory [2]. As an example (Figure3.1), instead of using an average particle size computed from a distribution, a closest fitted trapezoidal function can be used.

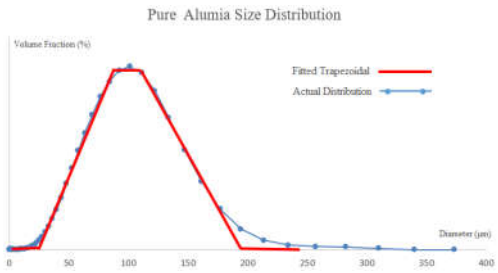

Figure 3.1: Alumina size distribution and fitted function

4 Results

As a numerical example, the following assumptions have been considered. The pure aluminum oxide powder (Al_2O_3) with average sphericity of 0.85 (while the experimental observation shows the range is between 0.7-0.9 and 0.85 is chosen for the average value). The experimentally determined void fraction is 0.44, which can vary in the range of 0.40-0.50. Particle size distribution is according to Figure 3.1, and the red line is the closest fitted trapezoidal function to this distribution (average diameter is 98 µm). The alumina (aluminum oxide) has the envelope and bulk density of 2000-2200 kg/m^3 and 980-1050 kg/m^{3,} respectively. On the other hand, the reactor temperature is kept in the range of 650-750℃. This means the fluid's physical properties are changing respectively.

Considering all uncertain and certain parameters together, the calculated minimum fluidization velocity is given in Figure 4.1.

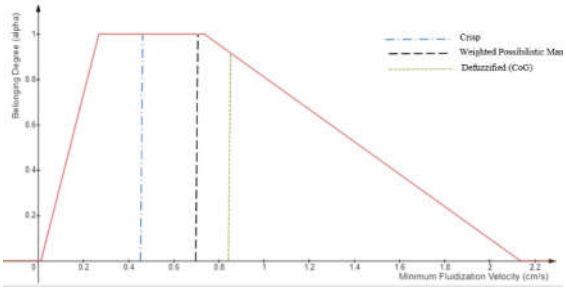

Figure 4.1: Calculated Fuzzy minimum Fluidization Velocity

5 Conclusions and future development

The results show that the minimum fluidization velocity without considering uncertainty is calculated as 0.42 cm/s, but there is more information when this method is utilized. This analysis illustrates that all in all and different possible conditions, the minimum fluidization velocity is not more than 2.15 cm/s and not less than 0.06 cm/s, but the velocities in the range [0.26, 0.73] cm/s is more possible.
Applying this method to fluidized bed calculation gives designers and analysts a more dependable tool to analyze the uncertainty. As can be seen in the result, the fuzzy model is efficient and valuable, and without introducing this method, it would not be possible to consider this genuine uncertainty.

References

[1] A. Tinke, *Minimum Sample Size and Measurement Uncertainty in the Particle Size Distribution Analysis of Powders*, 2020.
[2] L. A. Zadeh, "Fuzzy sets," *Information and Control,* vol. 8, pp. 338-353, 1965/06/01/ 1965.

The effect of impurities on γ-Alumina chlorination in a fluidized bed reactor: A CPFD study

Zahir Barahmand[a,1], Chameera Jayarathna[b], Chandana Ratnayake[a,b]
a University of South-Eastern Norway, Porsgrunn, Norway, [1]zbrahmand@gmail.com
b SINTEF Tel-Tek, SINTEF Industry, Porsgrunn, Norway

Abstract:

Alumina is one of the most widely used pure chemicals on the market today, with annual production totaling millions of tons of highly pure alumina. A large portion of this output is used to make aluminum, but a growing amount is used in ceramics, refractories, catalysts, and other various products. In nature and different thermal conditions, alumina is found in different phases. These phases can be transformed into each other in different temperatures. Among these, γ-alumina is used in the chlorination process in the aluminum production industry because of the higher reaction rates. α-Alumina has outstanding mechanical properties and superb thermal properties at high temperatures; polycrystalline α-alumina is used as a structural ceramic. As a result, this type has much lower reaction rates in the chlorination process. Previously, the chlorination of pure γ-alumina has been considered in the CPFD simulations. Extending previous researches, the present study investigates the effect of seven percent α-Alumina impurity on the overall chlorination reaction conversion, bed hydrodynamics, and composition of the outflow of the reactor using Barracuda®.

Keywords:
Barracuda, CPFD simulation, α-Alumina chlorination, γ-alumina chlorination, Fluidized bed reactor (FBR),

Zahir Barahmand*, Chameera Jayarathna, Chandana Ratnayake

The effect of impurities on γ-Alumina chlorination in a fluidized bed reactor: A CPFD study

Keywords: Barracuda, CPFD simulation, α-Alumina chlorination, γ-alumina chlorination, Fluidized bed reactor (FBR),

***Corresponding Author:**
Zahir Barahmand, University of South-Eastern Norway, E-mail: zbarahmand@gmail.com

Co-Authors:
Chameera Jayarathna, SINTEF Tel-Tek, SINTEF Industry E-mail: chameera.jayarathna@sintef.no
Chandana Ratnayake, University of South-Eastern Norway, & SINTEF Tel-Tek, SINTEF Industry E-mail: chandana.ratnayake@sintef.no

1 Background

Experiments of different CO/Cl_2 molar ratios revealed that CO/Cl_2 = 1 has the highest chlorination rate, and this is clear from overall chlorination reactions, which involve equimolar concentrations of CO and Cl_2 [1].
It is investigated [2] in an experiment with a fluidized bed reactor (0.075m diameter) and 66 mm of bed height, with 0.25 kg of Al_2O_3 particles with the mean size of 0.06-mm and approximately 3.9 moles per second of an equimolar CO and Cl_2 mixture flow.

2 Aims

In the previous study [3][1], the chlorination of the pure γ-alumina has been taken into account. The given alumina composition shows almost 7 percent contamination of α-alumina. The present study aims to study the conversion efficiency and composition of the outflow of the reactor, based on a CPFD simulation in the presence of α-alumina.

3 Alumina Chlorination

3.1 γ-Alumina Chlorination Kinetics

In 1981, Toth et al. [4] studied the temperature and partial pressure dependency and the influence of photo-irradiation of the reactive gases to find reaction rate for γ-alumina chlorination with carbon monoxide and chlorine in different temperatures.

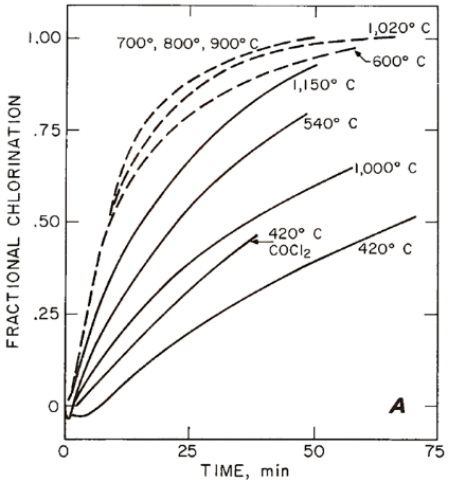

Figure 3.1: Chlorination of γ-alumina with CO/Cl2=1. Solid lines are for 9.7 mm particles; broken lines are for 0.125 mm particles [5].

Figure 3.1 further verifies the above described phenomenon, as the results of an experimental investigation [5] that has studied chlorination of two different sizes (7.9 mm and 0.125 mm) of γ-alumina with an equimolar mixture of CO and Cl2. The particle's surface area has a direct impact on the reaction [6]. As per the findings of this experiment, it is expected that the fluidized bed's reaction rate will be much quicker than the experiment, when very fine alumina particles are used in the reactor.

3.2 α-Alumina Chlorination Kinetics

As [7] reported, the reaction rate and activation energy of the α-alumina in a carbo-chlorination reaction is much lower than that of the γ type. In the range 800-900°C, the activation energy is 32$\pm$2.5 kJ/mole. In general,

$$r_{exp} = K\left(P_{cl_2}\right)^m (P_{CO})^n \quad (1)$$

where, P_x is the partial pressure of component x, m and n are reaction orders, K is the reaction constant, and r_{exp} is an experimentally calculated reaction rate. Table 3.1 gives calculated m and n in different temperatures.

[1] Submitted paper for SIMS 2021;

Table 3.1: Reaction orders in different temperatures

	Reaction Temperatures (°C)				
	800	**835**	**870**	**910**	**950**
m	0.71	0.60	0.59	0.56	0.48
n	0.77	0.72	0.66	0.65	0.65

The rate expression for the particular case considered under the experiment considerations can be written as,

$$r_{exp} = \tilde{k}\left(P_{cl_2}\right)(P_{CO}) \qquad (2)$$

where, $\tilde{k}$ is the apparent rate constant in $gg^{-1}min^{-1}atm$. Table 3.2 shows the different values for the apparent rate constant,

Table 3.2: Values of $\tilde{k}$ obtained by regression analysis of r_{exp} vs $\left(P_{cl_2}\right)(P_{CO})$ results

T (°C)	800	835	870	910	950
$\tilde{k}$	0.0234	0.0256	0.0281	0.0313	0.0368
$ln\tilde{k}$	-3.755	-3.665	-3.572	-3.464	-3.302
10000/T	9.3197	9.0253	8.8479	8.4531	8.1766

4 Results and Discussion

Figure 4.1 shows the α and γ-type alumina particle distribution through the reactor. However, because of the densification, α-alumina is relatively heavier than the γ-alumina; in steady-state, it has been distributed homogeneously.

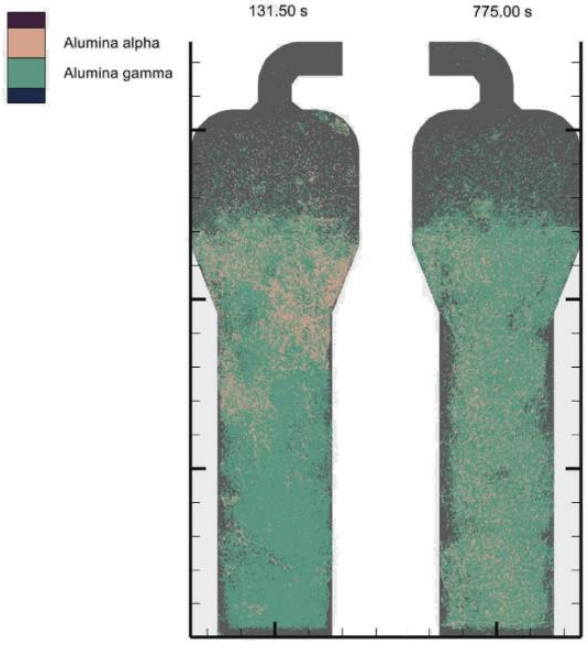

Figure 4.1 Different types of alumina particle's distribution after fluidization (left) in steady-state (right)

Relevant data of the particle outflow is given in Figure 4.2. The average escaping rate of α-alumina particles has been recorded as 6 g/s. In comparison, the corresponding value for γ-alumina is observed as 150 g/s. This clearly confirms that the α-alumina may not easily leave the system because of the higher density.

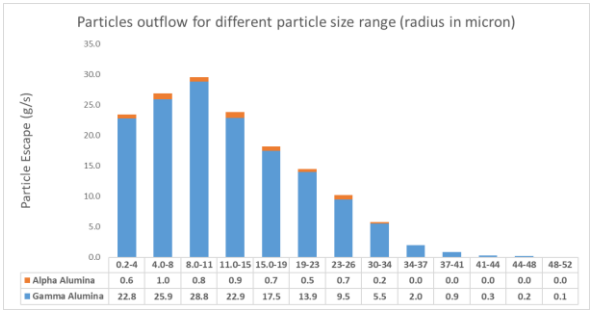

Figure 4.2 Different types of alumina particle's outflow (g/s)

5 Conclusion and Future Works

The results show that the alumina impurity does not affect the chlorination reaction itself. The overall particle outflow has become slightly higher in case of pure γ-alumina. Almost only 3 percent of the total particle outflow belongs to α-alumina, and consequently in long run, that may cause α-alumina accumulation in the reactor, which is not favorable. In the operating temperature, the reaction rate of α-alumina is much slower, and the accumulation of α-alumina will affect the overall reaction negatively. As remedies, adding a circulation path or speeding up the fluid inside the reactor to a certain point may be helpful, that can be investigated in future works.

References

[1] N. A. Gokcen, "Rates of chlorination of aluminous resource," United State1983.

[2] H. P. M. H. P. Alder, and W. Richarz, "Kinetic Study of the Alumina Chlorination.," *Light Metals,* vol. 1, pp. 219-232, 1977.

[3] C. J. Zahir Barahmand, Chandana Ratnayake, "CPFD simulations on a chlorination fluidized bed reactor for aluminum production: an optimization study," in *1st SIMS EUROSIM Conference on Modelling and Simulation*, Finland, 2021.

[4] A. Tóth, I. Bertóti, and T. Székely, "Kinetics of γ-alumina chlorination by carbon monoxide and chlorine," *Thermochimica Acta,* vol. 52, pp. 211-215, 1982/01/16/ 1982.

[5] D. Milne, "The Chlorination of Alumina and Bauxite with Chlorine and Carbon Monoxide," *Proc Australas Inst Min Metall,* vol. 260, pp. 23-31, 12/01 1976.

[6] D. Kunii and O. Levenspiel, "Fluidization Engineering," Second Edition ed Boston: Butterworth-Heinemann, 1991, p. 497.

[7] M. Soleiman and Y. Rao, "Kinetics and Mechanism of Chlorination of Alumina Grains with He–CO–Cl2 Gas Mixtures—I. Experimental," *Canadian Metallurgical Quarterly,* vol. 26, pp. 207-215, 07/01 1987.

Appendix E: Project Task Description

University of South-Eastern Norway

Faculty of Technology, Natural Sciences and Maritime Sciences, Campus Porsgrunn

FMH606 Master's Thesis

Title: Design of an Industrial Chlorination Reactor using CPFD Simulations

USN supervisor: Chandana Ratnayake

External partner: Chameera Jayarathna, SINTEF Tel-Tek

Task background:
The preliminary studies have shown that the CPFD simulations can be effectively used in designing and optimising performance of complex gas-particle flow situations in Fluidised Bed Reactors (FBRs). Alcoa has used FBR technology to produce aluminium chloride ($AlCl_3$) through a chlorination process of alumina particles and then reduce $AlCl_3$ to metal aluminum, as an alternative to the Hall-Heroult electrolyte process of aluminium production. The chlorination reactor of the Alcoa process is a complex unit, operated under chemically aggressive environment, where kinetics and hydrodynamics play crucial roles influencing its reliable and optimised operation.

Task description:
The project is aimed to design and optimise a fluidised bed chlorination reactor unit for an industrial application with the help of CPFD simulations (using Barracuda®). Most Important components (finding the optimum bed height base on the proper reaction rate, optimum reactor dimension to minimize the particle outflow as the highest priority and design and simulation of the circulating component (cyclone) as the possible next priority) will be considered in the design and their performances will be analysed to obtain the requirements of the application.

Student category: PT & EET students

The task is suitable for online students (not present at the campus): ~~Yes~~/No

Practical arrangements:
The software licences are provided by USN. The required training of using software and simulation methods will be assisted by SINTEF Tel-Tek.

Supervision:
As a general rule, the student is entitled to 15-20 hours of supervision. This includes necessary time for the supervisor to prepare for supervision meetings (reading material to be discussed, etc).

Signatures:

Supervisor (date and signature): 31-Jan. 2021

Student (write clearly in all capitalized letters): ZAHIR BARAHMAND

Student (date and signature): (29-Jan-2021)